ACCURACY OF IODINE-131 ACTIVITY QUANTIFICATION AND DOSIMETRY FOR THREE-DIMENSIONAL PATIENT-SPECIFIC MODELS

By

John Enyi Ejeh

This thesis is submitted in fulfilment of the requirements in respect of the degree of Doctor of Philosophy (PhD) in the Department of Medical Physics, in the Faculty of Health Sciences, at the University of the Free State

March 29, 2019

Promoter: Dr J.A. van Staden

Co-promoter: Dr H du Raan

DECLARATION

I declare that the Doctoral degree research thesis that I herewith submit for the Doctoral degree qualification at the University of the Free State is my independent work and that I have not previously submitted it for a qualification at another institution of higher education.

Bloemfontein

March 29, 2019

John Enyi Ejeh

DEDICATION

To the memory of my Father, Clement, who exposed me to education. Not only that, but he also fanned the embers, of the love for education, into the fire that culminated into this PhD; and to Bridget and Danielle for their understanding, support, and prayers during the period of my studies

"No king goes to war without planning"

Paraphrasing, Luke 14:31 – 32

(The African Bible)

ACKNOWLEDGEMENT

I Thank God for his love and blessings. I owe a debt of gratitude to my Promoter, Dr J.A. van Staden and co-Promoter, Dr H. du Raan. Their vast knowledge in nuclear medicine Physics, their willingness to share it with me, and their enthusiasm and passion for this project were very valuable for this degree. During the duration of the study, the relationship we had was more than a supervisor-student relationship, for this, I am and will eternally remain grateful. Their guidance throughout this period showed that they are good mentors. Thank you for this excellent mentorship.

I thank Prof William Rae and Dr Frederik du Plessis for their support, Prof Charles Herbst for providing technical support and developing the two in-house software packages used in this study, and Prof Michael Ljungberg of Lund University, Sweden for collaborating with us. He made SIMIND and LundADose freely available to us and also provided technical support. Dr Gert Engelbrecht, the Head of Nuclear Medicine and members of staff of the department, are highly appreciated for their immense support and for facilitating the access to patients' images. Modise Mongane and Dr Matthew Owolabi's friendship cannot be forgotten, it made the loneliness to be bearable. My thanks also go to other members of the Medical Physics department (staff and postgraduate students) for the many good moments we shared together. Particular reference is made to Michaella Morphis who put me through with the various software used for this project, thank you very much.

I am indebted to the Postgraduate School of UFS for the award of the PhD research bursary (partial tuition fee waiver) for the duration of the study and the additional funding that was provided through my supervisors. The Faculty of Health Sciences, UFS, is acknowledged for the award of the Postgraduate research bursary, for one year. I am also grateful for funding received from the NRF/STINT grant awarded to my supervisors. I wish to acknowledge both the Health Sciences Research Ethics Committee of the Faculty of Health Sciences, University of Free State and the Free State Department of Health for granting ethical approval for this project.

Finally, I am grateful to the Management of University College Hospital Ibadan for the three-year study leave given to me to undertake this study. Gratitude to my family and friends for their support, especially, Baba Manu, Bridget, and Danielle for spiritual support through prayers.

ABSTRACT

Iodine-131 (^{131}I) therapy of thyroid related and other diseases is limited by critical organ toxicity. Therefore, accurate activity quantification and dose calculation are important to optimise dose to tumours while limiting dose to critical organs. The aim of this study was to evaluate the accuracy of ^{131}I activity quantification and dosimetry for three-dimensional (3-D) patient-specific models.

Retrospective patient Computed Tomography (CT) data were segmented to create clinically realistic patient 3-D voxel-based models. These were used to simulate Single Photon Emission Computed Tomography (SPECT) data with a Monte Carlo (MC) simulation software, which was validated against physical measurements. The simulated SPECT data were reconstructed using an ordered-subsets expectation maximization (OS-EM) algorithm which includes scatter correction, CT-based attenuation correction, and 3-D collimator-detector response compensation. Predetermined recovery coefficients were used to compensate for partial volume effects. Image counts were converted to activity by using a predetermined calibration factor.

The patients' reconstructed activity maps and density maps were used to perform 3-D dosimetry with the MC program, LundADose. LundADose calculated mean tumour and organ absorbed doses were compared with OLINDA/EXM calculated mean absorbed doses using statistical analysis.

Validation of the simulation software resulted in a percentage difference of -6.50 % between the measured and simulated extrinsic energy resolution at the ^{131}I peak energy of 364 keV and -18.57 % error for the measured and simulated intrinsic energy resolution. The measured and simulated FWHM and FWTM of the camera for system spatial resolution had percentage differences of -7.41% and -7.38 % and an error of -1.50 % and -2.6 % for system sensitivity and collimator septal penetration fraction.

SPECT activity quantification was evaluated by comparing the true tumour activities defined for the patient models with the quantified activities obtained from the models' reconstructed SPECT images. The quantification error for the studied patient models was < 9.0 % and < 5.1 % for 3.0 and 6.0 cm spherical tumours situated in the lungs (mean values were 3.9 ± 3.3 % and -1.6 ± 1.9 %). The error for the two tumours in the liver was < 11.2 % (mean values of 7.7 ± 3.9 % and 8.4 ± 2.9 %).

The mean percentage differences between the mean absorbed doses calculated by LundADose and OLINDA/EXM for the left lung, right lung, liver, 3.0 cm ‘tumour’ and 6.0 cm ‘tumour’ were comparable. These mean percentage differences were -2.23 ± 1.98 %, -3.06 ± 1.67 %, 1.31 ± 4.15 %, -28.44 ± 18.36 %, and -5.10 ± 2.87% for the listed organs and tumours when the 3.0 cm tumour was located in the lung and the 6.0 cm tumour in the liver. For the scenario where the 3.0 cm tumour was positioned in the liver and the 6.0 cm tumour in the lung, the corresponding results were -2.84 ± 3.42 %, -1.49 ± 2.68 %, 3.97 ± 4.12 %, -28.80 ± 5.05 %, -8.21 ± 17.06 %.

The SIMIND MC model of the gamma camera was accurately validated with good agreement between results calculated from the physical measurements and simulation. Good accuracy of ^{131}I activity quantification and 3-D dosimetry was found for 3-D patient-specific models. Statistical analysis of the results of the comparison of LundADose and OLINDA/EXM showed that the two dosimetry programs were strongly correlated with R^2 values ranging from 0.85 to 1.00 for the mean absorbed dose in the various organs and tumours. Furthermore, the two (MC and MIRD) methods were found to agree well using Bland-Altman analysis of the dosimetry results. For ^{131}I, activity quantification and dosimetric accuracy better than 10 % were achieved using state-of-the-art hybrid equipment and sophisticated correction methods for image degrading factors.

Keywords:

SIMIND

Voxel-based 3-D models

Monte Carlo simulation

^{131}I activity quantification accuracy

^{131}I therapy

LundADose

OLINDA/EXM

Patient-specific

^{131}I dosimetry

Bland-Altman plot

LIST OF ACRONYMS

^{111}In	Indium-111
^{123}I, ^{124}I, ^{131}I	different isotopes of Iodine (Iodine-123, 124, and 131)
2-D, 3-D	two-dimension (al), three-dimension (al)
^{90}Y	Yittrium-90
^{99m}Tc	Technetium-99m
Bq, MBq, GBq	becquerel, Megabecquerel, Gigabecquerel
CDR	Collimator-detector response
CF	Calibration factor
CI	Confidence interval
CT	Computed tomography
DICOM	Digital imaging communication
DTC	Differentiated thyroid cancer
EBRT	External beam radiotherapy
EGS4	Electron gamma shower version 4
ESSE	Effective source scatter estimation
FBP	Filtered back projection
FOV	Field of view
FWHM	Full width at half maximum
FWTM	Full width at tenth maximum
HEAP	High energy all-purpose collimator

IAEA	International Atomic Energy Agency
keV, MeV	kiloelectronvolt, Megaelectronvolt
LET	Linear energy transfer
LL, RL, Liv	Left lung, Right lung, Liver
LLoA	Lower limit of agreement
MC	Monte Carlo
Gy, mGy	gray, milligray
MIRD	Medical internal radiation dose
ML-EM	Maximum likelihood expectation maximization
MRI	Magnetic resonance imaging
NaI (Tl)	Sodium iodide (Thallium)
NaI	Sodium iodide
NEMA	National Electrical Manufacturers Association
NET (s)	Neuroendocrine tumour (s)
NHL	Non-Hodgkin Lymphoma
NM	Nuclear medicine
OLINDA/EXM	Organ level internal dose assessment/exponential modelling
OS-EM	Ordered subset expectation maximization
SE	Standard error
PET	Positron emission tomography
PET/CT	Positron emission tomography/Computed tomography
PET/MRI	Positron emission tomography/Magnetic resonance imaging
PIXEL	Picture element

PMT	Photomultiplier tube
PVC	Partial volume correction
PVE	Partial volume effect
RAI	Radioiodine
RC (s)	Recovery coefficient (s)
RNT	Radionuclide therapy
ROI	Region of interest
SIMIND	Simulating medical imaging nuclear detectors
SPECT	single photon emission computed tomography
SPECT/CT	Single photon emission computed tomography/Computed tomography
TAC	Time-activity curve
Te	Tellurium
TRT	Targeted radionuclide therapy
ULoA	Upper limit of agreement
VOI (s)	Volume of interest (s)
VOXEL	Volume element

TABLE OF CONTENTS

CHAPTER ONE: Introduction

Table of Contents

1.1 Nuclear medicine

Nuclear medicine (NM) is a branch of medicine that utilizes ionizing radiation emanating from radionuclides in the diagnosis and treatment of different diseases. The diagnostic aspect of NM is aimed at making use of the information provided by the distribution of a pharmaceutical, which is labelled with a radionuclide, in space and/or in time, inside the human body. The information provided by this distribution pertains to the biochemical or physiological functioning or medical condition of a specific human body system, organ, or in a tumour within the body. The distribution of the radiopharmaceutical inside the human body can be imaged by using an imaging device and the image obtained can be valuable for medical diagnosis and for monitoring the response to the treatment of a disease (Lyra, 2009). Treatment planning can also be performed based on the imaging of the distribution of the radiopharmaceutical for radionuclide therapy (RNT).

The therapeutic aspect of NM deals mainly with the use of radionuclides to treat cancerous tumours of various kind, non-malignant conditions such as benign thyroid disorders, inflammatory joint disease etc. In a fashion similar to the diagnostic aspect, radiolabelled pharmaceuticals (radiopharmaceuticals) designed to have a high affinity for tumour tissues are administered to patients. The radiopharmaceuticals then accumulate and remain in these tumours for a period of time to irradiate diseased cells due to particles emanating from its radioactive moiety.

The fascinating thing about NM is the fact that its usefulness goes down to the cellular level. Therefore, it is able to diagnose diseases at the earliest stage possible (Mariani *et al.*, 2010) and it can also target diseases for destruction at the cellular environment. In NM, cancerous cells are also easily targeted at the molecular level. At the molecular level, high levels of radiation can be delivered to the diseased cells with minimal or no damage done to the surrounding healthy cells. NM thus can provide a means to combine diagnostic and therapeutic procedures (Carrasquillo, Pandit-taskar and Chen, 2016) therefore, coupled with rapid development in radiochemistry and radiopharmacy, a phenomenal growth is seen in RNT and molecular imaging in NM (Ahmadzadehfar and Essler, 2018).

In NM diagnosis, tracer amount of radiopharmaceuticals emitting gamma rays are either administered intravenously, orally, through inhalation etc. The radiopharmaceuticals are in such minute quantities that they do not cause any physiological change in the human body system. A gamma camera (also called Anger camera) can then be used to detect the gamma rays emitted from the patients (Powsner, Palmer and Powsner, 2013). The energy of some of the gamma rays is deposited in the detector of the gamma camera. The gamma camera uses information on the origin of the detected gamma rays to create an image of the patient's organ of interest from which a diagnosis can be made. NM therapy usually makes use of the targeting capability of labelled molecules, to which the radionuclide is attached, to selectively deliver cytotoxic levels of radiation to the disease site (Das and Pillai, 2013).

The usefulness of images in patient management cannot be over-emphasised. The information from medical images (NM images inclusive), can be used to perform non-invasive procedures in many patients. These images, to some extent, give a true representation of the medical condition of internal structures in such a way that diagnosis can relatively easily be made without the need for invasive interventions. Therefore, the number one benefit of the use of medical images is the ease of non-invasive diagnosis. Other areas where NM images play an important role are in the localization and staging of diseases such as cancer, treatment planning, and in the monitoring of treatment response. (Foster *et al.*, 2014; Velikyan *et al.*, 2015). NM images (especially single photon emission tomography (SPECT), positron emission tomography (PET), and hybrid – combination of a functional NM image and an anatomical [CT or MRI] image) are very useful in the treatment planning of many cancer patients both for External beam radiotherapy (EBRT) and for RNT. NM images, as important as they are in the tasks of diagnosis, staging, treatment planning and monitoring of therapy, are limited and degraded during the image formation process. Therefore, there is a need to improve the quality of these images if the aim of using them is to accomplish the above-mentioned tasks.

1.2 Radionuclide therapy

NM started with RNT. The use of radionuclides in the treatment of patients dates back as far as the 1900s. During this period, a variety of diseases were said to have been treated ranging from cancer of the skin and breast to epilepsy and syphilis (Eriksson, et. al., 2008). In 1901 radium was used for therapy by placing it in contact with a skin lesion. Thereafter, the first study on the intravenous injection of radium for therapy of different diseases was said to have been published in 1921 (Yeong, Cheng and Ng, 2014). The first human study employing radioactive tracers (diagnostic NM) was done by Blumgart and Weiss in 1927 (Cherry, Sorenson and Phelps, 2012). In 1936, phosphorus-32 was used to treat polycythaemia vera. This was followed with the administration of strontium-89 for metastatic bone disease in 1941 and iodine-131 (^{131}I) for hyperthyroidism in 1942 (Thomas, 2002; Skanjeti *et al.*, 2015). Since ^{131}I was first used for the treatment of differentiated thyroid carcinoma (DTC) in 1944, it became the therapy of choice for thyroid diseases (Thomas, 2002; Silberstein, 2012). The use of ^{131}I labelled to specific pharmaceuticals also became important for the treatment of other diseases such as neuroendocrine tumour (s) (NET(s)) and Non-Hodgkin Lymphomas (NHL) (Dewaraja *et al.*, 2005; Sisson and Yanik, 2012; Parisi *et al.*, 2016). ^{131}I is also used for the treatment of pancreatic and liver tumours in the form of ^{131}I-lipiodol and ^{131}I-Moabs respectively (Hoefnagel, 1998).

Even with its long history, there is still debate on the most appropriate ^{131}I dose to administer for radioiodine (RAI) ablation therapy (Thomas, 2002; Blumhardt et al., 2014; Skanjeti et al., 2015; Dorn et al. 2003). There is also not much information in the literature concerning the appropriate ^{131}I dose for paediatric patients with DTC (Luster *et al.*, 2017). Both researchers and clinicians alike have not agreed on this issue. Some support the empirical fixed-dose regimen because it is easy to apply. Others support the dosimetry-based method for therapeutic doses because it is more accurate since individualized patient doses are prescribed. Although dosimetry is challenging and specialized knowledge and experience are required to successfully carry out dosimetry, it has been the desire of medical physicists in NM to have routine dose planning in the clinic for each patient, similar to what is done in EBRT.

It was observed in 2007 that there is no existence yet of standard methods either for performing dosimetry or to evaluate the uncertainties inherent in the dosimetric calculations (Gear *et al.*, 2007). In 2018 it was suggested that a comprehensive analysis of uncertainty propagation inherent in every aspect of the dosimetry calculation needs to be obtained and used in NM centres where RNT is carried out (Gear *et al.*, 2018). Again, there is still some resistance among NM practitioners to bringing individualized RNT dose planning in the clinic to reality (Stabin & Flux, 2014). Therefore, dose planning in NM has remained largely in the laboratory and is limited to phantoms and/or clinical trials for newly developed therapeutic and diagnostic agents.

The introduction of hybrid SPECT/CT systems and iterative reconstruction algorithms, due to advances in computer processing power, have led to improved SPECT image quality and more accurate image quantification. Improved image quantification may provide more accurate dosimetry results which, coupled with the development of new easy-to-use software for dosimetry by different vendors, may facilitate wider application in RNT.

1.3 Limitation of fixed dose regimen

An empiric fixed dose method for ^{131}I therapy has been in use for a long time. Currently, a fixed dose is often administered to most patients for DTC (Shahbazi-Gahrouei and Nikzad 2011), For NHL (Loke et al. 2011) and NET patients (Olivier *et al.*, 2003) the dose is adjusted for total body weight or external body surface area. There are challenges, though, using a fixed-dose treatment method when the disease is at an advanced stage (Verburg *et al.*, 2017). At an advanced stage, the cancer cells can become resistant to the treatment (Sisson, 2002; Jentzen *et al.*, 2016) leading to the patients becoming refractory to iodine treatment (Pitoia, 2014). Hence, in order to have a successful treatment, the dose has to be increased as is widely recommended (de Keizer *et al.*, 2004). The question then becomes, to what extent should the dose be increased, since consideration needs to be given to organs that may be at risk of radiation toxicity? Therefore, a toxicity assessment is needed to determine the extent of a suitable dose increase, but such an assessment is often absent. The absence of a toxicity assessment in using fixed-dose regimen usually leads to the administration of lower doses of ^{131}I which also leads to under treatment (Wierts *et al.*, 2016)

The use of an effective RAI activity is especially important in the therapy of metastatic disease (an advanced cancer stage). Required dose levels sufficient for effective therapy in metastatic targets may be difficult to achieve, because of radiation exposure levels in critical tissues, like the bone marrow, which cannot be tolerated. However, radiation dosimetry has the potential of increasing the effectiveness of RAI treatments while preventing or limiting toxicity to normal tissues. Many NET are highly radiosensitive, so delivering an adequate dose to a tumour without planning can result in damage to the surrounding healthy tissues (Kaltsas, et. al., 2001). Thus proper dose planning is a requirement. According to Oyen and co-workers, the need for improvements in the treatment of B-cell lymphoma and the radio-sensitivity of the disease also provides the rationale for application of systemic radiotherapy (Oyen *et al.*, 2007). In radio-immunotherapy (RIT) with ^{131}I, because of the wide difference of whole-body (and organ) absorbed dose among patients, it is justified to apply individualised dosimetry for RIT with ^{131}I-labelled rituximab for such patients (Scheidhauer *et al.*, 2002).

In recent times, emphasis is being placed on individual patient dose planning in RNT, just as it is done in EBRT (Amato, et. al., 2011; Bodet-Milin, et. al., 2013; Brolin, et.al., 2015; Mínguez et al., 2015; Yue et al. 2016; Stokke *et al.*, 2017; Abuqbeitah *et al.*, 2018). This is because of the ever-increasing benefits of dose planning, especially with the individual nature of the patient in mind. It had been suggested that, for successful treatment to be obtained in RAI therapy, it is necessary to calculate the activity based on dose estimates (Shahbazi-Gahrouei D and Nikzad S, 2011; Parlak *et al.*, 2016). The standard fixed dose regimen is mostly practised because in the past tools were not readily available to calculate individual doses. Since these tools are becoming more readily available, it is important to improve the treatment outcome of the patients by utilising these tools. There is a large body of evidence in literature showing improved treatment outcome with patient-specific dosimetry (Stabin & Flux, 2014) compared to the fixed-dose therapy regimen. ^{131}I therapy is also said to be one therapeutic method with increased interest in patient-specific treatment planning (Braad *et al.*, 2016).

1.4 Dosimetry

A dosimetry-based approach in the application of radionuclides in cancer therapy patients can eliminate the challenge inherent in the conventional fixed-dose regimen. The challenge in fixed-dose regimen is that it cannot account for the wide range of inter-patient variability in uptake and retention of activity. Dosimetry can allow for the increase of administered therapeutic activity while undesired side effects are limited. Using this strategy, the absorbed dose to iodine-avid tissue (such as thyroid remnant tissue/Metastases, NHL, NET) can be optimised without inducing potential critical organ toxicity (Lassmann, *et. al.*, 2010). Individual dosimetry is necessary due to various factors contributing to the biological effectiveness in patients. Some of these factors are patient age, mass, and geometry, the renal function for ^{131}I clearance, organ and tumour size.

For patient-specific dose calculation in RNT, Thomas (Thomas, 2002) threw light on some common protocols. One of these protocols has been the calculation of the administered activity based on a predetermined radiation dose. The desired radiation dose, the remnant mass of thyroid tissue, effective half-life, and 24-hour uptake (measured with a thyroid uptake probe) are used in a formula to calculate the activity to be administered. In a second protocol, the quantitative diagnostic dosage, the desired radiopharmaceutical is administered to the patient and images of the patient are acquired over time to establish the bio-kinetic distribution of the tracer in the individual patient. The data collected from this procedure at different time points are used in an algorithm to estimate the appropriate activity dosage to be administered for therapy. This method, with some refinement, is the current gold standard in patient-specific dose planning in NM.

An example of an internal radiation dose algorithm is the medical internal radiation dose (MIRD) schema. The MIRD schema is today one of the most popular dosimetry methods and the standard in use for absorbed dose calculation. In recent times, Monte Carlo (MC)-based dosimetry methods have also become popular among medical physicists in NM. The MC-based calculations have the important advantage of modelling both radiation interactions and transport accurately; hence, it is able to account for most of the radiation depositing energy in the patient's tissue. In theory, the MC-based method is more accurate than the MIRD method that includes a number of assumptions, hence, the shift towards MC methods. This study includes a comparison of mean absorbed doses calculated with MIRD and MC algorithms.

1.5 Image quantification

Tailoring treatment to individual patients also improves survival of patients (Parisi *et al.*, 2016) and requires using an image-based 3-D dose estimation. As mentioned before, this will improve the efficacy of RAI therapy in DTC, NHL and NET. With the emergence of hybrid equipment, such as SPECT/CT, PET/CT and PET/MRI, 3-D dose estimation methods have become more readily available and more reliable as registration of functional and anatomical images is easily achievable.

Accurate quantification of radionuclide activity distribution in targeted radionuclide therapy is very important and necessary. This is because the radioactivity from patients detected by the gamma camera in the form of counts is sometimes lost due to image degrading factors as will be discussed in chapter 2. Therefore, to optimize the dose distribution in patients, the lost counts need to be 'recovered' first by correcting for the image degrading factors and then convert the counts to units of radioactivity such as the becquerel (Bq). In the presented work, state-of-the-art corrections for photon absorption, photon scatter and collimator-detector response (CDR) were used. Inaccuracies in dose calculation can have a significant effect on the efficacy of the treatment. Thus, it is imperative to quantify the images to be used for the dose estimation accurately since the quantified images serve as input for the dosimetry protocol. Image quantification provides a relatively accurate measure of radioactivity uptake in the organs or tumours of interest.

For absolute quantification, the sensitivity of the gamma camera (calibration factor that converts reconstructed SPECT counts to activity) must be determined using an appropriate method. For ^{131}I, in determining the calibration factor (CF), the collimator septal penetration and septal scatter (Dewaraja, Ljungberg and Koral, 2000; Pandey *et al.*, 2015) must be considered. Therefore, a method that approximates the scatter and attenuation conditions in patient imaging will be appropriate for this study, hence, a water-filled phantom with a spherical insert filled with activity was used to determine the CF for the gamma camera used in this study.

For activity quantification and dose estimation at the organ or tumour level, the volume of interest (VOI) must be accurately defined for the functional information to be properly utilized (Drever *et al.*, 2007). An image-based volumetric analysis tool was used to define the true size of the target (spheres and organs) volumes in this work.

Finally, absolute quantification of accuracies with errors below 10% had been reported for ^{131}I by some groups (Dewaraja *et al.*, 2013). Nevertheless, according to Silberstein (Silberstein, 2012), there are currently no validated techniques for ^{131}I SPECT quantification in clinical situations. This is also supported by Wierts et al (Wierts *et al.*, 2011). Even though improvement of image quantification techniques has been studied over the years (Pereira, Stabin and Lima, 2010) to characterize limitations in image quantification for different isotopes, shortcomings for high energy emitters remains a concern (Kuker, Sztejnberg and Gulec, 2017). Ritt (Ritt *et al.*, 2011) reported in 2011 that the accuracy of absolute quantification for high-energy radionuclides still needed evaluation and stated that more sophisticated correction methods must be utilized in order to further reduce quantification errors. More recently, Kuker, Sztejnberg and Gulec (2017) agree by concluding that improvement in the correction methods in quantification is needed to ensure the accuracy of diagnostic images, especially for radionuclides such as ^{131}I and other high energy emitters. Flux et al. stated that one of the challenges of personalized dosimetry that needs to be addressed is possible new ideas on how to organize the treatment of patients using ^{131}I (Flux *et al.*, 2017).

Therefore, this work finds its motivation in the fact that the quantification accuracy of ^{131}I, a high-energy radionuclide, which is very important and widely used in RNT (Grudzinski *et al.*, 2010; Das and Pillai, 2013; Ljungberg and Sjögreen-Gleisner, 2015), still needs to be investigated. It is now possible to reconstruct quantitative ^{131}I images using iterative techniques, which allow for the modelling of physical effects that degrade image quality. It is hoped that improved image quality will ultimately lead to improved image quantification and the accuracy of internal dosimetry of ^{131}I in the therapy of the diseases of interest in this work. The second motivation for this study is that personalized dosimetry in TRT is still being developed and remains an active field of research which is expanding rapidly, especially, in bringing it to the clinic (Wierts *et al.*, 2011; Flux *et al.*, 2017; Ljungberg, 2018; Lassmann and Eberlein, 2018).

1.6 Aim and objectives

The aim of this study, therefore, was to evaluate the accuracy of ^{131}I activity quantification and dosimetry for 3-D patient-specific models. This aim was achieved through the following objectives.

i. To validate image simulations obtained with SIMIND (**Si**mulating **M**edical **I**maging **N**uclear **D**etectors) against experimental measurements conducted with the Siemens Symbia T2 SPECT/CT gamma camera.

ii. To create clinically realistic patient SPECT simulation studies (3-D patient-specific models) from patient CT images for the evaluation of activity quantification and dose calculations.

iii. To assess the accuracy of ^{131}I SPECT quantification of spherical inserts in a water phantom as well as target organs and tumours in simulated 3-D patient-specific models.

iv. To determine the agreement between the standard, MIRD (OLINDA/EXM) and MC dose calculation (LundADose) methods by comparing mean absorbed doses calculated to target organs and tumours using these two methods.

1.7 Thesis outline

This thesis consists of eight chapters. In Chapter 1, a brief introduction to the problem and the objectives of the thesis has been provided. Chapter 2 deals with the fundamentals of ^{131}I imaging and therapy. This is for a better understanding of the basis of radiations emanating from ^{131}I, their interactions with matter, and the formation of ^{131}I images. It also covered the underlying physics of the image degrading factors (photon attenuation, photon scatter, and CDR) and the relevant physics of interaction of charged particles especially beta particles from ^{131}I, with matter. The chapter also included some insights into MC simulation in NM. The review on NM image quantification is the subject of Chapter 3. Amongst others, the theory of SPECT image quantification, reconstruction algorithms, compensation for image degrading factors, and some insight into the CF and delineation of the target volume were discussed. Chapter 4 focused on the review of internal dosimetry in NM. This covered all the relevant aspects of the internal dosimetry of TRT with emphasis on ^{131}I.

In chapter 5, a computer-generated model of the Siemens Symbia T2 SPECT/CT was created using the MC simulation software program SIMIND. The gamma camera model was validated by benchmarking data simulated with the gamma camera model with experimental measurements carried out on the physical gamma camera. In chapter 6 the computer-generated model of the gamma camera defined in SIMIND was used to simulate realistic patient SPECT ^{131}I data. SPECT data were simulated for different patient models created from CT images of real adult male and female patients. The simulated SPECT projection datasets of a water-filled cylindrical phantom and the above-mentioned patient models were quantified. The quantification of the patient models was focused on specified structures in these studies.

Chapter 7 focused on the dosimetry calculations for simulated patients using MC and MIRD algorithms. The MC dosimetry software program, LundADose was used to determine the absorbed dose to tumours and organs at risk for the simulated ^{131}I patients using the quantified images. The calculated cumulated activity from the quantified images simulated for different time points was used to obtain the mean absorbed dose with the MIRD-based software program OLINDA/EXM. Mean absorbed doses calculated using LundADose and OLINDA/EXM were compared.

Finally, chapter 8 contains the conclusion of the thesis findings and suggested future work.

1.8 References

Abuqbeitah, M., Demir, M., Çavdar, I., Tanyildizi, H., Yeyin, N., Uslu-Beşli, L., Kabasakal, L., Işıkcı, N. I. and Sönmezoğlu, K. (2018) ‘Red bone marrow dose estimation using several internal dosimetry models for prospective dosimetry-oriented radioiodine therapy’, *Radiation and Environmental Biophysics*. 57, pp. 395–404.

Ahmadzadehfar, H. and Essler, M. (2018) ‘It is time to move forward into the era of Theranostics’, *EJNMMI Research*., 8, p. 9.

Amato, E., Campenni, A., Herberg, A., Minutoli, F. and Baldari, S. (2011) 'Internal Radiation Dosimetry : Models and Applications', in Gholamrezanezhad, A. (edn.) *12 Chapters on Nuclear Medicine*. 1st ed. Rijeka, Croatia: InTech, pp. 25–46.

Blumhardt, R., Wolin, E. A., Phillips, W. T., Salman, U. A., Walker, R. C., Stack Jr, B. C. and Metter D. (2014) 'Current controversies in the initial post-surgical radioactive iodine therapy for thyroid cancer: A narrative review', *Endocrine-Related Cancer*, 21, pp. R473–R484.

Bodet-Milin, C., Ferrer, L., Pallardy, A., Eugene, T., Rauscher, A., Faivre-Chauvet, A., Barbet, J., and Kraeber.-Bodere, F. (2013) 'Radioimmunotherapy of B-cell non-Hodgkin's lymphoma', *Frontiers in Oncology*, 3, pp. 1–13.

Braad, P. E. N., Andersen, T., Hansen, S. B. and Hoilund-Carlsen, P. F. (2016) 'Strategies for CT tissue segmentation for Monte Carlo calculations in nuclear medicine dosimetry', *Med. Phys.*, 43, pp. 6507–6516.

Brolin, G., Gustafsson, J., Ljungberg, M. and Sjogreen-Gleisner, K. (2015) 'Pharmacokinetic digital phantoms for accuracy assessment of image-based dosimetry in ^{177}Lu-DOTATATE peptide receptor radionuclide therapy.', *Phys. Med. Biol.* 60, pp. 6131–6149.

Carrasquillo, J. A., Pandit-taskar, N. and Chen, C. C. (2016) 'I-131 Metaiodobenzylguanidine Therapy of Pheochromocytoma and Paraganglioma', *Semin. Nucl. Med.* 46, pp. 203–214.

Cherry, S. R., Sorenson, J. A. and Phelps, M. E. (2012) *Physics in Nuclear Medicine*. 4th edn. Philadelphia, PA: Elsevier Inc.

Das, T. and Pillai, M. R. A. (2013) 'Options to meet the future global demand of radionuclides for radionuclide therapy', *Nucl. Med. Biol.* 40, pp. 23–32.

de Keizer, B., Hoekstra, A., Konijnenberg, M. W., de Vos, F., Lambert, B., van Rijk, P. P., Lips, C. J. M. and de Klerk, J. M. H. (2004) 'Bone Marrow Dosimetry and Safety of High ^{131}I Activities Given After Recombinant Human Thyroid-Stimulating Hormone to Treat Metastatic Differentiated Thyroid Cancer', *J. Nucl. Med.*, 45, pp. 1549–1554.

Dewaraja, Y. K., Wilderman, S.J., Ljungberg, M., Koral, K. F., Zasadny, K. and Kaminiski, M. S. (2005) 'Accurate dosimetry in ^{131}I radionuclide therapy using patient-specific, 3-

dimensional methods for SPECT reconstruction and absorbed dose calculation.', *J. Nucl. Med.*, 46, pp. 840–849.

Dewaraja, Y. K., Ljungberg, M. and Koral, K. F. (2000) 'Characterization of Scatter and Penetration Using Monte Carlo Simulation in ^{131}I Imaging', *J. Nucl. Med.*, 41, pp. 123–131.

Dewaraja, Y. K., Ljungberg, M., Green, A. J., Zanzonico, P. B. and Frey, E. C. (2013) 'MIRD Pamphlet No. 24: Guidelines for Quantitative ^{131}I SPECT in Dosimetry Applications', *J. Nucl. Med.*, 54, pp. 2182–2188.

Dorn, R., Kopp, J., Vogt, H., Heidenreich, P., Carroll, R. G. and Gulec, S. A. (2003) 'Dosimetry-Guided Radioactive Iodine Treatment in Patients with Metastatic Differentiated Thyroid Cancer : Largest Safe Dose Using a Risk-Adapted Approach', *J. Nucl. Med.*, 44, pp. 451–456.

Drever, L., Roa, W., McEwan, A. and Robinson, D. (2007) 'Iterative threshold segmentation for PET target volume delineation', *Med. Phys.*, 34, pp. 1253–1265.

Eriksson, D., Riklund, K., Johansson, L. and Stigbrand, T. (2008) 'Radiation-Induced Cell Deaths', in Stigbrand, T., Carlsson, J., and Gregory, A. (eds) *Targeted Radionuclide Tumor Therapy: Biological Aspects*. New York: Springer Science, pp. 215–248.

Flux, G. D., Gleisner, K. S., Chiesa, C., Lassmann, M., Chouin, N., Gear, J., Bardies, M., Walrand, S., Bacher, K., Eberlein, U., Ljungberg, M., Strigari, L., Visser, E. and Konijnenberg, M. W. (2017) 'From fixed activities to personalized treatments in radionuclide therapy : lost in translation ?', *Eur. J. Nucl. Med. Mol. Imaging.* , pp. 12–14.

Foster, B., Bagci, U., Mansoor, A., Xu, Z. and Mollura, D. J. (2014) 'A Review on Segmentation of Positron Emission Tomography Images', *Comput. Biol. Med.*, 50, pp. 76–96.

Gear, J. I., Charles-Edwards, E., Patridge, M. and Flux, G. D. (2007) 'A Quality-Control Method for SPECT-Based Dosimetry in Targeted Radionuclide Therapy', *Cancer Biother. Radiopharm.*, 22, pp. 166–174.

Gear, J. I., Cox, M. G., Gustafsson, J., Gleisner, K. S., Murray, I., Glatting, G., Konijnenberg, M. and Flux, G. D. (2018) 'EANM practical guidance on uncertainty analysis for molecular radiotherapy absorbed dose calculations', *Eur J Nucl Med Mol Imaging*. 45, p. 2456.

Grudzinski, J. J., Yoriyaz, H., Deluca Jr, P. M. and Weichert, J. P. (2010) ‘Patient-specific treatment planning for systemically administered radiopharmaceuticals using PET / CT and Monte Carlo simulation’, *Applied Radiation and Isotopes*. 68, pp. 59–65.

Hoefnagel, C. A. (1998) ‘Radionuclide Cancer Therapy’, *Ann. Nucl. Med.*, 12, pp. 61–70.

Jentzen, W., Verschure, F., van Zon, A., van de Kolk, R., Wierts, R., Schmitz, J., Bockisch, A. and Binse, I. (2016) ‘^{124}I PET Assessment of Response of Bone Metastases to Initial Radioiodine Treatment of Differentiated Thyroid Cancer’, *J. Nucl. Med.*, 57, pp. 1499–1504.

Kaltsas, G. A., Mukherjee, J. J. and Grossman, A. B. (2001) ‘The value of radiolabelled MIBG and octreotide in the diagnosis and management of neuroendocrine tumours.’, *Annals of oncology*, 12, pp. S47-S50.

Kuker, R., Sztejnberg, M. and Gulec, S. (2017) ‘^{124}I Imaging and Dosimetry’, *Mol. Imaging Radionucl. Ther.*, 26, pp. 66–73.

Lassmann, M. and Eberlein, U. (2018) ‘The Relevance of Dosimetry in Precision Medicine.’, *J. Nucl. Med.* 59, pp. 1494–1499.

Lassmann, M., Reiners, C. and Luster, M. (2010) ‘Dosimetry and thyroid cancer: The individual dosage of radioiodine’, *Endocrine-Related Cancer*, 17, pp. R161–R172.

Ljungberg, M. (2018) ‘Absolute Quantitation of SPECT Studies’, *Semin. Nucl. Med.* 48, pp. 348–358.

Ljungberg, M. and Sjögreen-Gleisner, K. (2015) ‘Hybrid Imaging for Patient-Specific Dosimetry in Radionuclide Therapy’, *Diagnostics*, 5, pp. 296–317.

Loke, K. S. H., Padhy, A. K., Ng, D. C. E., Goh, A. S. W. and Divgi, C. (2011) ‘Dosimetric Considerations in Radioimmunotherapy and Systemic Radionuclide Therapies: A Review’, *World J. Nucl. Med.* 10, pp. 122–138.

Luster, M., Pfestroff, A., Hänscheid, H. and Verburg, F. A. (2017) ‘Radioiodine Therapy’, *Semin. Nucl. Med.* 47, pp. 126–134.

Lyra, M. (2009) ‘Single Photon Emission Tomography (SPECT) and 3D Images Evaluation in Nuclear Medicine’, in Yung-Sheng Chen (edn.) *Image Processing*. Rijeka, Croatia:

InTech, pp. 259–286.

Mariani, G., Bruselli, L., Kuwert, T., Kim, E. E., Flotats, A., Israel, O., Dondi, M. and Watanabe, N. (2010) ‘A review on the clinical uses of SPECT/CT’, *Eur. J. Nucl. Med. Mol. Imaging*, 37, pp. 1959–1985.

Mínguez, P., Flux, G., Genollá, J., Guayambuco, S., Delgado, A., Fombellida, J. C. and Gleisner, K. S. (2015) ‘Dosimetric results in treatments of neuroblastoma and neuroendocrine tumours with ^{131}I-metaiodobenzylguanidine with implications for the activity to administer’, *Med. Phys.* 42, pp. 3969–3978.

Olivier, P., Colarinha, P., Fettich, J., Fischer, S., Frôkier, J., Giammarile, F., Gordon, I., Hahn, K., Kabasakal, L., Mann, M., Mitjavila, M., Piepsz, A., Porn, U., Sixt, R. and van Velzen, J. (2003) ‘Guidelines for radioiodinated MIBG scintigraphy in children.’, *Eur. J. Nucl. Med. Mol. Imaging*, 30, pp. BP45-BP50.

Oyen, W. J. G., Bodei, L., Giammarile, F., Maecke, H. R., Tennvall, J., Luster, M. and Brans, B. (2007) ‘Targeted therapy in nuclear medicine - Current status and future prospects’, *Annals of Oncology*, 18, pp. 1782–1792.

Pandey, A. K., Sharma, S. K., Karunanithi, S., Kumar, P., Bal, C. and Kumar, R. (2015) ‘Characterization of parallel - hole collimator using Monte Carlo Simulation’, *Indian J. Nucl. Med.*, 30, pp. 128–134.

Parisi, M. T., Eslamy, H., Park, J. R., Shulkin, B. L. and Yanik, G. A. (2016) ‘^{131}I-Metaiodobenzylguanidine Theranostics in Neuroblastoma: Historical Perspectives; Practical Applications’, *Sem. Nucl. Med.*, 46, pp. 184–202.

Parlak, Y., Demir, M., Cavdar, I., Ereees, S., Gumuser, G., Uysal, B., Kaya G. C., Koç, M. and Sayit, E. (2016) ‘Bone marrow radiation dosimetry of high dose ^{131}I treatment in differentiated thyroid carcinoma patients’, *Int. J. Radiat. Res.*, 14, pp. 99–104.

Pereira, J., Stabin, M. and Lima, F. (2010) ‘Image Quantification for Radiation Dose Calculations - Limitations and Uncertainties’, *Health Phys*, 99, pp. 688–701.

Pitoia, F. (2014) ‘Advanced Metastatic Thyroid Cancer’, *Arch. Endocrinol. Metab.*, 58, pp. 37–41.

Powsner, R. A., Palmer, M. R. and Powsner, E. R. (2013) *Essentials of Nuclear Medicine Physics and Instrumentation*. 3rd edn. Chichester, West Sussex, UK: John Wiley and Sons. Ltd.

Ritt, P., Vija, H., Hornegger, J. and Kuwert, T. (2011) 'Absolute quantification in SPECT', *Eur. J. Nucl. Med. Mol. Imaging*, 38, pp. 69–77.

Scheidhauer, K., Wolf, I., Baumgartl, H., von Schilling, C., Schmidt, B., Reidel, G., Peschel, C. and Schwaiger, M. (2002) 'Biodistribution and kinetics of ^{131}I-labelled anti-CD20 MAB IDEC-C2B8 (rituximab) in relapsed non-Hodgkin's lymphoma', *Eur. J. Nucl. Med.*, 29, pp. 1276–1282.

Shahbazi-Gahrouei, D. and Nikzad, S. (2011) 'Determination of organ doses in radioiodine therapy using medical internal radiation dosimetry (MIRD) method', *Iran. J. Radiat. Res.*, 8, pp. 249–252.

Silberstein, E. B. (2012) 'Radioiodine : The Classic Theranostic Agent', *Sem. Nucl. Med.*, 42, pp. 164–170.

Sisson, J. C. (2002) 'Practical Dosimetry of ^{131}I in Patients with Thyroid Carcinoma', *Cancer Biother. Radiopharm.*, 17, pp. 101–105.

Sisson, J. C. and Yanik, G. A. (2012) 'Theranostics: Evolution of the radiopharmaceutical meta-iodobenzylguanidine in endocrine tumours.', *Sem. Nucl. Med.*, 42, pp. 171–184.

Skanjeti, A., Miranti, A., Yabar, G. M. D., Bianciotto, D., Trevisiol, E., Stasi, M. and Podio, V. (2015) 'A simple and accurate dosimetry protocol to estimate activity for hyperthyroidism treatment', *Nucl. Med. Rev.* 18, pp. 13–18.

Stabin, M. A. and Flux, G. D. (2014) 'The Use of Dosimetry in the Planning of Patient Therapy', in Baum, R. (ed.) *Therapeutic Nuclear Medicine*. 1st edn. Berlin Heidelberg: Springer-Verlag, pp. 867–877.

Stokke, C., Gabiña, P. M., Solný, P., Cicone, F., Sandström, M., Gleisner, K. S., Chiesa, C., Spezi, E., Paphiti, M., Konijnenberg, M., Aldridge, M., Tipping, J., Wissmeyer, M., Brans, B., Bacher, K., Kobe, C. and Flux, G. (2017) 'Dosimetry-based treatment planning for molecular radiotherapy : a summary of the 2017 report from the Internal Dosimetry Task Force', EJNMMI Physics, 4, pp. 1–9.

Thomas, S. R. (2002) ‘Options for radionuclide therapy: from fixed activity to patient-specific treatment planning.’, *Cancer Biother. Radiopharm.*, 17, pp. 71–82.

Velikyan, I., Bulenga, T. N., Selvaraju, R., Lubberink, M., Espes, D., Rosenström, U. and Eriksson, O. (2015) ‘Dosimetry of [^{177}Lu]-DO3A-VS-Cys40-Exendin-4 – impact on the feasibility of insulinoma internal radiotherapy’, *Am. J. Nucl. Med. Mol. Imaging*, 5, pp. 109–126.

Verburg, F. A., Luster, M., Giovanella, L., Lassmann, M., Chiesa, C., Chouin, N. and Flux, G. (2017) ‘The “reset button” revisited : why high activity ^{131}I therapy of advanced differentiated thyroid cancer after dosimetry is advantageous for patients’, *Eur J Nucl Med Mol Imaging*., 44, pp. 915–917.

Wierts, R., de Pont, C. D. J. M., Brans, B., Mottaghy, F. M. and Kemerink, G. J. (2011) ‘Dosimetry in molecular nuclear therapy’, *Methods*., 55, pp. 196–202.

Wierts, R., Brans, B., Havekes, B., Kemerink, G. J., Halders, S. G., Schaper, N. N., Backes, W. H., Mottaghy, F. M. and Jentzen, W. (2016) ‘Dose-Response Relationship in Differentiated Thyroid Cancer Patients Undergoing Radioiodine Treatment Assessed by Means of ^{124}I PET/CT’, *J. Nucl. Med.*, 57, pp. 1027–1032.

Yeong, C.-H., Cheng, M. and Ng, K.-H. (2014) ‘Therapeutic radionuclides in nuclear medicine: current and future prospects’, *J. Zhejiang Uni. SC.B*, 15, pp. 845–863.

Yue, J., Mauxion, T., Reyes, D. K., Lodge, M. A., Hobbs, R. F., Rong, X., Dong, Y., Herman, M. J., Wahl, R. L., Geschwind, J-F. H. and Frey, E. C. (2016) ‘Comparison of quantitative Y-90 SPECT and non-time-of-flight PET imaging in post-therapy radioembolization of liver cancer’, *Med. Phys.*, 43, pp. 5779–5790.

CHAPTER TWO: Fundamentals of ^{131}I Imaging and Therapy

Table of Contents

2.1 Introduction

In nuclear medicine (NM), Iodine-131 (^{131}I) is one of the most important radionuclides. Since its discovery, it has played a major role in NM practice, and it remains very relevant today (Yordanova, A., et. al., 2017), bringing much efficiency to clinical practice by facilitating diagnosis and therapy as a single agent (Sisson and Yanik, 2012). It is used as a 'Diapeutic' (*dia* – diagnostic and *peutic* – therapeutic) agent when it is combined with Iodine-123 or Iodine-124 (in PET) to assume diagnostic or therapeutic function (Grudzinski *et al.*, 2010; Lee *et al.*, 2010; Jentzen *et al.*, 2016; Wierts *et al.*, 2016). ^{131}I is a radioactive isotope of iodine that decays with a physical half-life of 8.02 days to stable ^{131}Xe. It primarily undergoes a beta decay process but also releases gamma radiation of different energies, of which one (the 364 keV) is very useful for diagnosis. It emits beta particles with a continuous spectrum of energies which makes ^{131}I suitable for radionuclide therapy (RNT). Hence, it is referred to as the classic 'theragnostic'(or 'theranostic', another compound name from therapy and diagnostic) agent (Silberstein, 2012; Srivastava and Mausner, 2013). ^{131}I also happens to be the first 'theranostic' agent to be used for dual-purpose (diagnosis and therapy). Therefore, ^{131}I can be said to be the legendary 'one stone used to kill two birds'.

^{131}I is usually administered in capsule form, which is ingested orally. In some centres, it is administered in a liquid form which is more problematic because of the challenge of possible radiation contamination and inhalation by staff members due to its volatility. Immediately after ingestion, ^{131}I is rapidly absorbed from the gastrointestinal tract into the extracellular body fluid, where it is distributed. In a normal patient, it will concentrate in the thyroid tissue, salivary glands, stomach (Thompson, 2001), choroid plexus, lactating mammary glands, liver, gall bladder, urinary system etc. either because they express the sodium iodide symporter or they metabolise/excrete iodine/iodinated tyrosyl residue. The 364 keV gamma rays emitted by ^{131}I can be used for imaging of the patient when positioned under the detector of a gamma camera. The gamma camera detector can detect the gamma rays emitted by the radioactive patient resulting in images of the biodistribution of the sodium iodide in the patient. Images can be acquired in planar or tomographic mode. These are discussed further in relevant sections of this chapter.

2.2 Radionuclide decay

Atoms are the smallest units of a chemical element possessing the properties of that element and often combine with one another to form molecules (Cherry et. al., 2012, Chandra 2004). NM is concerned with the reactions that take place among the constituents of the nucleus of an atom, collectively called nucleons (Podgorsak, et al., 2014). Depending on the number and distribution or arrangement of the nucleons, the nucleus can be either stable or unstable.

In an unstable nucleus, the nucleons adjust the arrangement in a spontaneous fashion in order to attain stability. In the course of this adjustment, particles and/or gamma rays are emitted, often accompanied with the release of energy and this phenomenon is known as radioactive decay or radionuclide decay (Powsner, et. al., 2013). This process results in the formation of new elements and the adjustment of the neutron to proton ratio. Radionuclide decay is governed by the decay equation

$$\mathbf{A}\,(\mathbf{t}) = \boldsymbol{\lambda N}\,(\boldsymbol{t}) \qquad 2.1$$

Where $\mathbf{A}\,(\mathbf{t})$ is the activity of the radioactive substance containing a large number $\boldsymbol{N}\,(\boldsymbol{t})$ of identical radioactive atoms and $\boldsymbol{\lambda}$ is the radioactive decay constant. $\mathbf{A}\,(\mathbf{t})$ is the total number of decays per unit time having the S.I unit of becquerel (Bq) and $1/\boldsymbol{\lambda}$ represents the probability that any particular atom of a radioactive substance that contains a large amount $\boldsymbol{N}\,(\boldsymbol{t})$ of identical radioactive atoms will decay in that time interval (Podgorsak, et al, 2014).

Radionuclides are atoms with unstable nuclei due to an excess number of protons or neutrons and will undergo radioactive decay to regain stability. These unstable nuclei can decay by alpha decay, beta decay, positron decay, electron capture, spontaneous fission and isomeric transition. In some of the decay processes, atomic electrons may become involved but radioactive decay is basically a nuclear process. In all of the decay processes the energy, charge and mass are conserved. Only decay processes relevant to ^{131}I will be discussed further.

2.2.1 Beta-minus decay

When the nucleus of an atom has an excess number of neutrons compared with the number of protons, the nucleus will adjust by some neutrons being transformed into protons with the simultaneous emission of a negatively charged beta (β^-) particle and an anti-neutrino ($\bar{\upsilon}$), Figure 2.1. In this case, if the neutron is seen as a proton attached with an electron (which makes it electrically neutral), then the transformation is simply the emission of the electron leaving behind the proton. Beta-minus decay can be described by the following equation.

$$\boldsymbol{n \rightarrow p^{+} + e^{-} + \bar{\upsilon}} \qquad 2.2$$

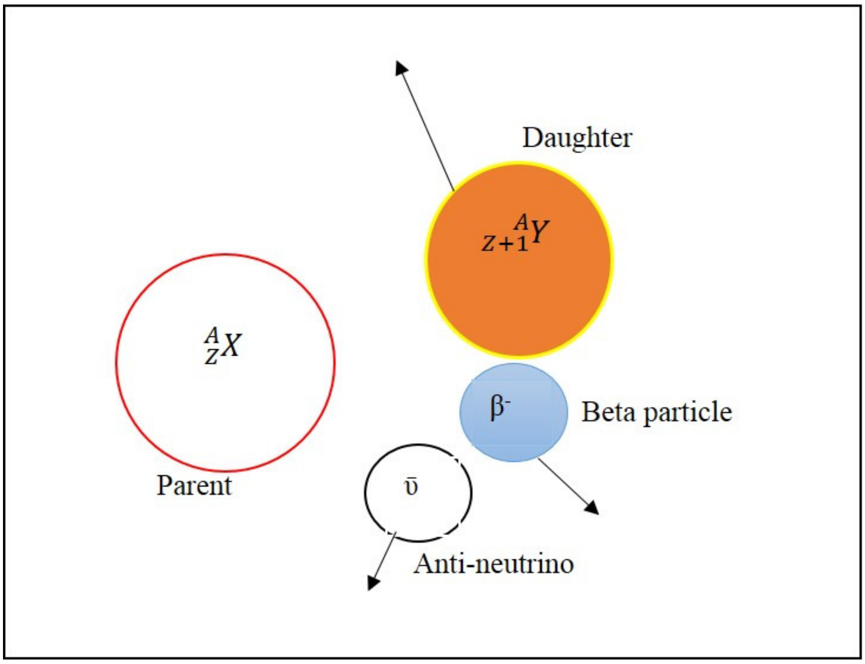

Figure 2. 1: ***Radionuclide decay by beta-minus emission***

The atomic mass, A, of the decay product in β^{-} decay remains the same as that of the parent. Its atomic number "Z" however, is one greater than that of the parent (a neutron has disappeared but has been replaced by a proton). The emission of a β^{-} particle is accompanied by the emission of an antineutrino (ῡ), which has no significance at all but is emitted to conserve mass and energy.

β^{-} particles are emitted with a whole continuous spectrum of energies, beginning from zero to some maximum energy which is unique for each β^{-} emitter. As a rule of thumb, the average particle energy ($\boldsymbol{E_{av}}$) in such a spectrum is calculated using equation 2.3 if the maximum energy ($\boldsymbol{E_{max}}$) is known.

$$\boldsymbol{E_{av} = \frac{1}{3} E_{max}} \qquad 2.3$$

^{131}I as a β^{-} particle emitter decays with a primary β^{-} emission with a maximum energy of 606 keV (89% abundance)(Grudzinski *et al.*, 2010). Other β^{-} emissions from ^{131}I decay have possible maximum energies ranging from 248 – 806 keV. The absolute maximum β^- energy of ^{131}I is therefore, 806 keV (Silberstein, 2012). Equation 2.4 illustrates beta emission of ^{131}I.

$$^{131}_{53}\boldsymbol{I} \rightarrow \boldsymbol{\beta}^{-}(\mathbf{606\ keV}) + \overline{\boldsymbol{\upsilon}} + {}^{131}_{54}\boldsymbol{Xe}^{*} \qquad 2.4$$

* indicates excited state

2.2.2 Gamma-ray emission

Gamma decay is not a primary mode of decay. Gamma rays are often emitted as the daughter nucleus undergoes an internal rearrangement and transition from an excited state to a lower energy state. The transition from excited states to lower energy states is almost instantaneously. In some nuclei the excited states persist for longer periods, ranging from nanoseconds to more than 30 years. In this state, the nucleus is said to be in a metastable state. Gamma decay, therefore, accompanies all the other types of decay. The gamma rays are emitted in order to rid the nucleus of excess energy produced during the decay. The gamma rays are identified by their characteristic energies which can also be used to identify the various radionuclides of interest, especially in NM. Figure 2.2 illustrates the emission of a gamma ray after a nuclear decay.

For ^{131}I, the principal gamma emission has an energy of 364 keV (with an 81.2% abundance). Other notable gamma-ray emissions are 637 keV (7.5%) and 723 keV (1.8%) (Song *et al.*, 2011). Equations 2.5 illustrates the gamma emission of ^{131}I.

$$^{131}_{54}\boldsymbol{Xe}^{*} \rightarrow {}^{131}_{54}\boldsymbol{X}_{\boldsymbol{e}} + \boldsymbol{\gamma}(\mathbf{364\ keV}) \qquad 2.5$$

$^{131}_{54}\boldsymbol{Xe}^{*}$ De-excites to give off gamma rays resulting in a stable isotope of xenon.

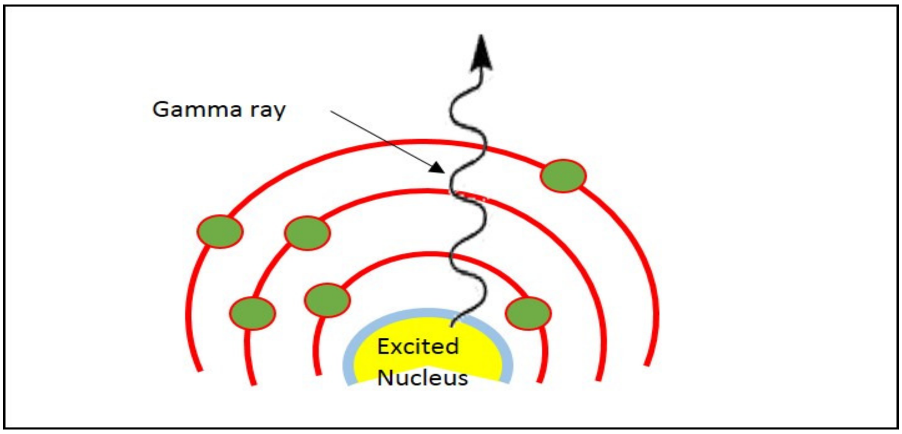

Figure 2. 2: ***Illustration of de-excitation of a nucleus with the emission of a gamma ray***

2.2.3 Internal conversion

Another way that an excited nucleus following a nuclear decay can rid itself of excitation energy is through internal conversion (Chandra, 2004). In internal conversion, the photon emitted as a result of de-excitation of the nucleus interacts with an orbital electron on exiting the nucleus thereby giving off all its energy to the electron. This electron is then ejected from the atom and is referred to as a conversion electron. Due to the ejection of the electron, another electron fills the vacancy left and this leads to the emission of characteristic x-rays. These x-rays can equally be absorbed by other orbital electrons, thereby ejecting them. Such ejected electrons are called Auger electrons. Auger electrons are gradually becoming useful in RNT (Dash, et. al., 2013). Internal conversion is illustrated in figure 2.3. All gamma rays and particles produced by nuclear decay and atomic emissions must be considered in internal dose calculations.

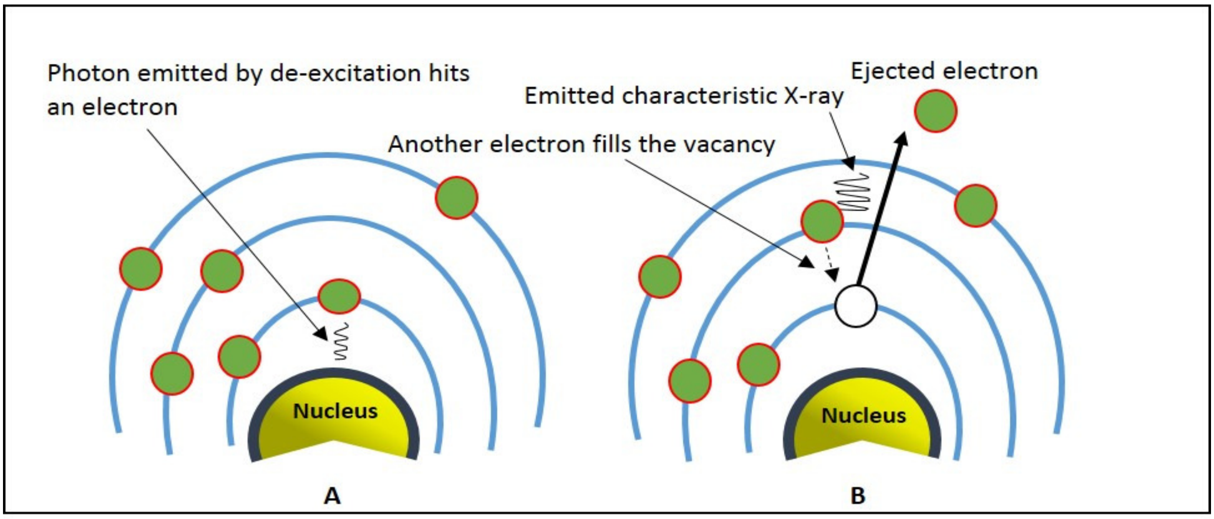

Figure 2. 3: ***Illustration of internal conversion. A. the gamma ray interacts with an orbital electron in the K shell. B. the electron is ejected from its orbit and another electron from the L shell comes to fill the vacancy with the emission of a characteristic X-ray.***

2.2.4 Decay schemes

Decay schemes are ways of representing the mode and frequency of decay, process of decay, the energy of different radiation emitted, half-life, the parent and daughter, energy levels including the ones for excited and metastable states, and other relevant information of radionuclides. This information shows the unique radioactive decay processes of particular radionuclides and are represented as line diagrams and may or may not be accompanied by decay data tables which provide information on all the significant ionizing radiations emitted from the atom due to the nuclear transformation (Bushberg, Seibert and Boone, 2012). The decay diagram and decay data table for ^{131}I are shown in Appendix I.

2.3 Interaction of Radiation with Matter

NM images are formed based on the interaction of gamma rays with matter. In the same way, RNT is based on the interaction of particulate radiation with matter. These interactions involve the transfer of energy from the radiation to matter. The transfer of energy can result in two effects, ionization and excitation, although, radiative losses such as Bremsstrahlung can also occur, these will not be discussed. Charged particles cause ionization and excitation directly whereas; gamma rays do that in an indirect way.

2.3.1 Interaction of gamma rays with matter

Gamma rays that travel through matter will either penetrate, scatter, or be absorbed. Four major types of interactions of x- and gamma-rays with matter are possible: (a) Photoelectric absorption (b) Compton scattering (c) Rayleigh scattering and (d) Pair production (Bushberg, Seibert and Boone, 2012).

Rayleigh scattering involves the interaction of a photon (gamma ray) with an atom as a whole. The interaction results in a scattered gamma ray that has the same energy as the incident gamma ray but in a slightly different direction. For gamma ray with an energy greater than 70 keV, Rayleigh scattering accounts for less than 5 % of interactions in tissue and therefore, Rayleigh scattering has little significance in this discussion.

Pair production on the other is an interaction that occurs between a gamma ray and the nucleus of an atom. In the process, the gamma-ray losses all of its energy and an electron-positron pair is created. The total kinetic energy of the electron and positron is equal to the energy of gamma ray minus the rest mass of the electron-positron pair (1.02 MeV). Thus pair production is possible when the incident gamma ray energy is at least 1.02 MeV. Since this thesis focuses on ^{131}I, pair production will not be discussed further. The most relevant gamma ray energies in NM are between 70 and 511 keV. The two dominant interactions at these energies are the photoelectric effect and Compton scattering.

2.3.1.1 Photoelectric effect

Photoelectric effect refers to a situation whereby a gamma ray collides with the orbital electron of the atom and depositing all its energy to the orbital electron. The orbital electron involved in this process must be bound so that momentum can be conserved through recoil of the atom. If the energy of the gamma ray is sufficient to overcome the binding energy of the electron, the electron is subsequently ejected from the atom and is called a photoelectron. Therefore, the kinetic energy of the photoelectron is equal to the difference between the energy of the incident gamma ray and the binding energy of the electron while in orbit. This is represented in equation 2.6 below (Bushberg, Seibert and Boone, 2012).

$$\boldsymbol{E_e = E_0 - E_b} \tag{2.6}$$

Where, $\boldsymbol{E_e}$ is the kinetic energy of the ejected electron, $\boldsymbol{E_0}$ is the incident gamma ray energy and $\boldsymbol{E_b}$ is the binding energy of the electron while in orbit. An electron moving from a higher energy orbit fills the resultant vacancy in the electron orbit. In moving from a higher to a lower energy orbit, the excess energy is released as a characteristic x-ray (or Auger electrons). The probability of a gamma ray undergoing a photoelectric interaction is proportional to the density of the absorbing material and highly dependent on its atomic number, being proportional to Z^3. This interaction is also more likely to occur at low energies (<0.2 MeV) as it is proportional to $1/E^3$. The likelihood of a gamma ray interacting by the photoelectric effect is greatest when $\boldsymbol{E_0}$ is equal to or slightly higher than the electron binding energy.

2.3.1.2 Compton scattering

Gamma-ray or photon scatter is one of the effects of interaction of gamma-ray with matter. It refers to the process whereby gamma rays that interact within the patient or within the detector system are emitted in a different direction (scattered) thereby losing some energy. The energy range for Compton scatter dominance is from 26 keV to 30 MeV (Bushberg, Seibert and Boone, 2012). This is an interaction in which part of the incident photon energy ($\boldsymbol{hv}$) is transferred to an outer shell electron ("free electron") thereby removing it from the atom. The removed electron is known as a Compton electron (or recoil electron) with a kinetic energy E_K and the photon which lost energy in the interaction is scattered and emerges with energy $\boldsymbol{hv^1}$ at an angle which is determined by the amount of energy transferred during the interaction. The angle of scatter, θ, measured between the incident photon direction and the scattered photon direction, ranges from nearly 0° to 180°. For the Compton electron, angle θ, measured between the incident photon direction and the direction of the ejected Compton electron is assigned.

If we consider the relativistic conservation of total energy and momentum, the relationship in equation 2.7 can be used to show or calculate what would happen to a photon scattered through a specific angle.

$$\boldsymbol{hv}^{1} = \boldsymbol{hv}\,\frac{\mathbf{1}}{\mathbf{1}+\boldsymbol{\varepsilon}(\mathbf{1}-\boldsymbol{cos\theta})} \qquad 2.7$$

Where $\boldsymbol{\varepsilon} = \frac{\boldsymbol{hv}}{\boldsymbol{m_e c^2}}$ represents the incident photon energy $\boldsymbol{hv}$ normalized to the electron rest energy $\boldsymbol{m_e c^2}$. Figure 2.4 is an illustration of photon scatter. In addition, it is possible for a photon to undergo several Compton interactions before being fully absorbed via the photoelectric effect, so, photons with a range of energies from close to zero to the photopeak energy can be detected. For the free electrons (in the outer shell) the probability of a Compton interaction decreases with photon energy ($\propto 1/E$). Unlike the photoelectric effect, the probability of Compton scattering is independent of Z and depends only on the electron density. This is due to the fact that the Compton effect occurs with a free electron and the total number of electrons per gram is fairly constant in tissue.

2.3.1.3 Photon attenuation

Photon attenuation refers to the loss of photons that are emitted from the radiation source due to absorption and/or the scattering of the photons. Photons originating from the source of decay that are not scattered and find their way to the imaging detector are ideally used for image formation. However, as discussed above some of these photons sometimes may be absorbed or scattered in the media in which they travel, such as patient tissue or collimator material.

The combined effect of the photoelectric effect (absorption) and photon scattering (scatter) known as photon attenuation results in the reduction of the number of useful photons been detected at the imaging detector. Photon attenuation thereby can induce artefacts which can degrade the image quality as well as introduce quantitative errors which need to be corrected for.

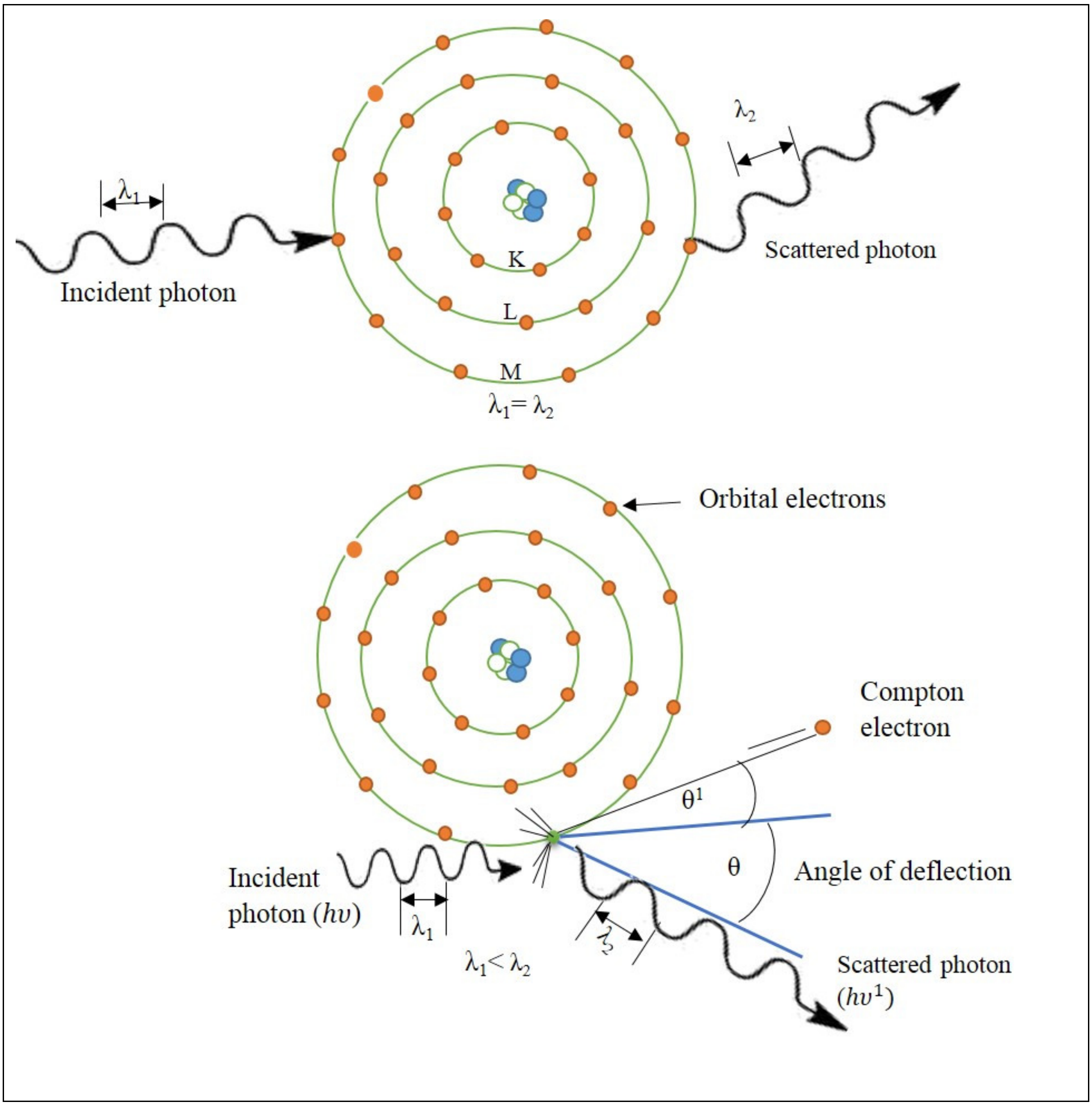

Figure 2. 4: ***Photon scatter: (above) Rayleigh Scatter (below) Compton scatter (Bushberg, Seibert and Boone, 2012).***

2.3.1.4 Attenuation coefficient

A photon beam (stream of photons) with intensity I_0 will have its intensity reduced when it passes through matter. This is due to the beam being attenuated by the medium, usually called an attenuator. Attenuation generally, is the ratio of the intensity after the beam exits the attenuator

I_e to the initial intensity I_0 of the beam. It is an exponential function of the thickness x of the attenuator expressed in centimetres. Thus, the relationship can be expressed as:

$$\frac{I_e}{I_0} = e^{-\mu x} \qquad 2.8$$

Where μ is a property of the attenuator and is known as the linear attenuation coefficient. It is expressed as per centimetre (cm^{-1}) when the thickness of the attenuator is measured in centimetres. The ratio of the linear attenuation coefficient to the density of the attenuator, ρ (g/cm^3), $\frac{\mu}{\rho}$ is known as mass attenuation coefficient and has a unit of cm^2/g. The attenuation coefficient of a material refers to its effectiveness as an attenuator.

2.3.2 Interaction of charged particles with matter

Charged particles are those radioactive particles that have electric charges, such as electrons (β) and alpha particles. They are very important in NM therapy since they cause direct ionization and excitation in matter. The charges that these particles carry interact electrically with the orbital electrons but rarely with nuclei of atoms that they encounter in matter (Saha, 2013). Energetic charged particles interact with matter by electrical forces and loose kinetic energy via ionization, excitation and radiative losses. Ionization occurs when the energy transferred by the charged particle is sufficient to remove orbital electrons from the atoms of matter thereby creating ion pairs. The orbital electron is ejected from the atom with kinetic energy equal to the energy lost by the incident charged particle in the collision minus the binding energy of the electron. The ejected electron may even have enough energy to create secondary ionizations, in which case secondary electrons, called delta rays (δ) are produced.

In excitation, however, the energy transferred is not sufficient to remove orbital electrons from the atoms of matter but only perturbs the electrons from their normal arrangement thereby creating atoms and molecules in an excited state.

The primary interaction event is ionization, hence, the term ionizing radiation, which refers to emissions from radioactive materials. The interaction is inherently an inelastic collision and manifests differently for lighter particles and for heavier particles. The lighter particles have masses in the order of the mass of an electron while the heavier particles have masses equal to or greater than that of the proton (Chandra, 2004). Radiative loses on the other hand can occur when a charged particle interacts with the electric field of the nucleus. This interaction causes a change in direction and deceleration of the charged particle. The loss of energy associated with the deceleration results in the emission of electromagnetic radiation called bremsstrahlung. Unlike photons that are used for imaging, charged particles are useless in image formation. This is because they are usually not able to escape from the human tissue due to their short penetration range compared to the penetration range of photons. However, these particles play an important role in the therapeutic effects of radiation.

2.3.2.1 Specific ionization

Specific ionization refers to the total number of ion pairs produced by a charged particle per unit length of the path of the incident radiation (Saha, 2013). The specific ionization of electrons (including beta particles) generally is said to be in the range of 5 to 10 ion pairs per mm of air (Bushberg, Seibert and Boone, 2012). When charged particles pass through matter, specific ionization is one of the quantities of interest associated with their interaction in the matter. Other important quantities are linear energy transfer (LET) and their range in the material. These quantities are very important and of interest in RNT and radiation protection. For the purpose of this work, we shall consider these in terms of their importance in RNT.

2.3.2.2 Linear energy transfer

As charged particles pass through a material, they constantly experience the electric field from surrounding atomic electrons and nuclei. Thus they continuously lose energy through collisional and radiative losses as they pass through matter. The energy a charged particle transfers along its track is called the LET. In radionuclide therapy, LET is a very important quantity. It is defined as the ratio of the amount of energy transferred, dE_{total} by a charged particle to the target atoms in the immediate vicinity of its path in traversing a small distance, dx, to the distance dx (Chandra, 2004). This is expressed in equation 2.9 below: (Powsner, Palmer and Powsner, 2013; Saha, 2013).

$$LET = \frac{-dE_{total}}{dx} \qquad 2.9$$

The LET is typically measured in units of keV/μm and its value for charged particles depends on the mass, charge, and energy of the particle. When comparing an electron and alpha particle of equal kinetic energy, the electron travels at a much higher velocity because of its lower mass. As a result, the electron spends a shorter time in the neighbourhood of any particular atom and is less likely than the alpha particle to interact. Furthermore, the greater charge on the alpha particle results in stronger electrical interaction with orbital electrons. As the mass and charge of a particle increase, the frequency of interaction increases.

2.3.2.3 Range

The range of a charged particle in a medium refers to the average distance it travels in the incident direction. The range of charged particles is affected by many factors such as **energy, mass, charge** and **density** of the material the particle is traversing. Recall that a charged particle loses energy when interacting with a material and it eventually loses all its kinetic energy and comes to a complete halt. For light particles, the definition for the range is the minimum thickness of a material that is just impenetrable for them. The range of charged particles is an important quantity whose usefulness in targeted radionuclide therapy (TRT) cannot be overemphasized. For example, in TRT the range of particles determines what particle emitter to use in terms of the size of the tumour of interest to be treated. β^--particles of short-range (e.g. ^{131}I β) are very often the choice for treatment of small tumour cells or disseminated tumour cells (Carlsson et. al., 2003; Dash et al. 2013) because they have very low LET. The main advantage of β-particles is that they exhibit a ‘crossfire’ effect on nearby cells and thereby counteracts heterogeneous uptake to a certain degree.

Because of the continuous β-energy spectrum, β-particles have a distribution of range in materials. The mean range of β-particles emitted by ^{131}I in human tissue is 0.45 mm (Lewington, 2003) while their maximum range is given as 2.4 mm (Hoefnagel, 1998). Hence, most of their energy end up being deposited within 1 mm (Sisson, 2002). Because of their short range, they can deposit most of their energy within the human tissue and are used to destroy diseased cells such as cancer cells.

Another important quantity that needs to be mentioned here is the particle path length. It is defined as the distance the particle travels, in contrast to the range which is the depth of penetration of the particle in the medium. The path length for light charged particles (e.g. electron) in a given medium are almost always more than their range whereas for heavier particle (e.g. an alpha particle), the range and the path length are always nearly equal.

2.4 Production of ^{131}I

2.4.1 Production Process

^{131}I is one of the reactor-produced radionuclides in use in NM. It is produced either by fission of ^{235}U or by neutron capture by ^{130}Te. The production of ^{131}I is shown in equation form below.

$$^{130}\text{Te}\ (\text{n}, \gamma)\ ^{131}\text{Te} \qquad 2.10$$

$$^{235}\text{U}\ (\text{n, f})\ ^{131}\text{Te} \qquad 2.11$$

$$^{131}\text{Te} \xrightarrow[25\ min]{\beta^-} {}^{131}\text{I} \qquad 2.12$$

$$^{235}\text{U}\ (\text{n, f})\ ^{131}\text{I} \qquad 2.13$$

Equation 2.10 shows a neutron capture reaction in which ^{130}Te captures a thermal neutron (0.025 eV) thereby producing a gamma photon and a new radionuclide ^{131}Te. ^{131}Te decays by emitting a beta particle after 25 minutes to produce ^{131}I as shown in equation 2.12. The production of ^{131}I by a nuclear fission reaction is shown by equation 2.11. During this process, Uranium-235 (^{235}U) is bombarded with a thermal neutron and it undergoes fission, hence, producing ^{131}Te which eventually decays to ^{131}I as shown by equation 2.12. ^{131}I can also be produced directly in the ^{235}U fission reaction as shown in equation 2.13.

When ^{131}I is produced as stated above, it is separated from the other nuclear products in the form of sodium iodide (NaI). Usually, it is available in a non-carrier added state. However, its solution is made isotonic with physiologic saline. Sodium ascorbate or thiosulfate is usually added to ^{131}I-NaI solution at alkaline pH to minimize air oxidation of the solution that causes the iodine to become volatile I_2.

2.4.2 Availability of ^{131}I

For a radionuclide to be used successfully in the clinic for both diagnosis and therapy, it should be easily produced, and should have the ability to be transported with minimum decay losses to the user. ^{131}I meets these requirements and is currently the most widely used therapeutic radionuclide with its use being extended from the traditional thyroid related diseases to haematological diseases such as Non-Hodgkin's lymphoma (Das and Pillai, 2013). The shelf life for a preparation of ^{131}I is four weeks after calibration (Saha, 2010). This is partly due to its comparatively longer half-life of 8.02 days and this characteristic of ^{131}I is one of the advantages it has over other radionuclides. In many parts of the world where nuclear reactors and cyclotrons are not readily available, radionuclides of clinical significance are imported from their production sites.

In Africa for instance, it is only in South Africa that radionuclides for use in NM are produced. Therefore, for the rest of Africa, these radionuclides have to be imported. The issues relating to the availability of clinically important radionuclides, ^{131}I inclusive, are very big challenges (Adedapo *et al.*, 2013, Orunmuyi *et al.*, 2019), especially in a developing country. Thus radionuclides that are cheap and affordable and have relatively long half-lives are required in such developing and resource-poor countries.

This requirement and the relatively long shelf life of ^{131}I as mentioned above and the fact that in the oxidized form, iodine binds strongly to various molecules (Saha, 2010), allows flexibility for labelling and for shipping (Carrasquillo, Pandit-taskar and Chen, 2016), thus this makes it a good candidate for use in these regions of the world. In contrast, ^{123}I which is diagnostically superior to ^{131}I in terms of image contrast, sensitivity and specificity (Sisson and Yanik, 2012), is relatively expensive and has a shorter half-life (13.2 h). The shorter half-life makes it unrealistic to transport across regions as this could take a few days. Hence, it is not readily available to NM centres across these regions. ^{123}I is also very expensive and unaffordable to many in poorer regions of the world who need it.

^{124}I with a half-life of 4.2 days which is a PET radiotracer, is also said to be superior to ^{131}I in terms of diagnostic accuracy (Beijst *et al.*, 2017). The issue with ^{124}I, especially in Africa, is that not many countries have PET scanners and there is a limited number of cyclotrons available for its production in Africa. It is also not cheap and has logistical issues that, according to Grewal, lead to a small number of patients been included in most published studies using ^{124}I PET or PET/CT (Grewal, Ho and Schöder, 2016). Additionally, it is said that approximately 22 % of the disintegration of ^{124}I produces positrons of relatively high energy gamma and x-rays (Grewal, Ho and Schöder, 2016). The presence of photon radiation of 603 keV (Wierts *et al.*, 2011; Kuker, Sztejnberg and Gulec, 2017) with a 61 % abundance (Saha, 2010), are of concern for the use of ^{124}I (Beijst *et al.*, 2017) in terms of radiation safety of the patient.

As mentioned before, ^{131}I is relatively cheap and affordable and readily available and has been so since 1946 (Silberstein, 2012). This is because it is produced in very large quantities at several production sites around the world and it is distributed globally with allowable decay loss (Das and Pillai, 2013). It is also easily labelled to different agents. Therefore, it remains a leading theranostic agent and will likely remain so for many years to come. The characteristics of ^{131}I mentioned above have ignited research into other cancers that are not related to the thyroid (Das and Pillai, 2013). However, the relatively high yield (81 % abundance) of the 364 keV gamma rays is a disadvantage in terms of radiation burden to the patients and NM staff. It is also said to de-iodinate in vivo hence, for diseases other than thyroid-related diseases, the released iodine is detrimental to the patients' thyroid as it gets accumulated in it (Das and Pillai, 2013) unless thyroid blockers are used (Scheidhauer *et al.*, 2002). Therefore, this study regarding ^{131}I is very relevant in our setting in Africa as ^{131}I is widely used just as in many other parts of the world.

2.5 Image Formation

Nuclear medical imaging is based on detecting nuclear radiation emitted from the body after introducing a radiopharmaceutical inside the body to tag a specific physiological function. The radiopharmaceutical may emit photons in the form of gamma rays or x-rays. As long as the photons emanating from the radionuclide have sufficient energy to escape from the human body in significant numbers, images can be generated that portray the in vivo distribution of the radiopharmaceutical. The success of diagnostic NM is premised on two reasons. Reliance on the use of (1) very small amounts of materials thus usually not having any effect on the process being studied and (2) the emissions of the radionuclides being used can penetrate tissue and be detected outside of the patients without affecting organ functions. The goal of imaging in NM is to measure and quantify the activity distribution of the radiopharmaceutical within the patient. While anatomical modalities like CT and x-ray rely on measuring the transmission of x-rays through the patient, NM imaging relies on the principle of emission imaging where the gamma-rays emitted from the radiopharmaceutical within the patient are measured with scintillation detectors. Two- and three-dimensional images can be acquired using a gamma camera.

For RNT dose planning, the need for high-quality images for reliable and accurate quantification of the radiopharmaceutical distribution in the patients is important. Therefore, it is necessary to produce high-quality gamma camera images. The following sections will give a brief overview of the gamma camera and its main components.

2.5.1 Gamma camera

The gamma or Anger camera was developed by Hal O. Anger at the Donner Laboratory in Berkeley, California, in the 1950s. Today the gamma camera is by far the most common NM imaging device. The main components of a gamma camera detector assembly are shown in Figure 2.5. It consists of a collimator, scintillation crystal, a light guide, photomultiplier tubes (PMTs), positioning and summing circuits, multi-channel pulse height analyzer (MCA), and computational image processing and display.

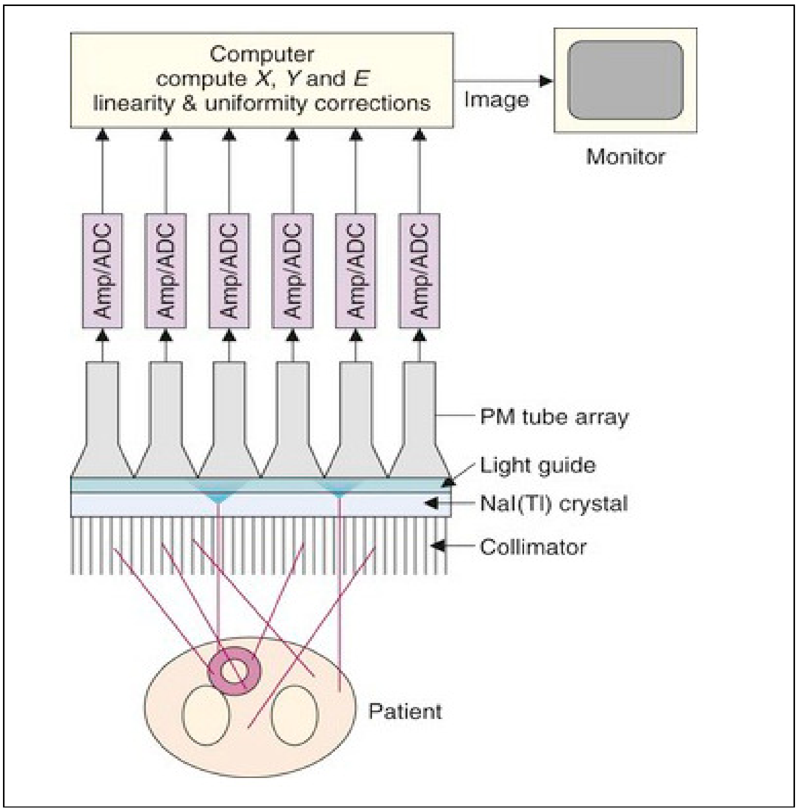

Figure 2. 5: ***Components of the gamma camera detector assembly***

(source: https://radiologykey.com/the-gamma-camera-basic-principles/ accessed on 12 November 2018).

2.5.1.1 The collimator

In NM studies gamma rays are emitted from the patient at a wide range of angles so they must be collimated in order to determine the point of origin. A gamma camera collimator is designed so that only gamma rays traveling in certain directions can pass through the holes of the collimator and reach the scintillation crystal of the gamma camera. All other gamma rays incident on the collimator should be absorbed. This process of absorptive collimation requires the collimator to be made of a heavy material with a high attenuation coefficient, such as lead. The most common type of collimator used in the NM clinic is a parallel-hole collimator. The parallel-hole collimator is designed so that only the gamma rays traveling in a direction nearly perpendicular to the detector will be measured. The parallel-hole collimators may include low-energy high-sensitivity; low-energy all-purpose; low-energy high-resolution; medium-energy, high-energy (for ^{131}I); and ultra–high-energy collimators.

Although the size of the image produced by a parallel-hole collimator is not affected by the distance of the object from the collimator, its spatial resolution degrades rapidly with increasing collimator-to-object distance. The spacing, length, and thickness of the collimator septa design are trade-offs between the detection efficiency and spatial resolution. High-energy collimators are typically used for radionuclides with higher energy emissions (such as ^{131}I) in order to reduce septal penetration.

2.5.1.2 The scintillation crystal

A scintillator is an organic (usually liquid) or inorganic material that produces a pulse of light when ionizing radiation interacts with it. Some of the gamma rays that pass through the collimator interact with the scintillation crystal which emits light in the ultraviolet/visible range after absorbing the energy of the gamma ray. The incident photons may be absorbed by a single photoelectric absorption or may undergo one or more Compton scatter before photoelectric absorption and/or pair production effects. This leads to ionization or excitation that raises the molecules and atoms in the material to a higher energy state, and on return to the stable state gives off light photons.

In the gamma camera, sodium iodide, doped with thallium (NaI (Tl)) is the scintillator that is commonly used. Its choice is based on the fact that it has a high density (3.67 g/cm^3) and the iodine has a high atomic number Z, of 53. These properties make it suitable for producing high light yield (approximately, 20 – 30 light photons per 1 keV of energy) (Saha, 2013). The modern gamma camera is equipped with a crystal which is typically 9.5 mm thick with dimensions of 600 × 405 mm resulting in a field of view (FOV) of about 550 × 400 mm. The scintillation crystal should have the following desirable properties: A relatively high scintillation efficiency, i.e. the fraction of incident photon energy that gets converted into detectable light must be high; the conversion should be linear so that the amount of light produced is proportional to the deposited energy; it should be transparent to its own scintillation light; the decay time of the scintillation process should be short so that high count rates are possible. The efficiency of the transfer of light photons from the crystal to the PMTs can be maximized by using a light guide in the form of a slab of Perspex (Lucite). Silicone grease is used to maintain good optical contact between the light guide and both the exit window of the detector and the entrance window of the PMTs.

2.5.1.3 The photomultiplier tubes

The purpose of the PMTs that are coupled to the backside of the scintillation crystal is to amplify the relatively weak light output from the scintillator and convert it into an electrical signal. This is accomplished by the PMTs by first converting the scintillation photons into electrons using a photocathode and then by creating secondary electrons using a series of dynode stages with increasing potential voltages. The output of each PMTs is used to define the X, Y coordinates of the point of interaction of the gamma ray in the detector by the use of an X- Y-positioning circuit and also is summed up by a summing circuit to form a pulse known as the Z pulse. The Z pulse is then subjected to pulse-height analysis and is accepted if it falls within the range of selected energies.

2.5.1.4 Energy discrimination/position information

The electrical signal produced by each PMT passes through a series of components including a preamplifier, amplifier and pulse height analyzer. These electronics are used to shape and amplify the electrical pulse and ultimately to determine the deposited gamma ray energy and location of the scintillation event. The position of the scintillation event on the crystal is calculated based on the differences between signals from each PMT and is performed by a dedicated onboard computer. In general, there is an inverse relationship between the light received by each PMT and the distance to the point of interaction in the crystal. Non-uniformities in the detector system output are compensated for using the data acquired in a calibration scan to form pre-calculated lookup tables. The total energy deposited by the absorbed gamma ray is computed by adding up the signals from all PMTs. A multichannel analyzer is used to measure the energy spectrum of the detected photons. Using the multichannel analyzer, an energy window is set over the photopeak(s) of the relevant radioisotope.

To deal with the limited energy resolution of the scintillation detector, the upper and lower level discriminators of the energy window are typically set to ± 10% from the primary gamma energy. Although separation is not perfect, this energy window helps to distinguish between primary and scattered photons. Photons detected with energies below the energy window have scattered and can no longer be used to provide information about the site of radioactive decay where they originated from. Scattered photons with energy that falls within the energy window will still be counted. Finally, the position of each detected emission within the patient is converted into a 2D array of 64 × 64 or 128 × 128 pixels typically with units of counts.

2.5.2 Image Acquisition: Planar/SPECT

A SPECT acquisition refers to obtaining 2-D images (planar imaging) of an object from projection measurements at different angles around the object. This is done by rotating the detector/s of the gamma camera around the object. It is carried out with the assumption that the activity distribution remains the same during the acquisition (Ljungberg and Gleisner, 2016). The 2-D image corresponds to the spatial distribution of the activity concentration of a gamma emitter in the object. Reconstructing the 2-D image dataset is a way of estimating the real 3-D distribution of the radioactivity in the imaged object from the different projections and is very important in SPECT image acquisition. Figure 2.6 is an example of a commercial SPECT/CT system.

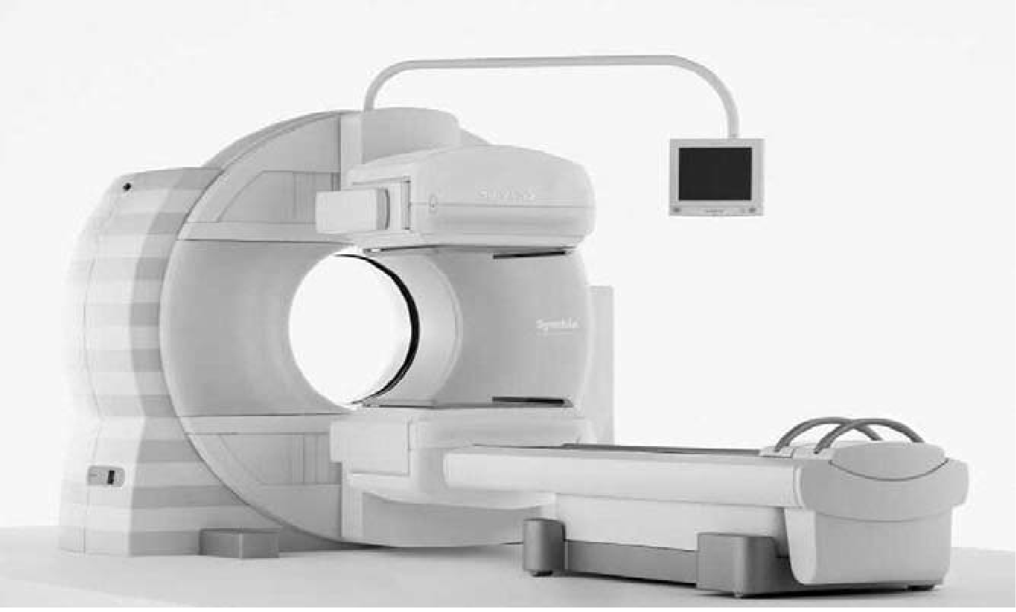

Figure 2.6: ***A Siemens Symbia system with an integrated gantry equipped with multi-detector computed tomography (MDCT) and dual-detector E-cam system (Siemens Medical Systems, Hoffman Estates, IL).***

SPECT offers greatly improved activity quantification, contrast, and spatial localization compared to planar scintigraphy. The number of projections acquired is an important parameter since angular undersampling can lead to image blurring and artifacts. As the number of projection angles are increased, sharper images can be reconstructed. Most SPECT acquisitions use between 60 and 128 projections. These SPECT images are acquired with the detector/s moving through an arc of either 180° or 360° and is determined by the size and position of the organ of interest. A 360° arc is less prone to image artifacts caused by attenuation and spatial resolution effects varying with distance from the camera. The acquisition can be carried out using either circular (with a fixed radius) or non-circular (following the patient's contour) orbits in either clockwise or anticlockwise direction. During acquisition, the detector/s can move continuously while acquiring the data or can move in a 'step and shoot' mode in which the detector/s remain stationary while acquiring and do not acquire when moving from one angle position to the other.

The number of counts and ultimately the noise in the projection images is determined by the frame duration of each camera stop. The orbit shape of the gamma camera can be chosen to follow a circular, elliptical or non-circular orbit. In the non-circular orbit mode, the detectors follow the patient contours using the infrared sensors of the detectors. For this acquisition mode, the depth-dependent spatial resolution loss by the gamma camera is thus limited by acquiring each projection angle as close to the patient as possible. SPECT images can be acquired using image matrices sizes ranging from 64 × 64 to 128 × 128 with different pixel sizes.

However, the optimal matrix and pixel size must be selected for each SPECT study. The choice of the matrix size, the angular sampling intervals as well as the inherent spatial resolution of the gamma camera determine the spatial resolution of the reconstructed images. The matrix size selection will thus depend on the frequency information that needs to be recovered. A decrease in voxel size improves the visual quality of the images, hence, the preferred matrix size for both acquisition and processing is the 128 × 128 matrix because it is suitable for acquisition of images for organs such as kidneys and thyroid gland. But, organs such as the myocardium or lung are usually acquired in a 64 × 64 matrix size. The 64 × 64 matrix size has the advantage of reduced storage requirements and has a shorter processing time. Nowadays, many commercially available SPECT systems include a low dose CT scanner that allows for improved attenuation corrections. A detailed overview of the data corrections needed for absolute activity quantification for SPECT is provided in section 3.4.

2.6 Monte Carlo simulation in nuclear medicine

2.6.1 Introduction

Computer modeling/simulation has found widespread use in many areas of human endeavour (McHaney 2009). Complex real-world systems are impossible to describe accurately using analytical methods, therefore there is a requirement for a tool that can accurately represent these complex systems. Computer simulations are used to model complex real-world situations.

One of the common computer simulation methods is Monte Carlo (MC) simulation which is increasingly being used in the NM field. MC simulations are used to create models that are similar to real life systems. The input parameters for a MC simulation code can be varied and thus, different behaviours of the modeled system are studied in order to understand its dynamics. It is, therefore, possible to study in detail the factors causing NM image degradation using computer modeling. They help us to understand natural phenomena from a different perspective by providing a theoretical basis for experimental results. This is done through the use of known probabilities of occurrence with a random sampling of the probability density functions (Landau and Binder, 2015). MC has the advantage of creating a controlled environment whereby many phenomena which are difficult or are impossible to measure physically are studied or evaluated. It also facilitates the calculation of complex parameters in experiments (Lee *et al.*, 2015), complex radioactive source distribution and easy description of NM scanner geometry (Karakatsanis *et al.*, 2006).

MC simulations are basically, a numerical sampling of random variables with specified PDFs (Saidi, Sadeghi and Tenreiro, 2013; Fasso, Ferrari and Sala, 2011). MC simulation is a random process, thus, it is also affected by the statistical variables that affect radioactivity. Therefore, due to the statistical and random nature of both radioactivity and MC simulation, MC simulations are suitable for mimicking the radioactive process. This is most important in particle transport and particle interactions, especially with matter (Fasso, Ferrari and Sala, 2011) since particle transport and interaction are good examples of physical stochastic processes which are well modelled by MC simulations.

In, NM, the use of MC simulations has become common among many research groups in recent years (Braad *et al.*, 2016) as it is useful for dosimetry modelling, computations in therapy and in diagnosis (detector modelling and design of imaging system) and pharmacokinetic modelling (Zaidi and Andreo, 2003; Asl *et al.*, 2015). This is due partly to the increase in computational power of present-day computers and their low cost and the ease with which they are made available (Zaidi and Sgouros, 2003) coupled with their usefulness in this medical field. MC simulations in NM are mainly used to model photon and particle transport for imaging and therapy. It is based on stochastic mathematical simulation of the interactions between photons and/or particles and matter.

Several MC software packages are available and used in NM image simulations and dose calculations (Zaidi 1999; Ljungberg, Strand and King, 1995; Sgouros et al. 2008; Zaidi 2006; Sgouros et al. 2011; Guy et al. 2003; Dewaraja et al. 2005; Kost et al. 2015). These MC packages can be classified as particle-tracking codes and dedicated analytic simulations. The particle-tracking codes are further divided into general-purpose and dedicated codes for emission tomography respectively (Gillam and Rafecas, 2016).

2.6.2 Sampling methods in Monte Carlo

MC has its foundation on a random-sampling technique to solve the Boltzmann transport equation. Therefore, it consists of two essential parts namely: the geometry and materials of the problem and sampling randomly the outcome of physical events from probability distributions (Fasso, Ferrari and Sala, 2011). To solve the Boltzmann integral, MC uses random and pseudorandom numbers sampled from values of a variable distributed according to a probability density function. Typically, when MC is used to mimic radiation transport and radiation interaction, each photon or particle is followed on its path through the matter with which it is interacting. At each step, the occurrence and the consequence of the interactions are arrived at by randomly making a selection from the appropriate probability distributions. The sequence of this selection and the events that follow are generally called the particle or photon history. Other sampling methods used, include sampling from a discrete distribution, sampling from a generic continuous distribution, and the rejection technique.

2.6.3 Events in Monte Carlo

The particle or photon histories are modelled by both discrete and continuous processes. Physical events, in reality, are discrete, however, for convenience sake, some events are described as continuous and sampled from a suitable distribution. All the interactions of radiation (photon and particle) with matter are considered to be discrete physical processes and they are sampled only when the energy of the radiation is higher than a given threshold (Fasso, Ferrari and Sala, 2011). On the other hand, simulating some of these discrete processes can be strenuous in terms of the amount of time needed. Therefore, a straight continuous step is used to condense the process. This is called condensed particle history.

The histories, when simulated are each assigned a weight which is usually updated from time to time until the photon or particle exits the medium of interaction. A number of the weights are therefore, generated based on the number of the histories and then the mean value of the weights is considered in order to estimate the value of the true behaviour of the modelled system. Since the confidence of the estimate cannot be measured using the mean value, the sample variance is rather used. So the sample variance will provide an estimate of how much the individual samples are spread around the mean value. This is very time-consuming and hence, methods are available to reduce the variance.

2.6.4 Variance reduction techniques

The MC method requires a lot of computer power and is very time-consuming. Since it is used to study the average or expected behaviour of a system, a large number of histories are required to be sampled and the outcome observed. It is then possible to evaluate the results in terms of accuracy and precision. To reduce the uncertainty of the simulation, some physical models are implemented. The variance reduction technique is an example of such a model.

The variance reduction technique is aimed at increasing the precision and at the same time reducing the relative error in the simulations without increasing the number of histories. Many variance reduction techniques (such as Splitting/Roulette, energy cut off, time cut off, implicit capture, and forced collisions) are usually applied to reduce the simulation time and in modern times very fast computer systems are available, therefore, simulations can be carried out with relatively shorter times than previously possible.

2.6.5 Monte Carlo code used in this work for modelling SPECT imaging

The MC code used in this project for simulating the SPECT imaging process is SIMIND (Simulating Medical Imaging Nuclear Detectors) (Ljungberg & Strand 1989). The code was developed and is maintained/updated by Prof M. Ljungberg at the Department of Medical Radiation Physics, University of Lund, Sweden. SIMIND is used to model photons which are emitted from isotropic point sources and are followed while they interact with the phantom according to the probability distributions of the physical processes that they may undergo photoelectric absorption, coherent (Rayleigh) scattering or incoherent (Compton) scattering.

SIMIND was designed mainly to model clinical scintillation and SPECT systems. SIMIND is made of two parts, the CHANGE program where the input to SIMIND are defined and the main program, SIMIND. Parameters describing models of the scintillator are input into CHANGE and SIMIND reads the input file and execute the simulation specified. The current version of SIMIND is incorporated with a 'penetrate' scoring routine which models the CDR for medium and high energy gamma emitters and therefore, can accurately simulate SPECT images of ^{131}I. In this work, the SIMIND MC code was first used to model a typical gamma camera used in our clinic and was validated for this camera before been used to simulate SPECT images for the various patient models.

In this chapter, the basic physics underlying ^{131}I imaging and therapy had been briefly discussed. Images formed as discussed here need to be absolutely quantified to make them relevant for accurate absorbed dose calculation in patient-specific dosimetry, therefore, ^{131}I SPECT image quantification will be the subject of discussion in the next chapter (Chapter 3).

2.7 References

Adedapo, K. S., Onimode, Y. A., Ejeh, J. E. and Adepoju, A. O. (2013) ‘Avoidable challenges of a nuclear medicine facility in a developing nation.’, *Indian J. Nucl. Med.,* 28, pp. 195–199.

Asl, R. G., Nasseri, S., Parach, A. A., Zakavi, S. R., Momennezhad, M. and Davenport, D. (2015) ‘Monte Carlo and experimental internal radionuclide dosimetry in RANDO head phantom’, *Australas. Phys. Eng. Sci. Med.*, 38, pp. 465–472.

Beijst, C., de Keizer, B., Lam, G. E. H., Janssens, G. O., Tytgat, G. A. M. and de Jong, H. W. A. M. (2017) ‘A Phantom study: Should ^{124}I-mIBG PET/CT replace ^{123}I-mIBG SPECT/CT?’, *Med. Phys.*, 44, pp. 1624–1631.

Braad, P. E. N., Andersen, T., Hansen, S. B. and Hoilund-Carlsen, P. F. (2016) ‘Strategies for CT tissue segmentation for Monte Carlo calculations in nuclear medicine dosimetry’, *Med. Phys.*, 43, pp. 6507–6516.

Bushberg, J. T., Seibert, J. A. and Boone, J. M. (2012) *The Essential Physics of Medical Imaging*. 3rd edn. Philadelphia, PA: Lippincott Williams and Wilkins.

Carlsson, J., Aronsson, E. F., Hietala, S-O., Stigbrand, T. and Tennvall, J. (2003) ‘Tumour therapy with radionuclides: Assessment of progress and problems’, *Radiotherapy and Oncology*, 66, pp. 107–117.

Carrasquillo, J. A., Pandit-taskar, N. and Chen, C. C. (2016) ‘^{131}I Metaiodobenzylguanidine Therapy of Pheochromocytoma and Paraganglioma’, *Semin. Nucl. Med.*, 46, pp. 203–214.

Chandra, R. (2004) *Nuclear Medicine Physics: The Basics*. 6th edn. Philadelphia, PA: Lippincott Williams and Wilkins.

Cherry, S. R., Sorenson, J. A. and Phelps, M. E. (2012) *Physics in Nuclear Medicine*. 4th edn. Philadelphia, PA: Elsevier Inc.

Das, T. and Pillai, M. R. A. (2013) ‘Options to meet the future global demand of radionuclides for radionuclide therapy’, *Nucl. Med. Biol.*, 40, pp. 23–32.

Dash, A., Russ Knapp Jr, F. F. and Pillai, M. R. A. (2013) ‘Targeted Radionuclide Therapy - An Overview’, *Current Radiopharmaceuticals*, 6, pp. 1–29.

Dewaraja, Y. K., Wilderman, S.J., Ljungberg, M., Koral, K. F., Zasadny, K. and Kaminiski, M. S. (2005) ‘Accurate dosimetry in ^{131}I radionuclide therapy using patient-specific, 3-dimensional methods for SPECT reconstruction and absorbed dose calculation.’, *J. Nucl. Med.*, 46, pp. 840–849.

Fasso, A., Ferrari, A. and Sala, P. R. (2011) ‘Principles of Monte Carlo Calculations and Codes’, in Cantone, M. C. and Hoeschen, C. (eds) *Radiation Physics for Nuclear Medicine*. Heidelberg: Springer Science, pp. 35–57.

Gillam, J. E. and Rafecas, M. (2016) ‘Monte-Carlo simulations and image reconstruction for novel imaging scenarios in emission tomography’, *Nucl. Inst. Methods Phys. Res., A*., 809, pp. 76–88.

Grewal, R. K., Ho, A. and Schöder, H. (2016) ‘Novel Approaches to Thyroid Cancer Treatment and Response Assessment’, *Semin. Nucl. Med.*, 46, pp. 109–118.

Grudzinski, J. J., Yoriyaz, H., Deluca Jr, P. M. and Weichert, J. P. (2010) ‘Patient-specific treatment planning for systemically administered radiopharmaceuticals using PET / CT and Monte Carlo simulation’, *Applied Radiation and Isotopes*. 68, pp. 59–65.

Guy, M. J., Flux, G. D., Papavasileiou, P., Flower, M. A. and Ott, R. J. (2003) ‘RMDP: A Dedicated Package for ^{131}I SPECT Quantification, Registration and Patient-Specific Dosimetry.’, *Cancer Biother. Radiopharm.*, 18, pp. 61–69.

Hoefnagel, C. A. (1998) ‘Radionuclide Cancer Therapy’, *Ann. Nucl. Med.*, 12, pp. 61–70.

Jentzen, W., Verschure, F., van Zon, A., van de Kolk, R., Wierts, R., Schmitz, J., Bockisch, A. and Binse, I. (2016) ‘^{124}I PET Assessment of Response of Bone Metastases to Initial Radioiodine Treatment of Differentiated Thyroid Cancer’, *J. Nucl. Med.*, 57, pp. 1499–1504.

Karakatsanis, N., Sakellios, N., Tsantilas, N. X., Dikaios, N., Tsoumpas, C., Lazaro, D., Loudos, G., Schmdtlein, C. R., Louizi, K., Valais, J., Nikolopoulos, D., Malamitsi, J., Kandarakis, J. and Nikita, K. (2006) ‘Comparative evaluation of two commercial PET scanners , ECAT EXACT HR + and Biograph 2 , using GATE’, *Nucl. Inst. Methods Phys. Res., A*, 569, pp. 368–

372.

Kost, S. D., Dewaraja, Y. K., Abramson, R. G. and Stabin, M. G. (2015) 'VIDA: A Voxel-Based Dosimetry Method for Targeted Radionuclide Therapy Using Geant4.', *Cancer Biother. Radiopharm.*, 30, pp. 16–26.

Kuker, R., Sztejnberg, M. and Gulec, S. (2017) '^{124}I Imaging and Dosimetry', *Mol. Imaging Radionucl. Ther.*, 26, pp. 66–73.

Landau, D. P. and Binder, K. (2015) *A Guide to Monte Carlo Simulations in Statistical Physics*. 4th edn. United Kingdom: Cambridge University Press.

Lee, C.-L., Wahnishe, H., Sayre, G. A., Cho, H-M., Kim, H-J., Hernandez-Pampaloni, M., Hawkins, R. A., Dannoon, S. F., VanBrocklin, H. F., Itsara, M., Weiss, W. A., Yang, X., Hass-Kogan, D. A., Matthay, K. K. and Seo, Y. (2010) 'Radiation dose estimation using preclinical imaging with ^{124}I-metaiodobenzylguanidine (MIBG) PET.', *Med. Phys.*, 37, pp. 4861–4867.

Lee, H., Yoon, G., Cho, S., Park, S. H. and Lee, W. (2015) 'The Adaptation Method in the Monte Carlo Simulation for Computed Tomography', *Nucl. Eng. Technol.*, 47, pp. 472–478.

Lewington, V. J. (2003) 'Targeted radionuclide therapy for neuroendocrine tumours', *Endocrine-Related Cancer*, 10, pp. 497–501.

Ljungberg, M. and Gleisner, K. S. (2016) 'Personalized Dosimetry for Radionuclide Therapy Using Molecular Imaging Tools', *Biomedicines*, 4, pp. 25–45.

Ljungberg, M., Strand, S.-E. and King, M. A. (1995) *Monte Carlo Calculations in Nuclear Medicine Applications in Diagnostic Imaging*. 1st edn. Edited by M. Ljungberg, S.-E. Strand, and M. A. King. Bristow and Philadelphia: IOP Publishing.

Ljungberg, M. and Strand, S. E. (1989) 'A Monte Carlo program for the simulation of scintillation camera characteristics', *Comput. Methods Programs Biomed.*, 29, pp. 257–272.

McHaney, R. (2009) *Understanding Computer Simulation*. 1st edn. Bookboon e-book company.

Orunmuyi, T. A., Sathekge, M. M. and Buscomb, R. J. (2019) 'Ensuring effective and sustenable radionuclide delivery and its impact on the development of nuclear medicine in the developing world with special reference to Nigeria.' *World J Nucl Med.* 18, pp. 2 - 7.

Podgorsak, E. B., Kesner, A. L. and Soni, P. S. (2014) 'Basic Physics for Nuclear Medicine', in Bailey, D. L. et al. (eds) *Nuclear Medicine Physics. A Handbook for Teachers and Students.* Vienna: International Atomic Energy Agency (I.A.E.A).

Powsner, R. A., Palmer, M. R. and Powsner, E. R. (2013) *Essentials of Nuclear Medicine Physics and Instrumentation*. 3rd edn. Chichester, West Sussex, UK: John Wiley and Sons. Ltd.

Saha, G. B. (2010) *Fundamentals of Nuclear Pharmacy*. 6th edn. New York: Springer Science.

Saha, G. B. (2013) *Physics and Radiobiology of Nuclear Medicine*. 4th edn. New York: Springer Science.

Saidi, P., Sadeghi, M. and Tenreiro, C. (2013) 'Variance Reduction of Monte Carlo Simulation in Nuclear Engineering Field', in Chan, V. (ed.) *Theory and Applications of Monte Carlo Simulations*. Rijeka, Croatia: InTech, pp. 153–172.

Scheidhauer, K., Wolf, I., Baumgartl, H., von Schilling, C., Schmidt, B., Reidel, G., Peschel, C. and Schwaiger, M. (2002) 'Biodistribution and kinetics of ^{131}I-labelled anti-CD20 MAB IDEC-C2B8 (rituximab) in relapsed non-Hodgkin's lymphoma', *Eur. J. Nucl. Med.*, 29, pp. 1276–1282.

Sgouros, G., Frey, E., Wahl, R., Bin, H., Andrew, B. and Hobbs, R. (2008) '3-D Imaging-Based, Radiobiological Dosimetry', *Semin. Nucl. Med.,* 38, pp. 321–334.

Sgouros, G., Hobbs, R. F., Atkins, F. B., van Nostrand, D., Ladenson, P. W. and Wahl, R. L. (2011) 'Three-dimensional radiobiological dosimetry with ^{124}I PET for ^{131}I therapy of thyroid cancer', *Eur. J. Nucl. Med. Mol. Imaging*, 38, pp. S41–S47.

Silberstein, E. B. (2012) 'Radioiodine : The Classic Theranostic Agent', *Semin. Nucl. Med.*, 42, pp. 164–170.

Sisson, J. C. (2002) 'Practical Dosimetry of ^{131}I in Patients with Thyroid Carcinoma', *Cancer Biother. Radiopharm*, 17, pp. 101–105.

Sisson, J. C. and Yanik, G. A. (2012) 'Theranostics: Evolution of the radiopharmaceutical meta-iodobenzylguanidine in endocrine tumours.', *Semin. Nucl. Med.*, 42, pp. 171–184.

Song, N., Du, Y., He, B. and Frey, E/ C. (2011) 'Development and evaluation of a model-based downscatter compensation method for quantitative I-131 SPECT', *Med. Phys.*, 38, pp. 3193–3204.

Srivastava, S. C. and Mausner, L. F. (2013) 'Therapeutic Radionuclides: Production, Physical Characteristics, and Applications', in Baum, R. P. (ed.) *Therapeutic Nuclear Medicine*. Berlin Heidelberg: Springer-Verlag, pp. 11–50.

Thompson, M. A. (2001) 'Radiation Safety Precautions in the Management of the Hospitalized ^{131}I Therapy Patient', *J. Nucl. Med. Technol.*, 29, pp. 61–66.

Wierts, R., de Pont, C. D. J. M., Brans, B., Mottaghy, F. M. and Kemerink, G. J. (2011) 'Dosimetry in molecular nuclear therapy', *Methods.*, 55, pp. 196–202.

Wierts, R., Brans, B., Havekes, B., Kemerink, G. J., Halders, S. G., Schaper, N. N., Backes, W. H., Mottaghy, F. M. and Jentzen, W. (2016) 'Dose-Response Relationship in Differentiated Thyroid Cancer Patients Undergoing Radioiodine Treatment Assessed by Means of ^{124}I PET/CT', *J. Nucl. Med.*, 57, pp. 1027–1032.

Yordanova A., Eppard, E., Kurpig, S., Bundschuh, R., Schonberger, S., Gonzalez-Carmona, M., Feldmann, G., Ahmadzadehfar, H. and Essler, M. (2017) 'Theranostics in nuclear medicine practice', *OncoTargets and Therapy*, 10, pp. 4821–4828.

Zaidi, H. (1999) 'Relevance of accurate Monte Carlo modelling in nuclear medical imaging', *Med. Phys.*, 26, pp. 574 - 608.

Zaidi, H. (2006) 'Monte Carlo Modeling in Nuclear Medicine Imaging', in Zaidi, H. (ed.) *Quantitative Analysis in Nuclear Medicine Imaging*. New York: Springer Science, pp. 358–390.

Zaidi, H. and Andreo, P. (2003) 'Monte Carlo techniques in nuclear medicine dosimetry', in Zaidi, H. and Sgouros, G. (eds) *Therapeutic Applications of Monte Carlo Calculations in Nuclear Medicine*. London: IOP Publishing, pp. 28–54.

Zaidi, H. and Sgouros, G. (2003) *Therapeutic Applications of Monte Carlo Calculations in Nuclear Medicine*. Edited by H. Zaidi and G. Sgouros. London: IOP Publishing.

CHAPTER THREE: I-131 SPECT Image Quantification

Table of Contents

3.1 Introduction

Image quantification is needed when accurate information regarding radionuclide uptake is of interest. This can be helpful in clinical diagnosis, e.g. in renal function glomerular filtration rate calculations, radionuclide dosimetry for therapeutic purposes etc. Accurate image quantification is a prerequisite for accurate absorbed dose calculation and comparison of clinical images before and after therapy to assess the treatment outcome. Although simple quantitative measurements can be carried out on planar images, it is accepted that planar imaging is limited by its inherent lack of depth information and therefore, for accurate quantitation, three-dimensional (3-D) Single Photon Emission Computed Tomography (SPECT) imaging is required. SPECT absolute activity quantification of nuclear medicine (NM) images simply refers to the determination of numerical values for the uptake or distribution of radionuclides in patients (IAEA, 2014). This involves the conversion of the detected incidents or counts that formed the image, to activity.

To successfully do this, the following steps need to be followed. First, there is the need to reconstruct a 3-D image from the two-dimensional (2-D) projection images. Accurate image quantification in NM requires good image spatial resolution, image contrast and fewer image artefacts. Therefore, during the reconstruction process, some image degradation effects (e.g. photon scatter, photon absorption, and spatial resolution) are corrected for. The final step is to apply a calibration factor (CF) to convert image counts from reconstructed data into activity values (Ritt *et al.*, 2011). In this chapter, image reconstruction methods as well as correction techniques which affect the accuracy of quantitative SPECT imaging, namely attenuation, scatter, collimator-detector-response (CDR) and partial volume effect (PVE) will be discussed.

Image quantification can be classified into relative quantification and absolute quantification.

3.1.1 Relative quantification

Relative quantification is simpler than absolute quantification since the requirements are less rigorous than that for absolute quantification. It requires using the information derived from the image counts without necessarily converting the counts to activity or without the need to apply any corrections to the image. Relative quantification is used to compare radioactivity distribution between two datasets, either between two or more regions in a particular image or between datasets obtained from different images. It can also be used to compare the image with normal or abnormal datasets. Clinical examples of the application of relative quantification are; comparison of stress and rest images of the left ventricle in adults with possible ischemia; comparison of myocardial perfusion image of a patient diagnosed of coronary artery disease with a database of healthy individuals (e.g. Cedar-Sinai myocardial perfusion database (Fredericks *et al.*, 1999)) for assessing coronary artery disease and heart muscle damage following infarction; comparison of radioactivity distribution between brain grey matter and white matter; accumulation of radiotracer in both primary and metastatic lesions in oncologic studies etc. (Cherry et al., 2012).

3.1.2 Absolute quantification

Absolute quantification, unlike relative quantification, is more challenging. It is the process by which radioactivity concentration in a particular region of interest (ROI) in NM image is determined in a way that it reliably reflect the activity concentration in the imaged object. To do this, corrections for several factors that influence the accuracy of image quantification in NM need to be applied to the acquired data. This is needed in order to accurately convert the acquired counts to activity by using a predetermined CF as will be discussed. This type of quantification is useful, not only with regards the total activity in an area or volume defined in the image but also the details about the activity distribution (Shcherbinin and Celler, 2010). Absolute quantification has particular application in targeted radionuclide therapy dosimetry.

The main aim of absolute quantification in SPECT is to accurately recover the 3-D activity distribution in objects or regions in the body from the NM images (Shcherbinin and Celler, 2010). This leads to better diagnostic and therapeutic judgments from these images (Frey, Humm and Ljungberg, 2012). To achieve the best accuracy possible, the quality and quantity of the data that form the image have to be improved upon. This is done by acquiring data during the image formation process and correcting for the image degrading factors during the image reconstruction process as will be discussed.

3.2 Image reconstruction methods

As mentioned above, image reconstruction is very important for absolute activity quantification. SPECT data is acquired as a set of planar 2-D images (projections) of a 3-D source distribution at different angles as explained in chapter 2 section 2.5.2. The projections can be used to generate a 3-D source distribution within the patient using an appropriate image reconstruction algorithm. The two most commonly used methods for SPECT image reconstruction are analytical and iterative reconstruction algorithms and will be discussed individually in the next sections.

3.2.1 Analytical reconstruction methods

Analytical reconstruction algorithms use mathematical solutions that are exact in reconstructing the radionuclide distribution in an image. Analytical methods include amongst others, Simple Back Projection and its variants (such as Filtered Back Projection (FBP), Back Projection of Filtered Projections etc.), convolution Back Projection, Re-binning method for fan-beam geometries, fast volume reconstruction algorithm etc. (Tsui and Frey, 2006). Most of the analytical reconstruction methods are simple and easy to implement, however, they possess the shortcoming of assuming that during the image acquisition process there were no image degrading effects from instrumentation, physical factors and patient motions, which is far from reality.

Because of this assumption, the correction methods for these effects are not modelled in the analytical reconstruction algorithm, hence, they are only suitable for relative quantification and not absolute quantification. For the FBP, which used to be the most widely used reconstruction method in the NM clinic, there is an additional shortcoming of producing reconstructed images with streak artefacts that are very prominent near hot structures as well as high noise enhancements in the reconstructed images (Hutton, Nuyts and Zaidi, 2006). These streak artefacts are a result of poor counting statistics or random ‘noise’ spikes (Cherry, Sorenson and Phelps; 2012). However, these artefacts can be suppressed by using a k-space filter with a strong roll-off at high spatial frequencies but with loss of image resolution. These shortcomings of analytical methods showed the need for an alternative method. The alternative to analytical reconstruction is the iterative reconstruction technique.

3.2.2 Iterative reconstruction methods

When considering the reality of NM images, we note that data collected during the imaging process are dominated by statistical noise, and there are missing data, which are not acquired in between projection steps, therefore, not all projection views are fully sampled (Gillam and Rafecas, 2016). Hence, a reconstruction algorithm that considers the nature of noise within the data and can ‘fill in the gap’ for the missing data is required. This algorithm should have the ability to model noise directly so that the final reconstructed 3-D image will have improved noise properties. This kind of algorithm is known as a statistical or an iterative algorithm, in which a noise model is incorporated and can handle missing data as well. The noise model accounts for the statistical variations in the measured data (Gillam and Rafecas, 2016).

The general concepts of iterative reconstruction are outlined in Figure 3.1. The principle of the iterative reconstruction algorithm is a feedback process in which the projection image generated (forward projected) from an initial estimate of the acquired image is compared with the acquired image projection to form an error estimate. The initial estimate of the acquired image can be very simple, such as a uniform image, or it could be a FBP reconstructed image. The difference or error estimate between the two projection images is used to update the current estimate (back projected) in order to bring it closer to the measured object. The process is repeated several times (iterated) until there is a convergence, i.e. the difference between the estimated distribution and the measured distribution becomes sufficiently small (Ljungberg and Sjögreen-Gleisner, 2015). This reconstruction method aims to determine the 'best' estimate of the activity distribution based on measured projections (Hutton, Nuyts and Zaidi, 2006). It also has the advantage of being able to handle complex models of the physics underlying the emission of radiation and its detection during the image formation process. At the same time, it also reduces substantially, the streaking artefacts that are found in images reconstructed with analytical methods (Hutton, Nuyts and Zaidi, 2006). However, this reconstruction method can be very slow because of it being computationally intensive. However, due to advances in computer speed and memory, it is now less slow compared with previously.

According to Zeng, in mathematical terms, an iterative reconstruction method discretizes the image into pixels and each pixel value is then treated as an unknown value and thereafter, a system of linear equations can be set up according to the imaging geometry and physics (Zeng, 2001). He further mentioned that the system of linear equations can be represented in a matrix form by $FX = P$. For this matrix, each element (X_j) in X is a pixel value and each element (P_i) in P is a projection measurement, and F_{ij} in F is a coefficient that is the contribution from pixel j to the projection bin i which will be solved with an iterative algorithm.

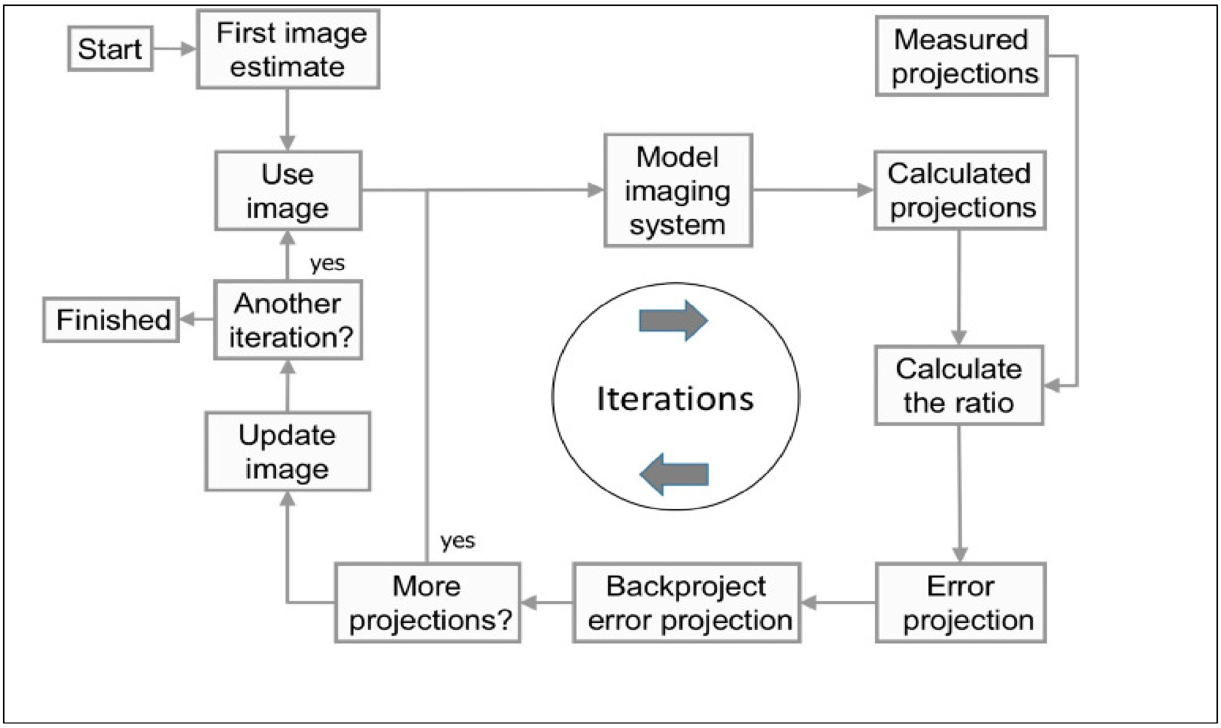

Figure 3. 1: *Flowchart of the iterative reconstruction technique*

Two popular iterative reconstruction methods that are used for processing clinical images in NM are the Maximum Likelihood-Expectation Maximization (ML-EM) and the Ordered Subset-Expectation Maximization (OS-EM).

3.2.2.1 Maximum Likelihood-Expectation Maximization

To properly model the image acquisition in NM, the random Poisson nature of the radioactive decay should be considered. Therefore, an iterative reconstruction technique that determines the Maximum Likely (ML) solution (called Maximum Likelihood) for the Poisson nature of the image needs to be applied. The most commonly used of this approach is the Expectation Maximization (EM).

ML-EM which models the emission process as a Poisson probability distribution is given by equation 3.1 as:

$$f_j^{new} = \frac{f_j^{old}}{\sum_i a_{ij}} \sum_i a_{ij} \frac{P_i}{\sum_k a_{ik} f_k^{old}} \qquad 3.1$$

Where f_j^{new} refers to the estimated intensity value of pixel j in the new estimate while f_j^{old} refers to the estimated intensity value of pixel j in the old estimate and P_i is the measured events in projection bin i and a_{ij} represents the elements for non-uniform attenuation, collimator-detector response (CDR) and or scatter. The term $\sum_k a_{ik} f_k^{old}$ in the above equation represents a summation over all image pixels and usually, it is first evaluated before summation over the j projection elements can be computed. It is given a different pixel index k to avoid being confused with i. In ML-EM each update involves back projection and forward projection for all projections. A disadvantage of ML-EM is thus that many iterations are required to achieve a satisfactory agreement between the estimated and measured images, therefore, it is very time-consuming. Furthermore, as the number of iterations increases, the reconstructed image noise increases. An accelerated version of the ML-EM algorithm is the OS-EM algorithm.

OS-EM (Hudson and Larkin, 1994) is a modification of ML-EM which is introduced to speed up the iteration process. In OS-EM, projections are grouped into a number of subsets separated by some fixed projection angles. It is possible to update an image several times towards convergence in a single iteration by using this approach. Therefore, this leads to a reduction in the number of iterations used. The equation for OS-EM is very similar to the ML-EM equation above but differ only by the use of subsets S_n, where $n \in N$, the total number of projections divided by the number of projections per subset or subset size.

$$f_j^{new} = \frac{f_j^{old}}{\sum_{l \in S_n} a_{lj}} \sum_{i \in S_n} a_{ij} \frac{P_i}{\sum_k a_{ik} f_k^{old}} \qquad 3.2$$

This model properly models the noise properties of projections into reconstruction images. A single iteration is said to be completed after all the subsets are processed. So that a single iteration of OS-EM with n subsets processed is similar to n iterations of ML-EM using all projections, which substantially reduces the time of reconstruction. A single subset containing all of the projections is equivalent to standard ML-EM, which uses all of the projection data to perform one update. In general, OS-EM speeds up ML-EM by a factor that is approximately equal to the number of subsets used.

3.2.2.2 OS-EM 3-D Technology

Gamma camera vendors have incorporated various iterative reconstruction software programs that are optimized for quality and accuracy of patient data when compared to previously used software. These advanced iterative reconstruction software programs incorporate corrections for image degrading factors into the reconstruction algorithms and are also developed for use with advanced SPECT/CT systems. These iterative reconstruction programs make provision for improvements in image contrast, noise reduction, CT-based attenuation correction, advanced scatter correction and 3-D resolution recovery. The Siemens Symbia T SPECT/CT system used in this work is equipped with the SYNGO workstation using the Flash 3D advanced resolution recovery software (Hawman *et al.*, 2014).

3.3 Factors influencing SPECT quantification

3.3.1 Attenuation

Attenuation (which is a combination of photoelectric absorption and Compton scatter as discussed in chapter 2, section 2.3) of useful photons during the image formation process will reduce the number of detected photons in the image. Attenuation takes place in two locations, namely: inside the patient and at the gamma camera collimator surface. In SPECT, the severity of the effects of attenuation inside the patient is more for structures that are located deeper in the patient (this means that photon attenuation in SPECT is depth-dependent). Again, those photons that escape attenuation in the patient may eventually be attenuated by the collimator, thereby, further degrading the image that will be formed. The effects of photon attenuation on SPECT images are clearly one of the main limitations and needs to be corrected for, especially when one is interested in the accurate quantification of the image. For large objects, attenuation is the single largest factor that degrades quantitative accuracy. Attenuation of photons is described in relation to the linear attenuation coefficient as discussed in chapter 2. Linear attenuation coefficients assume that a photon is removed from the beam once it has been fully absorbed or scattered. These linear attenuation coefficients are referred to as narrow beam attenuation coefficients and are applicable when scatter corrections are applied to SPECT images.

3.3.2 Scatter

When scattered photons are included in a SPECT image, they lead to the degradation of the image contrast, spatial resolution, and quantification accuracy (Dewaraja, Ljungberg and

Koral, 2000). This is because scattered photons give false information about their origin. When they find their way through the collimator holes, the gamma camera 'sees' them as coming from a point in the imaged object which is directly along the same line as the collimator hole. This direction is actually incorrect and a result of the scatter which leads to a change in direction. Images reconstructed with attenuation compensation but without scatter compensation result in a spurious increase in image intensity, especially in the interior of the image. The magnitude of scatter effects depends on photon energy, source depth, energy window setting, and the energy resolution of the system. Scatter effects are larger for lower energy photons and for radionuclides with multiple-photon emission.

3.3.3 Collimator-detector response

The CDR function primarily determines the image resolution and it consists of four components, namely: the intrinsic response, geometric response, septal scatter and septal penetration and are illustrated in Figure 3.2 (Ritt *et al.*, 2011). The intrinsic response describes the effect of photon interactions in the detector system without the collimator, it includes photon scatter and the statistical uncertainty in the estimated origin of the photon. The intrinsic resolution is therefore, limited by the resolution of the crystal and by the accuracy of the positioning electronics. The geometric response models the source-to-collimator distance effects since the measured response in the crystal vary with source-to-collimator distance due to the absorptive parallel-hole collimation of the photons. Septal penetration and scatter are the components of the collimator response corresponding to photons that pass through the collimator septa, further degrading the spatial resolution. The effects of septal penetration and scatter are especially important for medium and high energy gamma rays. The effects of these four components of CDR known as response functions can be incorporated as a mathematical model into the iterative reconstruction algorithm (Ritt *et al.*, 2011).

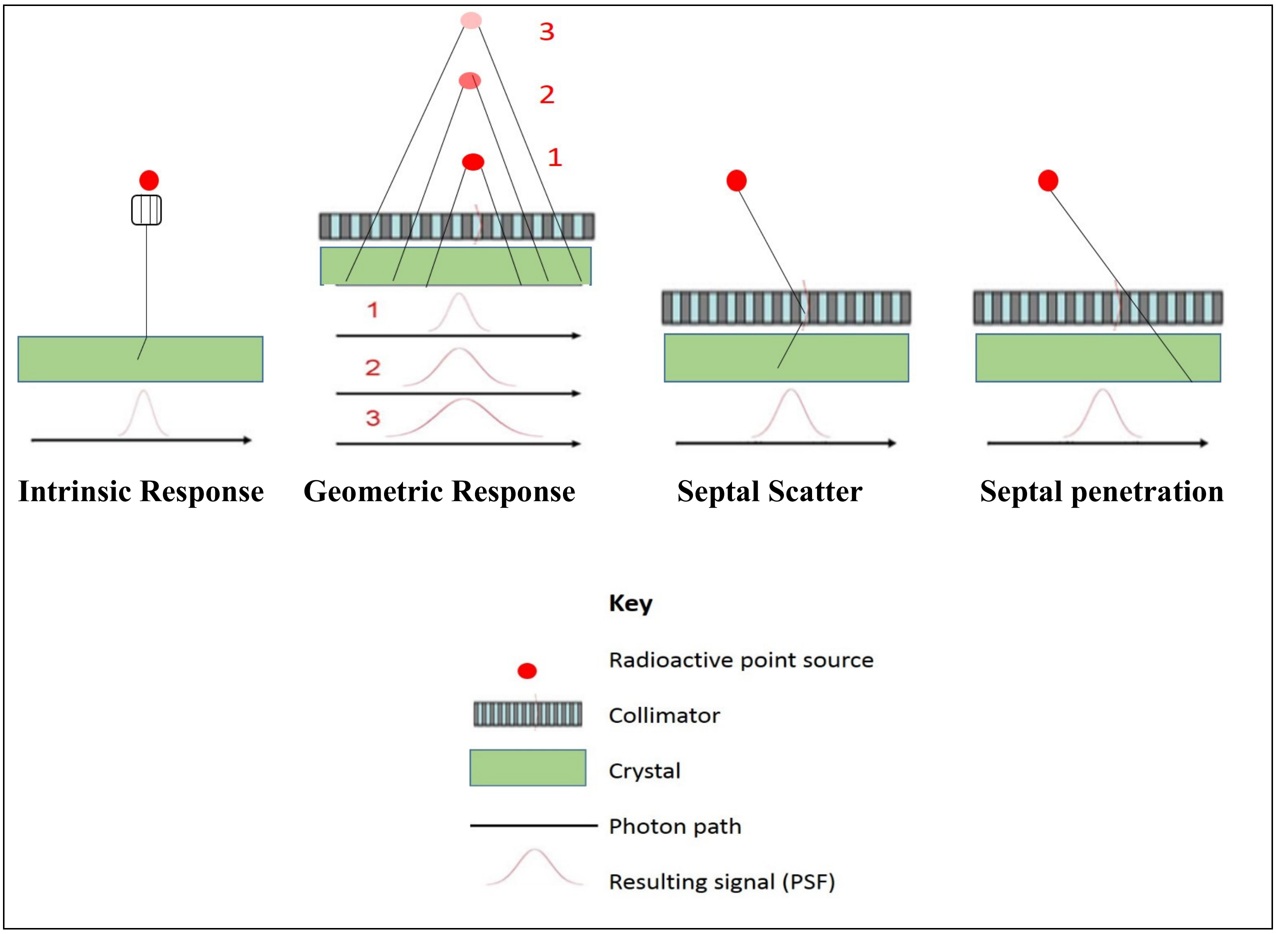

Figure 3. 2: ***Illustration of the four components of CDR***

3.3.4 Partial volume effect

PVE is another important effect that impacts image quantification. There are two factors that combine to cause PVE in NM images. The first is image sampling, that is, each SPECT voxel has a 3-D cubical shape with a definite size and hence, delineating the shape of organs correctly is difficult to achieve. Pixilation is often visible when delineating an object of interest. This leads to a difficulty in getting the accurate values of activity concentration in voxels located at the organ boundaries as it is assumed that the activity is uniformly distributed throughout the voxel.

The second component of PVE is related to the limited spatial resolution of the gamma camera. Structures of interest with diameters less than approximately twice the full width at half maximum of the spatial resolution of the gamma camera are more affected by the PVE. Image counts in tumours and organs of interest are affected by PVE, which can lead to an underestimation (due to spill out of counts) or an over-estimation (due to spill in of counts) of radiopharmaceutical concentrations in organs and tumours. The PVE can be the most dominant source of error in quantitative SPECT studies of small structures (Cherry, Sorenson and Phelps, 2012) and depends on the characteristics of the imaging system. The PVE also depends on the object and activity distribution both inside and outside the object. Spatial and/or temporal variations in PVE can often be confounding factors in image quantification. These factors, lead to blurring of the images, resulting in activity from multiple objects or organs contributing to the intensity of a given image voxel (Frey, Humm and Ljungberg, 2012; Shcherbinin & Celler, 2011).

3.3.5 Additional factors influencing quantification accuracy

There are additional factors that influence the accuracy of SPECT image quantification. These include: noise, background activity, radioactive decay, count rate performance of the camera, patient motion (voluntary and involuntary), and effects on sensitivity such as collimator efficiency, detector detection efficiency, and window fraction as well as the kinetics of the radiopharmaceutical during the period of imaging. Hence, it is very difficult even with all the corrections mentioned earlier, to recover fully the activity during quantification. It is not feasible for now to correct for all of these factors. Therefore, it is important to determine what the extent of the quantification error is for a specific imaging procedure.

3.4 Corrections for SPECT quantification

Internal dose calculations require quantitative SPECT images in order to produce accurate estimates of the radiation dose distribution in the patient. However, the image degrading factors described in the previous section introduce image artifacts and affect the quantitative accuracy. In this section, the methods used to correct for the most important effects are described.

3.4.1 Attenuation correction

The advantages of carrying out attenuation correction on emission images include avoidance of artefacts and false information in the reconstructed image. It also leads to the elimination of underestimation of values of quantities of interest in the image for quantification purposes (Ljungberg and Sjögreen-Gleisner, 2015). However, finding reliable attenuation-correction factors for compensation of lost photons has been identified as the primary challenge of attenuation correction (Berker and Li, 2016).

The attenuation correction can be applied either pre-reconstruction, during reconstruction or post-reconstruction respectively. Various methods for attenuation correction had been proposed and used in the past such as the Chang method (Chang, 1978). Others can be found in these references (Bailey, Hutton and Walker, 1987; Cao and Tsui, 1992; Tan *et al.*, 1993; Celler *et al.*, 1998; Kojima *et al.*, 2004; Sayed, Zakaria and Nik, 2008) and more recently (van Staden *et al.*, 2011). These methods can be classified in two categories, namely analytical and iterative correction techniques (Ishikawa and Ogawa, 2006). The analytical method is said to be fast and is completed in a single process (Ishikawa and Ogawa, 2006). The iterative techniques are incorporated in the reconstruction algorithms and are computationally intensive, which may result in long reconstruction times. An attenuation term for the projection data is usually included in the iterative method in addition to the correction terms for the additional physical factors. Some of these methods assume a uniform distribution of the attenuation medium, while others are built on realistic non-uniform distributions.

The most commonly used realistic attenuation correction today is CT-based correction. The emergence of hybrid imaging made this an acceptable option for many users. A downside of the use of the CT-based method is that it produces beam hardening artefacts which can influence the accuracy of the attenuation correction. However, modern systems are configured to correct for beam hardening (O'Connor and Kemp, 2006; Seo, Aparici and Hasegawa, 2008). There is also a challenge of converting the Hounsfield units of the CT to linear attenuation coefficient values (Bailey and Willowson, 2014; Berker and Li, 2016) which fortunately had to some extent been solved by manufacturers of SPECT/CT (Frey, Humm and Ljungberg, 2012) by implementing the proposed bi-linear conversion model (Blankespoor *et al.*, 1996). One other shortcoming of this method is mis-alignment between the transmission and the emission data, but automatic registration of the two sets of data is now possible with modern hybrid gamma cameras. Once the relevant attenuation map for the patient is obtained, attenuation is accounted for using an iterative reconstruction algorithm.

The reconstruction platform used in this study (LundADose) is also equipped with a bilinear conversion capability, converting Hounsfield numbers to density values. In spite of the mentioned downsides, it is possible to obtain high resolution, high count rate and low noise attenuation maps by using CT-based attenuation correction, which has been shown to improve diagnostic capability of myocardial perfusion imaging in particular (Mariani *et al.*, 2010) and improvement in quantification accuracy.

3.4.2 Scatter correction

If attenuation correction is applied and scatter effects are not accounted for, then the reconstructed counts will be an overestimate. This is because the linear attenuation coefficients used to calculate the transmission factor assume that a photon is removed from the beam once it has been fully absorbed or scattered. These linear attenuation coefficients are called narrow beam attenuation coefficients. The problem is that in NM there is a significant fraction of scattered photons that are still counted by the detector.

Several correction methods for photon scatter in NM imaging had also been proposed and implemented (Buvat *et al.*,1994, Ogawa, 2004, Bokuli *et al.*, 2004; Dewaraja, Ljungberg and Fessier, 2006; Xiao *et al.*, 2007). The most commonly used of these methods in SPECT are the window-based (Zaidi and Koral, 2004) and model-based methods (Frey and Tsui, 1996) . The window-based methods are practical in the clinical environment and have been implemented by commercial gamma camera vendors (Dewaraja *et al.*, 2012). The disadvantages of these window-based methods are that they tend to increase image noise and they wrongly assume that the spatial distributions of scattered photons of different energies are the same. Methods that employ scatter modelling or model-based methods are the more accurate scatter correction techniques, but they can also be very computationally expensive.

One of the model-based scatter correction methods is the Effective Source Scatter Estimation (ESSE) proposed in 1996 by Frey and Tsui (Frey and Tsui, 1996). This will be the only model-based method discussed here because of its relevance to our work. This method makes use of pre-calculated scatter kernels for each radionuclide that is to be modelled in the SPECT projection (Ljungberg and Sjögreen-Gleisner, 2011). The spatially variant object dependent scatter response is modelled by calculating it as the attenuated profile of an effective scatter source. This provides an estimate of the scatter component of the projection data. It then combines two kernels (a 3-D effective source scatter kernel and a 3-D relative scatter attenuation kernel) which are pre-calculated and are filtered with the activity distribution in the frequency plane.

The combined filtered image volumes represent the image volume called the effective scatter source. The attenuated profile of this image gives the scatter estimate. This method is usually included in the forward projection step of an iterative reconstruction algorithm but can also be included in the back projection. The ESSE scatter correction method is incorporated into the LundADose non-commercial software program used for the reconstruction of SPECT acquired projection images in this project and was the scatter correction method used throughout this work. It was used to compensate for scatter in the simulated SPECT images used. This method involves a 3-D Fourier transform coupled with the pixel to pixel operations for each projection (Ljungberg *et al.*, 2002).

3.4.3 Collimator-detector response compensation

As mentioned in section 3.2.2.2, the advanced resolution recovery method incorporated into OS-EM image reconstruction software compensates well for the intrinsic and geometric components of CDR (also referred to as resolution recovery). According to Knoll, using these advanced reconstruction algorithms led to the largest improvement in image resolution and contrast when the images are scatter corrected without applying post-reconstruction filtering (Knoll *et al.*, 2012). However, Onishi and co-workers mentioned that these programs are more effective at reducing noise than improving resolution (Onishi *et al.*, 2013). But when they compared the performance of Evolution, Astonish, Flash 3-D and Toshiba 3-D-OS-EM with standard OS-EM and FBP in terms of image resolution and quality using many parameters, they concluded that the optimal effective number of iterations (number of subset × number of iteration) is dependent on each resolution recovery algorithm. All the above mentioned commercial software programs except one got closer to a true image when the effective number of iterations updates were increased.

Yet in another study (Gruning, Jones and Heales, 2013), it was concluded that using the reconstruction algorithm, Flash 3-D with scatter correction produced the least number of non-diagnostic or difficult-to-interpret scans as compared to FBP and standard OS-EM. Applying resolution recovery can help in the reduction of activity administered to patients for scans especially cardiac scans since even one-half of the standard counts can be used (Pagnanelli and Borges-neto, 2015). Images reconstructed with resolution recovery algorithms are different from images reconstructed with iterative reconstruction alone or FBP. According to Pagnanelli and Borges-neto, in general, compared to standard acquisition and processing, images processed with the resolution recovery software will likely have better contrast and resolution (Pagnanelli and Borges-neto, 2015).

Seret and co-workers (Seret, Nguyen and Bernard, 2012) also investigated the reconstruction algorithms, Evolution, Astonish and Flash 3D in terms of accuracy of attenuation and scatter correction, contrast recovery for small hot and cold structures, and quantitative capabilities. They concluded that the three iterative reconstruction algorithms with attenuation and scatter corrections as well as resolution recovery achieved satisfactory quantitative results and improved contrast for small structures. However, they reported reconstruction artefacts with all software packages, which are clearly obstacles to accurate quantification in SPECT. As good as this advanced algorithm is, unfortunately, the collimator septal scatter and septal penetration in the case of high energy photon emitters, such as ^{131}I are yet to be modelled and incorporated in them. Meaning that they only model the intrinsic and geometric components and not the full CDR. Therefore, this all-important interaction in emission tomography remains a big challenge.

Compensation for the CDR is accomplished by modelling the CDR in the forward and backward projection steps of the iterative reconstruction algorithm. Often only the geometrical component is modelled because analytical formulas for the geometrical CDR are available. For high-energy photons, it may be desirable to model the full CDR, which includes penetration and collimator scatter. Using MC simulations, the distance-dependent geometric response of the detector-collimator system as well as collimator scatter and penetration can be modelled very well. The option of full CDR is incorporated into the Lundadose reconstruction software. Compensating for the CDR reduces PVEs and is important for quantitative applications where PVE is significant.

3.4.4 Partial volume effect correction

It may be necessary to apply PVE correction in radionuclide therapy applications, particularly when calculating the dose to small tumours. Since PVE is due to limited spatial resolution, this effect can be reduced by including resolution recovery in the iterative reconstruction algorithm. However, collimator detector response compensation does not completely eliminate PVEs, especially in the case of small objects.

Traditionally, one of the most popular strategies to correct for PVE is the use of recovery coefficients (RCs). A RC is defined as the ratio of activity concentration measured in the SPECT image to the true activity concentration. Physical phantoms involving spheres of different sizes filled with known activity concentrations can be used to obtain a set of RCs that can be applied to approximately spherical objects of similar sizes. However, this simple correction method will be inaccurate when applied to irregularly shaped tumours surrounded by non-uniform background activity. Recently, more sophisticated methods have been developed. For example, voxel based methods, such as the iterative template based technique, have been proposed (Shcherbinin and Celler, 2011). Advanced PVE correction is still an active area of research and no widely accepted method exists.

According to Erlandsson et al., partial volume correction (PVC) could be achieved using inverse filter technique, which reverses the effect of the system point spread function, but the limitation of these methods is that they usually amplify the noise and increase image artefacts (Erlandsson et al. 2012). Many research groups had suggested different correction methods for PVE (Erlandsson, et.al., 2012; Varghese 2016). Erlandsson and co-workers (Erlandsson *et al.*, 2011) listed the limitation of traditional PVC methods as correcting only a single region, giving only mean value of regions of interest or assuming a stationary point spread function. They presented a new method based on the iterative OS-EM algorithm and concluded that this method resulted in images with significantly higher contrast as compared to FBP and OS-EM alone.

The development of correction methods for PVE has received little attention compared to the effort put into the development of correction techniques for scatter and attenuation (Erlandsson, et. al., 2012; Shcherbinin & Celler 2011). This could be attributed to the fact that PVE is only really important for small structures as opposed to scatter and attenuation effects. In this regards, therefore, more work needs to be done on partial volume correction. PVC is especially important for ^{131}I because of the poor spatial resolution and is recommended for small organs or tumours (diameters less than 2 times the system spatial resolution). A practical post-reconstruction approach for PVC at the regional level is the use of volume-dependent RCs determined by physical phantom measurements or well validated MC simulation. The RC, defined as the ratio of recovered activity concentration to true activity concentration, can be applied to adjust the activity of structures after quantification.

Because RCs depends not only on target volume but also on other factors such as target shape, more sophisticated PVC methods like anatomical-based PVC methods (Gutierrez *et al.*, 2012; Márta and Szirmay-kalos, 2012) are available and are recommended for objects not well approximated as spheres. With the advent of hybrid imaging such as SPECT/CT, both functional and anatomical images are acquired within one imaging session with close alignment. Anatomical-based PVC methods are particularly promising for hybrid scanners, as various regions could be segmented into several templates accurately from anatomical images. For multi-region anatomical-based PVC methods, both spill-in and spill-out contamination among different regions could be taken into account during compensation.

But in this work, the volume-dependent RCs were applied to correct for PVE in structures of interest. The RCs were sufficient for the correction because the structures of interest were spheres used to mimic tumours in patients and the smallest of the spheres had a diameter of 3.0 cm, which was slightly higher than twice the FWHM of the simulated gamma camera used (1.2 cm) and, hence, PVE was not expected to have much influence on the quantified images.

3.4.5 Correction methods for additional factors

Methods are available to correct for some of the additional factors that influence quantification accuracy. For background activity, a background correction can be applied and for patient motion, the patient can be restrained during image acquisition to limit patient voluntary motion. For simulation studies, the issue of patient motion does not arise as only digital models are used.

Mathematical models are available (Cherry, Sorenson and Phelps, 2012) for the correction of dead time losses during image acquisition but generally, these corrections are said to become increasingly inaccurate as counting losses increase. In a simulation study, such as the ones in this work, the problem of count rate losses is also absent, therefore, no contribution was received from this influence on the quantification accuracy of the simulated SPECT images.

3.5 Absolute quantification

3.5.1 Volume delineation

For SPECT imaging, the method to define the target volume is either manually by employing high-resolution anatomic CT images or using an automatic threshold-based contouring method on the SPECT images. The preferred method is to contour the target on a high-resolution anatomic image dataset and apply it to the co-registered SPECT image set. When anatomic imaging-based target delineation is not feasible, i.e., when the target is difficult to delineate on CT, SPECT-based target delineation is an option. For SPECT-based target delineation either a fixed threshold or a more sophisticated adaptive thresholding method can be used (Jentzen, 2015; Jentzen et al., 2007). When fixed thresholds are used, the threshold required for accurate target delineation is a function of object shape and size relative to the system spatial resolution and target-to-background image contrast (Erdi, et al, 1995). The optimum threshold for patient studies should, therefore, be based on system-specific phantom calibration experiments (to determine threshold-volume curves) and a priori estimates of the volume and contrast of the anatomic structure. The threshold that gives the best estimate of the object volume is not necessarily the same as the threshold that gives the best estimate of object activity.

For correct delineation of organs of interest (lungs and liver) in simulated ^{131}I patients' SPECT images in this work, the 3-D isocontour volume delineation tool of AMIDE (Loening and Gambhir, 2003) which follows a user-defined threshold value, was used. The 3-D isocontour can be defined in such a way that it encompasses all neighbouring values either above a certain minimum value, below a certain maximum value, or between a minimum and a maximum value. It also allows for modification of the VOI in order to fit correctly to the shape of the object of interest. For the spheres (mimicking tumours in this study), the ellipsoid VOI tool was used to define the sphere geometric sizes. This tool can be used to specify a diameter for each x, y, and z-direction and in the special case whereby $x = y = z$, the ellipsoid defines a sphere.

3.5.2 Calibration factor

For absolute quantification, the CF, that converts reconstructed SPECT counts to activity must be determined by imaging a known activity amount. The simplest calibration procedure uses a planar acquisition with a point-source to determine the "in air camera sensitivity" assuming negligible scatter and attenuation. To minimize the effects of imperfect corrections, the preferred procedure is to perform a calibration measurement with a phantom that approximates the scatter and attenuation conditions in patient imaging, such as in a water-filled tank with spherical insert (Dewaraja *et al.*, 2013). It is recommended that acquisition and processing of the calibration phantom (water-filled tank with spherical insert), including delineation of the spherical target, should be performed in the same manner as in the patient study. The CF, in units of cps/MBq, is then determined by dividing the total volume of interest reconstructed counts of the sphere by the known activity and acquisition time. After the CF had been determined, the tumour and organ activity maps will be obtained by dividing the image counts from the reconstructed SPECT images by the predetermined CF (cps/MBq).

The issue of obtaining the CF for absolute quantification is still on the front burners as researchers are still looking for the optimum way to obtain CFs for quantification. According to Zhao et al (Zhao *et al.*, 2018), currently, there is no consensus on the best method of obtaining the CF for NM imaging equipment. There has been several investigations on CF (Mezzenga *et al.*, 2017; Zhao *et al.*, 2018) and newer proposed methods were suggested (Halty *et al.*, 2018). For this study, however, the CF for the SPECT/CT camera was defined using a 7.0 cm diameter sphere, which has limited PVE influence, in a water-filled cylindrical phantom with hot background reflecting a clinical situation. The sphere volume was defined by the sphere's physical size because of the background activity used in the phantom and the voxel-based patient models (refer to chapter 6).

3.6 ^{131}I Quantification

The literature on SPECT quantification accuracy for ^{131}I exists but little work had been done using voxel-based models. Dewaraja and co-workers (Dewaraja et al. 2005; Dewaraja, Ljungberg and Fessier, 2006; Dewaraja et al. 2000; Ljungberg et al. 2002; Schipper et al. 2012; Dewaraja et al. 2009) had done some work on ^{131}I quantification using both Monte Carlo simulations and phantom measurements. Other groups that had also carried out some work on ^{131}I quantification accuracy are listed in Medical Internal Radiation Dose (MIRD) pamphlet no. 24 (Dewaraja *et al.*, 2013) with the various methods used and the respective quantification accuracy results. These results ranged from 3 – 4 % errors for 32 ml volumes to 31 % error for a 4 ml sphere.

In evaluating the effects of object shape in ^{131}I SPECT tumour activity quantification Dewaraja et al., (Dewaraja, Ljungberg and Koral, 2001), found that there was a large error in the quantification of different tumour shapes. These errors were as large as -39 % for a 50 ml cylinder in a cold background and -35 % for a 20 ml irregular structure. The authors also found that simple sphere-based PVC improved the accuracy of quantification of non-spherical objects. They concluded that correcting for PVE in patients studies may provide improved quantification accuracy. This group had previously investigated the accuracy of ^{131}I tumour quantification using an ultra-high-energy collimator (Dewaraja et al. 2000). Their findings show that using an ultra-high-energy collimator results in a large reduction in ^{131}I collimator septal penetration which, as pointed out before, is a very significant factor in ^{131}I image degradation. The contrast of typical patient images was also found to be improved but the sensitivity was reduced, although by only a factor of 1.6. Finally, they showed that good quantification accuracy with an error < 6.5 % was achieved when the tumour size was the same as the size of the sphere used for calibration. Activities for smaller tumours were however said to be overestimated by up to 27 %.

From the above discussion it is evident that if the guidelines set in the MIRD pamphlet No. 24 for SPECT imaging and quantification for ^{131}I were followed, improved accuracies better than 15% for most organs of interest in radionuclide therapy could be obtained.

The relevant aspects of absolute quantification of SPECT images had been discussed in this chapter. As mentioned, absolute quantification is very important for accurate absorbed dose calculation. The next chapter (Chapter 4) will discuss relevant aspects of internal dosimetry as it relates to ^{131}I radionuclide therapy.

3.7 References

Bailey, D. L., Hutton, B. F. and Walker, P. J. (1987) 'Improved SPECT using simultaneous emission and transmission tomography', *J. Nucl. Med.*, 28, pp. 844–851.

Bailey, D. L., and Willowson, K. P. (2014) 'Quantitative SPECT / CT : SPECT joins PET as a quantitative imaging modality', *Eur. J. Nucl. Med. Mol. Imaging*, 41), pp. S17–S25.

Berker, Y. and Li, Y. (2016) 'Attenuation correction in emission tomography using the emission data — A review', *Med. Phys.*, 43, pp. 807–832.

Blankespoor, S. C., Xu, X., Kaiki, K., Brown, J. K., Tang, H. R., Cann, C. E. and Hasegawa, B. H. (1996) 'Attenuation correction of SPECT using X-ray CT on an emission-transmission CT system: myocardial perfusion assessment', *IEEE Trans. Nucl. Sc.*, 43, pp. 2263–2274.

Bokuli, T., Vastenhouw, B., de Jong, H. W. A. M., van Dongen, A. J., van Rijk, P. P. and Beekman, F. J. (2004) 'Monte Carlo-based down-scatter correction of SPECT attenuation maps', *Eur. J. Nucl. Med. Mol. Imaging*, 31, pp. 1173–1181.

Buvat, I., Benali, H., Todd-Pokropek, A. and Di Paola, R. (1994) 'Scatter correction in scintigraphy : the state of the art', *Eur. J. Nucl. Med.*, 21, pp. 675–694.

Cao, Z. J. and Tsui, B. M. W. (1992) 'Performance characteristics of transmission imaging using a uniform sheet source with a parallel-hole collimator', *Med. Phys.*, 19, pp. 1205–1212.

Celler, A., Sitek, A., Stoub, E., Hawman, P., Harrop, R. and Lyster, D. (1998) 'Multiple line source array for SPECT transmission scans:. simulation, phantom, and patient studies', *J. Nucl. Med.*, 39, pp. 2183–2189.

Chang, L. (1978) 'A method of attenuation correction in radionuclide computed tomography', *IEEE Trans. Nucl. Sc.*, 25, pp. 638–643.

Cherry, S. R., Sorenson, J. A. and Phelps, M. E. (2012) *Physics in Nuclear Medicine*. 4th edn. Philadelphia, PA: Elsevier Inc.

Dewaraja, Y. K., Wilderman, S.J., Ljungberg, M., Koral, K. F., Zasadny, K. and Kaminiski, M. S. (2005) 'Accurate dosimetry in ^{131}I radionuclide therapy using patient-specific, 3-dimensional methods for SPECT reconstruction and absorbed dose calculation.', *J. Nucl. Med.*, 46, pp. 840–849.

Dewaraja, Y. K., Wilderman, S. J., Koral, K. F., Kaminski, M. S. and Avram, A. M. (2009) 'Use of Integrated SPECT / CT Imaging for Tumor Dosimetry in I-131 Radioimmunotherapy: A Pilot Patient Study', *Cancer Biother. Radiopharm.*, 24, pp. 417–426.

Dewaraja, Y. K., Frey, E. C., Sgouros, G., Brill, A. B., Robertson, P., Zanzonico, P. B. and Ljungberg, M. (2012) 'MIRD Pamphlet No. 23: Quantitative SPECT for Patient-Specific 3-Dimensional Dosimetry in Internal Radionuclide Therapy', *J. Nucl. Med.*, 53, pp. 1310–1325.

Dewaraja, Y. K., Ljungberg, M., Green, A. J., Zanzonico, P. B. and Frey, E. C. (2013) 'MIRD Pamphlet No. 24: Guidelines for Quantitative ^{131}I SPECT in Dosimetry Applications', *J. Nucl. Med.*, 54, pp. 2182–2188.

Dewaraja, Y. K., Ljungberg, M. and Fessier, J. A. (2006) '3-D Monte Carlo-based scatter compensation in quantitative I-131 SPECT reconstruction', *IEEE Trans. Nucl. Sc.*, 53, pp. 181–188.

Dewaraja, Y. K., Ljungberg, M. and Koral, K. F. (2000) 'Accuracy of ^{131}I tumor quantification in radioimmunotherapy using SPECT imaging with an ultra-high-energy collimator: Monte Carlo study.', *J. Nucl. Med.*, 41, pp. 1760–1767.

Dewaraja, Y. K., Ljungberg, M. and Koral, K. F. (2001) ‘Monte Carlo evaluation of object shape effects in iodine-131 tumor activity quantification’, *Eur. J. Nucl. Med.*, 28, pp. 900–906.

Edyvean, S. and Weston, J. (2007) *Imaging Performance Assessment of CT Scanners*, *Gammex RMI CT Phantom, 438 User Guide*. London.

Erdi, Y. E., Wessels, B. W., Love, M. H. and Erdi, A. K. (1995) ‘Threshold estimation in single photon emission computed tomography and planar imaging for clinical radioimmunotherapy.’, *Cancer research*, 55, p. 5823s–5826s.

Erlandsson, K., Buvat, I., Pretorius, P. H., Benjamin, B. A. and Hutton, B. F. (2012) ‘A review of partial volume correction techniques for emission tomography and their applications in neurology, cardiology, and oncology’, *Phys. Med. Biol.*, 57, pp. R119–R159.

Erlandsson, K., Thomas, B., Dickson, J. and Hutton, B. F. (2011) ‘Partial volume correction in SPECT reconstruction with OSEM’, *Nucl. Instrum. Methods Phy. Res. A.,* 648, pp. S85–S88.

Fredericks, N., Baxter, P., McKay, E. and Smart, R. (1999) ‘An assessment of the sensitivity of the Cedars-Sinai quantitative gated SPECT software to changes in the reconstruction of the short-axis slices.’, *J. Nucl. Med. Technol.*, 27, pp. 123–126.

Frey, E. C., Humm, J. L. and Ljungberg, M. (2012) ‘Accuracy and precision of radioactivity quantification in nuclear medicine images’, *Semin. Nucl. Med.*, 42, pp. 208–218.

Frey, E. C., and Tsui, B. M. W. (1996) ‘A New Method for Modelling the Spatially-Variant, Object dependent Scatter Response Function in SPECT’, in *IEEE Nucl. Sci. Symposium*, pp. 1082–1086.

Gillam, J. E., and Rafecas, M. (2016) ‘Monte-Carlo simulations and image reconstruction for novel imaging scenarios in emission tomography’, *Nucl. Instrum. Methods Phy. Res., A.*, 809, pp. 76–88.

Gruning, T., Jones, I. W. and Heales, J. C. (2013) ‘Efficacy of various SPECT reconstruction algorithms in differentiating bowel uptake from inferior wall uptake in myocardial perfusion scans’, *Nucl. Med. Commun.*, 34, pp. 113–116.

Gutierrez, D., Montandon, M-L., Assal, F., Allaoua, M., Ratib, O., Lövblad, K-O. and Zaidi, H. (2012) ‘Anatomically guided voxel-based partial volume effect correction in brain PET: Impact of MRI segmentation’, *Comput. Med. Imaging Graphics*. 36, pp. 610–619.

Halty, A., Badel, J-N., Kochebina, O. and Sarrut, D. (2018) ‘Image-based SPECT calibration based on the evaluation of the Fraction of Activity in the Field of View’, *EJNMMI Physics*., 5, pp. 1–15.

Hawman, E., Vija, A. H., Daffach, R. and Ray, M. (2014) *Flash 3D Technology Optimizing SPECT Quality and Accuracy*. Available at: http://www.siemensmedical.com/nuclear. Last accessed on 6th December 2016.

Hudson, H. M. and Larkin, R. S. (1994) ‘Accelerated Image Reconstruction Using Ordered Subsets of Projection Data’, *IEEE Trans Med Imag*, 13, pp. 601–609.

Hutton, B. F., Nuyts, J. and Zaidi, H. (2006) ‘Iterative Reconstruction Methods’, in Zaidi, H. (ed.) *Quantitative Analysis in Nuclear Medicine Imaging*. New York: Springer Science, pp. 107–140.

IAEA (2014) *Quantitative Nuclear Medicine Imaging: Concepts, Requirements and Methods*, *IAEA Human health series: Human Health Reports*. Vienna: I.A.E.A.

Ishikawa, A. and Ogawa, K. (2006) ‘Analytical correction methods for aperture and attenuation effects in SPECT’, *Electron Comm. Jpn P3*, 89, pp. 42–50.

Jentzen, W., Freudenberg, L., Eising, E. G., Heinze, M., Brandau, W. and Bockisch, A. (2007) ‘Segmentation of PET volumes by iterative image thresholding.’, *J. Nucl. Med.,* 48, pp. 108–114.

Jentzen, W. (2015) ‘An Improved Iterative Thresholding Method to Delineate PET Volumes Using the Delineation-Averaged Signal’, *J. Nucl. Med. Technol*, 43, pp. 28–36.

Knoll, P., Kotalova, D., Köchie, G., Kuzeelka, I., Minear, G., Mirzael, S., Ŝämal, M., Zadrazil, L. and Bergmann, H. (2012) ‘Comparison of advanced iterative reconstruction methods for SPECT / CT’, *Z. Med. Phy.*, 22, pp. 58–69.

Kojima, A., Kawanaka, K., Nakaura, T., Shiraishi, S., Utsunomiya, D., Katsuda, N., Tomiguchi, S., Yamashita, Y., Matsumoto, M., Motomura, N. and Ichihara, T. (2004) ‘Attenuation correction using combination of a parallel hole collimator and an uncollimated non-uniform line array source’, *Ann. Nucl. Med.*, 18, pp. 385–390.

Ljungberg, M., Sjögreen, K., Liu, X., Frey, E., Dewaraja, Y. and Strand, S-E. (2002) ‘A 3-Dimensional Absorbed Dose Calculation Method Based on Quantitative SPECT for Radionuclide Therapy: Evaluation for ^{131}I Using Monte Carlo Simulation’, *J. Nucl. Med.*, 43, pp. 1101–1109.

Ljungberg, M. and Sjögreen-Gleisner, K. (2011) ‘The accuracy of absorbed dose estimates in tumours determined by quantitative SPECT: a Monte Carlo study.’, *Acta oncologica (Stockholm, Sweden)*, 50, pp. 981–989.

Ljungberg, M. and Sjögreen-Gleisner, K. (2015) ‘Hybrid Imaging for Patient-Specific Dosimetry in Radionuclide Therapy’, *Diagnostics*, 5, pp. 296–317.

Ljungberg, M. and Gleisner, K. S. (2016) ‘Personalized Dosimetry for Radionuclide Therapy Using Molecular Imaging Tools’, *Biomedicines*, 4, pp. 25–45.

Loening, A. M. and Gambhir, S. S. (2003) ‘AMIDE: A Free Software tool for multimodality Medical Image Analysis’, *Mol. Imaging*, 2, pp. 131–137.

Mariani, G., Bruselli, L., Kuwert, T., Kim, E. E., Flotats, A., Israel, O., Dondi, M. and Watanabe, N. (2010) ‘A review on the clinical uses of SPECT/CT’, *Eur. J. Nucl. Med. Mol. Imaging*, 37, pp. 1959–1985.

Márta, Z. and Szirmay-kalos, L. (2012) ‘Partial Volume Effect Correction using Segmented CT Images with Distance Mapping’, in *Sixth Hungarian Conference on Computer Graphics and Geometry, Budapest, 2012*, pp. 1–8.

Mezzenga, E., D'Errico, V., D'Arienzo, M., Strigari, L., Panagiota, K., Matteucci, F., Severi, S., Paganelli, G., Fenwick, A., Bianchini, D., Marcocci, F. and Sarnelli, A. (2017) ‘Quantitative accuracy of ^{177}Lu SPECT imaging for molecular radiotherapy’, *PLoS ONE*, 12, pp. 1–18.

O’Connor, M. K. and Kemp, B. J. (2006) ‘Single-Photon Emission Computed Tomography/Computed Tomography: Basic Instrumentation and Innovations’, *Semin. Nucl. Med.*, 36, pp. 258–266.

Ogawa, K. (2004) ‘Image distortion and correction in single photon emission CT’, *Ann. Nucl. Med.*, 18, pp. 171–185.

Onishi, H., Motomura, N., Fujino, K., Natsume, T. and Haramoto, Y. (2013) ‘Quantitative performance of advanced resolution recovery strategies on SPECT images : evaluation with use of digital phantom models’, *Radiol. Phys. Technol.*, 6, pp. 42–53.

Pagnanelli, R. and Borges-neto, S. (2015) ‘Technical aspects of resolution recovery reconstruction’, *J. Nucl. Cardiol.*, 23, pp. 149–152.

Ritt, P., Vija, H., Hornegger, J. and Kuwert, T. (2011) ‘Absolute quantification in SPECT’, *Eur. J. Nucl. Med. Mol. Imaging*, 38, pp. 69–77.

Sayed, I. S., Zakaria, A. and Nik, N. (2008) ‘Comparison of Chang's with Sorenson's Attenuation Correction Method by Varying Linear Attenuation Coefficient Values in Tc-99m SPECT Imaging’, in Gao, X. et. al. (ed.) *MIMI 2007, LNCS 4987*. Berlin Heidelberg: Springer-Verlag, pp. 216–222.

Schipper, M. J., Koral, K. F., Avram, A. M., Kaminski, M. S. and Dewaraja, Y. K. (2012) ‘Prediction of therapy tumor-absorbed dose estimates in I-131 radioimmunotherapy using tracer data via a mixed-model fit to time activity.’, *Cancer Biother. Radiopharm.*, 27, pp. 403–411.

Seo, Y., Aparici, C. M. and Hasegawa, B. H. (2008) ‘Technological Development and Advances in SPECT/CT’, *Semin. Nucl. Med.*, 38, pp. 177–198.

Seret, A., Nguyen, D. and Bernard, C. (2012) ‘Quantitative capabilities of four state-of-the-art SPECT-CT cameras’, *EJNMMI Research*, 2, pp. 1- 19.

Shcherbinin, S. and Celler, A. (2010) ‘An enhancement of quantitative accuracy of the SPECT/CT activity distribution reconstructions: Physical phantom experiments’, *Comput. Med. Imaging Graphics*. 34, pp. 346–353.

Shcherbinin, S. and Celler, A. (2011) ‘Assessment of the severity of partial volume effects and the performance of two template-based correction methods in a SPECT/CT phantom experiment’, *Phy. Med. Biol.*, 56, pp. 5355–5371.

Tan, P., Bailey, D. L., Mekle, S. R., Eberl, S., Fulton, R. R. and Hutton, B. F. (1993) ‘A scanning line source for simultaneous emission and transmission measurements in SPECT', *J. Nucl. Med.*, 34, pp. 1752–1760.

Tsui, B. M. W. and Frey, E. C. (2006) 'Analytic Image Reconstruction Methods in Emission Computed Tomography', in Zaidi, H. (ed.) *Quantitative Analysis in Nuclear Medicine Imaging*. New York: Springer Science, pp. 82–106.

van Staden, J. A., du Raan, H., Lötter. M. G., Herbst, C. P., van Aswegen, A. and Rae, W. I. D. (2011) 'Evaluation of an uncollimated printed paper transmission source used under scatter limiting conditions', *Physica Medica*, 27, pp. 11–20.

Varghese, B. S. (2016) 'A Survey on Segmentation – Based Correction of Partial Volume Artifacts for the Accurate Volumetric Measurement of Solid Lung Lesions on CT Images', *Int. J. Scient. Eng. Appl. Sci.*, 2, pp. 459–465.

Xiao, J., de Wit, T. C., Zbijewski, W., Staelens, S. G. and Beekman, F. J. (2007) 'Evaluation of 3D Monte Carlo – Based Scatter Correction for ^{201}Tl Cardiac Perfusion SPECT', *J. Nucl. Med.*, 48, pp. 637–644.

Zaidi, H. and Koral, K. F. (2004) 'Scatter modeling and compensation in emission tomography', *Eur. J. Nucl. Med.*, 31, pp. 761–782.

Zeng, G. L. (2001) 'Image reconstruction - A tutorial', *Comput. Med. Imaging Graphics*, 25, pp. 97–103.

Zhao, W., Esquinas, P. L., Hou, X., Uribe, C. F., Gonzalez, M., Beauregard, J-M., Dewaraja, Y. K. and Celler, A. (2018) 'Determination of gamma camera calibration factors for quantitation of therapeutic radioisotopes', *EJNMMI Physics*. 5, pp. 1–16.

CHAPTER FOUR: Internal Dosimetry for ^{131}I Radionuclide Therapy

Table of Contents

4.1 Introduction

Internal dosimetry refers to the dosimetry of internally distributed radionuclides (Ljungberg and Sjögreen Gleisner, 2016). It is aimed towards the determination of radiation energy deposited in different parts of the human body by internal radiation sources. This makes it possible to evaluate the risks and benefits of the different diagnostic and therapeutic procedures carried out in nuclear medicine (NM). The immediate consequence of the deposition of the kinetic energy of radiation, as it decelerates through collision with atoms of human tissues is the absorbed dose. In cancer radiation treatment it is important to estimate the absorbed dose to structures / organs in order to determine the radiobiological effect of the radiation. The absorbed dose is defined as the mean energy imparted to the matter in a volume with a specific mass.

Internal dosimetry in RNT has evolved over the years from the technique of blood and urine measurements to image-based whole body dose determination (Dorn *et al.*, 2003). Image-based dosimetry is now greatly improved and substantially more detailed with the introduction of hybridization of equipment (PET/CT, SPECT/CT, and PET/MRI) and improvement in correction techniques for image degrading factors as discussed in chapter 3. Therefore, with quantification errors that are far below 10% for some of the clinically relevant radioisotopes such as ^{111}In/^{90}Y surrogate pair (Ljungberg *et al.*, 2003; Sjögreen *et al.*, 2005; Yue *et al.*, 2016) being achieved, it is now possible to achieve a much improved accuracy and reproducibility of dosimetric calculations (Dorn *et al.*, 2003; Sgouros and Hobbs, 2014) in contrast to the fixed dose regimen and its shortcomings as discussed in Chapter 1.

Accuracy in the calculation and measurement of internal dosimetry is essential for the optimization of patient treatment and patient safety in targeted RNT (The goal of every radionuclide treatment is to deliver a lethal dose of radiation to the diseased site, in order to maximize damage to a tumour, while at the same time delivering minimal or no radiation dose to disease-free sites thereby aiming to achieve the highest possible therapeutic ratio (Dale, 1996)).

^{131}I is classified as a low energy β^- emitter alongside ^{177}Lu ($E_{avg} = 0.08 - 0.18$MeV and mean range of 0.4 – 0.9 mm) which are best suited to treatment of small target sites (Dash, Russ Knapp Jr, and Pillai, 2013). However, currently, ^{131}I is used for the therapy of metastases due to thyroid cancer, ablation of thyroid remnant tissue after thyroidectomy and therapy of Non-Hodgkin's lymphoma and Neuroendocrine tumours. With the large body of evidence and arguments in favour of dosimetry generally and in particular with ^{131}I (see for instance, (Wierts *et al.*, 2011; Stabin and Flux, 2014; Strigari *et al.*, 2014; Stabin, 2017)), dosimetry in RNT is still not practiced by many practitioners (Wierts *et al.*, 2011; Gleisner *et al.*, 2017). Even in some centres where dosimetry is practiced, it is reserved only for certain cases (Gleisner *et al.*, 2017), especially for pediatric patients (Luster *et al.*, 2017).

Dosimetry can be classified as model-based dosimetry (for estimating radiation risks to a population of patients in NM diagnostic procedures or accidental intake of radionuclides) and patient-specific dosimetry (for cancer therapy of individual patients). Patient-specific (personalized) dosimetry satisfies the need for estimation of absorbed dose to the patient on an individual basis. This has become a requirement in the new EU directive 2013/59/EURATOM Article 56 (Ljungberg and Sjögreen Gleisner, 2016; Ljungberg, 2018) aimed at the optimization of the treatment in targeted radionuclide therapy. Model-based dosimetry involves the use of standard phantoms representing human anatomy of a group of patients, proposed by the International Commission on Radiological Protection (ICRP) or the Medical Internal Radiation Dose (MIRD) committee of the Society of Nuclear Medicine of the United States of America (Villoing *et al.*, 2017). Such models are either defined by equations (stylized), or mathematical functions (voxel-based) or a combination of both (volume arrays or equation-voxel models) (Zaidi and Xu, 2007).

Due to the unrealistic nature of anatomical representation of patients by these models, efforts were geared towards developing anatomically realistic models using CT and MRI images of patients, which allow for a 3-D visualization of internal organs of the patients. The advantage of these 3-D voxel-based models created from digital CT and MRI images of patients, is that such models can be created for individual patients, hence, patient-specific. In this way, we have a realistic representation of the individual patient anatomy for a realistic dosimetric calculation of radiation absorbed dose to organs of (and tumours in) the patient. In the clinic today, patient-specific dosimetry involves using the acquired images of the individual patient directly in image reconstruction and dose calculation systems to plan or assess the absorbed dose to the patient's organs and any tumours in the patient.

4.1.1 Basic concept of radionuclide dosimetry in nuclear medicine

The mean absorbed dose can roughly (because the calculation requires the knowledge of the physical and biological parameters which are estimated and not exactly determined) be calculated assuming an average tissue deposition of energy and a uniform distribution of the radiopharmaceutical. Absorbed doses from internal emitters deposited in a particular region are simply calculated based on the summation of all the energy contributions from source organs (regions that contain activity greater than the average concentration of activity in the total body) and from the region itself which is absorbed in such a region. For energy $\boldsymbol{E_i}$ absorbed in this region, the absorbed fraction,ϕ_i, a dimensionless parameter defined as the fraction of energy emitted that is absorbed in the target for radiation, $\boldsymbol{i}$, accounts for the fact that not all the energy emitted in the organ may be absorbed by the organ. When the absorbed fraction is divided by the mass of the region, we have specific absorbed fraction ϕ_i.

For non-penetrating radiations (α and β, Auger electrons, conversion electrons and photons with energy below 13 keV) having typical ranges in matter that are shorter than the dimensions of any organ, the absorbed fraction is 1 when the target organ is also the source organ and equal to 0 otherwise, since it is assumed that they are completely absorbed in the immediate vicinity of their production (A MIRD concept, the MIRD formalism is discussed in detail in section 4.2.2). For photons, the value of absorbed fraction is between 0 and 1 (Stabin and Xu, 2014). The absorbed dose rate in the target region is thus obtained using the equation below.

$$\dot{\mathrm{D}} = \frac{\boldsymbol{kA}\sum_i \boldsymbol{n_i E_i} \phi_i}{\boldsymbol{m}} \qquad 4.1$$

Where $\dot{\mathrm{D}}$ is the absorbed dose rate (Gy/s) in an organ, $\boldsymbol{A}$ is the activity in the organ (MBq), $\boldsymbol{n_i}$ is the frequency of radiation with energy $\boldsymbol{E_i}$ (MeV) emitted per nuclear transition**,** ϕ_i is the absorbed fraction, $\boldsymbol{m}$ is the mass of the target region (kg), and $\boldsymbol{k}$ is a proportionality constant (Gy-kg/MBq-s-MeV). It is assumed in the equation above that the target has a uniform activity concentration (MBq/ml) which isotropically, emits photons or particulate radiations of energy $\boldsymbol{E}$ with abundance, $\boldsymbol{n}$. The integration of equation 4.1 over time gives the absorbed dose. But this integration usually only involves the integration of the activity since the other terms in the equation do not vary with time. Thus, we have

$$\int_0^{\infty} \dot{D}\, dt = D = \frac{k \sum_i n_i E_i \Phi_i}{m} \int_0^{\infty} A\, dt \qquad 4.2$$

Where **D** has the unit of Gy. The integral of the activity in an organ over time expresses the number of disintegrations that occurred in the organ since activity is expressed as disintegration per unit time. The time integral is called cumulated activity, which is usually given as Ã. Hence, the cumulated absorbed dose is given by:

$$D = \frac{k \tilde{A} \sum_i n_i E_i \Phi_i}{m} \qquad 4.3$$

4.1.2 Factors that influence the calculation of the cumulated activity

An amount of radioactive material in the body will be cleared from the body by two processes, namely physical decay of the radioactive material and biological disappearance determined by the removal rate of the material (radiopharmaceutical) from the body. The effective half-life combines the physical decay and the biological washout using the following equation.

$$T_e = \frac{T_b \times T_p}{T_b + T_p} \qquad 4.4$$

With T_e the effective half-life, T_b the biological half-life and T_p the physical half-life of the isotope (Stabin, 2008). The removal of the radiopharmaceutical with time can easily map the decay by plotting the activity of the radionuclide with time, resulting in a time-activity curve (TAC) and is discussed briefly below.

4.1.3 Time-activity curve and cumulated activity

The TAC for a particular organ enables the calculation of the cumulated activity in that organ. This is facilitated by the calculation of the integral of the TAC which is the total number of nuclear transformations from the radionuclide in the particular source organ been considered. Cumulated activity is further discussed in section 4.2.2.

4.2 Dosimetry formalisms

Dosimetry had been applied in the use of ^{131}I as a therapeutic agent from earlier times, however, because of its cumbersome nature, it was not very popular. In this section, therefore, the dosimetry formalisms, beginning from the earlier periods will be discussed briefly.

4.2.1 Historical overview

The earliest dosimetric approach to internal dosimetry was said to be that of Marinelli presented in 1942 for beta-emitting radionuclides (McParland, 2010), specifically for the treatment of leukaemia with ^{32}P. Marinelli showed that the knowledge of the bio-distribution, especially the excretion of the radionuclide was essential to accurate dosimetry (McParland, 2010). This method was developed alongside Marinelli's colleagues, Quimby and Hine and it gives the dose from a beta emitter that completely decays in a tissue as:

$$\boldsymbol{D_\beta = 73.8CE_\beta T} \qquad 4.5$$

$\boldsymbol{D_\beta}$ stands for the dose in rad, **C** is the concentration of the radionuclide in micro curies per gram, $\boldsymbol{E_\beta}$ is the mean energy emitted per decay of the nuclide and T is the half-life of the nuclide in the tissue (Stabin, 2006). The proportionality constant defined in equation 4.1 can be calculated as $\boldsymbol{k}$ = 73.8/1.443 = 51.1. The value 1.443 defines the cumulated activity (Stabin, 2008) (cumulated activity = (1/ln2) × initial activity). This formalism was also extended to dosimetry of gamma emitting isotopes and developed what is thought of today as the Marinelli-Quinby-Hine system (Marinelli, Quinby and Hine, 1948).

Patient-specific dosimetry for ^{131}I therapy of hyperthyroidism was thereafter, quickly recognized as a way of optimizing therapy for individual patients. To achieve this, specified activity concentrations (2000 – 3000 MBq/g or 55 – 80 µCi/g) of ^{131}I in the thyroid were prescribed. The prescription incorporated the two dosimetric variables of thyroid uptake and mass into the calculation of activity to be administered. However, the implicit assumption of a constant thyroid half-life of radio-iodine was used (Zanzonico, 2000). Therefore, to calculate the administered dose the following equation is used.

$$\boldsymbol{A\ (kBq) = \frac{AD\ (cGy) \times gland\ mass\ (g) \times 6.67 \times 37}{(T_{1/2})_{eff}(days) \times 24{-}h\ \%\ uptake}} \qquad 4.6$$

Where $\boldsymbol{A}$, stands for administered activity, $\boldsymbol{AD}$ is prescribed absorbed dose, $\boldsymbol{24 - h\ \%\ uptake}$ is the % uptake of ^{131}I in the thyroid 24 hours after administration and $\boldsymbol{(T_{1/2})_{eff}}$ is the effective half-life of radioiodine in the thyroid. The factor 6.67 was derived by Marinelli-Quinby-Hine (Zanzonico, 2000) with the assumption that the thyroid has a mass of 25 g and consisting of 2 unit density tangent spheres each of mass 12.5g and radius of 1.44 cm. They also assumed that the radioiodine followed a mono-exponential time-activity function and used a mean beta energy of 0.191 MeV and a specific gamma ray constant of 0.00223 R cm^2/mCi/h for ^{131}I. There was also the incorporation of the appropriate unit conversion factors (Zanzonico, 2000). The shortcoming of this method is that it is made of many assumptions which may not reflect reality.

4.2.2 Medical Internal Radiation Dose Schema

Advanced imaging techniques such as the gamma camera emerged in the 1950s and 1960s for activity quantification. This was followed by the development of more sophisticated internal dosimetry methods. The MIRD committee of the Society of Nuclear Medicine was established and they developed a method for dose calculation to selected organs and the total body due to internally administered radionuclides (Stabin and Siegel, 2003). The MIRD dosimetry method is a standard method developed for correlation of delivered activity with radiation dose (Simpkin, 1999; Skanjeti et al., 2015). The MIRD formalism calculated the mean absorbed dose (D_T) to an organ (target organ, T) by the following equation which is based on equation 4.3:

$$\boldsymbol{D_T} = \sum_h \boldsymbol{\widetilde{A}_h} \times \boldsymbol{S}(\boldsymbol{r_T} \leftarrow \boldsymbol{r_h}) \qquad 4.7$$

According to the MIRD formalism, the source volume containing the activity is defined as r_h and the target volume for which the dose is calculated $\boldsymbol{r_T}$. $\boldsymbol{D_T}$ (Gy) is the mean absorbed dose delivered to the target, $\boldsymbol{\widetilde{A}_h}$ (Bq.s) is the cumulated activity in the source organ and $\boldsymbol{S}(\boldsymbol{r_T} \leftarrow \boldsymbol{r_h})$ (Gy.Bq^{-1}.s^{-1}) is the organ S factor defined in equation 4.8 below, and is the mean absorbed dose delivered to the target organ per unit cumulated activity in the source organ. $\boldsymbol{S}(\boldsymbol{r_T} \leftarrow \boldsymbol{r_h})$, is dependent on the type and energy of the radiation, the size, shape and composition of the source and target; and the distance between the source and target as well as the type of material separating them. The cumulated activity $\boldsymbol{\widetilde{A}_h}$ is the integral of the activity-time curve for the source volume, the total number of decays that occur in the source volume.

$$\boldsymbol{S_{T \leftarrow h}} = \sum \Delta_i \cdot \frac{\phi_i(\boldsymbol{T \leftarrow h})}{\boldsymbol{m_T}} \qquad 4.8$$

Where Δ_i, is the mean energy emitted as radiation $\boldsymbol{i}$, per decay, ϕ_i is the absorbed fraction in the target volume $\boldsymbol{T}$ of the radiation $\boldsymbol{i}$ emitted in $\boldsymbol{h}$ and $\boldsymbol{m_T}$ is the mass of the target volume.

Equation 4.7 is the 3-D form of the MIRD schema (Amato *et al.*, 2011), with the simplified 2-D form given as:

$$\boldsymbol{D}\,(\boldsymbol{r_T} \leftarrow \boldsymbol{r_h}) = \boldsymbol{\tilde{A}_h S}\,(\boldsymbol{r_T} \leftarrow \boldsymbol{r_h}) \qquad 4.9$$

Where all the symbols have their usual meaning.

In principle, the MIRD formalism is a way of applying equation 4.3 by splitting the determination of absorbed dose into two tasks. These are the (1) determination of the cumulated activity Ã and (2) calculation of the source and geometry dependent S-value (Bardiès and Buvat, 2011). The cumulated activity can be calculated from a series of quantitative planar or SPECT scans acquired at multiple times after injection in order to map the radiopharmaceutical's pharmacokinetics. The total activity within each region of interest (ROI) or VOI at each time point is calculated by fitting the time-activity data to one or more exponential functions or by compartmental modelling of the pharmacokinetics of the radiopharmaceutical in use.

Some simple kinetic models representing the accumulation and elimination of radionuclide from the organ of interest can be applied as well with a good approximation. For organ-level calculations, the total ROI activity is assumed to be uniformly distributed within each ROI. The activity as a function of time, or TAC, is fit with a linear or exponential equation and the cumulated activity is calculated by integrating over time (Figure 4.1).

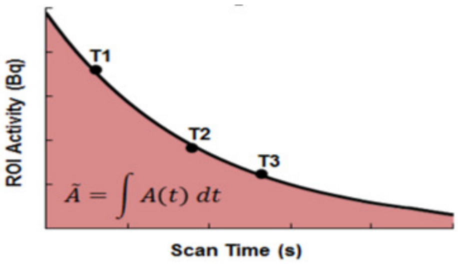

Figure 4.1: ***Calculation of cumulated activity in a ROI by fitting the total activity at each time-point (T1, T2 …) with an analytical fit and integrating the analytical fit over time.***

The integration over time could be by direct analytical integration or by other methods such as piecewise linear (trapezoid) fit method or by Riemann integration (Hindorf, C., 2014). The cumulated activity as explained earlier is the activity-time integral of the TAC and thus can be expressed by analytical integration as:

$$\tilde{A} = \int_0^\infty \boldsymbol{A}\,(\boldsymbol{t})\boldsymbol{dt} = \boldsymbol{A_0} \int_0^\infty \boldsymbol{f}(\boldsymbol{t})\boldsymbol{dt} \qquad 4.10$$

Where $\boldsymbol{A_0}$ is the activity administered to the patient at time t = 0 and $\boldsymbol{f}(\boldsymbol{t})$ is the fractional distribution function for the source volume (i.e. fraction of administered activity present in the source volume at time t) and in many instances, $\boldsymbol{f}(\boldsymbol{t})$ may be modelled as a sum of exponential functions. From equation 4.10, equation 4.11 below can be derived:

$$\tilde{A} = \boldsymbol{1.44}\,\boldsymbol{f}\boldsymbol{A_0}\,\boldsymbol{T_e} \qquad 4.11$$

Where $\boldsymbol{1.44}\ \boldsymbol{T_e}$ is the mean lifetime of the radionuclide and $\boldsymbol{T_e}$ is the effective half-life as given in equation 4.4; $\boldsymbol{f}$ is the fraction of administered activity $\boldsymbol{A_0}$ in the source organ. When there is no biological elimination, then $\boldsymbol{T_e} = \boldsymbol{T_p}$ as is the case in this study, thus, equation 4.11 can be reduced to:

$$\tilde{A} = \boldsymbol{1.44}\,\boldsymbol{A_0}\,\boldsymbol{T_p} \qquad 4.12$$

To calculate the area under the curve by the piecewise linear trapezoid method, the area under the TAC is divided into different trapezoids using the different time-points on the curve and the sum of the areas of the trapezoids estimates the cumulated activity, the same also applies to the Riemann integral method in which the area under the TAC is divided into rectangles instead of trapezoids. For all these methods of integrating the TAC, the selection of the optimal time points in order to obtain the total number of radionuclide decays occurring in the source/target organ or tumour for the purpose of calculating the cumulated activity is very important (Siegel *et al.*, 1999; Stabin, 2008; Eberlein, Cremonesi and Lassmann, 2017).

Siegel et al (1999) in MIRD pamphlet 16 suggested a minimum of three-time points for each clearance exponential which may be based on physical or effective half-life. An inadequate number of time points leads to difficulties in correctly characterizing the decay of the radiopharmaceutical. Furthermore, the extrapolation of the integral of the TAC to infinity will be inacurate if enough data is not collected due to inadequate time points (Lassmann and Eberlein, 2018) and this strongly influences the calculation of the cumulated activity.

The organ level S-values are calculated for a specific radionuclide using Monte Carlo (MC) and can be based on computational models representing reference individuals of variable sex, size/weight and age (Figure 4.2). However, the calculation of S-values nowadays has changed. This is due to the use of CT-based geometry definition to calculate the S value for individual patients (Stabin and Bardiès, 2010). The *S*-value for many radionuclides of interest in NM is published in MIRD pamphlet 11(Simpkin, 1999) and updated to include over 800 radionuclides of interest (Stabin and Siegel, 2003). The dose deposition within each target volume is thus calculated from equation 4.7 and the dose is assumed to be uniformly distributed within the volume. MIRD method is simple in terms of measurement and it standardizes the dosimetric procedure which makes it easy to compare results among scientists.

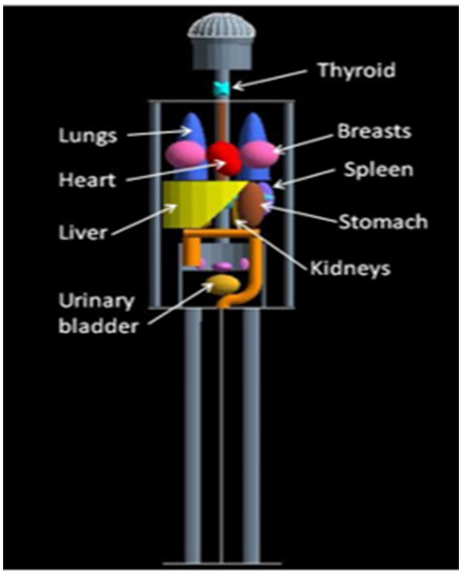

Figure 4. 2: ***A reference female computational model used for organ level dose calculations***

It is pertinent to also mention the dosimetry model of the ICRP which is almost identical to the MIRD method. Although, the ICRP had made several contributions to NM radiation dosimetry through its publications, e.g. ICRP 26, 30, 53, 60 etc. and by introducing and refining the 'Reference Man', 'Woman' and various 'reference pediatric' phantoms, it will not be discussed further. This is because its focus is mostly on the radiological protection of the worker exposed to ionizing radiation rather than an exclusive emphasis on NM patients, especially in radionuclide therapy.

4.2.2.1 OLINDA/EXM

The software OLINDA/EXM (Organ Level INternal Dose Assessment/Exponential Modelling), henceforth to be alternately referred to as OLINDA/EXM, is an extended version of the MIRDOSE software series (MIRDOSE 1 – 3) (Stabin, 1996) and it replaced the series as a treatment planning device. OLINDA/EXM provides *S*-values for the over 800 radioelements mentioned above in Stabin and Siegel (2003) which were calculated via a Monte Carlo method. It uses standard models for 10 whole-body phantoms representing reference adults, children, and pregnant women at different stages of pregnancy.

To standardize and simplify dose calculation for internal emitters, especially for therapeutic purposes, phantoms are used. These phantoms, which are modelled after animals (rabbits and rats) or humans comprised of stylized, voxel-based, and BREP (Boundary Representation) or Hybrid phantoms (Stabin, 2006, Stabin and Xu, 2014, Zubal *et al.*, 1994, Segars, Lalush and Tsui, 1999, Segars *et al.*, 2010) as mentioned in section 4.1. The phantoms used in OLINDA/EXM are standard stylized phantoms which are comprised of 3 tissue types of bone, soft tissue, and lung. A complete list of the various phantoms developed worldwide for internal dosimetry and their evolution can be found in the book edited by Xu and Eckerman (2010).

OLINDA/EXM calculates absorbed doses using the organ-level MIRD formalism. It uses organ S-values that are pre-computed in the various human models contained therein as mentioned above. Average organ doses are then computed by entering the measured, patient-specific cumulated activity $\boldsymbol{\widetilde{A}_h}$ for each organ and using the pre-computed S-values from the most appropriate human model as shown in equations 4.7 and 4.9. The patients' cumulated activities must be calculated outside of the OLINDA/EXM software and manually entered into the software. The contributions of self-irradiation and cross-irradiation from other source organs are included in the mean dose of each target organ of interest. The average doses calculated by OLINDA/EXM are assumed to be uniformly distributed throughout the organ.

Tumour doses are computed differently since they are not modelled within the human models in OLINDA/EXM and do not have pre-computed S-factors within these models. The nodule module in the OLINDA/EXM is used to calculate absorbed doses to tumours. Tumours are modelled as unit-density spheres isolated in an infinite unit-density medium. The self-absorbed *S*-values for unit-density spheres of masses that ranged from 0.01 g to 6000 g is calculated for radionuclides of interest. The sphere mass is assumed to be the same as that of the tumour and the total cumulated activity is uniformly distributed within the sphere. It is important to note that the activity of the tumour is not accounted for when calculating organ dose using the OLINDA/EXM since there is no means of defining the correct location of the module in the patient.

The mean absorbed dose estimated to organs by using the standard phantom-based dosimetry models of OLINDA/EXM are said to likely be of limited accuracy (Ljungberg *et al.*, 2003). This is because of the inherent differences in patient organ geometry which the OLINDA/EXM software cannot model well because of the fixed organ geometry of the mathematical phantoms. Additionally, the assumption of a uniform radionuclide activity and absorbed dose within each organ does not take into account heterogeneous uptake and dose deposition.

There are also many problems that result from the tumour not being modeled as part of the phantom. Firstly, the dose to normal tissues will likely be underestimated as the dose from the activity within a tumour is not taken into account. This underestimation could lead to an increased risk of normal tissue toxicities. Secondly, the dose to the tumour will also likely be underestimated because only the self-absorbed dose is calculated and the dose from other organs is ignored. Therefore, the OLINDA/EXM dosimetry program may be appropriate for calculating mean doses for diagnostic applications but for therapeutic applications voxel level calculations that fully take into account patient-specific anatomy are needed for more accurate dose estimation.

In spite of all these drawbacks of the OLINDA/EXM software and MIRD method in general, it had been shown that when organ masses of individual patients are corrected for in relation to the organ masses of the standard phantoms used in OLINDA/EXM, results that are close to those calculated using the MC method can be achieved (Divoli *et al.*, 2009). Patient organ masses can be corrected for by using equation 4.13 below.

$$S\,(r_h \leftarrow r_h)(pat) = S\,(r_h \leftarrow r_h)(std) \times \frac{m_h\,(std)}{m_h\,(pat)} \qquad 4.13$$

Where $S\,(r_h \leftarrow r_h)(pat)$ represents the patient self S factor and $S\,(r_h \leftarrow r_h)(std)$ is the self S factor for the MIRD standard phantom, and $m_h\,(std)$ and $m_h\,(pat)$ are the organ masses for the standard phantom and patient respectively.

4.2.3 Voxel-level dosimetry method

As mentioned above, a shortcoming of the MIRD (OLINDA/EXM) method is its failure to recognize the fact that non-homogenous activity distribution in the organs/tumour exists. The MIRD method therefore assumes the radiation in the organ and tumour to be uniformly distributed. Therefore, to extend dosimetry to sub-organ voxel dimensions, a voxel-level dosimetry method is required because it offers drastic improvements over the organ-level approach. This is because it is able to take into account heterogeneities in radiopharmaceutical uptake, material composition, and dose deposition at a voxel-level.

While not widely used in routine clinical practice, currently, three main approaches exist that are capable of calculating internal dosimetry on voxel-level: dose point kernel convolution, dose voxel kernel convolution which uses voxel-level /S-values based on the MIRD formalism, and direct MC radiation transport. Of these three, voxel-level dosimetry methods, only direct MC radiation transport method was used in this study for patient voxel-based model dosimetry and would be discussed in the next section.

4.2.4 Monte Carlo dosimetry method

The use of MC dosimetry in NM therapy is on the rise in recent times (Braad *et al.*, 2016). Using MC-based dosimetry methods to model radiation transport is the most accurate means of predicting absorbed dose distributions in organs and tumours (Ljungberg and Sjögreen-Gleisner, 2011; Xie *et al.*, 2013). It is also very accurate in deriving the 3-D estimates of radiation dose on a voxel by voxel basis thereby not depending on standard models of the body and the organs. There exists today, many radionuclide dose planning systems of which some are routinely used in the clinic. These are, LundADose (a research tool), 3D-ID, SIMDOS, RTDS, RMDP, DOSE3D with 3D-ID been more routinely used in the clinic than the others (Stabin and Brill, 2008). Since LundADose is the method of choice that will be used in this work it is discussed in more detail in the following section.

4.2.4.1 LundADose Monte Carlo dosimetry software

LundADose is a MC program for calculation of the absorbed dose rate from quantitative SPECT/CT images in both two-dimensional and three-dimensional dosimetry. It calculates the absorbed dose rate using the electron-gamma shower version 4 (EGS4) (Nelson et al., 1985) MC program. This code converts the distribution of activity into absorbed dose distribution (Ljungberg *et al.*, 2003; Ljungberg and Sjögreen Gleisner, 2016). LundADose is a very robust patient-specific voxel-level MC dose planning system because it is supported with a well-established and a well-validated general purpose photon and electron transport MC code (EGS4).

The software was developed in Interactive Data Language by Prof M. Ljungberg and co-workers at the Department of Medical Radiation Physics, University of Lund, Lund Sweden (Sjögreen et al., 2005). It contains methods for SPECT/CT voxel-based dosimetry, including OSEM image reconstruction, detailed CT-based corrections for attenuation, correction for scatter (using the ESSE scatter model) and collimator-detector response which also included septal penetration, resulting in images of Bq/voxel units. It also incorporated software for deformable image registration. This enables LundADose to carry out CT-CT image registration, with the application of the spatial transformation to the patient SPECT images.

LundADose performs dosimetry based on *S*-values which are generated in the code based on the specific patient geometry and gives absorbed doses for VOI as total, mean, maximum, and minimum. LundADose also includes curve-fitting procedures in order to obtain cumulated activity, from a series of scintillation images as described in section 4.2.2, in the organs and tumours of interest. The generation of both integral and frequency Dose Volume Histogram (DVH), as well as biologically effective dose (BED) to the organs and tumours for individual patients, makes LundADose a software of choice for absorbed dose evaluation.

In this work, the LundADose software was used to calculate the absorbed dose to tumours and organs of interest due to its ability to consider the patient, tumour and organ geometry in the calculations. As mentioned above it also provided additional information such as maximum and minimum doses in each VOI. For this study, the results of the ^{131}I mean absorbed doses calculated using LundADose were compared to the mean absorbed doses obtained with OLINDA/EXM for the lung, liver, and tumours in simulated patient studies. The comparison was analyzed using simple descriptive statistics such as mean, range, standard deviation; linear regression analysis, and Bland-Altman plots to evaluate the agreement between the two methods. Researchers had compared the MIRD dosimetry method with various MC dose calculation programs (Divoli *et al.*, 2009; Howard *et al.*, 2011; Shahbazi-Gahrouei and Ayat, 2012; Brolin *et al.*, 2015; Skanjeti *et al.*, 2015) and reported some differences in accuracy between them.

4.3 Bland-Altman analysis

A Bland-Altman plot is a measure of the degree of agreements between two methods measuring the same variables (Bland and Altman, 1986; Earthman, 2015). The plot is constructed by plotting the difference between the two methods on the vertical axis and the mean of the methods on the horizontal axis. This is used to assess the agreement which may be poor even with a good correlation between the two methods. The Bland-Altman plot is more informative than the correlation analysis as it also facilitates the investigation of any possible relationship between the measurement error and the true value, which in this case is the mean of the two measurements (Giavarina, 2015). Standard errors and confidence intervals can be calculated and used to see how precise the estimates of the limit of agreement between the two methods are if and only if the differences between them follow a normal distribution, of which 95 % of the difference between the two methods should lie between the lower limit and upper limit of agreement calculated.

4.4 Practical implementation of dosimetry

The current standard practice of dosimetry in RNT (Zanzonico, 2000; Bardiès and Buvat, 2011; Wierts *et al.*, 2011; Eberlein, Cremonesi and Lassmann, 2017) involves the following steps; first, images are acquired at different time points for quantification purposes using planar and or SPECT images. Some practitioners use only planar images while some use only SPECT images, and some others use planar images combined with SPECT acquired at one or more time points (Roth *et al.*, 2018). The benefit of this hybrid method is that it performs better than methods based on planar images alone (Roth *et al.*, 2018). This enables the assessment of the activity in the organ (or tumour) of interest over time. Another step is to determine the CF. To accurately quantify the images, there is the need for a reliable calibration of the camera to obtain a CF for the conversion of counts in the image into activity. The accurate determination of the volume of the organ or lesion of interest (Eberlein, Cremonesi and Lassmann, 2017) so as to avoid the under or overestimation of the absorbed doses is the next step.

The generation of TAC follows in order to determine the cumulated activity as described in sections 4.1.3 and 4.2.2. It is important to choose regular and sufficient time intervals to obtain the biological washout of the radiopharmaceutical from the organ or tumour, this is necessary to allow for the collection of adequate data from the radionuclide decay in the structure of interest.

The absorbed dose distribution in the organ or lesion of interest is finally calculated using either the MIRD dosimetry method, voxel-level dosimetry method or the direct MC method using a suitable MC dose calculation code as discussed in section 4.2.4. Due to the increase in the use of radionuclides for therapeutic purposes, the requirement for accuracy in the calculation of absorbed dose has also increased. Although, many limitations, as discussed in previous chapters, and in absorbed dose planning such as uncertainties in the calculation methods as mentioned in chapter 1, section 1.2 still exist, there is a crucial need for treatment planning in the therapeutic applications of radionuclides in NM.

The next chapter (Chapter 5) deals with the creation and validation of the virtual gamma camera model used in this study for simulating ^{131}I SPECT studies.

4.5 References

Amato, E., Campenni, A., Herberg, A., Minutoli, F. and Baldari, S. (2011) 'Internal Radiation Dosimetry : Models and Applications', in Gholamrezanezhad, A. (ed.) *12 Chapters on Nuclear Medicine*. 1st edn. Rijeka, Croatia: InTech, pp. 25–46.

Bardiès, M. and Buvat, I. (2011) 'Dosimetry in Nuclear Medicine Therapy: What are the specifics in image quantification for dosimetry?', *QJ. Nucl. Med. Mol. Imaging*, 55, pp. 5–20.

Bland, J. M. and Altman, D. G. (1986) 'Statistical Methods For Assessing Agreement Between two methods of Clinical Measurement', *Lancet*, i, pp. 307–310.

Braad, P. E. N., Andersen, T., Hansen, S. B. and Hoilund-Carlsen, P. F. (2016) 'Strategies for CT tissue segmentation for Monte Carlo calculations in nuclear medicine dosimetry', *Med. Phys.*, 43, pp. 6507–6516.

Brolin, G., Gustafsson, J., Ljungberg, M. and Gleisner, K. S. (2015) 'Pharmacokinetic digital phantoms for accuracy assessment of image-based dosimetry in ^{177}Lu-DOTATATE peptide receptor radionuclide therapy.', *Phys. Med. Biol.* 60, pp. 6131–6149.

Dale, R. G. (1996) 'Dose-rate effects in targeted radiotherapy.', *Phys. Med. Biol*, 41, pp. 1871–1884.

Dash, A., Russ Knapp Jr, F. F. and Pillai, M. R. A. (2013) 'Targeted Radionuclide Therapy - An Overview', *Current Radiopharmaceuticals*, 6, pp. 1–29.

Divoli, A., Chiavassa, S., Ferrer, L., Barbet, J., Flux, G. D. and Bardiès, M. (2009) 'Effect of patient morphology on dosimetric calculations for internal irradiation as assessed by comparisons of Monte Carlo versus conventional methodologies', *J. Nucl. Med.;* 50, pp. 316–323.

Dorn, R., Kopp, J., Vogt, H., Heidenreich, P., Carroll, R. G. and Gulec, S. A. (2003) 'Dosimetry-Guided Radioactive Iodine Treatment in Patients with Metastatic Differentiated Thyroid Cancer : Largest Safe Dose Using a Risk-Adapted Approach', *J. Nucl. Med.*, 44, pp. 451–456.

Earthman, C. P. (2015) 'Body Composition Tools for Assessment of Adult Malnutrition at the Bedside : A Tutorial on Research Considerations and Clinical Applications Introduction to Lean Tissue Terminology', *JPEN J. Parenter. Enteral. Nutr.*, 39, pp. 787–822.

Eberlein, U., Cremonesi, M. and Lassmann, M. (2017) 'Individualized Dosimetry for Theranostics: Necessary, Nice to Have, or Counterproductive?', *J. Nucl. Med.*, 58, p. 97S–103S.

Giavarina, D. (2015) 'Lessons in biostatistics Understanding Bland Altman analysis', *Biochemia Medica*, 25, pp. 141–151.

Gleisner, K. S., Spezi, E., Solny, P., Gabina, P. M., Cicone, F., Stokke, C., Chiesa, C., Paphiti, M., Brans, B., Sandström, M., Tipping, J., Konijnenberg, M. and Flux, G. (2017) 'Variations in the practice of molecular radiotherapy and implementation of dosimetry : results from a European survey', *EJNMMI Physics*, 4, pp. 1–20.

Hindorf, C., (2014) 'Internal Dosimetry', in Bailey, D. L. et al. (eds) *Nuclear Medicine Physics. A Handbook for Teachers and Students.* Vienna: International Atomic Energy Agency (I.A.E.A).

Howard, D. M., Kearfott, K. J., Wilderman, S. J. and Dewaraja, Y. K. (2011) 'Comparison of I-131 Radioimmunotherapy Tumor Dosimetry: Unit Density Sphere Model Versus Patient-Specific Monte Carlo Calculations', *Cancer Biother. Radiopharm.*, 26, pp. 615–621.

Lassmann, M. and Eberlein, U. (2018) 'The Relevance of Dosimetry in Precision Medicine.', *J. Nucl. Med.* 59, pp. 1494–1499.

Ljungberg, M., Frey, E., Sjögreen, K., Liu, X., Dewaraja, Y. and Strand, S-E. (2003) '3D absorbed dose calculations based on SPECT: evaluation for 111-In/90-Y therapy using Monte

Carlo simulations.', *Cancer Biother. Radiopharm.*, 18, pp. 99–107.

Ljungberg, M. and Sjögreen-Gleisner, K. (2011) 'The accuracy of absorbed dose estimates in tumours determined by quantitative SPECT: a Monte Carlo study.', *Acta oncologica (Stockholm, Sweden)*, 50, pp. 981–989.

Ljungberg, M. and Sjögreen-Gleisner, K. (2016) 'Personalized Dosimetry for Radionuclide Therapy Using Molecular Imaging Tools', *Biomedicines*, 4, pp. 25–45.

Ljungberg, M. (2018) 'Absolute Quantitation of SPECT Studies', *Semin. Nucl. Med.* 48, pp. 348–358.

Luster, M., Pfestroff, A., Hänscheid, H. and Verburg, F. A. (2017) 'Radioiodine Therapy', *Semin. Nucl. Med.* 47, pp. 126–134.

Marinelli, L. D., Quinby, E. H. and Hine, G. J. (1948) 'Dosage determination with radioactive isotopes; practical consideration in therapy and protection.', *Am J. Roentgenol. Radium Ther*, 59, pp. 260–281.

McParland, B. J. (2010) *Nuclear Medicine Radiation Dosimetry-Advanced Theoretical Principles*. London: Springer-Verlag.

Nelson, W.R., Hirayama, H., and Rogers, D.W.O. (1985). *'EGS4 code system'*. Report SLAC-265, Stanford Linear Accelerator Centre Stanford, CA.

Roth, D., Gustafsson, J., Sundöv, A. and Gleisner, K. S. (2018) 'A method for tumor dosimetry based on hybrid planar-SPECT / CT images and semiautomatic segmentation', *Med. Phys.*, 45, pp. 5004–5018.

Segars, W., Lalush, D. and Tsui, B. M. W. (1999) 'A realistic spline-based dynamic heart phantom', *IEEE Trans. Nucl. Sc.*, 46, pp. 503–506.

Segars, W. P., Sturgeon, G., Mendonca, S., Grimes, J. and Tsui, B. M. W. (2010) '4D XCAT phantom for multimodality imaging research', *Med. Phys.*, 37, pp. 4902–4915.

Siegel, J. A., Thomas, S. R., Stubbs, J. B., Stabin, M. G., Hays, M. T., Koral, K. F., Robertson, J. S., Howell, R. W., Wessels, B. W., Fisher, D. R., Weber, D. A. and Brill, A. B. (1999) 'MIRD Pamphlet No . 16 : Techniques for Quantitative Radiopharmaceutical

Biodistribution Data Acquisition and Analysis for Use in Human Radiation Dose Estimates', *J. Nucl. Med.*, 40, pp. S37–S61.

Sgouros, G. and Hobbs, R. F. (2014) 'Dosimetry for Radiopharmaceutical Therapy', *Semin. Nucl. Med.*, 44, pp. 172–178.

Shahbazi-Gahrouei, D. and Ayat, S. (2012) 'Comparison of Three Methods of Calculation, Experimental and Monte Carlo Simulation in Investigation of Organ Dose (Thyroid, Sternum, Cervical Vertebra) in Radioiodine Therapy', *J. Med. Signals Sens.*, 2, pp. 149–152.

Simpkin, D. J. (1999) 'Imaging & Therapeutic Technology The AAPM/RSNA Physics Tutorial for Residents Radiation Interactions and Internal Dosimetry in Nuclear Medicine 1', *RadioGraphics*, 19, pp. 155–167.

Sjögreen, K., Ljungberg, M., Wingärdh, K., Minarik, D. and Strand, S-E. (2005) 'The LundADose method for planar image activity quantification and absorbed-dose assessment in radionuclide therapy.', *Cancer Biother. Radiopharm.*, 20, pp. 92–97.

Skanjeti, A., Miranti, A., Yabar, G. M. D., Bianciotto, D., Trevisiol, E., Stasi, M. and Podio, V. (2015) 'A simple and accurate dosimetry protocol to estimate activity for hyperthyroidism treatment', *Nuclear Med. Rev.* 18, pp. 13–18.

Stabin, M. (2006) 'Nuclear medicine dosimetry.', *Phys. Med. Biol.*, 51, pp. R187--R202.

Stabin, M. A. and Flux, G. D. (2014) 'The Use of Dosimetry in the Planning of Patient Therapy', in Baum, R. (ed.) *Therapeutic Nuclear Medicine*. 1st edn. Berlin Heidelberg: Springer-Verlag, pp. 867–877.

Stabin, M. G. (1996) 'MIRDOSE: personal computer software for internal dose assessment in nuclear medicine.', *J Nucl Med*, 37(3), pp. 538–546

Stabin, M. G. (2008) *Fundamentals of Nuclear Medicine Dosimetry*. New York: Springer Science.

Stabin, M. G. (2017) *The practice of internal dosimetry in nuclear medicine*. Florida: Taylor and Francis.

Stabin, M. G. and Bardiès, M. (2010) 'Applications to Nuclear Medicine', in Xu, X. G.

and Eckerman, K. F. (eds) *Handbook of anatomical models for radiation dosimetry.* New York: Taylor and Francis, pp. 471–486.

Stabin, M. G. and Brill, B. A. (2008) 'State of the Art in Nuclear Medicine Dose Assessment', *Semin. Nucl. Med.*, 38, pp. 308–320.

Stabin, M. G. and Siegel, J. A. (2003) 'Physical Models and Dose Factors for Use in Internal Dose Assessment', *Health Phys.*, 85, pp. 294–310.

Stabin, M. and Xu, X. G. (2014) 'Basic Principles in the Radiation Dosimetry of Nuclear Medicine', *Semin. Nucl. Med.*, 44, pp. 162–171.

Strigari, L., Konijnenberg, M., Chiesa, C., Bardies, M., Du, Y., Gleisner, K. S., Lassmann, M. and Flux, G. (2014) 'The evidence base for the use of internal dosimetry in the clinical practice of molecular radiotherapy', *Eur. J. Nucl. Med. Mol. Imaging*, 41, pp. 1976–1988.

Villoing, D., Marcatilli, S., Garcia, M-P. and Bardies, M. (2017) 'Internal dosimetry with the Monte Carlo code GATE : Validation using the ICRP / ICRU female reference computational model Internal dosimetry with the Monte Carlo code GATE : validation using the ICRP / ICRU female reference computational model', *Phys. Med. Biol.*, 62, pp. 1885–1904

Wierts, R., de Pont, C. D. J. M., Brans, B., Mottaghy, F. M. and Kemerink, G. J. (2011) 'Dosimetry in molecular nuclear therapy', *Methods.*, 55, pp. 196–202.

Xie, T., Bolch, W. E., Lee, C. and Zaidi, H. (2013) 'Pediatric radiation dosimetry for positron-emitting radionuclides using anthropomorphic phantoms.', *Med. Phys.*, 40, pp. 102502-1-102502–14.

Xu, X. G. and Eckerman, K. F. (eds) (2010) *Handbook of Anatomical Models for Radiation Dosimetry*. New York: Francis & Taylor.

Yue, J., Mauxion, T., Reyes, D. K., Lodge, M. A., Hobbs, R. F., Rong, X., Dong, Y., Herman, M. J., Wahl, R. L., Geschwind, J-F. H. and Frey, E. C. (2016) 'Comparison of quantitative Y-90 SPECT and non-time-of-flight PET imaging in post-therapy radioembolization of liver cancer', *Med. Phys.*, 43, pp. 5779–5790.

Zaidi, H. and Xu, X. G. (2007) 'Computational Anthropomorphic Models of the Human

Anatomy : The Path to Realistic Monte Carlo Modeling in Radiological Sciences', *Annu. Rev. Biomed. Eng.*, 9, pp. 471–500.

Zanzonico, P. B. (2000) 'Internal radionuclide radiation dosimetry: a review of basic concepts and recent developments.', *J. Nucl. Med.*, 41, pp. 297–308.

Zubal, I. G., Harrell, C. R., Smith, E. O., Rattner, Z., Gindi, G. and Hoffer, P. B. (1994) 'Computerized three-dimensional segmented human anatomy.', *Med. Phys.*, 21, pp. 299–302.

CHAPTER FIVE: Creation and validation of a Monte Carlo model of the Siemens Symbia SPECT/CT gamma camera

Table of Contents

5.1 Introduction

Computer simulation software as discussed in Chapter 2 use random sampling in modelling real systems and this introduces some uncertainty in the output of the simulation. Therefore, the output is usually an estimate of the true behaviour of the real system. There is then the need to reduce uncertainty in the output to make the estimate to be as close as possible to the real world system and to use statistics to interpret such outputs. It is usually a requirement to validate these software programs before using them for simulations.

Validation of simulation codes is a process which ensures that the computer model accurately represents the system being studied. It involves benchmarking of the simulation code against actual experiments carried out so as to ensure the accuracy of the simulated model (Bostani et al. 2015). Monte Carlo (MC)) methods are recognized as being particularly useful for the simulation of new detectors for nuclear medicine (NM) applications. They have been applied to the study of detector efficiency in the design and optimization of imaging systems and in the development and evaluation of image correction strategies. (Karakatsanis et al. 2006). Simulating Medical Imaging Nuclear Detectors (SIMIND) (Ljungberg, 2018) is a MC code which can be used to model a standard clinical gamma camera and can be modified to simulate planar and single photon emission computed tomography (SPECT) NM studies (Ljungberg 2017).

Validating SIMIND for simulating imaging systems is very important and National Electrical Manufacturers Association (NEMA) tests (National Electrical Manufacturers Association, 2013) can be used for the validation. The NEMA tests used in this study for the validation were the intrinsic and system energy resolution, system spatial resolution, and system sensitivity (Karakatsanis et al. 2006; Lazaro et al. 2004; Schmidtlein et al. 2006; Momennezhad et al. 2012; Gustafsson et al. 2015; Strydhorst et al. 2016; Gustafsson et al. 2000; Dewaraja et al. 2000). Due to the collimator septal penetration phenomena with ^{131}I, a septal penetration fraction test was also included. Collimator septal penetration is an undesirable effect in NM imaging especially with high energy emitters such as ^{131}I. This is because it degrades the spatial resolution and contrast of the imaging system (Min et al. 2009) and also influences the quantitation accuracy of the study (Dewaraja et al. 2000).

The aim of this chapter was to validate image simulations obtained with SIMIND against experimental measurements conducted with the Siemens Symbia T2 SPECT/CT gamma camera.

The dimensions of the detector, collimator and intrinsic characteristics of the gamma camera were defined using available documentation from the manufacturer and acceptance test measurements. This MC model of the gamma camera was validated by testing the modeled gamma camera's ability to match the aforementioned acquired standard NEMA performance tests. The validated gamma camera model was then used to simulate SPECT acquisitions of voxel-based patient models. The creation and validation of the MC gamma camera model are described below.

5.2 Materials and methods

5.2.1 Radioactive source

The radioisotope used in the simulations was Iodine-131 (^{131}I), which is used in nuclear medicine. As mentioned in Chapter 2, the four highest intensity emissions of gamma rays for ^{131}I are 284 (6.1%), 364 (81.2%), 637 (7.5%), and 723 keV (1.8%). The 637- and 723-keV photons are low in intensity but contribute significantly to the image because, compared with the 364-keV photons, they have relatively low attenuation in the patient and a higher probability of penetrating the collimators that are optimized for 364 keV photons.

5.2.2 Equipment

These ^{131}I sources used for this study were measured using a Biodex Atomlab$^{\text{TM}}$ 500 dose calibrator (Biodex Medical Systems New York, NY, USA) located at the NM department at Universitas Hospital Bloemfontein, Figure 5.1. The accuracy of the dose calibrator for ^{131}I was traceable to a secondary standard through the National Metrology Institute of South Africa (NMISA) in Cape Town, South Africa. This dose calibrator was used for all the studies to ensure consistency.

The Siemens Symbia T (Siemens Medical Solutions, Inc. Hoffman Estates, IL., USA) SPECT/CT gamma camera used for the validation is stationed at the Nuclear Medicine Department at Universitas Hospital Bloemfontein, Figure 5.2. All the NM images needed for the validation were acquired with only one detector of the gamma camera which was in the H-mode for the duration of this part of the study. For extrinsic measurements, the detectors of the gamma camera were equipped with high energy all-purpose (HEAP), low penetration collimators.

Figure 5. 1: ***Biodex Atomlab 500 Dose Calibrator***

The CT component of the Siemens Symbia T SPECT/CT was used to acquire high-resolution CT images of the experimental setup for the validation measurement with a CT tube voltage of 130 kV and an effective tube current of 15 mAs. The reconstructed CT images of the validation tests were processed and used as part of the input to the SIMIND simulation code to simulate the aforementioned validation measurements.

For the simulation and validation of the above-mentioned gamma camera, all simulations and data processing were carried out using a Lenovo Laptop with Intel® Core (™) i3-4030U CPU, with a processing speed of 1.90GHz and installed memory (RAM) of 6.00 GB. It operates on a 64-bit operating system, ×64 based processor running Microsoft Windows 10 Enterprise 2016.

5.2.3 Software

The reconstructed CT images of the experimental set up were segmented using version 3.6.0 of ITK-SNAP released on 29th of October 2016 (Yushkevich et al. 2006). SIMIND MC code (Ljungberg & Strand 1989) version 5.0 was used to create a virtual model of the gamma camera. It was used to simulate all the planar and SPECT image data sets for the entire project.

Figure 5. 2: ***Siemens Symbia T SPECT/CT gamma camera at Universitas Hospital***

The public domain software, ImageJ (version 1.50i) (Ferreira & Rasband 2012) was used to display and process the DICOM files from the gamma camera and to import and display all the binary files simulated with the SIMIND code. Microsoft Excel (Microsoft Cooperation, 2013) was also used for data analysis.

5.2.4 Creation of the Siemens Symbia T SPECT gamma camera in SIMIND

To create the Siemens Symbia T SPECT system in SIMIND, the dimensions for the field of view (FOV) of the detector and the intrinsic characteristics of the gamma camera were defined using the Siemens Symbia T SPECT/CT specification sheet (Siemens 2010). Acceptance test results of the performance criteria of the Symbia T dual-head gamma camera were also defined in the CHANGE program (The SIMIND set up code). The intrinsic spatial resolution and energy resolution of the gamma camera defined in SIMIND were the measured values obtained with ^{99m}Tc. These were the results of the measurements obtained from acceptance testing of the gamma camera. The acceptance test results for the intrinsic spatial resolution and energy resolution of the gamma camera were 0.38 cm for the full width at half maximum (FWHM) and 9.9 % respectively.

The gamma camera settings were as follows: The detector head and crystal size (FOV) was set to dimensions of 53.3 × 38.7 cm^2. Thus to model this geometry in SIMIND, the detector length (half-length) was set to 26.65 cm and the detector width (half-width) was set to 19.35 cm. The crystal was modelled using the material cross-section of NaI with a thickness of 0.95 cm and it was enclosed by a 0.1 cm thick aluminium cover. SIMIND does not model any photomultiplier tubes, light pipes or other components contained within the gamma camera detector. These parts may contribute to the backscatter of incident photons. To account for this, the backscattering material was modelled as a 40 cm thick region of water. The pixel size for the output was set to 0.48 cm to match the pixel size in the recorded Digital Communication (DICOM) files from the Siemens Symbia gamma camera. The collimator was defined in the command prompt as **sy-he** (Siemens Symbia HEAP collimator). The description of this collimator is contained in a database in SIMIND that covers most of the commercial collimators available in the market for NM systems. The collimator settings correspond to the Siemens specifications and are outlined in Appendix II.2.

For the simulations the gamma rays of the ^{131}I were tracked until they had undergone 10 scattering events. The solid angle for the photon was set to 1. This setting is one of SIMIND's variance reduction techniques called photon forcing. It improves the detection efficiency by only generating and tracking photons within the geometry that have a chance of interacting with the crystal. All simulations were done using the SCATTWIN routine that allows the setting of multiple (as many as the user requires) energy windows. This routine records images that contain only primary photons and images that contain only the photons that have undergone scattering events. For the simulations of the validation tests, three energy windows: 364 keV photopeak window (336.7 – 391.2 keV), lower scatter window (283.8 – 336.7 keV) and upper scatter window (391.2 – 445.9 keV) were set. The energy windows were set using an ASCII text file.

The SCATTWIN routine also allows for the modelling of photon interaction in the collimator, thereby allowing for all lead X-rays generated in the collimator to be tracked and recorded using the "Delta Scattering Technique". It is worthy to note that in defining the characteristics of the simulation, characteristic x-ray emission was included. This technique was developed mainly for modelling higher energy radionuclides such as ^{131}I but the code records and tracks all lead x-rays that are generated in the collimator. Also included are the interactions in the phantom, aluminium cover and backscattering material. For the whole camera to be exposed to the photons, the solid angle was set so that SIMIND will calculate it using the phantom and camera dimensions.

The simulation of energy resolution in the crystal was turned on and forced interaction upon a photon entering the crystal was also included. The full list of command line switches is outlined in Appendix II.3.

5.2.5 Validation tests

Experimental measurements were acquired using the Siemens Symbia T2 dual head SPECT/CT gamma camera. The planar validation tests were performed using NEMA recommendations stipulated for gamma camera performance criteria. The tests as mentioned earlier, were the intrinsic and extrinsic energy resolution, system spatial resolution, system sensitivity, and collimator septal penetration. The detectors were peaked for all the tests at the 364 keV photopeak using the aforementioned energy window settings. Each test was done three times over three consecutive days. Since ^{131}I has a half-life of 8.02 days, the decay did not affect the measurements. These repetitions were performed in order to obtain the statistical variation in the measurements.

Planar images were acquired for each of the NEMA tests. This was followed by the CT acquisition of the experimental set up to be used as input into SIMIND to simulate the measurements. The CT scan was acquired using the CareDose 4D protocol (CareDose, Siemens Medical Solutions Germany) with a CT tube voltage of 130 kV and an effective tube current of 15 mAs. The data were acquired in a 512 × 512 matrix with a pixel size of 0.127×0.127 cm^2 and a slice thickness of 0.5 cm. The CT data reconstructed with a smooth kernel (B08s) were used for attenuation correction. These reconstructed CT images were segmented with the public domain segmentation software ITK-SNAP version 3.6.0. A radioactive source map was created with ITK-SNAP by assigning a unique value to each of the segmented regions. The information from the source map was used to create a text file (Zubal file) containing user-defined indexes for the radioactive concentrations assigned to these segmented regions. The Zubal file information for each validation test is given in Appendix II.4.

The segmented images (16-bit) were converted to 8-bit images using ImageJ. These files were used as input to CHANGE for SIMIND simulation. A density map of the CT data was created by using in-house developed software. This software program converts the CT Hounsfield units of the CT data to density values. The source map, text file and density map, generated for each experiment, were used as the phantom design input into the CHANGE program. For all the NEMA tests the planar images were simulated similar to the way the images were acquired on the physical gamma camera. Since, acceptance tests of the Symbia T dual-head SPECT/CT camera showed little difference between the two detectors, all validation tests measurements were acquired using only detector 1 of the gamma camera.

5.2.6 Experimental and simulation set up of the validation tests

5.2.6.1 Energy resolution

The following experiment was performed to determine both the intrinsic and extrinsic energy resolution values. For the acquisition of the intrinsic energy resolution, the collimator was removed. A 5 ml Perspex syringe containing a 5 kBq solution of ^{131}I supported by Styrofoam was positioned on the patient bed as shown in Figure 5.3 (A). The detector and patient bed were fully retracted for the intrinsic (without the collimator) acquisition. After acquiring the intrinsic energy spectrum, the HEAP collimators were fitted to the detectors of the gamma camera and the extrinsic energy spectrum was acquired. The intrinsic and extrinsic energy spectra of the gamma camera were exported as text files for analysis. Figure 5.3 (B) is an illustration of the experimental set up for this test.

The intrinsic and extrinsic energy spectra were simulated with the SIMIND code with the option to include the collimator in the simulation being switched off to match the experimental conditions using the same experimental set up as described previously. As mentioned above, ITK-SNAP was used to segment the experimental CT data (syringe, Styrofoam and bed). Finally, the option to include the collimator in the simulation was switched on to match the experimental conditions for the extrinsic energy spectrum. The SIMIND settings used for the simulation of the energy resolution and system spatial resolution validation tests are outlined in Appendix II.5. The text files created by SIMIND for the intrinsic and extrinsic energy spectra were used for analysis.

5.2.6.2 System spatial resolution

Two capillary tubes of an inner diameter of approximately 1mm were used to determine system spatial resolution. The two capillary tubes were filled with 9.8 MBq and 9.2 MBq respectively and were placed on a Styrofoam block and positioned on the patient bed. The set up was as illustrated in Figure 5.3 (A) and (C), the two capillary tubes were placed inside a transparent plastic bag to avoid contamination. The Styrofoam block with the two capillary tubes were placed in the X-direction (axial position) 10.0 ± 0.5 cm apart and 10.0 ± 0.5 cm away from detector 1. After the acquisition in the X-direction, the block with the two tubes were rotated through 90 degrees for acquisition in the Y-direction (transaxial position). The camera set up for these acquisitions was a matrix size of 512 × 512 with a corresponding pixel size of 0.12 cm. As mentioned before, a 15% energy window, which was centred over the 364 keV photopeak of ^{131}I was used for all the acquisitions. The static images of the capillary tubes were acquired until a total of 4 000 000 counts had been recorded. Thereafter the CT image of the set-up was acquired.

Figure 5. 3 (A): ***Experimental set up for the NEMA tests carried out.***

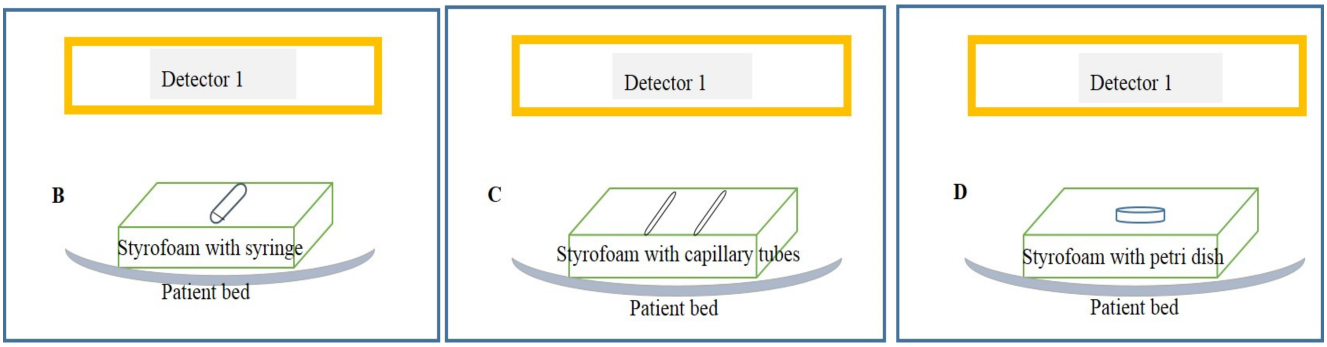

Figure 5. 3 (B, C, and D): ***Illustration of the experimental set up for energy and system spatial resolution, system sensitivity and collimator septal penetration fraction.***

The same experimental sets were defined in the CHANGE program for SIMIND and the acquisitions of the system spatial resolution were simulated. The CHANGE settings for these acquisitions are the same as in Appendix II.5.

5.2.5.3 System sensitivity

As mentioned before the system sensitivity of a gamma camera is a measure of count rate obtained per unit activity (cps/MBq). Therefore, the accuracy of the radioactivity used to obtain the gamma camera system sensitivity is important for this test. To limit the uncertainty in the accuracy of the dose calibrator used in this study a calibrated ^{131}I source was obtained from a standard laboratory (NMISA). In order to determine the system sensitivity, a petri dish with an inner diameter of 6.4 cm was filled with water to a 0.3 cm depth. Liquid ^{131}I with an activity of 137.3 MBq was drawn in a plastic syringe. This activity was dispersed from the syringe into the water in the petri dish. The residual activity in the syringe was promptly measured and the decay corrected activity value subtracted from the original activity value. The total activity in the petri dish after decay correction was 135.7 MBq.

The prepared phantom (petri dish with activity) was placed on a Styrofoam block and positioned on the patient bed. The phantom was placed in the centre of the field of view of the gamma camera and 10.0 ± 0.5 cm from the face of detector 1. A static image of the set up was acquired with a total count of 4 000 000 using a matrix size of 256 × 256 with a pixel size of 0.24 cm. Dead time correction was not necessary because of the resulting low count rate at the detector (< 10k counts/sec). The experimental set up is illustrated in Figure 5.3 (A) and (D).

The same set up was simulated in SIMIND and the CHANGE settings for this simulation are outlined in Appendix II.6.

5.2.6.4 Collimator septal penetration fraction

In order to determine the collimator septal penetration fraction, exactly the same set-up as that of the system sensitivity was used. The two tests are the same, except that the system sensitivity is measured only at the 10 cm distance from the face of the collimator. The collimator septal penetration test is carried out by varying the distance from the phantom to the collimator face. The test was first acquired at a distance of 2 cm with 4000 000 counts as the stop condition. The same acquisition was carried out at 5, 10, 15, 20, 25, 30, and 35 cm distances respectively. The duration of acquisition ranged from 600 s for the 2 cm acquisition to 780 s for the 40 cm acquisition.

The same set up was simulated in SIMIND and the CHANGE settings for this simulation is the same as outlined in Appendix II.6. However, the SPECT orbital rotation fraction was varied according to the distance between phantom and detector surface while index 12 in CHANGE (Height to detector surface) was kept constant

For all the validation tests, at the completion of the simulation, SIMIND created images and header files which were imported with ImageJ software as raw images in a 32-bit real format for image analysis.

5.2.7 Data and image analysis

5.2.7.1 Energy resolution

The measured and simulated extrinsic and intrinsic energy spectra for the Symbia T2 gamma cameras were imported into Microsoft Excel and ImageJ (Fiji) (Schindelin *et al.*, 2012) for analysis. Each energy spectrum was normalized to the maximum value (at 364 keV) in the file and overlaid with the corresponding simulated energy spectrum, Figure 5.4 (A) and (B). ImageJ was used to fit a Gaussian function over the 364 keV photopeak of the energy spectra. The fitted Gaussian function was used to determine the FWHM. From the FWHM the energy resolution (%) of the ^{131}I energy spectrum was calculated using Equation 5.1.

$$R_E = \frac{FWHM}{E_0} \times 100\% \qquad 5.1$$

Where $R_E$is the energy resolution and E_0 is the peak energy, in this case 364 keV.

5.3.7.2 System spatial resolution

The measured and simulated images of the capillary tubes were imported into ImageJ and line profiles were drawn across them to obtain activity line spread functions (LSFs). A Gaussian function was then fitted to each of these LSFs. The FWHM and full width at tenth maximum (FWTM) were determined from the fitted Gaussian functions and were deemed to be representative of the system's spatial resolution.

5.2.7.3 System sensitivity

The measured and simulated images of the petri dish acquired at 10 cm distance from the detector of the gamma camera were used for the system sensitivity test. These images were imported into ImageJ and analysed. The system sensitivity was calculated using decay corrected count rate or counts per second (cps), obtained from the summed counts over the entire image and respective acquisition time, per activity as measured in the dose calibrator as indicated in Equation 5.2.

$$System\ Sensitivity\ \left(\frac{cps}{MBq}\right) = \frac{total\ counts\ in\ image}{time\ (s) \times activity\ (Bq)} \qquad 5.2$$

Where cps stands for counts per second.

5.2.7.4 Collimator septal penetration fraction

The measured and simulated images of the petri dish at the different distances from the collimator were imported into ImageJ. Circular ROI with diameters of 60% the diameter of the petri dish were drawn and centred over the activity region in the images. The decay-corrected count rate for each acquired image was determined using Equation 5.3.

$$R_i = C_i\, e^{(\frac{(T_i - T_{cal})}{T_{half}} ln2)} \times (\frac{ln2}{T_{half}})(1 - e^{(-\frac{T_{acqi}}{T_{half}} ln2)})^{-1} \qquad 5.3$$

Where R_i stands for decay-corrected count rate, C_i summed counts over the circular ROI in the i^{th} image, T_i is the start time of the i^{th} acquisition, $T_{acq,i}$ is the duration of the i^{th} acquisition, T_{cal} is the time of activity calibration and T_{half} is the half-life of the radionuclide respectively.

Using ImageJ, the decay-corrected count rates and the variable distances from the source to the collimator were fit to the function in Equation 5.4

$$R_i = c_0 + c_1 \exp(-c_2 D_N) \qquad 5.4$$

Where c_0, c_1, and c_2 are fitting parameters and D_i is the distance from the face of the collimator of the detector to the bottom of the petri dish. The collimator penetration fraction (PF) was computed at a distance D_N, where D_N = 10 cm, using Equation 5.5.

$$PF = \frac{C_1 e^{(-C_2 D_N)}}{C_0 + C_1 e^{(-C_2 D_N)}} \qquad 5.5$$

5.3 Results and discussion

5.3.1 Energy resolution

Figure 5.4 (A) and (B) show the ^{131}I intrinsic and extrinsic measured and simulated energy spectra respectively. These energy spectra were normalized to the maximum value obtained at 364 keV. Table 5.1 shows the corresponding results for both measured and simulated intrinsic and extrinsic energy resolutions for the radionuclide ^{131}I.

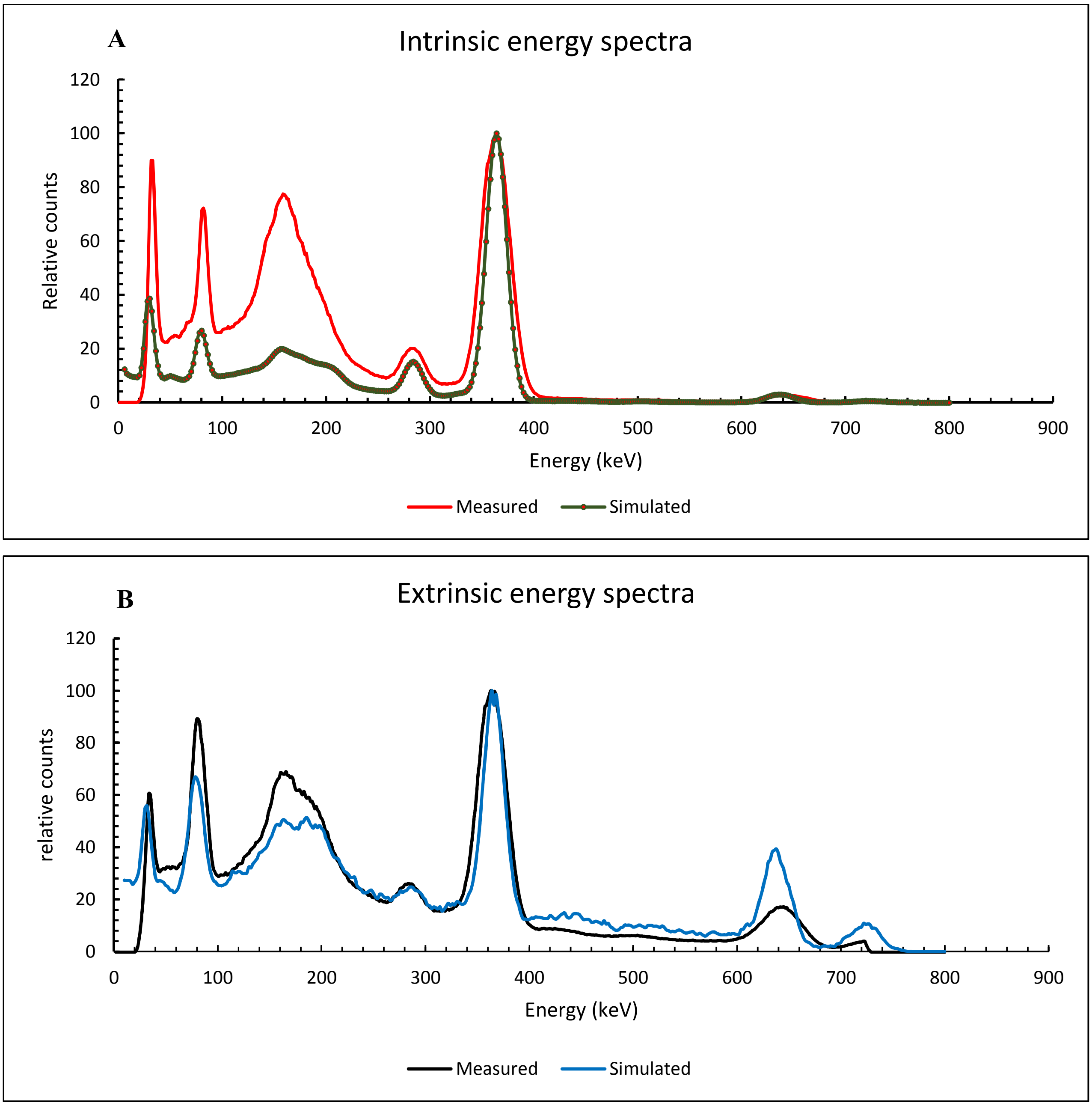

Figure 5. 4*: (A) Normalized ^{131}I intrinsic energy spectra and (B) Normalized ^{131}I extrinsic energy spectra.*

From the normalized measured and simulated intrinsic spectra the photopeaks of ^{131}I can be seen at 284 keV, 364 keV and 637 keV respectively. The measured energy spectra were cut-off for energies smaller than 20 keV. The cut-off for energies smaller than 20 keV attempts to eliminate electronic noise from the electronics of the gamma camera. A photopeak was visible at 28 keV that can be attributed to the interaction of the characteristic iodine K-shell x-rays in the sodium iodide crystal. Lead x-ray peaks were visible at 80 - 90 keV resulting from the photoelectric interaction of gamma rays with lead (shielding of the detector) and is evident in both the measured and simulated spectra.

For the intrinsic energy spectra it was clear that there was a difference in the energy resolution at 364 keV for the simulated and measured spectra (as can be seen in Table 5.1). The version of SIMIND (SIMIND v. 5) used in this study did not allow for the experimental energy resolution value obtained for the ^{131}I at the 364 keV photopeak to be used as input into the CHANGE program. The gamma camera energy response was modelled from an on-line convolution of the imparted energy from each photon history using an energy-dependent Gaussian function that varies with 1/√E (Ljungberg 1998) and this results in better energy resolution with an increase in photon energy. The reference point for the energy resolution was given as the percentage FWHM at 140 keV. Therefore photon energies above 140 keV have energy resolution values better than the reference point at 140 keV. Hence the narrower photopeaks obtained for the simulated energy spectra (extrinsic and intrinsic) at higher energies (364 keV, 637 keV and 723 keV) in comparison to the reference point at 140 keV resulting in an increased amplitude. This general approximation used by SIMIND is different from what was measured with the physical gamma camera. The physical gamma camera appears to have a more linear energy response.

Table 5. 1: Results for measured and simulated energy resolution

	Intrinsic		Extrinsic	
	Resolution (%)		Resolution (%)	
	Measured	Simulated	Measured	Simulated
	9.2	7.5	9.1	8.6
	9.5	7.6	9.3	8.8
	9.4	7.8	9.3	8.5
Mean ±SD	9.37 ± 0.15	7.63 ± 0.15	9.23 ± 0.12	8.63 ± 0.15
Absolute diff.	1.74		0.60	
Difference (%)	-18.57		-6.50	

From Figure 5.4 (A) it is clear that there are differences between the amplitudes of the measured and the simulated intrinsic energy spectra. For the energies below 364 keV the amplitudes of the simulated spectrum underestimated the measured spectrum. The underestimation of the simulated spectrum observed at energies below 364 keV can be attributed to the normalization of the energy spectra of ^{131}I at the 364 keV photopeak.

From the normalized measured and simulated extrinsic spectra the same photopeaks of ^{131}I can be seen and in addition the 723 keV photopeak is also visible. The higher energy photopeaks (637 and 723 keV) are more prominent on the extrinsic spectra due to a larger relative contribution because more of the lower (364 keV and below) energy photo peaks being absorbed by the collimator. The lead x-ray peaks visible at 80 - 90 keV are more prominent than on the intrinsic energy spectra due to the interactions in the lead collimator.

For the extrinsic energy spectra the difference in the energy resolution at 364 keV was smaller between the simulated and measured spectra (as can be seen in Table 5.1) when compared to the intrinsic spectra. It is also clear from the extrinsic spectra that the energy resolution for the high photototopeaks (637 and 723 keV) on the simulated spectrum are better than for the measured spectrum. This is also due to the modelling of the energy resolution in the SIMIND software as explained above.

In Figure 5.4 (B) the differences between the amplitudes of the measured and the simulated intrinsic energy spectra below 364 keV are less pronounced than for the intrinsic spectra. This is due to the fact that the measured and simulated energy resolutions were more comparable. The amplitude of the simulated high energy photopeaks however exceeded the measured value. This is due to the better energy resolution of the simulated spectrum. Consequently, the difference between the simulated and measured energy spectra, especially the intrinsic spectra, is largest at energies corresponding to interactions in the crystal and may not have a big influence on the quantitative data required from the 364 keV photopeak.

Therefore, with this observation of the difference in energy response between the physical and virtual gamma camera, the developer of SIMIND made it possible in version 6.1.2 of SIMIND to input the measured energy resolution into the CHANGE program thereby rendering the gamma camera energy response to be linear instead of using the Gaussian dependent function mentioned above, with the spectra at lower energies becoming better resolved. With this possibility, the measured and simulated energy resolution could be better matched with little or no difference between them. However, this version of SIMIND was released when this project had reached an advanced stage and the version 6 was not used since that will mean repeating the entire study in the light of time constraint.

5.3.2 System spatial resolution

Figure 5.5 (A) and (B) shows images of the measured and simulated capillary tubes in the vertical direction for the 364 keV photopeak obtained at a source-detector distance of 10 ± 0.5 cm with the detector fitted with a HEAP collimator. The corresponding profiles obtained for the measured and simulated images in the vertical direction are shown in Figure 5.6 (A) and (B). Table 5.2 shows the results for the system spatial resolution obtained from the Gaussian function fitted to the line spread function of the measured and simulated images in Figure 5.6.

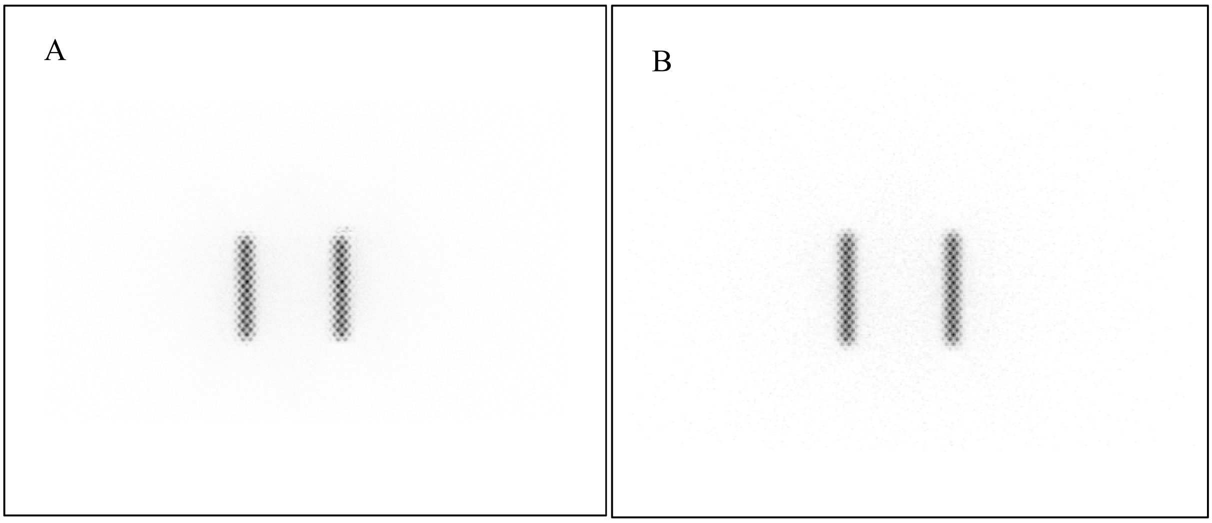

Figure 5. 5: ***Static images of (A) measured and (B) simulated capillary tubes in the vertical direction used to calculate the system spatial resolution of ^{131}I at 364 keV photopeak for a HEAP collimator.***

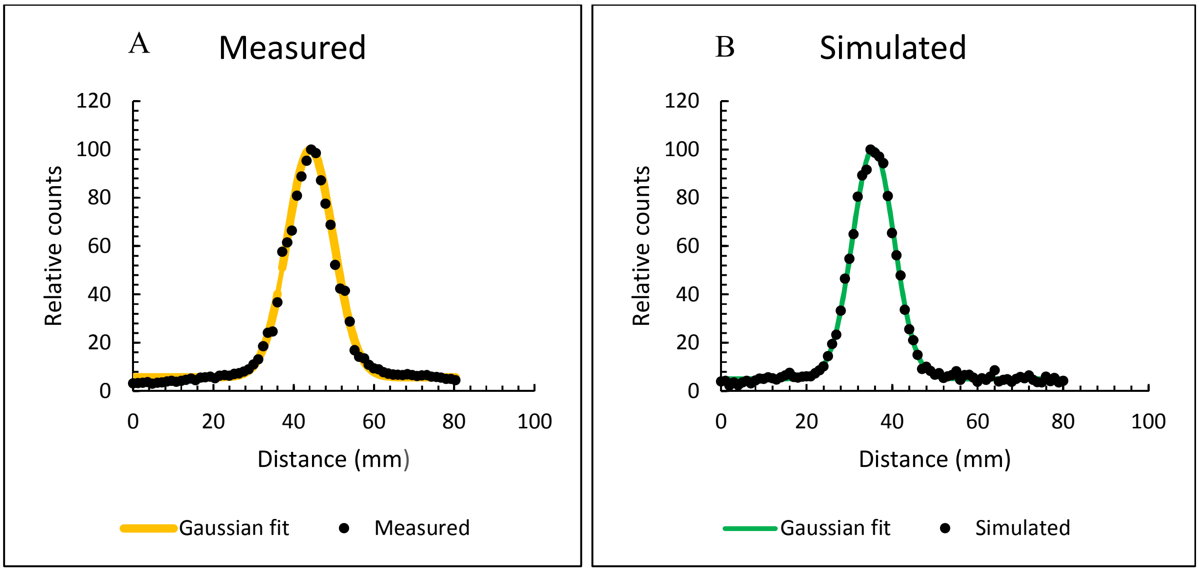

Figure 5. 6: ***Normalized line spread functions along the axial direction corresponding to the (A) measured and (B) simulated system spatial resolution acquired 10 cm from the HEAP collimator.***

Table 5. 2: Measured and simulated system spatial resolution (FWHM and FWTM) values for the 364 keV photopeak.

System spatial resolution	FWHM (mm)		FWTM (mm)	
	Measured	Simulated	Measured	Simulated
1	13.14	12.10	23.96	22.06
2	13.04	12.12	23.77	22.09
3	13.08	12.14	23.85	22.12
Mean ± SD	13.09 ± 0.05	12.12 ± 0.02	23.85 ± 0.10	22.09 ± 0.03
Absolute difference (mm)	0.97		1.76	
Percentage difference (%)	-7.41		-7.38	

Table 5.2 shows the results obtained from the Gaussian function fitted to the line spread functions obtained from the images in Figure 5.5. The calculated FWHM values were 13.09 ± 0.05 mm and 12.12 ± 0.02 mm for the experimental and simulated line spread functions respectively. These results indicated good agreement between the FWHM with a percentage

difference of -7.41 % and an absolute difference of 0.97 mm. These measured and simulated FWHM were in good agreement with the specification value (13.4 mm) given by the manufacturer of the gamma camera. The corresponding FWTM values for the line spread functions for the experimental and simulated system spatial resolution (23.85 ± 0.10 mm vs. 22.09 ± 0.03 mm) compare favourably with a percentage difference of -7.38 % and an absolute difference of 1.76 mm. These reported values were for the profiles drawn across the capillary tube in the vertical direction. The images of the capillary tubes acquired in the horizontal direction could not be used for spatial resolution analysis due to the construction of the HEAP collimator.

5.3.3 System sensitivity

Figure 5.7 shows the static images obtained for the measured and simulated petri dish uniformly filled with ^{131}I obtained in a 15% energy window over the 364 keV using a HEAP collimator. The Biodex Atomlab 500 dose calibrator used to measure the activity dispersed in the petri dish underestimated the ^{131}I activity measured by NMISA with 4.85 ± 0.22 %. This underestimation was incorporated into the calculation for system sensitivity. Table 5.3 shows the results of the measured (48.70 ± 0.30 cps/MBq) and simulated (47.97 ± 0.32 cps/MBq) system sensitivity respectively. The percentage difference (-1.50 %) and absolute difference (0.73 cps/MBq) showed good agreement between the measured and simulated system sensitivity values.

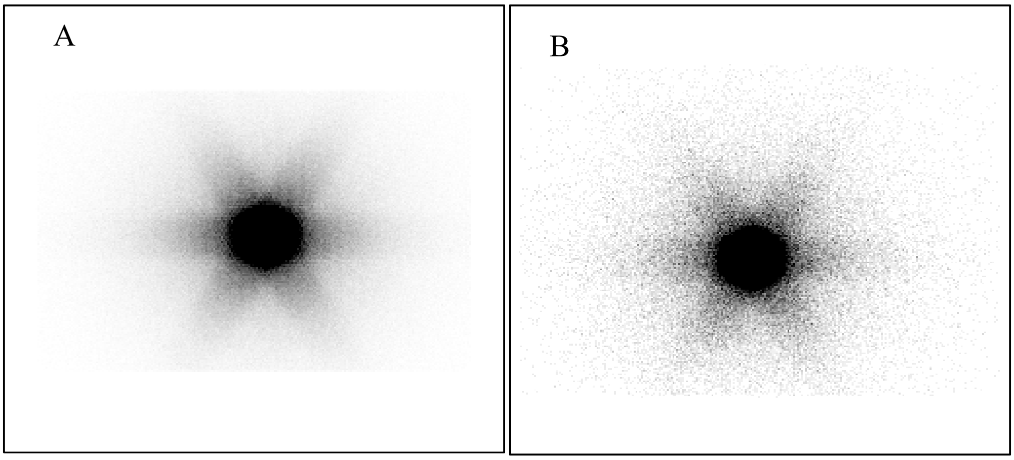

Figure 5.7: ***(A) Measured and (B) simulated system sensitivity images for 15 % window width over the 364 keV photopeak obtained using a petri dish with a HEAP collimator.***

Table 5. 3: Measured and simulated system sensitivity for the 364 keV photopeak.

System sensitivity	(cps/MBq) Measured	(cps/MBq) Simulated
1	49.0	48.1
2	48.4	48.2
3	48.7	47.6
Mean ± SD	48.7 ± 0.30	48.0 ± 0.32
Absolute difference	0.73	
Percentage difference (%)	-1.50	

The system sensitivity accounts for the number of photons recorded by the detector system for a given activity. The system sensitivity depends on the crystal thickness of the detector, type of collimator, radionuclide energy, energy window width settings and imaging geometry. Activity measurements play a vital role in the determination of the gamma camera sensitivity factor. And traceability to a secondary standard reduced the uncertainty in the activity inaccuracy of the dose calibrator used in this study. This was demonstrated from the good agreement found between the measured and simulated system sensitivity values obtained in the study (Table 5.3).

5.3.4 Collimator septal penetration fraction

The collimator septal penetration fraction was calculated using equation 5.5. Figure 5.8 is the scatter plot of the decay corrected count rate versus distance of the radioactive source from the face of the collimator. It also shows the exponential fit fitted to the scatter plot. Although the effect of collimator septal penetration is evident, nevertheless, we had confidence in using the simulation software in simulating our patient models since there is consistency in the results presented above for measured and simulated tests. The collimator septal penetration fraction was calculated as 3.8 % and 3.7 % for the measured and simulated for the HEAP collimator. These results deferred from each other by only 0.1 amounting to a percentage difference of -2.6 with SIMIND underestimating the penetration fraction. The collimator septal penetration fraction values for the HE collimator compare well with the value (3.5 %) quoted by the manufacturer of the gamma camera.

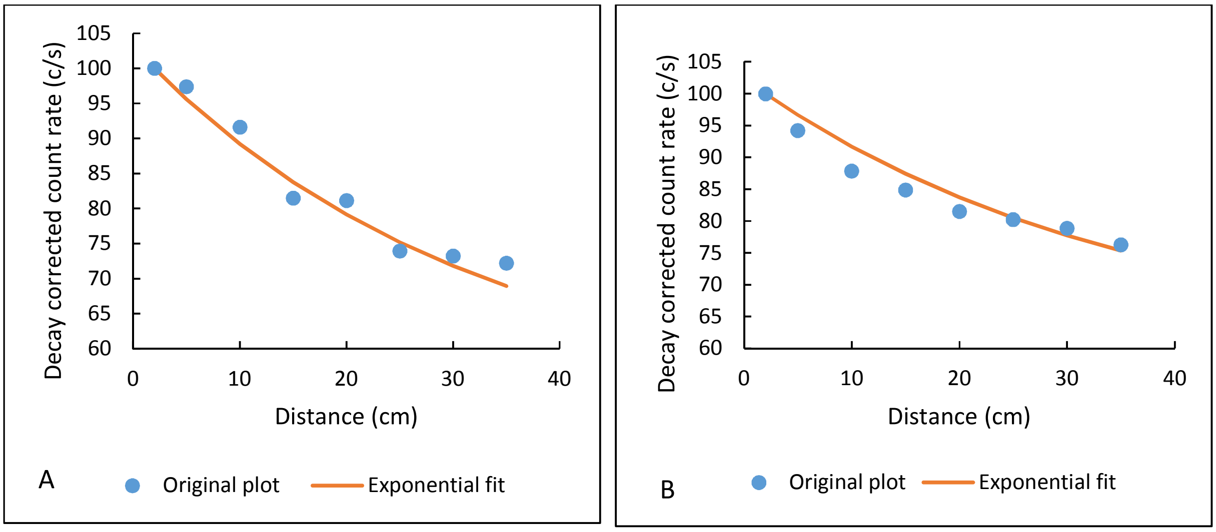

Figure 5.8: ***Scatter plot of decay corrected count rate versus distance with the exponential fit for (A) the measured data and (B) Simulated data respectively.***

5.4 Conclusion

Computer modelling is a powerful tool to assess the performance of nuclear medicine imaging devices. In this part of the study a simple model of the Siemens Symbia T dual-head SPECT/CT gamma camera was created with the MC program SIMIND. To validate the gamma camera model created by SIMIND the accuracy of the model was evaluated by comparing the data simulated with the gamma camera model to data acquired with the Siemens Symbia T dual-head SPECT/CT gamma camera. From the results of the data of the performance criteria tests it is evident that there is good agreement between the data simulated with SIMIND and that acquired with the Siemens Symbia T dual-head SPECT/CT gamma camera.

Although the measured and simulated energy spectra for the gamma camera compared well the small differences between the energy resolutions values suggested that the MC model of the gamma camera can still be improved upon. This can be done by obtaining an energy response function of the gamma camera from measured energy spectra data of different radionuclides with a range of photon energy values that include low as well as high energy values. This function can then be used for the simulation process instead of $\frac{1}{\sqrt{E}}$ energy relation function. The use of a measured energy response function will further improve the MC model of the gamma camera. This will assist scientist to optimize image acquisition and processing protocols for image quantification accuracy and dosimetry which is the focus of this study and will be address in the next two chapters of this study.

Similar validation results for SIMIND, for different gamma camera models and different radionuclides were reported by other researchers (Toossi et al. 2010; Rong et al. 2012; Gustafsson et al. 2015; Azarm et al. 2015; Vicente et al. 2017) and thus, SIMIND was also used by them for simulation of NM studies.

The validated virtual gamma camera created in this chapter was used to simulate clinically realistic ^{131}I 3-D patient-specific SPECT studies. The next chapter (chapter 6) deals with the simulation and quantification of these patients' images and that of a cylindrical phantom which was used to generate volume dependent recovery coefficients which were used as part of the quantification process.

5.5 References

Azarm, A., Islamian, J. P., Mahmoudian, B. and Gharepapagh, E. (2015) 'The Effect of Parallel-hole Collimator Material on Image and Functional Parameters in SPECT Imaging : A SIMIND Monte Carlo Study', *World J. Nucl. Med.*, 14, pp. 160–164.

Bostani, M., Mueller, J. W., McMillan, K., Cody, D. D., Cagnon, C. H., DeMarco, J. J. and McNitt-Gray, M. F. (2015) 'Accuracy of Monte Carlo simulations compared to in-vivo MDCT dosimetry', *Med. Phys.*, 42, pp. 1080–1086.

Dewaraja, Y. K., Ljungberg, M. and Koral, K. F. (2000) 'Characterization of Scatter and Penetration Using Monte Carlo Simulation in ^{131}I Imaging', *J. Nucl. Med.*, 41, pp. 123–131.

Ferreira, T. and Rasband, W. (2012) 'ImageJ User Guide', *Image J user Guide*.

Gustafsson, A., Ärlig, Å., Jacobsson, L., Ljungberg, M. and Wikkelsö, C. (2000) 'Dual-window scatter correction and energy window setting in cerebral blood flow SPECT : a Monte Carlo study', *Phys. Med. Biol.*, 45, pp. 3431–3440.

Gustafsson, J., Brolin, G., Cox, M., Ljungberg, M., Johansson, L. and Gleisner, K. S. (2015) 'Uncertainty propagation for SPECT/CT-based renal dosimetry in ^{177}Lu peptide receptor radionuclide therapy', *Phys. Med. Biol.* 60, pp. 8329–8346.

Karakatsanis, N., Sakellios, N., Tsantilas, N. X., Dikaios, N., Tsoumpas, C., Lazaro, D., Loudos, G., Schmdtlein, C. R., Louizi, K., Valais, J., Nikolopoulos, D., Malamitsi, J., Kandarakis, J. and Nikita, K. (2006) 'Comparative evaluation of two commercial PET scanners, ECAT

EXACT HR + and Biograph 2, using GATE', *Nuclear Inst. Methods Phys. Research, A*, 569, pp. 368–372.

Lazaro, D., Buvat, I., Loudos, G., Strul, D., Santin, G., Giokaris, N., Donnarieix, D., Maigne, L., Spanoudaki, V., Styliaris, S., Staelens, S. and Breton, V. (2004) 'Validation of the GATE Monte Carlo simulation platform for modelling a CsI(Tl) scintillation camera dedicated to small-animal imaging', *Phys. Med. Biol.*, 49, pp. 271–285.

Ljungberg, M. (1998) 'The SIMIND Monte Carlo Program', in Ljungberg, M., Strands, S.-E., and King, M. A. (eds) *Monte Carlo Calculations in Nuclear Medicine Applications in diagnostics Imaging.* 2nd edn. Florida: Francis & Taylor, pp. 111–128.

Ljungberg, M. (2017) 'The SIMIND Monte Carlo program version 6.0', *SIMIND Manual version 6*, pp. 1–54.

Ljungberg, M. (2018) 'Absolute Quantitation of SPECT Studies', *Semin. Nucl. Med.* 48, pp. 348–358.

Ljungberg, M. and Strand, S. E. (1989) 'A Monte Carlo program for the simulation of scintillation camera characteristics', *Comp. Methods Prog. Biomed.*, 29, pp. 257–272.

Min, B. J., Choi, Y., Lee, N-Y., Lee, K., Ahn, Y. B. and Joung, J. (2009) 'Design consideration of a multi-pinhole collimator with septa for ultra high-resolution silicon drift detector modules', *Nuclear Inst. Methods Phys. Res. A.*, 606, pp. 755–761.

Momennezhad, M., Sadeghi, R. and Naseri, S. (2012) 'Development of GATE Monte Carlo simulation for a dual-head gamma camera', *Radiol. Phys. Technol.*, 5, pp. 222–228.

National Electrical Manufacturers Association (2013) *NEMA Standards Publication NU 1-2012 Performance Measurements of Gamma Cameras*. Virginia.

Rong, X., Du, Y., Ljungberg, M., Rault, E., Vandenberghe, S. and Frey, E. (2012) 'Development and evaluation of an improved quantitative ^{90}Y bremsstrahlung SPECT method', *Med. Phys.*, 39, pp. 2346–2358.

Schindelin, J., Arganda-carreras, I., Frise, E., Kaynig, V., Longair, M., Pietzsch, T., Preibisch, S., Rueden, C., Saalfeld, S., Schmid, B., Tinevez, J-y., White, D, J., Hartenstein, V., Eliceiri, K., Tomancak, P. and Cardona, A. (2012) 'Fiji : an open-source platform for biological-image analysis', *Nature Methods*, 9(7), pp. 676–682.

Schmidtlein, C. R., Kirov, A. S., Nehmeh, S. A., Erdi, Y. E., Humm, J. L., Amois, H. I., Bidaut, L. M., Ganin, A., Steams, C. W., McDaniel, D. L. and Hamacher, K. A. (2006) ‘Validation of GATE Monte Carlo simulations of the GE Advance/Discovery LS PET scanners’, *Med. Phys.*, 33, pp. 198–208.

Siemens, A. G. (2010) ‘Symbia S and T System Specifications’. Erlangen Germany, pp. 1–12. Available at: www.siemens.com/healthcare. Last accessed on 23rd December 2016.

Strydhorst, J., Carlier, T., Diedonné, A., Conti, M. and Buvat, I. (2016) ‘A gate evaluation of the sources of error in quantitative ^{90}Y PET.’, *Med. Phys.*, 43, pp. 5320–5329.

Toossi, B. M. T., Islamian, P., Momennezhad, M., Ljungberg, M. and Naseri, S. H. (2010) ‘SIMIND Monte Carlo simulation of a single photon emission CT’, *J. Med. Phys.*, 35, pp. 42–47.

Vicente, E. M., Lodge, M. A., Rowe, S. P., Wahl, R. L. Frey, E. C. (2017) ‘Simplifying volumes-of-interest (VOIs) definition in quantitative SPECT : Beyond manual definition of 3D whole-organ VOIs’, *Med. Phys.*, 44, pp. 1707–1717.

Yushkevich, P. A., Piven, J., Hazlett, H. C., Smith, R. G., Ho, S., Gee, J. C. and Gerig, G. (2006) ‘User-guided 3D active contour segmentation of anatomical structures: Significantly improved efficiency and reliability’, *NeuroImage*, 31, pp. 1116–1128.

CHAPTER SIX: Quantification Accuracy of I-131 (in Simulated Water Phantom and 3-D Patient-specific Models)

Table of Contents

6.1 Introduction

Carrying out patient-related research in nuclear medicine (NM) comes with the ethical challenges of radiation exposure to research subjects and researchers. Computer-based simulations enable the researcher to overcome these challenges since simulations can be performed that reflect clinical situations, without exposing subjects or researchers to radiation. In this study, the simulating medical imaging nuclear detectors (SIMIND) Monte Carlo (MC) simulation code was used to simulate single photon emission computed tomography (SPECT) phantom and patient images. SIMIND was validated for a Siemens Symbia T2 dual head SPECT/CT gamma camera for ^{131}I studies in chapter 5 and good agreement was found between measured and simulated data for the gamma camera (Ejeh, van Staden and du Raan, 2019).

It is very important in NM to accurately quantify radioactivity distributions in organs and tumours as mentioned in chapter 3. This is a requirement for targeted radionuclide therapy dosimetry (Frey, Humm and Ljungberg, 2012). Presently, treatment planning for individual patients, in radionuclide therapy, is getting more and more advanced but a number of factors as discussed in chapter 3 still pose a challenge. The physical and technical nature of the acquisition procedure linked with patient- related factors contribute to the challenge of accurate quantification, which will influence proper dosimetry. Unless these phenomena are corrected for, accurate quantification remains a major drawback in the process of dosimetry. Specific challenges in imaging ^{131}I include collimator septal scatter and penetration as well as down scatter of photons of higher energies (637 and 723 keV) into the lower photopeak energy window (15 % at 364 keV). Septal scatter and penetrations as well as photon down scatter results in blurring effects which lead to difficulty in accurate quantification of ^{131}I distributions. The decay scheme of ^{131}I is shown in Appendix I.

Work carried out in this field with ^{131}I was mostly based on analytical phantom measurements/simulations (Dewaraja *et al.*, 2012; Dewaraja *et al.*, 2013). Iodine-131 voxel model-based quantification studies performed by Dewaraja and co-workers (Dewaraja, Ljungberg and Koral, 2001; Dewaraja, Ljungberg and Fessier, 2006) employed the Zubal voxel-man phantom (Zubal *et al.*, 1994). This is a single phantom which is used to represent a whole population of patients.

The aim of this chapter, therefore, (i) to create clinically realistic patient SPECT simulation studies from patient CT images and (ii) to assess the accuracy of ^{131}I in SPECT studies in simulated water and voxel-based three-dimensional (3-D) patient-specific SPECT models. A wide range of retrospective patient studies reflecting different habitus were included in the study. The quantification accuracy of ^{131}I will be investigated for different sphere sizes located in varying positional geometries in the patient models. The results of these variations will be expressed in terms of activity (MBq) and percentage differences from the true or expected activity. Differences between the true and the measured activities will be determined to obtain the quantification accuracy for SPECT imaging.

6.2 Materials and methods

6.2.1 Generation of the voxelized models

The evaluation of the quantification accuracy was carried out using digital models created from computed tomography (CT) images of a water-filled cylindrical phantom (the Carlson phantom (Dondi *et al.*, 2009; Sadremomtaz and Taherparvar, 2013)) and a wide range of retrospective patients who underwent NM and CT examinations. Spheres of different sizes were simulated as inserts in the cylindrical and patient models to mimic tumours. SIMIND MC software was used to simulate all water-filled cylinder and patient projection images, as explained previously, on a Lenovo Laptop with Intel® Core (™) i3-4030U CPU, which runs on a 64-bit operating system, x64 based processor, with Microsoft Windows 8.1. The installed memory (RAM) of this PC is 6 GB and a processing speed of 1.90GHz.

The Siemens Symbia T2 dual head SPECT/CT gamma camera with 3/8 inch NaI (Tl) detectors fitted with high energy All Purpose (HEAP) collimators was modelled using SIMIND as explained in chapter 5. As mentioned above, CT images of the water-filled cylinder and pre-selected patient studies were used to create voxel-based 3-D models which were used as input to SIMIND. The voxel-based models based on CT data were created as follows:

6.2.1.1 Cylinder model with spherical inserts

CT images of a water-filled Carlson phantom (Dondi *et al.*, 2009; Sadremomtaz and Taherparvar, 2013) without inserts were acquired with the Siemens Symbia T2 dual head SPECT/CT gamma camera. The CT scan was acquired with 130 kVp, 30 mAs and a slice thickness of 0.5 cm (Figure 6.1). These CT images were reconstructed using a smooth reconstruction kernel (B08s; Siemens Medical Solution, Germany). The reconstructed CT images (with pixel size of 1.27 × 1.27 cm^2) were segmented using ITK SNAP software (Yushkevich *et* *al.*, 2006). During the segmentation process, each segmented region of the model was assigned a unique value thereby generating a source distribution map (Figure 6.2A). Spheres with diameters of 3.0, 4.0, 4.5, 5.0, 5.5, 6.0, and 7.0 cm were also incorporated into the voxelized model during the segmentation process. These spheres will be referred to as T3, T4, T4.5, T5, T5.5, T6, and T7 respectively. The information from the segmentation process was used to create a text file, containing indexes for the segmented regions as well as radioactive concentrations assigned to these regions.

A density map of the voxelized model (Figure 6.2B) was created with in-house Visual Basic software (DensityMaps). This software converts CT Hounsfield numbers to density values based on the bi-linear conversion model (Blankespoor *et al.*, 1996) by using the results of measurements carried out with the Gammex RMI-465 phantom (Edyvean and Weston, 2007). The aforementioned source map, density map, and text file were used as the phantom design input into the MC program.

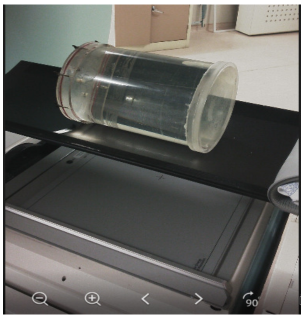

Figure 6. 1: ***Carlson Phantom filled with water positioned on the gamma camera bed.***

Figure 6. 2: ***Segmented (A) source map and (B) density map of the water-filled Carlson phantom***.

6.2.1.2 Patient-specific 3-D models with spherical inserts

Evaluation of the accuracy of ^{131}I activity quantification for different sphere sizes in patients' clinical studies was based on simulated patient-specific 3-D models. These computer models were created from retrospectively selected CT images of diagnostic ^{131}I patient studies. Ethical approval for the selection of retrospective patient data for this study was obtained from the Health Sciences Research Ethics Committee of the University of Free State and the Free State Department of Health. Table 6.1 details the demographic data of the pre-selected patients for the 3-D models. Tumours were mimicked using spherical inserts in the lungs and liver of the created models. Patient datasets that included less than 80 % of the liver in the CT images were excluded from the study. A large liver area was prerequisite in order to accommodate the larger spheres

CT data of the various patients were obtained according to clinical protocols and reconstructed as mentioned in section 6.2.1.1 above. The liver, lungs and remaining tissue in the CT slices were segmented with ITK SNAP. In the initial phase, a single patient study was randomly selected to study the quantification accuracy for different sphere sizes of 3.0, 4.5, 5.0, 6.0, and 7.0 cm in diameter referred to as T3, T4.5, T5, T6, and T7. Two spheres were positioned at a time in the segmented patient model, one in the lungs and one in the liver with source activity of 92.5 MBq in each sphere. Density and source maps were created for each set of spheres in the liver and lungs, as described above, with tumour to background activity concentration ratio of 5:1 for input to SIMIND. A total of five density and source map combinations (study groups) with spheres positioned as indicated in Table 6.1 were created.

Table 6.1: Density and source maps created for the initial phase of the patient quantification accuracy study

Study group	Sphere diameter in the liver	Sphere diameter in the left lung
1	3.0 cm	3.0 cm
2	4.5 cm	4.5 cm
3	5.0 cm	5.0 cm
4	6.0 cm	6.0 cm
5	7.0 cm	7.0 cm

Figure 6.3 (a – d) show samples of the created density and source maps for the initial test patient model.

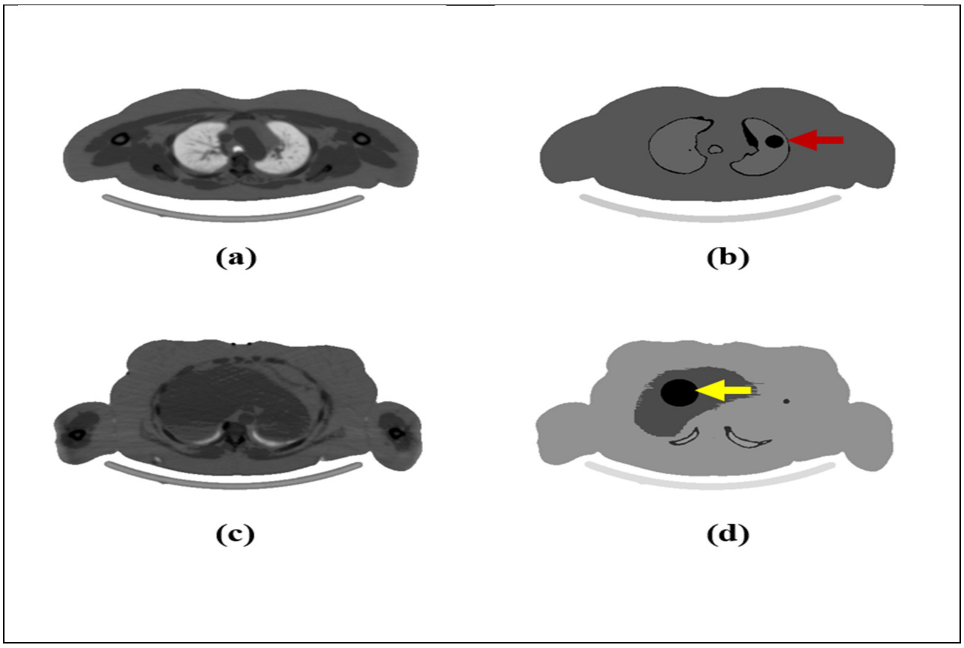

Figure 6.3: ***Transaxial slices through the voxel-based patient model showing the superimposed tumours. Density maps of the patient model showing (a) the lungs and (c) the liver. Source maps of the patient phantom with 3.0 cm and 6.0 cm spheres inserted in one of the (b) lungs (red arrow) and (d) the liver (yellow arrow).***

Subsequently, for the follow-up phase of the study 18 additional patients' density and source maps were created from the previously routinely acquired CT data. Body mass index values for these patients were not available, therefore, in order to classify the patients according to body habitus, the anteroposterior and transverse cross-sectional measurements on axial CT images (Kalra *et al.*, 2003; Kleinman *et al.*, 2010) at the upper abdomen level of the patients were used (Table 6.2).

Table 6.2: Demographic data for selected patients for the study.

Patient	**Age** (years)	**Sex**	**Anteroposterior (AP) dimension*** (cm)	**Transverse (T) dimension*** (cm)	**AP x T**** (cm^2)
1	59	F	30	19	570
2	46	F	30	20	600
3	73	F	32	22	704
4	40	F	33	22	726
5	51	F	31	24	744
6	56	M	35	22	770
7	43	F	35	22	770
8	66	M	34	23	782
9	65	M	35	23	805
10	50	F	35	23	805
11	50	F	35	23	805
12	39	F	35	24	840
13	40	F	34	27	918
14	61	F	33	28	924
15	38	F	39	24	936
16	55	F	35	27	945
17	22	F	34	29	986
18	57	F	36	28	1008
Mean ± SD	51 ± 12	M:F = 1:5	34 ± 2	24 ± 3	813 ± 123

**Anteroposterior (AP) and transverse (T) dimensions were measured on the CT data just above the liver.*

***AP x T = area obtained by multiplying anteroposterior and transverse dimensions.*

F = female; M = male; M: F = male to female ratio; SD = standard deviation

For these patient studies, only two spheres, T3 and T6 were included. This simulation study is similar to Dewaraja et al; who used sphere sizes of 2.9 cm and 5.8 cm (Dewaraja, Ljungberg and Fessier, 2006) and injected activity values of 74 MBq or 80 MBq (Willegaignon *et al.*, 2016). These two spheres (T3 and T6) were inserted alternately in the source maps in the lung and liver of the digitally created patient models to emulate tumours. Source and density maps along with the spherical tumours were used to mimic typical clinical situations of a neuroendocrine tumour in the liver and DTC metastatic tumour in the lung.

Two scenarios of the patient models with emulated tumours were created. **Scenario 1** was the setup of the simulated patient models whereby the 3.0 cm tumour (T3) was embedded in the left lung while the 6.0 cm tumour (T6) was simultaneously embedded in the liver. For **scenario 2**, T6 was inserted in the right lung while T3 was embedded in the liver.

Figure 6.4 shows some of the digitally created 3-D patient models that formed part of the follow-up phase for the patient model study.

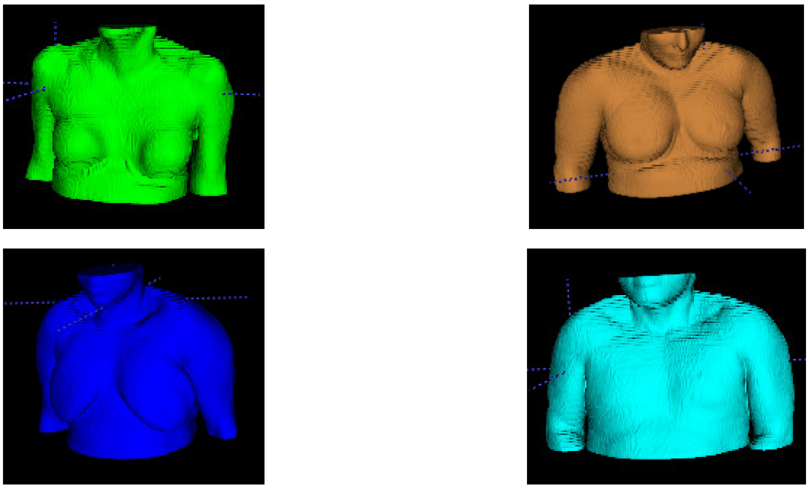

Figure 6. 4: ***Samples of voxel-based images of a selection of the digital 3-D patient models used in the follow up patient study***.

6.2.2 Simulation with SIMIND

6.2.2.1 Simulation of spheres in the water phantom

All SPECT studies were done by MC simulation using SIMIND with density and source distribution maps serving as input to SIMIND as explained above. Spheres of different sizes as mentioned in section 6.2.1.1 were simulated in the cylindrical model. All spheres were simulated with 92.5 MBq without background activity in the surrounding water. The spheres were also simulated with background activity in the surrounding water with a sphere to background ratio of 5:1 to reflect clinical scenarios with ^{131}I imaging (Dewaraja, Ljungberg and Koral, 2001).

The simulations were set to simulate 2 × 10^8 (photons/projection) histories. All the SPECT studies were simulated using the Siemens Symbia dual head SPECT/CT gamma camera with HELP collimators. For each tomographic scan, 64 projections were acquired with non-circular orbit using a 128 × 128 matrix (pixel size of 0.48 cm) and three (15 % width)) energy windows: 364 keV photopeak window (336.7 – 391.2 keV), lower scatter window (283.8 – 336.7 keV) and upper scatter window (391.2 – 445.9 keV). These parameters were chosen to reflect a typical clinical protocol (Dewaraja *et al.*, 2013) and were used as standard protocol throughout this study. Detailed simulation parameters are given in Appendix II.

6.2.2.2 Simulation of 3-D patient-specific models

Patient model SPECT images were simulated using the same simulation parameters and clinical protocol as those of the water cylinder simulations. After simulation, binary image files were converted to DICOM format using (X)-MedCon (Nolf, 2003). In-house Visual Basic developed software (DICOMHeader), was used to attach a relevant header file acquired on the physical gamma camera to the simulated SPECT projection images. The information contained in the DICOM header file was required by the reconstruction software.

Initial patient model study

Similar to the water cylinder study, the patient model was simulated with two different activity distributions. The activity-filled spheres were placed in the lungs and liver of the patient and the study was simulated (i) without and (ii) with background activity in the surrounding tissue and organs. During the second study, the sphere to background concentration ratio (5:1) was selected to reflect a clinical scenario with ^{131}I (Dewaraja *et al.*, 2013). Note that SIMIND uses the volume of an organ to calculate the activity allocated to it using the concentration ratio above. The patient's segmented source and density maps (Figure 6.3) were used by SIMIND to create simulated SPECT projection images (Figure 6.5) mimicking the clinical ^{131}I protocol mentioned above.

Follow up patient models study

On completion of the initial patient model study, simulations were repeated for 18 additional 3-D patient-specific models. This was done in order to evaluate the quantification accuracy in a range of patient models with different body habitus. Figure 6.5 shows the anterior and posterior projections of a simulated patient model.

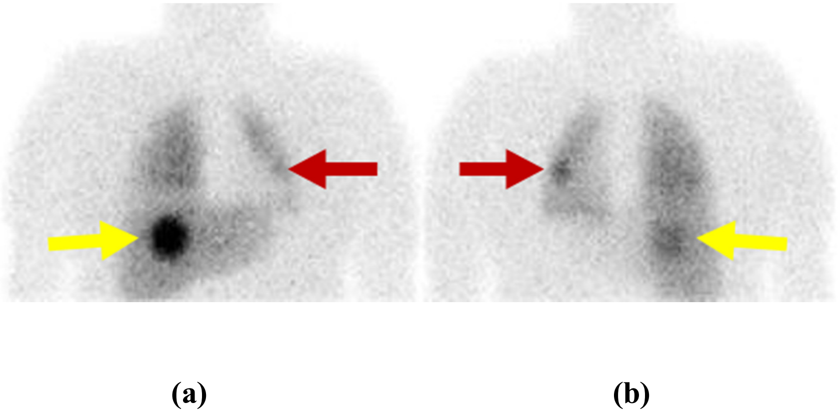

Figure 6. 5: ***An (a) anterior and (b) posterior projection of the simulated patient model study mimicking the 3.0 cm spherical tumour (red arrow) in the left lung and the 6.0 cm spherical tumour (yellow arrow) in the liver (an example of scenario 1).***

6.2.3 Reconstruction of simulated images

The SPECT projection images of the simulated spheres (Section 6.2.2.1) in the water-filled cylindrical phantom and patient studies were reconstructed using an iterative 3-D reconstruction software program incorporated in the dosimetry software package LundADose, version 2.7.3. The software program includes corrections for attenuation, based on bi-linear extrapolation of energy from values of the automatically registered SPECT/CT image (Ljungberg and Gleisner, 2016). It also includes scatter compensation by convolving the current image estimate with the Effective Source Scatter Estimation (ESSE) scatter kernels and incorporating it into the reconstruction, as well as a full 3-D collimator-detector response correction (Frey and Tsui, 1996; Yue *et al.*, 2016).

Iterative reconstruction of the images was carried out using six iterations and eight subsets without applying any post-reconstruction filters.

6.2.4 Absolute quantification of activity in spheres

To quantify radioactive count distribution accurately in terms of activity it is necessary to recover count loss due to the inherent limitations of the gamma camera and imaging process. Absolute quantification as discussed in chapters 1 and 3, is a method by which the reconstructed counts in a voxel are converted to absolute activity concentration in the volume of interest. In addition to applying the quantitative corrections as described in sections 3.4 and 6.2.3, absolute quantification also requires a camera calibration factor (CF) as mentioned in section 1.5. Instead of using a planar source in air to determine the CF a more robust method was used in this study to obtain a CF for the SPECT studies. To determine the SPECT CF, the simulated projection images of the 7.0 cm diameter sphere in the water-filled cylindrical phantom was used to calculate a SPECT CF.

The projection images of the sphere in the water-filled cylindrical phantom were reconstructed using the same parameters used for the simulated patient studies. The reconstructed counts in the sphere volume were divided by the activity in the sphere to obtain counts per activity, i.e. the SPECT CF. This method of determining the SPECT CF is superior to the in-air planar method because it partially compensates for inaccuracies in the attenuation and scatter corrections.

6.2.5 Data analysis

Reconstructed SPECT images were analysed with AMIDE by means of a volumetric analysis tool (Loening and Gambhir, 2003). For each sphere inside the cylindrical water and patient models, a spherical volume of interest (VOI) (generated with a fixed diameter) were drawn on the reconstructed SPECT images to match the geometric size of the simulated sphere. The physical size of the spheres was used to obtain the VOI in order to limit the inclusion of background activity when drawing the VOI larger than the physical size of the sphere. The total number of reconstructed counts was obtained from the product of the mean counts per voxel and the number of voxels in the spherical VOI. In order to minimise the uncertainty in the positioning of the VOI centrally over the spheres, each VOI was manually shifted by one voxel in negative and positive x, y and z-direction (Zeintl *et al.*, 2010) and the maximum counts of these different locations were noted and used to calculate the reconstructed counts.

The counts were converted to activity (MBq) by applying a calibration factor, CF for the SPECT/CT gamma camera as explained in section 6.2.4. The CF was calculated using equation 6.1.

$$CF = \frac{C_m/s}{A_{true}} \qquad 6.1$$

Where C_m was the maximum measured counts obtained from shifting the VOI as described above, s is the time used for the acquisition of the image in seconds and A_{true} represents the true simulated activity value in the sphere. The recovered activity (A_{rec}) was then calculated using equation 6.2.

$$A_{rec} = \frac{(counts\ per\ voxel) \times (number\ of\ voxels)}{CF} \qquad 6.2$$

The RC was calculated to correct the activity in the spheres that are affected by the partial volume effect (PVE) using equation 6.3.

$$RC = \frac{A_{rec}}{A_{true}} \qquad 6.3$$

Where A_{rec} the recovered activity is calculated from equation 6.2 and A_{true} is the true activity in the simulated sphere. Recovery curves of the RCs (which was calculated for the different sized spheres in the water phantom) were generated for simulations without and with background activity using equation 6.4 (Willowson, Bailey and Baldock, 2008).

$$RC = 1 - a * e^{-b*D} \qquad 6.4$$

With ***a, b*** as fitting parameters, ***D*** the diameter of the sphere in cm and ***RC*** the recovery coefficient.

6.3 Results and discussion

6.3.1 Spheres in the water phantom

The CF obtained from the sphere (7.0 cm diameter) in the water-filled cylindrical phantom (as discussed in section 6.2.4) calculated from equation 6.1 was 37.4 cps/MBq. This CF was used for absolute activity calculation by applying equation 6.2. Recovered activity from the various size spheres were compared to the true activity in each sphere by calculating the percentage difference (Sichani *et al.*, 2014)). Table 6.3 shows the results for recovered activity (A_{rec}) calculated as well as the RCs for the different sphere sizes. The percentage difference between the true (A_{true}) and recovered activity is also reported. Results are given for the datasets simulated without and with background activity. The VOI size refers to the size of the volume of interest drawn in AMIDE using the volumetric analysis tool in cm^3.

Table 6.3: Recovered activity (A_{rec}), true activity (A_{true}) and emission recovery coefficients for the different sized spheres simulated.

		Without background activity				With background activity			
Sphere	VOI (cm^3)	A_{true} (MBq)	A_{rec} (MBq)	%-diff	RC	A_{true} (MBq)	A_{rec} (MBq)	%-diff	RC
T3	27.0	92.5	83.7	-9.5	0.91	108.0	100.8	-6.6	0.93
T4	64.0	92.5	86.7	-6.2	0.94	4.7	4.5	-3.9	0.96
T4.5	91.1	92.5	87.7	-5.2	0.95	7.2	7.1	-1.6	0.98
T5	125.0	92.5	88.5	-4.4	0.96	9.2	9.1	-1.5	0.99
T5.5	166.4	92.5	89.9	-2.8	0.97	13.1	13.0	-0.9	0.99
T6	216.0	92.5	90.1	-2.6	0.97	16.6	16.5	-0.6	0.99
T7	343.0	92.5	92.5	0.0	1.00	25.7	25.8	0.4	1.00
Mean ± SD of the % diff				-4.4 ± 3.0				-2.1 ± 2.4	

Key: D = diameter, A_{true} = true activity, A_{rec} = recovered activity, % diff = percentage difference, RC = Recovery coefficient, SD = Standard deviation

Table 6.3 shows that the percentage difference between the true activity and the recovered activity is ≤ 10% for all the sphere sizes in the water-filled Carlson phantom. Mean % differences of -4.4 ± 3.0 % and -2.1 ± 2.4 % were obtained for quantification results without and with background activity respectively. The quantification for the different size spheres shows good agreement between the recovered activity and the true activity.

The RC results are shown graphically in Figure 6.6. The calculated RC's are shown as a function of the sphere diameter simulated without (red) and with (black) background activity in the surrounding water. The graphs provide information of the P VE relative to reconstructed spherical objects with different diameters.

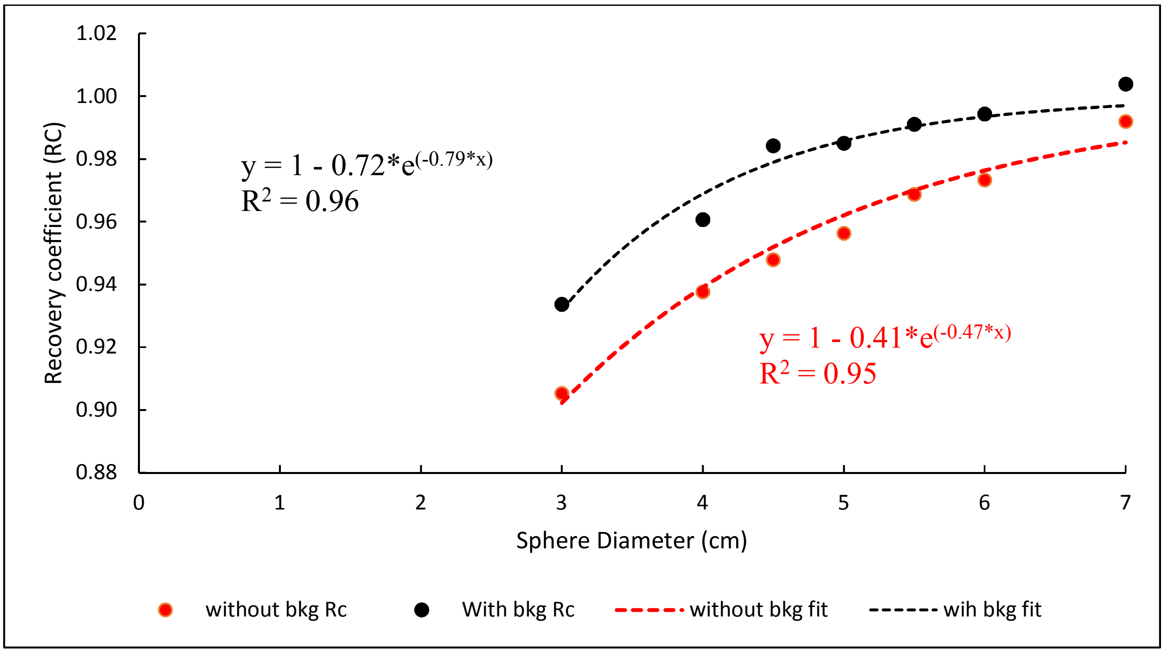

Figure 6. 6: ***Recovery coefficient versus sphere diameter for without (red) and with (black) background (bkg) activity.***

In Figure 6.6 the loss of emission recovery due to spill out at the object boundaries is shown for the different sphere sizes used. The values are derived from simulations when a no background activity was used as well as when a target-to-background ratio of 5:1 was simulated. If an imaged object is smaller than approximately 2 × FWHM of the system, the regional maximum counts per pixel in the resulting image will no longer represent a linear relationship with the radionuclide concentration at that location. Objects smaller than the resolution volume will have all their counts detected but over a larger volume. The counts will be ‘spread out’ thus the recorded concentration of activity will be lower than the actual concentration. The ratio of these concentrations is the RC. The RC reported in Table 6.3 and shown in Figure 6.6 varied between 0.91 and 1.00. From the results, it is evident that the influence of the PVE is less for the larger spheres and more prominent for the smaller spheres. These results obtained for RCs are in good agreement with the literature (Zeintl *et al.*, 2010). For the smallest sphere of 3.0 cm diameter, the PVE had only a 9 % influence on the accuracy of the quantification results. This is due to the SPECT spatial resolution of the gamma camera system being simulated as 1.2 cm (see chapter 5).

The RCs for the spheres simulated with background activity were slightly higher than the ones without background activity as shown in Figure 6.6. The difference in RCs without and with background activity can be explained by the fact that, the spill-in from the background activity of the water cylinder to the spheres partially compensates for spill-out from the spheres to the background activity of the water cylinder. The results of the RCs showed that both spill-out and spill-in effects increase with decreasing object size. This underscores the need to produce different RC curves for the different target to background activity concentration ratios in clinical practice.

6.3.2 Three-dimensional patient-specific models with spherical inserts

The activity concentration used in the spherical inserts in all patient models (for the initial as well as follow-up patient model studies) was the same and the activities obtained were quantified after correcting for the physical processes of attenuation, scatter and depth-dependent collimator response and partial volume effect. The CF from sphere T7 simulated in the water cylinder was used to convert image counts to activity. Partial volume corrections (PVC) were applied to the spherical inserts by applying the appropriate RCs obtained in section 6.3.1.

6.3.2.1 Initial patient model study

The quantified activity values obtained for the different size spheres in the lung and liver after applying attenuation, scatter and PVE corrections are summarised in Tables 6.4 and 6.5. Table 6.4 shows the results for quantification of the spheres placed in the lungs (without and with background activity). Similarly, the results for the quantification of the sphere inserted in the liver is shown in Table 6.5. The tables include the results for the initial patient model study without and with background activity. The true activity (A_{true}), calculated (recovered) activity (A_{rec}), as well as the percentage difference, are shown.

Table 6.4: Quantified activity values for the different sized spheres in the lungs of the initial patient model.

	Without Background activity			With Background activity		
Sphere	A_{true} (MBq)	A_{rec} (MBq)	%-diff	A_{true} (MBq)	A_{rec} (MBq)	%-diff
T3	92.5	97.8	5.8	13.7	14.3	4.2
T4.5	657.5	599.6	-8.8	49.0	48.4	-1.2
T5	885.0	826.7	-6.6	66.0	65.7	-0.5
T6	1525.0	1456.2	-4.5	114.8	114.0	-0.7
T7	2435.0	2279.6	-6.4	185.8	185.6	-0.1
Mean ± SD of % diff			-4.1 ± 5.1			0.3 ± 2.0

Key: A_{true} = true activity, A_{rec} = recovered activity, % diff = percentage difference, SD = Standard deviation

From Table 6.4 it is shown that the activity values in all the different sphere sizes located in the lungs were underestimated except for the T3 size. The maximum percentage difference was an 8.8 % underestimation for T4.5 without background activity. The underestimation of the activity in the spherical inserts in the lung, even for larger spheres, could be related to model-based scatter correction (ESSE) applied during the iterative reconstruction process. As explained in chapter 3 section 3.4.2 this scatter correction makes use of pre-calculated scatter kernels for the relevant radionuclide that is to be modelled in the SPECT projection. These scatter kernels were obtained from MC simulations in water phantoms. The scatter contribution from water is more than for lung tissue and therefore an overestimation of the scatter from the simulation in water cause an underestimation of the activity in the larger spheres. Overall, the quantification results showed differences of less than ± 10 % which is an acceptable quantification accuracy for ^{131}I.

Table 6.5: Quantified activity values for different sized spheres positioned in the liver of the initial patient model.

Without Background activity				With background activity		
Sphere	A_{true} (MBq)	A_{rec} (MBq)	%-diff	A_{true} (MBq)	A_{rec} (MBq)	%-diff
T3	92.5	102.7	11.1	13.7	14.3	4.6
T4.5	657.5	684.8	4.2	49.0	50.0	2.1
T5	885.0	913.3	3.2	66.0	71.6	8.5
T6	1535.0	1613.6	5.1	115.5	125.6	8.7
T7	2435.0	2531.0	3.9	185.8	199.6	7.4
Mean ± SD of the % diff			5.5 ± 2.9			6.3 ± 2.5

Key: A_{true} = true activity, A_{rec} = recovered activity, % diff = percentage difference, SD = Standard deviation

From Table 6.5 it can be seen that the spherical insert in the liver resulted in an overestimation of the recovered activity for all sphere sizes. The overall quantification accuracy for the spherical insert in the liver was within 10 %. The exception was for T3 when no added background activity was present in the water cylinder (11.1 % overestimation). A mean % difference of 6.3 ± 2.5 % for the 'with background' activity study was obtained for the spherical inserts.

6.3.2.2 Follow-up patient models' study

Additional patient models were generated as explained before and quantification of the spherical inserts in these models were performed. The reason for these additional patient models was to investigate the effect of different patient body types on the quantification accuracy. The quantified results for the additional 18 simulated voxel-based patients are shown in Table 6.6. The A_{rec}, as well as the percentage difference between the A_{rec} and A_{true}, are listed.

Table 6.6: Quantified activity values for spheres positioned in the lung and liver of the follow-up patient model study with background activity

	Lung				Liver			
Sphere insert	T3		T6		T3		T6	
Patient ID	A_{rec} (MBq)	%-diff	A_{rec} (MBq)	% diff	A_{rec} (MBq)	%-diff	A_{rec} (MBq)	% diff
1	0.73	4.1	9.50	-3.8	1.34	7.5	6.46	10.6
2	0.73	3.9	5.72	-1.0	0.80	8.3	6.74	9.9
3	0.66	4.4	5.30	-0.5	0.71	11.2	5.57	9.3
4	0.65	4.6	5.00	-1.9	0.68	9.5	5.61	10.4
5	0.67	5.3	5.26	-0.4	0.70	9.7	5.70	7.5
6	0.61	7.1	4.83	0.0	0.56	-4.1	5.20	9.8
7	0.50	0.9	4.04	-1.5	0.55	9.2	4.56	10.4
8	0.56	-0.3	4.37	-4.6	0.62	10.7	5.00	8.8
9	0.66	5.8	5.06	-2.0	0.65	4.7	5.25	1.6
10	0.75	6.5	5.62	0.4	0.76	10.3	6.32	9.0
11	0.66	1.9	5.17	-2.4	0.72	10.4	5.70	7.0
12	0.53	-0.4	4.30	-1.7	0.57	7.7	4.55	3.3
13	0.58	7.1	4.22	-5.1	0.59	9.7	4.81	8.1
14	0.64	9.0	4.91	1.3	0.64	7.7	5.39	10.4
15	0.60	7.4	4.60	0.5	0.62	10.5	5.09	10.0
16	0.61	-3.6	4.61	-3.9	0.43	1.2	3.5	3.2
17	0.40	1.2	3.05	0.1	0.43	5.8	3.70	11.2
18	0.50	4.6	3.81	-3.0	0.52	9.3	4.34	10.5
Mean ± SD for % diff	3.9 ± 3.3		-1.6 ± 1.9		7.7 ± 3.9		8.4 ± 2.9	

% diff = percentage difference between true and recovered activity; A_{rec} = recovered activity; SD = standard deviation.

From Table 6.6, the overall quantification accuracy is ≤ 9.0 % and ≤ 5.1 % respectively, for the T3 and T6 in the lungs for the 18 simulated voxel-based patients. In Table 6.6 a mean % difference of 3.9 ± 3.3 % and -1.6 ± 1.9 % was reported for the spheres T3 and T6 respectively when positioned in the lungs. The reported % differences ranges were (-9.0 % – -0.3 %) and (-5.1 % – 0.4 %) for the two spheres. The corresponding quantification accuracy for the two spheres in the liver is ≤ 11.2 %. For spheres in the liver, the mean differences were 7.7 ± 3.9 % (ranging from -4.1 % – 11.2 %) for T3 and 8.4 ± 2.9 % (1.6 % – 11.2 %) for T6. The results obtained here tallies with the work of others as cited in MIRD pamphlet No. 24 (Dewaraja *et al.*, 2013).

6.4 Conclusion

The percentage difference between the true activity and the recovered activity for the cylindrical water phantom study is less than 10 % for all the simulated sphere sizes. Since the smallest sized sphere (D = 3.0 cm) is more than twice the full width at half maximum of 1.2 cm of the simulated gamma camera, PVE was obtained as can be seen from Figure 6.6 (Dewaraja et al 2001; Ejeh et al , 2019). In order to improve the quantification accuracy, correction for the PVE is necessary. A difference in the RC results for the study without and with background activity (Figure 6.6) was noted. This underscores the need to produce different RC curves for different target to background activity concentration ratios in clinical practice as reported in the literature (Dewaraja et al 2001).

The percentage difference between the true and recovered activity was determined for T3 and T6 placed in the liver and the lung of patient models. The percentage difference was calculated for each sphere size directly from the SIMIND defined sphere activity and the SPECT reconstructed recovered activity in the sphere VOI. To achieve accurate quantification results using the aforementioned method, RCs must be applied to the sphere.

There was a consistent underestimation of the spherical activity in the lung of the initial patient model study, even after correction for PVE using the RC (Table 6.4). In contrast, when the sphere was located within the liver an overestimation was obtained (Table 6.5). The reason for the underestimation of the activity values for the spheres in the lungs, is that the lung has a composition made of mostly air and water, with a mixture of blood and tissue which, according to Chen et al., complicates quantification in the lung, as the relative volume of lung cells, air, blood, and water are found to influence the activity concentration in the lung (Chen et al., 2017). One of the suggestions of these authors, is that compartmental modelling could be used to estimate the fraction of air in the lung. However, they mentioned that there is yet no complete modelling solution that include the other components of the lung, which has been tested. The percentage difference between the true and recovered activity was however better than 10% indicating an acceptable quantification accuracy for ^{131}I.

The group of 18 simulated voxel-based patient models shows quantification accuracy of better than 12% for all simulated sphere sizes. Quantification evaluation is routinely done in phantom studies. These simulated patient models mimic the true clinical environment. Therefore, it can be concluded that quantification errors of less than 12% can be expected in clinical scenarios for ^{131}I. The results obtained here are comparable to those of other researchers as mentioned above. No trend could be seen between the quantification accuracy and the patient size.

In conclusion, literature and the results of our study show that SPECT with high energy emitter, ^{131}I can be quantitatively accurate with errors smaller than 12 %. These accuracies can only be accomplished with state-of-the-art SPECT/CT systems able to accurately correct for image-degrading factors such as attenuation, scatter and partial volume effects. The use of a simple sphere-based PVC for spherical structures is important and improved the quantification accuracy. Furthermore, we have the confidence that such accuracy can be achieved with real patients in clinical studies as shown by our patient simulation studies.

6.5 References

Blankespoor, S. C., Xu, X., Kaiki, K., Brown, J. K., Tang, H. R., Cann, C. E. and Hasegawa, B. H. (1996) ‘Attenuation correction of SPECT using X-ray CT on an emission-transmission CT system: myocardial perfusion assessment’, *IEEE Trans. Nucl. Sc.*, 43, pp. 2263–2274.

Chen, D. L., Cheriyan, J., Chilvers, E. R., Choudhury, G., Coello, C., Connell, M., Fisk, M., Groves, A. M., Gunn, R. N., Holman, B. F., Hutton, B. F., Lee, S., MacNee, W., Mohan, D., Parr, D., Subramanian, D., Tal-Singer, R., Thielemans, K., van Beek, E. J. R., Vass, L., Wellen, J. W., Wilkinson, I. and Wilson, F. J. (2017) ‘Quantification of Lung PET Images: Challenges and Opportunities’, *J. Nucl. Med.*, 58, pp. 201–207.

Dewaraja, Y. K., Frey, E. C., Sgouros, G., Brill, A. B., Robertson, P., Zanzonico, P. B. and

Ljungberg, M. (2012) ‘MIRD Pamphlet No. 23: Quantitative SPECT for Patient-Specific 3-Dimensional Dosimetry in Internal Radionuclide Therapy’, *J. Nucl. Med.*, 53, pp. 1310–1325.

Dewaraja, Y. K., Ljungberg, M., Green, A. J., Zanzonico, P. B. and Frey, E. C. (2013) ‘MIRD Pamphlet No. 24: Guidelines for Quantitative ^{131}I SPECT in Dosimetry Applications’, *J. Nucl. Med.*, 54, pp. 2182–2188.

Dewaraja, Y. K., Ljungberg, M. and Fessier, J. A. (2006) ‘3-D Monte Carlo-based scatter compensation in quantitative I-131 SPECT reconstruction’, *IEEE Trans. Nucl. Sc.*, 53, pp. 181–188.

Dewaraja, Y. K., Ljungberg, M. and Koral, K. F. (2001) ‘Monte Carlo evaluation of object shape effects in iodine-131 tumour activity quantification’, *Eur. J. Nucl. Med.*, 28, pp. 900–906.

Dondi, M., Palm, S., Bussmann Sokole, E., Stodilka, R. Z., Wegst, A. V. and Zimerman, R. E. (2009) *Quality Assurance for SPECT Systems*, *IAEA Human Health Series. No. 6*.

Edyvean, S. and Weston, J. (2007) *Imaging Performance Assessment of CT Scanners, Gammex RMI CT Phantom, 438 User Guide*. London.

Ejeh, J. E., van Staden, J. A. and du Raan, H. (2019) ‘Validation of SIMIND Monte Carlo Simulation Software for Modelling a Siemens Symbia T SPECT Scintillation Camera’, in Lhotska, L. et al. (eds) *World Congress on Medical Physics and Biomedical Engineering 2018. IFMBE Proceedings*. Springer, Singapore, pp. 573–576.

Frey, E. C., Humm, J. L. and Ljungberg, M. (2012) ‘Accuracy and precision of radioactivity quantification in nuclear medicine images’, *Semin. Nucl. Med.*, 42, pp. 208–218.

Frey, E. C. and Tsui, B. M. W. (1996) ‘A New Method for Modelling the Spatially-Variant, Object dependent Scatter Response Function in SPECT’, in *IEEE Nucl. Sci. Symposium*, pp. 1082–1086.

Kalra, K. M., Maher, M. M., Prasad, R. S., Hayat, S. M., Blake, A. M., Vargese, J., Halpern, F. E. and Saini, S. (2003) 'Correlation of Patient Weight and Cross-Sectional Dimensions with subjective Image Quality at Standard Dose Abdominal CT'., Korean J. Radiol., 4, pp. 234 - 238.

Kleinman, P. L., Strauss, K. J., Zurakowski, D., Buckley, K. S. and Taylor, G. A. (2010)

'Patient Size Measured on CT Images as a Function of Age at Tertiary Care Children Hospital'., AJR, 194, pp. 1611 - 1619.

Ljungberg, M. and Gleisner, K. S. (2016) ‘Personalized Dosimetry for Radionuclide Therapy Using Molecular Imaging Tools’, *Biomedicines*, 4, pp. 25–45.

Loening, A. M. and Gambhir, S. S. (2003) ‘AMIDE: A Free Software tool for multimodality Medical Image Analysis’, *Mol. Imaging*, 2, pp. 131–137.

Nolf, E. (2003) ‘An Open-source medical image conversion toolkit’, *Eur. J. Nucl. Med.*, 30, p. S 246.

Sadremomtaz, A. and Taherparvar, P. (2013) ‘The influence of filters on the SPECT image of Carlson phantom’, *J. Biomed. Sc. Eng.*, 6, pp. 291–297.

Sichani, M. R. T., Amoui, M., Akhlaghpoor, S. and Hosntalab, M. (2014) ‘Quantitative SPECT and planar ^{32}P bremsstrahlung imaging for dosimetry purpose – An experimental phantom study’, *Int. J.Radiat. Res.,* 12, pp. 129–138.

Willegaignon, J., Pelissoni, R. A., Lima, B. C. D., Sapienza, M. T., Coura-Filho, G. B., Queiroz, M. A. and Buchpiguel, C. A. (2016) ‘Estimating ^{131}I biokinetics and radiation doses to the red marrow and whole body in thyroid cancer patients: probe detection versus image quantification.’, *Radiologia brasilei*, 49, pp. 150–157.

Willowson, K., Bailey, D. L. and Baldock, C. (2008) ‘Quantitative SPECT reconstruction using CT-derived corrections’, *Phys. Med. Biol.*, 53, pp. 3099–3112.

Yue, J., Mauxion, T., Reyes, D. K., Lodge, M. A., Hobbs, R. F., Rong, X., Dong, Y., Herman, M. J., Wahl, R. L., Geschwind, J-F. H. and Frey, E. C. (2016) ‘Comparison of quantitative Y-90 SPECT and non-time-of-flight PET imaging in post-therapy radioembolization of liver cancer’, *Med. Phys.*, 43, pp. 5779–5790.

Yushkevich, P. A., Piven, J., Hazlett, H. C., Smith, R. G., Ho, S., Gee, J. C. and Gerig, G. (2006) ‘User-guided 3D active contour segmentation of anatomical structures: Significantly improved efficiency and reliability’, *NeuroImage*, 31, pp. 1116–1128

Zeintl, J., Vija, A. H., Yahil, A., Hornegger, J. and Kuwert, T. (2010) ‘Quantitative accuracy of clinical ^{99m}Tc SPECT/CT using ordered-subset expectation maximization with 3-dimensional resolution recovery, attenuation, and scatter correction', *J. Nucl. Med.*, 51, pp. 921–928.

Zubal, I. G., Harrell, C. R., Smith, E. O., Rattner, Z., Gindi, G. and Hoffer, P. B. (1994) 'Computerized three-dimensional segmented human anatomy.', *Med. Phys.*, 21, pp. 299–302.

CHAPTER SEVEN: Iodine-131 Internal Dosimetry for 3-D Patient-specific Models

Table of Contents

7.1 Introduction

During radionuclide therapy (RNT) as mentioned before, radionuclides that emit high levels of radiation are attached to agents that target specific organs or tissues. These radiolabelled agents are administered to patients in order to deliver high radiation doses to tumours in the target organ or tissue. Radionuclides of interest in RNT are usually those that emit particulate radiation such as alpha- (α) particles, beta- (β) particles, and Auger/conversion electrons (Dash, et. al., 2013). These particles have the capability to induce cytotoxicity in the diseased cells due to their short range biological effectiveness. ^{131}I is a radionuclide that meets the requirement of theranostic isotopes, i.e. diagnosis via imaging as well as therapy.

Image-based patient-specific dosimetry in RNT is receiving much attention in recent times (Ljungberg, 2018). Its benefits had been discussed in chapters 1 and 4. As mentioned before, cumulated activity is required in order to perform dosimetry. Accurate quantification of activity distribution is therefore a prerequisite for accurate patient dosimetry. The quantification of ^{131}I SPECT images for the purpose of treatment planning was dealt with in chapter 6. Theoretical aspects of radionuclide internal dosimetry were discussed in chapter 4 and in this chapter, the calculation of mean absorbed dose to target organs and spherical "tumours" in simulated patient-specific models will be discussed.

Two dose estimation methods, (i) based on the Medical Internal Radiation Dose (MIRD) approach (Organ Level Internal Dose Assessment/EXponential Modelling [OLINDA/EXM] software) and (ii) a Monte Carlo (MC) simulation approach (LundADose software) have been presented. From the discussion in chapter 4, it is evident that MIRD and MC dosimetry methods vary in complexity and accuracy of the dose estimates that they produce. MIRD dose calculations are performed relatively easy by using pre-calculated organ and tumour level S values based on reference phantoms. MC dose calculations, on the other hand, are more rigorous, and in turn, are very computer intensive. The aim of this chapter was to determine the agreement between organ-level MIRD dosimetry calculated with OLINDA/EXM and MC simulations for dosimetry calculated with LundADose by comparing mean absorbed doses calculated, using the two methods, for target organs and tumours for simulated ^{131}I patient studies.

7.2 Dose calculation methods for simulated images

7.2.1 Generation of time-activity information

In chapter 6, the quantification of reconstructed simulated projection data was done for a single imaging time point (it was assumed to be time point 1 at time zero). In order to obtain cumulated activity over time, it is required to acquire data at additional time points. In this chapter, four additional time points were created by introducing exponential decay to the original projection data of the 18 simulated patient models. These additional patient projection datasets were reconstructed and organ and tumour activities were quantified similarly to quantification done in chapter 6. Mean absorbed radiation doses were calculated for organs and spherical tumours that have limited partial volume effect. The reconstructed activity images of the five time points of the patients were used by LundADose to calculate the mean absorbed doses. Cumulated activity was obtained from these reconstructed images in order to calculate the mean absorbed dose using OLINDA/EXM.

The number of time points selected in order to calculate the cumulated activity is important as mentioned in chapter 4 section 4.2.2. This study was based only on physical decay of ^{131}I, similar to what was reported by Pacilio et al (Pacilio *et al.*, 2016). The biological wash out of the radionuclide in the patients was not modelled; only physical decay of ^{131}I was considered and used to represent the effective half-life of the radionuclide in each simulated patient. Therefore, an effective half-life of 8.0 days was assumed to create the different time points for generating the TACs for the lungs, liver and the spherical 'tumours'. In order to have an adequate sampling of the radionuclide decay, 5-time points were chosen as used by Abuqbeitah et al (Abuqbeitah *et al.*, 2018). These time points were evenly spaced one effective half-life (8.0 days) apart, resulting in time points at 0, 192, 384, 576, and 768 h. Since the duration of sampling was long, the remnant activity after the last time point was considered negligible (Stabin, 2008; Stabin, 2017).

7.2.2 Absorbed dose calculation with OLINDA/EXM S-factors

Volumes of interest (VOIs) were drawn over the liver, lungs and spherical 'tumours' on the reconstructed images of the 5 simulated acquisition time points of each patient using the AMIDE volumetric analysis tool as explained in chapter 6 (section 6.2.5) to obtain the activity in the VOI for the various time points. The cumulated activity (GBq-s) for each organ or tumour was obtained by plotting the activity from the 5-time points against time to generate the respective TACs. The calculated cumulated activities for each organ and tumour were used with the appropriate MIRD S-values, obtained from the software (Stabin, Sparks and Crowe, 2005) to calculate the mean absorbed dose according to equation 4.7.

OLINDA/EXM provides tabulated spherical S-values for uniform unit-density spheres of masses ranging from 0.01 – 6000 g isolated in a uniform unity-density medium (Siegel and Stabin, 1994). These S-values for the spherical phantoms in OLINDA/EXM were used to calculate the tumour dose from the cumulated activity of the spherical tumours obtained from the simulated ^{131}I SPECT images. To evaluate the effect of correcting for the tumour mass, since OLINDA/EXM considers only unit density spheres, the tumour mass was calculated using two methods. For both of these methods, the tumour volume was calculated from the predetermined sphere (tumour) volumes. For the first method (i.e. no tumour density correction), the mass was calculated assuming a water equivalent unit-density (according to OLINDA/EXM). For the second method (i.e. tumour density correction), the mass was calculated from the average tumour density obtained from an HU-to-density conversion.

The mean absorbed dose calculated for the target organs included both self-dose and cross-dose contributions from neighbouring source organs. In the simulated patients, the cross-dose contributions from the liver to the lungs and from the lungs to the liver were the only ones used for the calculations. The contributions from the background activity distribution were considered negligible since the ratio of background to organ was low (1:5). Cross-dose was not considered in this work for the MIRD method for the spherical ‘tumours’ because OLINDA/EXM software does not make provision for this.

The mean absorbed organ doses were normalized for organ masses for each patient as well as the tumour masses as mentioned above. This was necessary since the masses of the various organs used in the MIRD standard phantoms may differ from the organ masses of the various patients studied. Therefore, mean absorbed doses were calculated without and with mass correction for organs and tumours. The mass correction was applied using equation 4.13 as explained by Divoli et al (Divoli *et al.*, 2009).

7.2.3 Absorbed dose calculation with LundADose

The 3-D dose distributions for the quantified simulated patient models were calculated using MC simulations based on the electron gamma shower version 4 (EGS4) software (Nelson et al., 1985; Hirayama *et al.*, 2016) incorporated in LundADose (Ljungberg and Gleisner, 2016). Table 7.1 summaries the dose calculation setup.

Table 7.1: Dose calculation setup for LundADose

Parameter	Value	Unit
Type of transport	Photon and electron	
Cut off energies	0.01 and 0.1	MeV
Number of histories	25	$\times 10^6$
Coherent Rayleigh scatter	Included in simulation	
Media simulated	Tissue, bone, lung	
Output images	Absorbed dose	mGy

The absorbed dose rate distribution was calculated for each set of reconstructed activity images using the Lundadose dose calculation software and the setup in Table 7.1. Similar as for OLINDA/EXM these absorbed dose rate images were exported and analysed using AMIDE volumetric analysis tool. The organs of interest (lungs and liver) and the 3.0 cm and 6.0 cm spherical tumours (T3 and T6) embedded in the lungs and liver (see chapter 6) were delineated on the absorbed dose rate images. AMIDE was used for consistency to delineate the organs and tumours on the absorbed dose rate images. These VOIs created in AMIDE were the same as the VOIs used for the calculation of the cumulated activity in OLINDA/EXM on the activity images. The mean absorbed dose value calculated from the VOI for each organ and tumour in the dose rate images were recorded. The mean absorbed dose for each organ and tumour was calculated by plotting the absorbed dose rate from the 5-time points against time to generate the time-dose rate curve. This was done similar to the TACs generated in section 7.2.2. These were used to calculate the mean absorbed dose by calculating the area under the curve using analytical integration.

7.2.4 MIRD versus LundADose absorbed doses

As mentioned above the same VOIs contours for tumours and organs created with AMIDE were used for the MIRD and MC dosimetry. The mean absorbed doses calculated using OLINDA/EXM and LundADose for each organ or 'tumour' were compared by calculating the percentage difference between results from the two software programs using equation 7.1.

$$\frac{D_L - D_O}{D_L} \times 100\% \qquad 7.1$$

Where, D_L is the mean absorbed dose calculated from LundADose (L) and D_O is the mean absorbed dose calculated using OLINDA/EXM (O).

The absorbed doses from the two software programs were analysed statistically by regression and Bland-Altman analysis (Bland and Altman, 1986) to measure the agreement between the two dose calculation software programs. How small the limit of agreement should be to conclude that methods sufficiently agree is not a statistical decision though, rather it is a clinical decision. The classification of agreement as good or poor or providing guidance on which method to use when considering the amount of disagreement is dependent on the purpose for which measurements are being made (e.g. dosimetry for diagnostic procedures versus dosimetry for therapeutic procedures as is the case here) (Cecconi *et al.*, 2009). Therefore, the clinician takes the final decision on how small the level of agreement should be, to be acceptable.

To determine if the limit of agreement satisfies the condition of acceptable agreement, the 95 % confidence intervals for the bias and lower and upper limits of agreement for the two methods that are compared should be calculated.

Therefore, the following parameters were calculated to assess the level of agreement between OLINDA/EXM and LundADose. The bias, lower limit of agreement (LLoA) and upper limit of agreement (ULoA), precision of the bias and limits of agreement, calculated as 95 % confidence interval (CI) of the bias and the limits of agreement.

The *bias* ($\bar{d}$) was calculated as the mean of the differences between the two methods while the limits of agreement (LLoA and ULoA) were calculated as:

$(\bar{d} - 1.96 \times \text{SD})$ and $(\bar{d} + 1.96 \times \text{SD})$.

SD refers to the standard deviation of the differences obtained between the two methods.

To calculate the 95 % CI of the bias and the limits of agreement, the standard error (SE) for each was first obtained using equations 7.2 and 7.3 taken from Bland and Altman (Bland and Altman, 1986). The SE of the bias $SE_{\bar{d}}$ was calculated using equation 7.2.

$$SE_{\bar{d}} = \sqrt{\frac{SD^2}{n}} \qquad 7.2$$

With n the sample size of 18 for this study. Similarly, the SE of the lower and upper limits of agreement (SE_{LLoA} and SE_{ULoA}) were obtained with equation 7.3a and 7.3b.

$$SE_{LLoA} = \sqrt{\frac{3SD^2}{n}} \qquad 7.3a$$

$$SE_{ULoA} = \sqrt{\frac{3SD^2}{n}} \qquad 7.3b$$

The 95 % CIs were calculated by first finding the appropriate point of the t-distribution with (n – 1) degree of freedom. In this study, there are 17 degrees of freedom and t = 2.11. Thus, the 95 % CI for the bias ($CI_{\bar{d}}$) and the Level of agreements (CI_{LLoA} and CI_{ULoA}) were calculated as follows:

$$CI_{\bar{d}} = \bar{d} \pm (\text{t} \times SE_{\bar{d}}). \qquad 7.4$$

$$CI_{LLoA} = \text{LLoA} \pm (\text{t} \times SE_{LLoA}). \qquad 7.5a$$

$$CI_{ULoA} = \text{ULoA} \pm (\text{t} \times SE_{ULoA} \qquad 7.5b$$

Results of the analysis are presented in tables and diagrams.

7.3 Results and discussions

7.3.1 Comparison of LundADose and OLINDA/EXM

Calculated mean absorbed doses to the lungs, liver and tumours T3 and T6 for the 18 individual patients are presented below in graphs and discussed in detail. These values are also tabulated in **Appendix** III. The results obtained from both scenarios as explained in chapter 6 (section 6.2.1.2) are shown.

Scenario 1 was the setup of the simulated patients whereby the 3.0 cm tumour (T3) was embedded in the left lung while the 6.0 cm tumour (T6) was simultaneously embedded in the liver. For **scenario 2**, T6 was in the right lung while T3 was embedded in the liver. The presented results for OLINDA/EXM are those calculated after patient organ mass and tumour density corrections have been applied. OLINDA/EXM with organ mass correction and density correction for the tumours are further discussed in section 7.3.2. All the patient data are also available in **Appendix** III (**Table**s 1 – 10). **Tables** III 1 and III 2 in **Appendix** III summarise the calculated cumulated activity for organs and tumours simulated in this study as discussed in chapter 6. **Tables** III 3 – 5 show the mean absorbed doses calculated to the organs and tumours using OLINDA/EXM without organ mass correction and assuming unit tumour density, as well as the mean, absorbed doses obtained through LundADose. The mean absorbed doses calculated using OLINDA/EXM with organ mass corrections and tumour density corrections are presented in **Tables** III 6 – 8.

Figures 7.1 – 7.3 show the mean absorbed dose results for the lungs, **Figures** 7.4 – 7.7 for the liver and **Figures** 7.8 – 7.12 for the tumours. Mean absorbed doses to the different organs and tumours are also summarised in **Table** 7.2 which follows after **Figure** 7.10. The results are discussed in detail below.

LUNGS:

A comparison of the mean absorbed doses to the lungs without and with an embedded tumour in the lung for each of the 18 patients calculated with LundADose and OLINDA/EXM with organ mass corrections for the lungs are shown in **Figure 7.1 A** and **B**. For the left lung and right lung without an embedded tumour the calculated mean doses with OLINDA/EXM were larger than doses obtained with LundADose for 33 (92%) of the 36 lungs for the 2 scenarios. For the 2 scenarios of the lungs with an embedded tumour the corresponding calculated mean doses with OLINDA/EXM were larger than those calculated with LundADose in 28 (78%) of the 36 lungs.

The percentage differences of the mean absorbed doses to the lungs without and with an embedded tumour between LundADose and OLINDA/EXM are shown in **Figure 7.2 A** and **B.** From **Figure 7.2 A** and **B** it can be seen that the percentage differences of the mean absorbed doses between LundADose and OLINDA/EXM were smaller than 10%. The average percentage differences between LundADose and OLINDA/EXM for the left and right lung respectively were

-3.36 ± 2.40% and -3.06 ± 1.67%. When T3 and T6 were embedded in the left and right lung these percentage difference values were similar (-2.24 ± 1.98% and -0.34 ± 3.71%). Because the S-values for the lung used by OLINDA/EXM account for self-dose as well as the cross-dose from target organs (liver), it is expected that absorbed doses calculated with OLINDA/EXM with organ mass corrections would compared favourably to doses obtained from LundADose which accounts for both the self-dose and the dose from target organs of the patients.

From equation 4.13 it is evident that the self-dose from the mass correction applied in OLINDA/EXM is dependent on the organ (lung) mass derived from the patient's organ volume and density. These organ masses were calculated from the lung volume and density from the patient's CT images. From these calculated values it is evident that the reference values for lung masses for men (1000g) and women (800g) for OLINDA/EXM (Stabin, 2008) were on average larger than the calculated values for all patients (Appendix III, **Table** III.9 & III.10). These calculated mass values for the lung of each patient were used for the mass correction in OLINDA/EXM.

Figure 7.3 A, B, C and **D** show the linear regression and Bland Altman analysis for the above-mentioned results. Results for the left and right lung without **(A & B)** and with embedded tumours (**C & D)** are shown separately. The squared Pearson correlation coefficient (R^2) calculated to quantify the linear correlation between the LundADose and OLINDA/EXM mean doses and the null hypothesis of no correlation was tested to calculate p-values for each calculation method.

The statistical parameters of the linear regression for each case are summarized on the graphs. A perfect one-to-one correlation would lie upon the line of unity with a slope of one and a y-intercept of zero ($m = 1, b = 0, R^2 = 1$). The linear correlation was statistically significant for all cases ($p < 0.05$) shown in **Figure 7.3**. The slopes of the linear regression varied between 0.892 and 1.05 with R^2 values larger than 0.980. The Bland Altman results showed the bias of OLINDA/EXM vs LundADose to vary between -23.4 and -13.7 mGy for the LL, RL and LL (T3) confirming that OLINDA/EXM overestimates the LundADose values for the lung. However, the right lung with the T6 embedded (RL (T6)) showed an average difference of 2.16 mGy.

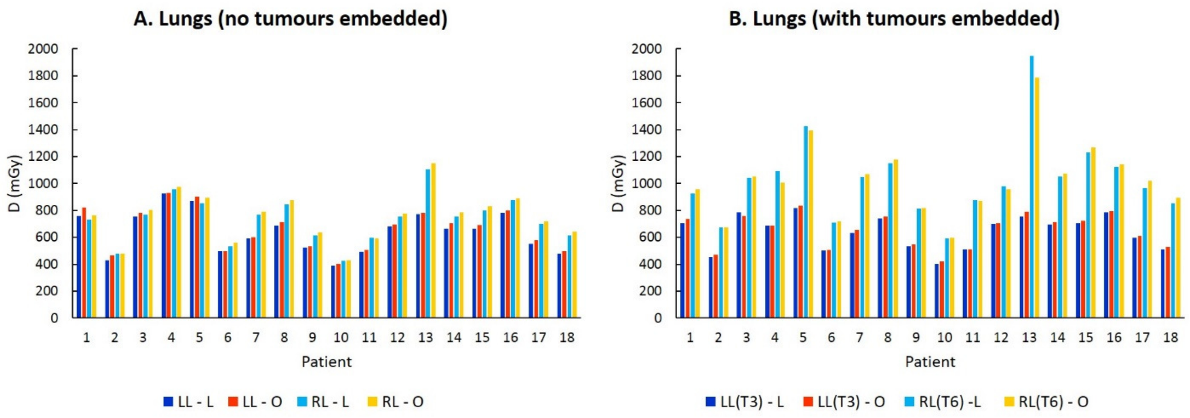

Figure 7.1: *A comparison of the mean absorbed doses (D) calculated with LundADose (L) and OLINDA/EXM (O) for (A) the left lung (LL) and right lung (RL) with no embedded tumours and for (B) the lungs with T3 embedded in the left lung (LL (T3)) and T6 embedded in the right lung (RL (T6)). The results calculated with OLINDA/EXM were obtained after applying organ mass corrections*.

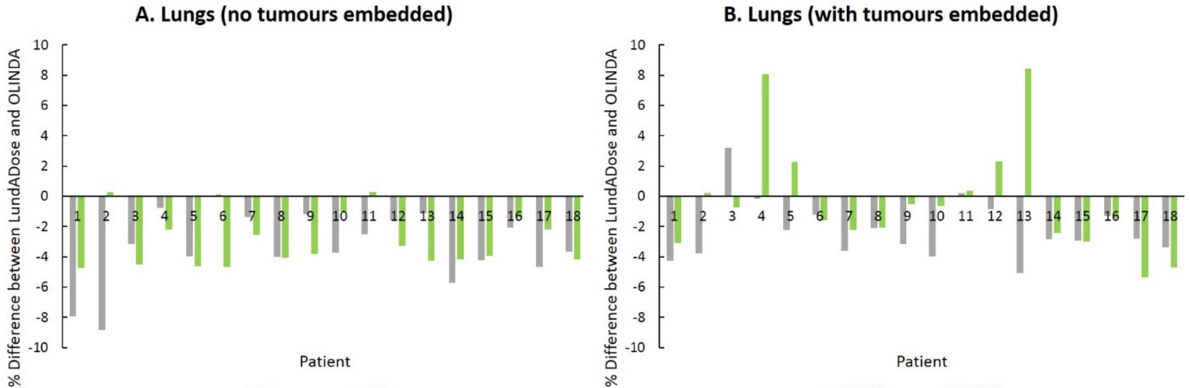

Figure 7.2: *The percentage differences between the LundADose and OLINDA/EXM mean absorbed doses calculated for the left lung (LL) and right lung (RL) (A) without and (B) with embedded tumours T3 and T6. LL (T3) indicates left lung with T3 embedded and RL (T6) right lung with T6 embedded. A negative difference indicates that LundADose was lower than the mean absorbed doses calculated by OLINDA/EXM.*

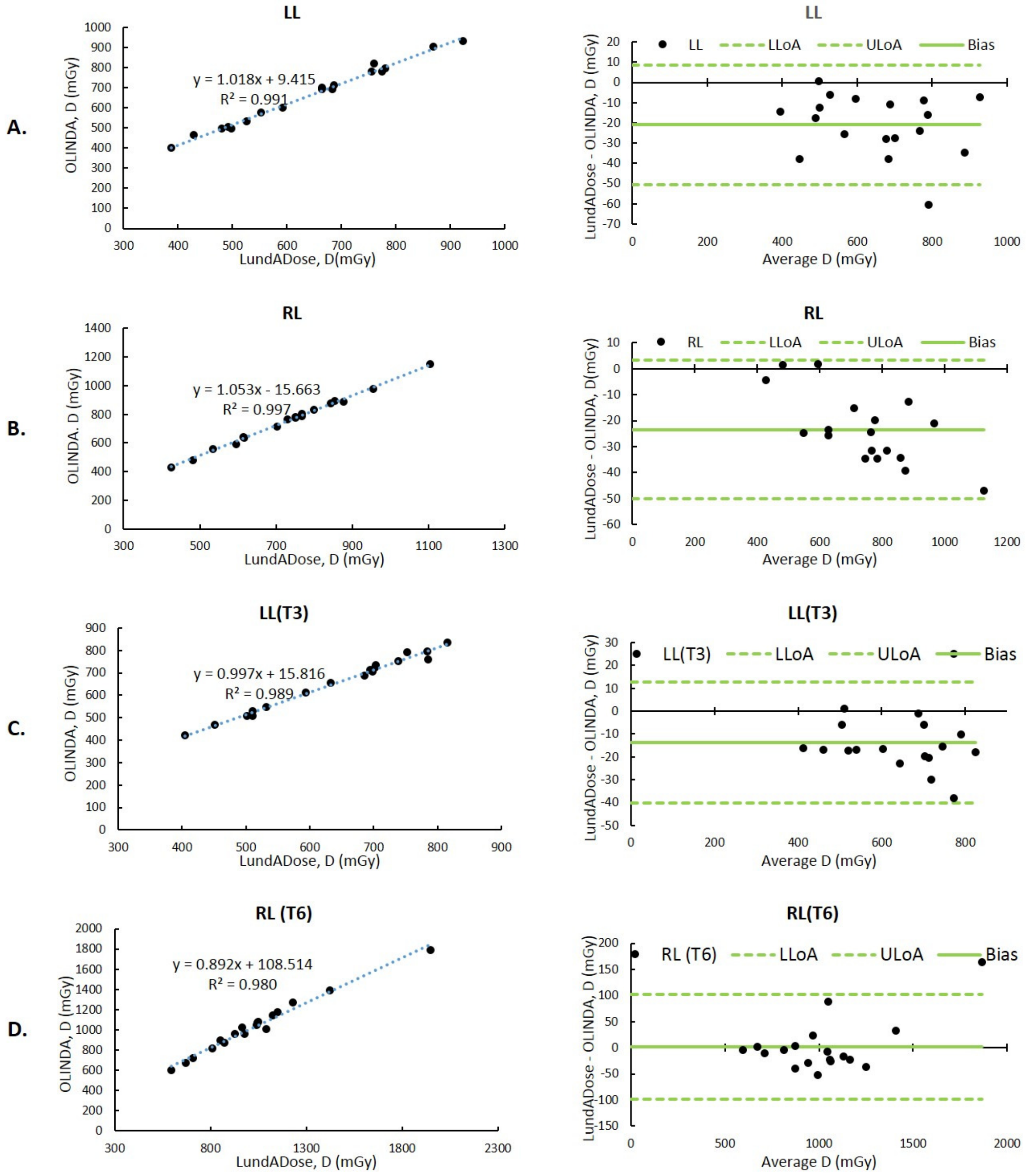

Figure 7.3: *The correlation between the mean absorbed lung doses (D) calculated with LundADose vs OLINDA/EXM. Correlation (graphs on the left hand side) as well as Bland-Altman plots (graphs on the right hand side) of mean absorbed doses to (A) the left lung (LL),*

(B) the right lung (RL), (C) the left lung with T3 embedded (LL(T3)) as well as (D) the right lung with T6 embedded (RL(T6)) are shown.

The correlation graphs show the linear regression between LundADose and OLINDA/EXM as well as the correlation coefficients R^2. The Bland-Altman graphs plot the difference between the mean absorbed doses calculated with LundADose and OLINDA/EXM vs the average of these mean absorbed dose values. The bias as well as the lower limit of agreement (LLoA) and upper limit of agreement (ULoA) are indicated on the graphs.

LIVER:

The results for the mean absorbed doses to the liver with the T3 and T6 embedded tumours for each of the 18 patients are shown in **Figure 7.4**. The percentage differences of the mean absorbed doses to the liver between LundADose and OLINDA/EXM are shown in **Figure 7.5.** From **Figure 7.4** and **7.5** it can be seen that the percentage differences of the mean absorbed doses between LundADose and OLINDA/EXM was smaller than 10% in most cases with the mean absorbed doses calculated with LundADose larger than when calculated with OLINDA/EXM. For one patient when T3 was embedded in the liver the difference exceeds 10% (16%). As explained for the lungs the mass correction applied in OLINDA/EXM is dependent on the organ mass. From the calculated liver masses it is evident that the reference liver mass for men (1910 g) (Stabin, 2008) were on average larger than the calculated patient values, while for the women the reference value (1400 g) (Stabin, 2008) were comparable to the calculated liver masses (Appendix III, **Table** III.10). These differences in the liver mass explain the small differences that were observed in the absorbed dose calculations when comparing LundADose and OLINDA/EXM.

Figure 7.6 A and **B** show the linear regression and Bland Altman analysis for the liver results with (**A**) T3 embedded and with (**B**) T6 embedded.

The graphs also present the statistical parameters of the linear regression for each case. The results show that the linear correlation was statistically significant for both scenarios ($p < 0.05$). The slopes of the linear regression were 0.836 and 0.958 respectively, with R^2 values larger than 0.918. The Bland Altman results showed the bias of OLINDA/EXM vs LundADose to be 19.1 mGy for the liver with T3 and 7.64 mGy for the liver with T6 embedded. T3 was always placed centrally in the liver, which is not the case with T6 due to the size. This can result in LundADose estimating a lower absorbed dose. **Figure 7.7** shows image samples of T3 and T6 embedded in the liver for two different patient phantoms.

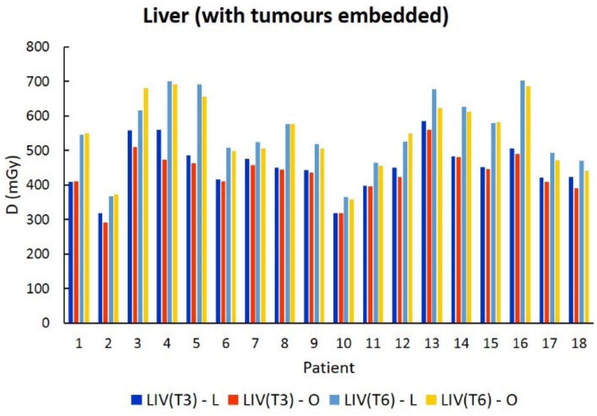

Figure 7.4: ***A comparison of the mean absorbed doses (D) calculated with LundADose (L) and OLINDA/EXM (O) for the liver with T3 (LIV (T3)) and T6 embedded in the liver (LIV (T6)). The results calculated with OLINDA/EXM were obtained after applying organ mass and tumour density corrections.***

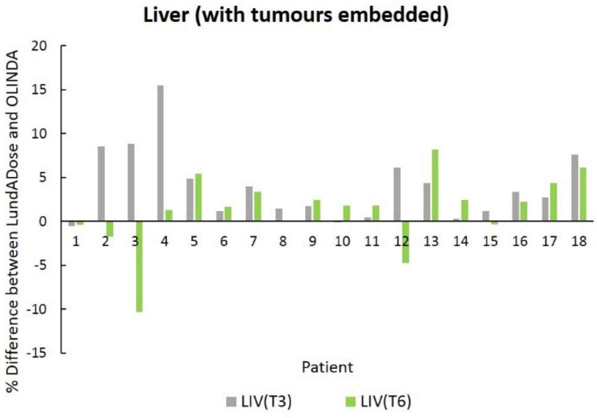

Figure 7.5: ***The percentage difference between the LundADose and OLINDA/EXM mean absorbed liver doses when T3 and T6 were respectively embedded in the liver (LIV (T3) and LIV***

(T6)). A negative difference indicates that LundADose was lower than the mean absorbed doses calculated by OLINDA/EXM.

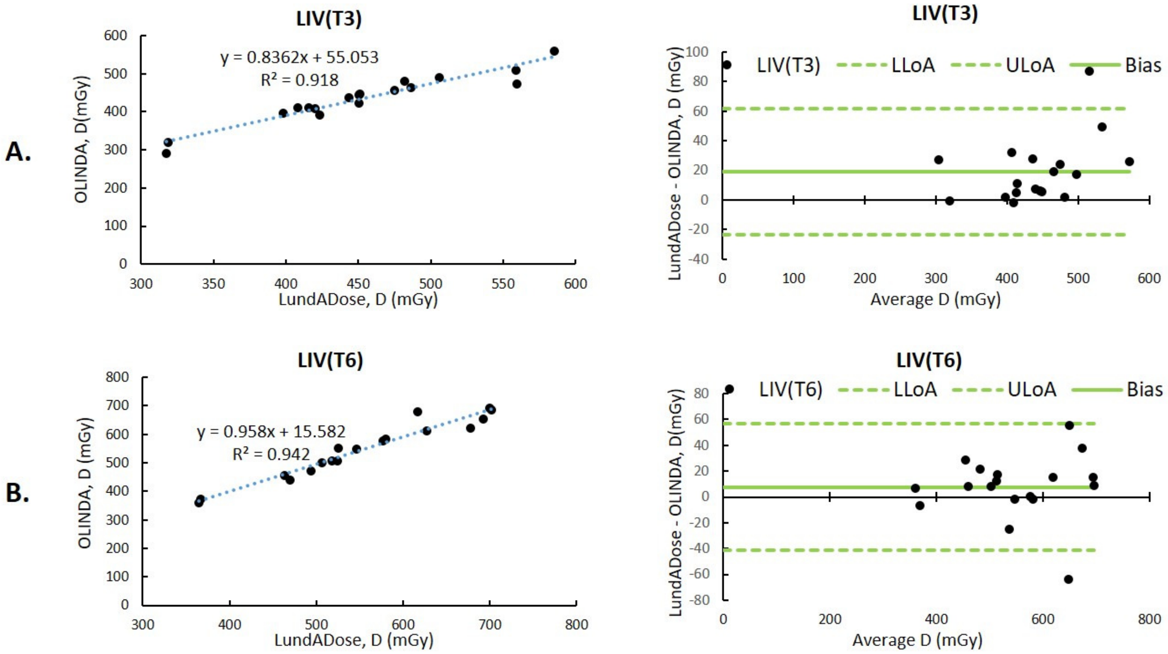

Figure 7.6: ***The correlation between the mean absorbed liver doses (D) calculated with LundADose vs OLINDA/EXM. Correlation (graphs on the left hand side) as well as Bland-Altman plots (graphs on the right hand side) of mean absorbed doses to the liver when T3 as well as when T6 are embedded in the liver are shown***.

The results are shown for when **(A)** T3 was embedded in the liver (LIV (T3))) as well as for when **(B)** T6 was embedded in the liver (LIV (T6)). The correlation graphs show the linear regression between LundADose and OLINDA/EXM as well as the correlation coefficients R^2. The Bland-Altman graphs plot the difference between the mean absorbed doses calculated with LundADose and OLINDA/EXM vs the average of these mean absorbed dose values. The bias as well as the lower limit of agreement (LLoA) and upper limit of agreement (ULoA) are indicated on the graphs.

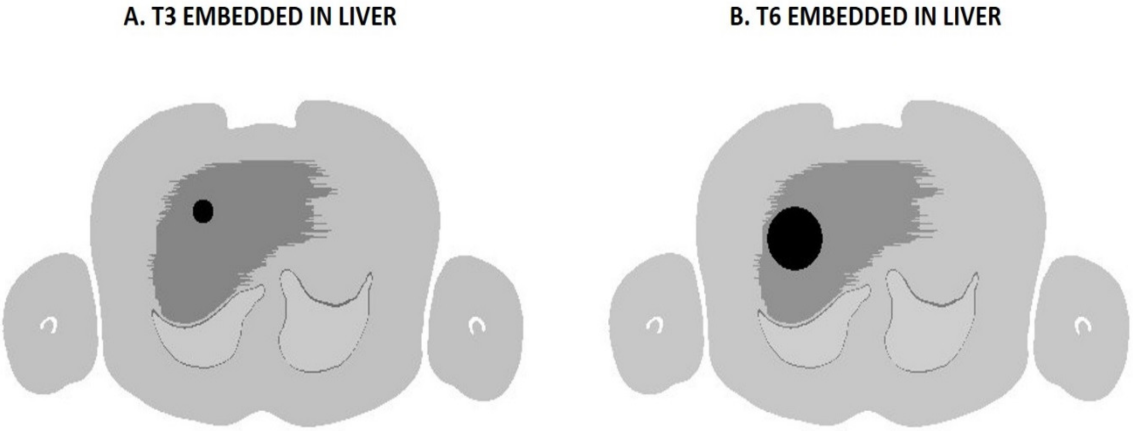

Figure 7.7: ***Segmented slices of two simulated patient phantoms showing the liver with (A) T3 and (B) T6 respectively embedded. Note the position of the tumours relative to the edge of the liver.***

TUMORS:

A comparison of the mean tumour doses calculated with OLINDA/EXM and LundADose using a CT-based density is shown in **Figure 7.8 A** and **B** for T3 and T6 respectively**.** From these figures, all T3 tumour mean doses calculated with OLINDA/EXM were larger than LundADose. This was the case when T3 was embedded in the lungs as well as in the liver. However, for T6, 10 patients (56%) resulted in a similar trend when T6 was embedded in the lung and 17 patients (94%) when T6 was embedded in the liver. **Figure 7.8 A** and **B** show that the mean absorbed doses to tumours (T3 and T6) embedded in the lungs were larger than the tumours embedded in the liver. This large difference between mean tumours doses in the lung and liver of the patients can be attributed to the larger contribution from the surrounding activity of the lungs to the tumour. This is due to the longer beta range in lung tissue.

Because the spherical S-values by OLINDA/EXM only accounts for self-dose and not for cross-dose from source organs it is expected that OLINDA/EXM would underestimate the tumour doses compare to LundADose which accounts for both the self-dose and the dose from source organs. However this was not seen in the results for T3. This may be due to the cross-dose from the tumour to the lungs that reduces the mean tumour dose when calculated with LundADose. Since the radioactive concentration of activity in the lung is low in comparison to the tumour (1:5) and due to the small volume (14 ml) of T3, the contribution of cross-dose from the lung to the tumour is minimal. For T6 embedded in the lung the loss due to cross-dose from the tumour to the lung is less due to the larger tumour, however the contribution of cross-dose from the lung to T6 can be more significant due to the larger tumour volume. When considering the tumours in the liver, the higher density of the liver resulted in a lower cross-dose contribution to the tumours from the liver.

Figure 7.9 A and **B** show the percentage differences of the mean absorbed doses to T3 and T6 between LundADose and OLINDA/EXM. For T3 the maximum percentage difference between the two methods was 75%. The average percentages differences for T6 (embedded in the lung: -8.21 ± 17.1 %; embedded in the liver: -5.10 ± 2.87 %) was less than for T3 (embedded in the lung: -28.4 ± 18.4 %; embedded in the liver: -28.8 ± 5.05 %), with a maximum difference of 54%.

Figure 7.10 A, B, C and D show the linear regression and Bland Altman analysis for the tumour results. Results for T3 embedded in (**A**) the left lung and (**B**) liver and T6 embedded in the **(C)** right lung and **(D)** liver are shown separately.

Similar to the results obtained for the lungs and liver the linear correlation was statistically significant for all embedded tumours ($p < 0.05$). All the R^2 values were larger than 0.853 confirming a good correlation. The Bland Altman results for T3 shows a bias of OLINDA/EXM vs LundADose of -910 mGy when embedded in the lung and -308 mGy when in the liver, confirming the differences that were observed before. These bias values were smaller when T6 was embedded in the lung (-218m Gy) as well as when embedded in the liver (-74 mGy).

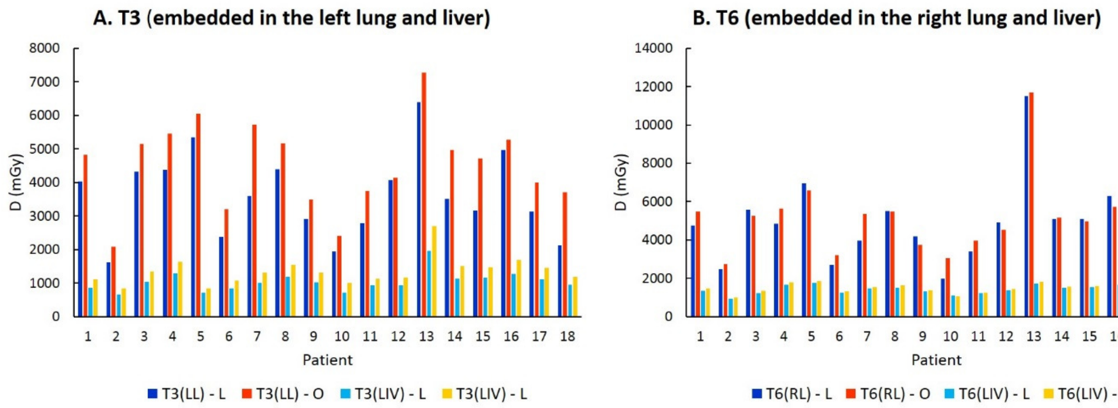

Figure 7.8: *A comparison of the mean absorbed doses (D) calculated with LundADose (L) and OLINDA/EXM (O) for (A) T3 embedded in the left lung (T3(LL)) and in the liver (T3(LIV) and for (B) T6 embedded in the right lung (T6(RL)) and in the liver (T6(LIV)). The results calculated with OLINDA/EXM were obtained after applying organ mass and tumour density corrections.*

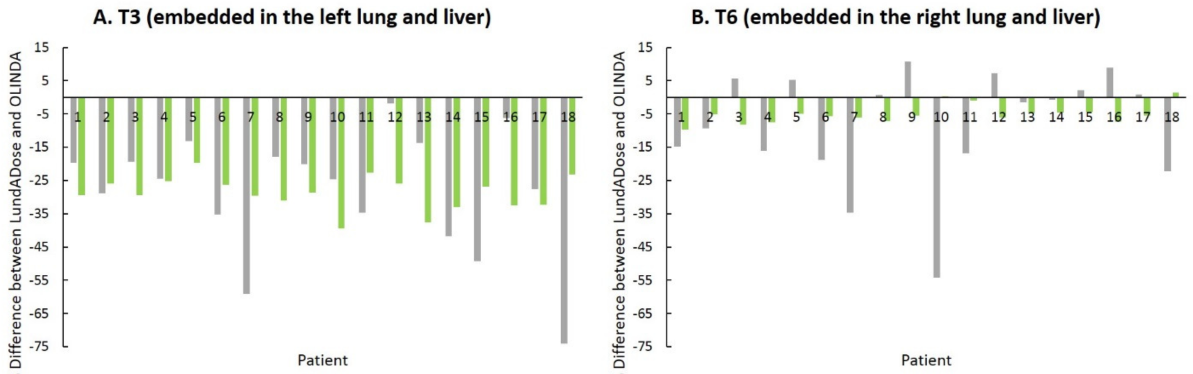

Figure 7.9: *The percentage differences between the LundADose and OLINDA/EXM mean absorbed doses calculated for tumours (A) T3 when embedded respectively in the left lung (T3(LL)) and the liver (T3(LIV)) and (B) T6 when embedded respectively in the right lung (T6(RL)) and in the liver (T6(LIV)). A negative difference indicates that LundADose was lower than the mean absorbed doses calculated by OLINDA/EXM.*

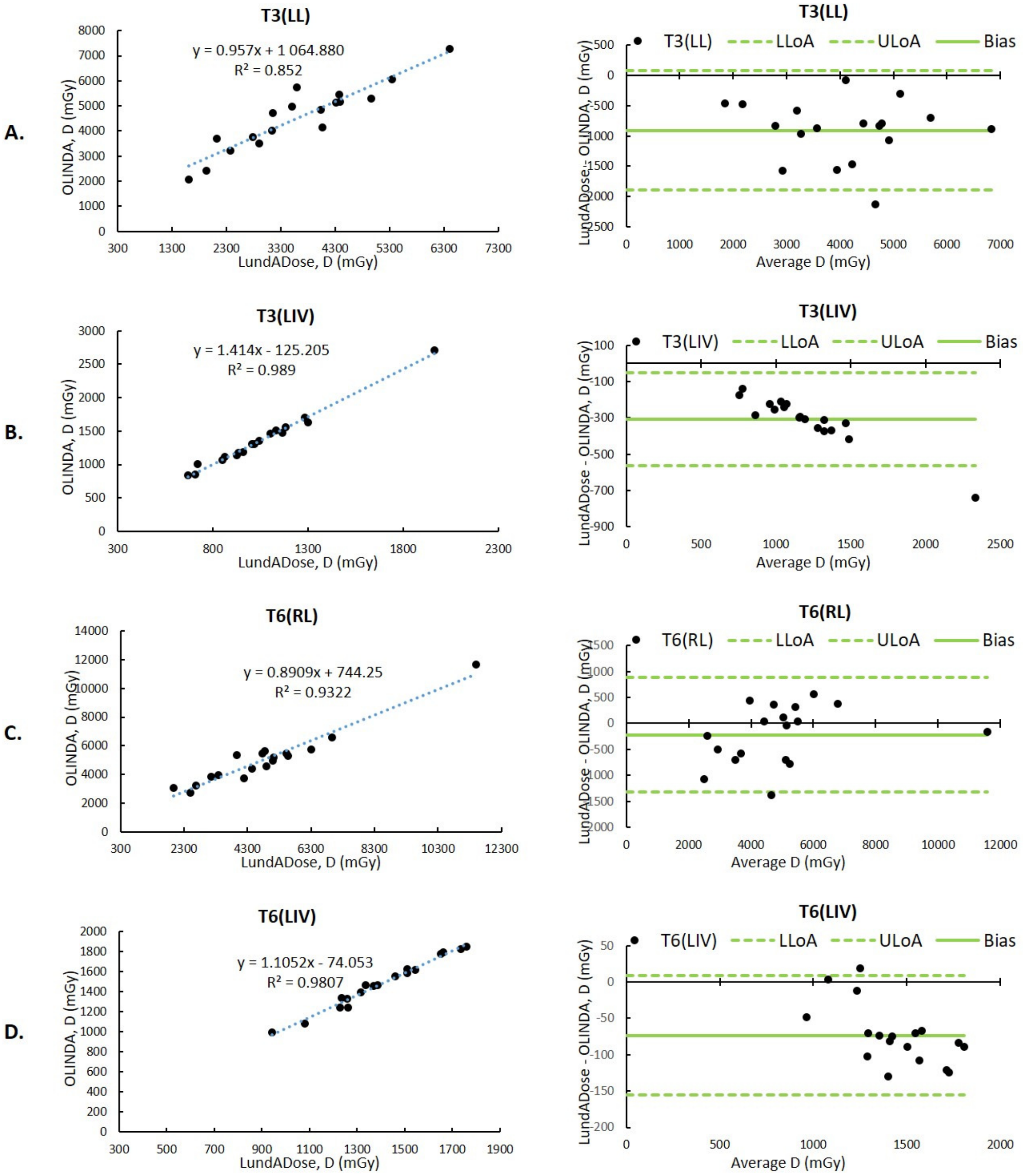

Figure 7.10: ***The correlation between the mean absorbed tumour doses (D) calculated with LundADose vs OLINDA/EXM. Correlation (graphs on the left hand side) as well as Bland-Altman plots (graphs on the right hand side) of mean absorbed doses to tumours T3 and T6 are shown. The results are shown for (A) T3 when embedded in the left lung (T3(LL)) and (B)***

when embedded in the liver (T3(LIV)) as well as for (C) T6 when embedded in the right lung (T6(RL)) and (D) when embedded in the liver (T6(LIV)).

The correlation graphs show the linear regression between LundADose and OLINDA/EXM as well as the correlation coefficients R^2. The Bland-Altman graphs plot the difference between the mean absorbed doses calculated with LundADose and OLINDA/EXM vs the average of these mean absorbed dose values. The bias as well as the lower limit of agreement (LLoA) and upper limit of agreement (ULoA) are indicated on the graphs.

All organ and tumour mean absorbed doses as displayed in the graphs are summarised in **Table 7.2**. The OLINDA/EXM tabulated values were obtained after applying organ mass correction as well as a tumour CT-based density correction. The range of the mean absorbed dose as well as the average values for the 18 patient models for each organ and tumour obtained with OLINDA/EXM and LundADose are included. The average percentage difference values between OLINDA/EXM and LundADose are also reported.

Table 7.2: Summary of the mean absorbed doses calculated with OLINDA/EXM applying organ mass correction as well as a tumour CT-based density correction, and LundADose. For each organ in the two scenarios.

	Absorbed Dose (mGy)				
	OLINDA/EXM *		**LundADose**		
Organ	**Range**	**Average**	**Range**	**Average**	**Percentage difference (%)**
LL	401– 931	661 ± 157	387 – 924	640 ± 154	-3.36 ± 2.40
RL	430 – 1150	755 ± 179	425 – 1103	731 ± 169	-3.06 ± 1.67
LL(T3)	420 – 834	652 ± 126	404 – 816	639 ± 126	-2.24 ± 1.98
RL(T6)	597 – 1785	1025 ± 277	593 – 1949	1027 ± 308	-0.34 ± 3.71
LIV(T3)	291 – 560	434 ± 64	318 – 586	453 ± 73	3.97 ± 4.12
LIV(T6)	358 – 691	545 ± 102	365 – 702	553 ± 104	1.31 ± 4.15
T3(LL)	2079 – 7280	4523 ± 1303	1613 – 6398	3613 ± 1257	-28.44 ± 18.36
T6(RL)	2728– 11678	5044 ± 1963	1975 – 11511	4827 ± 2127	-8.21 ± 17.06
T3(LIV)	841 – 2705	1354 ± 420	668 – 1966	1046 ± 295	-28.80 ± 5.05
T6(LIV)	990 – 1849	1476 ± 249	941 –1761	1403 ± 223	-5.10 ± 2.87

*with organ mass and tumour density correction

LL: left lung; RL: right lung; T3: tumour with 3cm diameter; T6: tumour with 6cm diameter; LIV: liver; LL(T3): LL with T3 embedded; RL(T6): RL with T6 embedded; LIV(T3): LIV with T3 embedded; LIV(T6): LIV with T6 embedded; T3(LL): T3 embedded in LL; T6(RL): T6 embedded in RL; T3(LIV): T3 embedded in LIV; T6(LIV): T6 embedded in LIV.

7.3.2 Tumour doses calculated with OLINDA/EXM with density correction

To evaluate the accuracy of the sphere model used to estimate dose to tumours by OLINDA/EXM, absorbed doses to unit density spheres ("not corrected" (NC)) were compared for the same spheres with absorbed doses calculated with sphere density correction ("corrected" (C)).

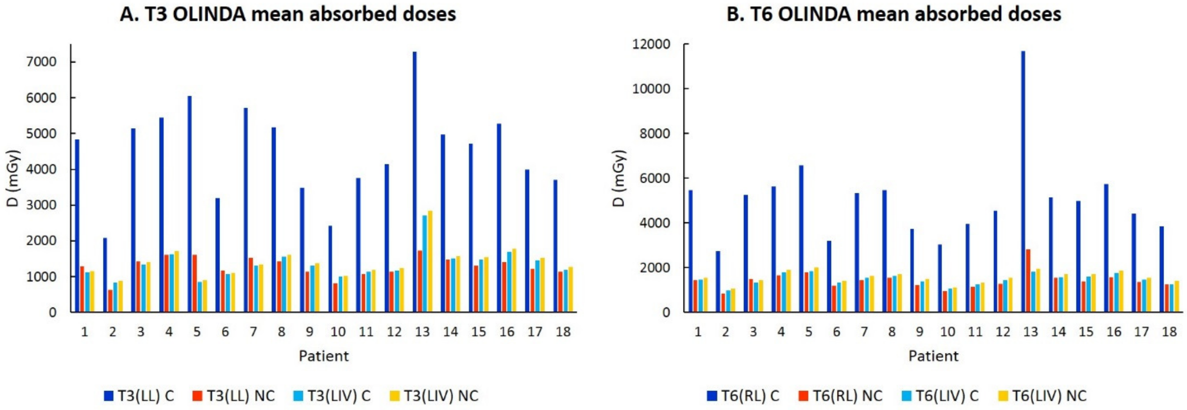

Figure 7.11: *A comparison of OLINDA/EXM mean absorbed tumour doses for (A) T3 and (B) T6 calculated using CT-based density corrected spheres (C) and unit density spheres (NC). Values are shown for T3 embedded in the left lung (T3(LL)) and in the liver (T3(LIV)) as well as for T6 embedded in the right lung (T6(RL)) and in the liver (T6(LIV)).*

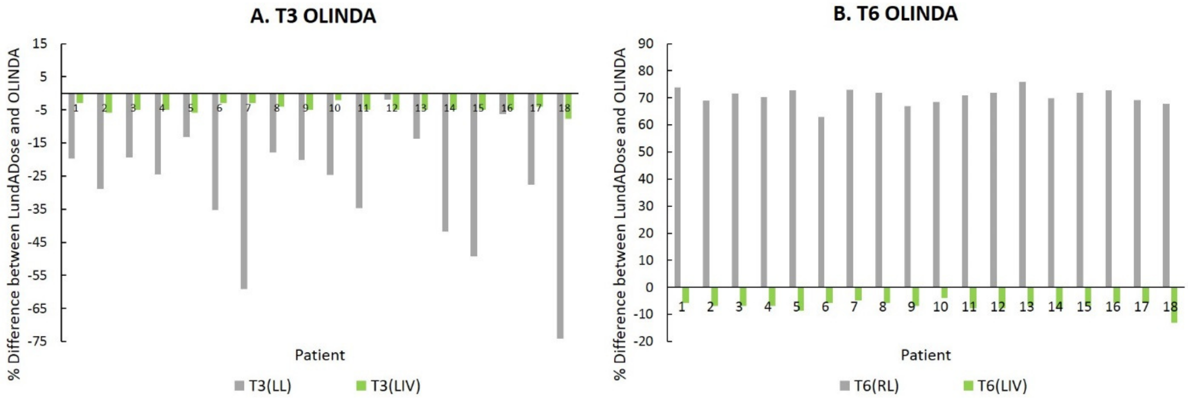

Figure 7.12: ***The percentage differences between the OLINDA/EXM mean absorbed tumour doses calculated by assuming a CT-based density and a unity density sphere for (A) T3 when embedded respectively in the left lung (T3(LL)) and the liver (T3(LIV)) and for (B) T6 when embedded respectively in the right lung (T6(RL)) and in the liver (T6(LIV)).***

From **Figure 7.11**, the need for correction for tumour density when using OLINDA/EXM for clinical dosimetry is emphasized. The tumours in this study were embedded in the organs and therefore had the same density as the organs. The average liver density was 1.06 gcm^{-3} (Appendix III, Table III.10), which is close to the unit density used in OLINDA/EXM for tumour inserts, while the average lung density was 0.26 g/cm^3. (Appendix III, Table III.9). The percentage differences for tumour doses are shown in **Figure 7.12** for OLINDA/EXM using CT-based density values (C) and unit density spheres (NC). For the tumours embedded in the liver, the comparison showed small discrepancies between tumour with and without density correction (percentage differences of less than 10% were observed). Tumours embedded in the lungs resulted in more pronounced differences (average difference of 71% was observed) due to the lower lung density. Therefore, it is recommended that when using OLINDA/EXM for tumour dosimetry, tumour density corrections (density values can be obtained from patient CT images) should be applied.

7.4 Conclusion

Large dosimetric differences can result from using different dose calculation techniques such as conventional organ-level MIRD methods and voxel-level direct MC methods. This chapter focused on the calculation of mean absorbed dose using OLINDA/EXM software (based on the conventional MIRD dosimetry approach) and LundADose MC Simulation software. The more accurate method to predict absorbed dose distributions in patient organs and tumours is said to be the MC method (Ljungberg & Gleisner, 2016). Results presented here show that the MIRD method agrees with the MC method to some extent when accurate quantification of images used for dose planning (by doing proper image reconstruction) is carried out and patient organ masses are normalized with respect to the organ masses of the standard phantom of MIRD. However, for the lungs care must be taken when the MIRD approach is used for dosimetry since there is a likelihood of overestimation of the absorbed doses.

Results from this study clearly indicate that for patient-specific dose calculation, it is necessary to do a proper image reconstruction/quantification first, and it is desirable to use an MC based method for dose calculation. Nevertheless, the MIRD method can be used with some accuracy when patient organ mass corrections are applied. Although, MC based dose calculation methods are gradually overcoming the challenge of slow computer speed with advancement in computer technology, the computer-based dose calculation codes and commercial dose calculation software are still expensive, especially for resource-poor nuclear medicine centres that are interested in patient-specific dosimetry. Using the MIRD method to calculate absorbed doses from reconstructed patient images by applying the organ mass corrections can lead to S factors similar to the patient-specific S factors generated by MC based dose calculation systems, hence, the absorbed doses calculated in this way can be reliable estimates that will be relevant to those who cannot access MC based codes for dose calculation.

7.5 References

Abuqbeitah, M., Demir, M., Çavdar, I., Tanyildizi, H., Yeyin, N., Uslu‑Beşli, L., Kabasakal, L., Işıkcı, N. I. and Sönmezoğlu, K. (2018) ‘Red bone marrow dose estimation using several internal dosimetry models for prospective dosimetry-oriented radioiodine therapy’, *Radiation and Environmental Biophysics*. 57, pp. 395–404.

Bland, J. M. and Altman, D. G. (1986) ‘Statistical Methods For Assessing Agreement Between two methods of Clinical Measurement’, *Lancet*, I, pp. 307–310.

Cecconi, M., Rhodes, A., Poloniecki, J., Rocca, G. D. and Grounds, R. M. (2009) ‘Bench-to-bedside review : The importance of the precision of the reference technique in method comparison studies – with specific reference to the measurement of cardiac output’, *Critical Care*, 13, p. 20.

Dash, A., Russ Knapp Jr, F. F. and Pillai, M. R. A. (2013) ‘Targeted Radionuclide Therapy - An Overview’, *Current Radiopharmaceuticals*, 6, pp. 1–29.

Divoli, A., Chiavassa, S., Ferrer, L., Barbet, J., Flux, G. D. and Bardiès, M. (2009) ‘Effect of patient morphology on dosimetric calculations for internal irradiation as assessed by comparisons of Monte Carlo versus conventional methodologies’, *J. Nucl. Med.;* 50, pp. 316–323.

Hirayama, H., Namito, Y., Bielajew, A. F., Wilderman, S. J. and Nelson, W. R. (2016) 'The EGS5 code system' Report SLAC-R-730, KEK-2005-8., Stanford Linear Accelerator Centre, Stanford CA.

Ljungberg, M. (2018) ‘Absolute Quantitation of SPECT Studies’, *Semin. Nucl. Med.*, 48, pp. 348–358.

Ljungberg, M. and Gleisner, K. S. (2016) ‘Personalized Dosimetry for Radionuclide Therapy Using Molecular Imaging Tools’, *Biomedicines*, 4, pp. 25–45.

Nelson, W.R., Hirayama, H., and Rogers, D.W.O. (1985). '*EGS4 code system'*. Report SLAC-265, Stanford Linear Accelerator Centre Stanford, CA.

Pacilio, M., Ferrari, M., Chiesa, C., Lorenzon, L., Mira, M., Botta, F., Becci, D., torres, L. A., Perez, M. C., Gil, A. V., Basile, C., Ljungberg, M., Pani, R. and Cremonesi, M. (2016) ‘Impact of SPECT corrections on 3D-dosimetry for liver transarterial radioembolization using the patient relative calibration methodology', *Med. Phys.*, 43, pp. 4054–4063.

Siegel, J. A. and Stabin, M. (1994) 'Absorbed Fractions for Electrons and Beta Particles in Spheres of Various Sizes', *J. Nucl. Med.*, 35, pp. 152–156.

Stabin, M. G. (2008) *Fundamentals of Nuclear Medicine Dosimetry*. New York: Springer Science.

Stabin, M. G. (2017) The practice of internal dosimetry in nuclear medicine. Florida: Taylor and Francis.

Stabin, M. G., Sparks, R. B. and Crowe, E. (2005) 'OLINDA/EXM: The Second-Generation Personal Computer Software for Internal Dose Assessment in Nuclear Medicine', *J. Nucl. Med.*, 46, pp. 1023–1027.

CHAPTER EIGHT:

Conclusions and Future Work

8.1 Conclusion

The aim of this thesis was to evaluate the accuracy of ^{131}I activity quantification and absorbed dose calculations to target organs and tumours in three-dimensional (3-D) patient-specific models. In Chapter 5, the first step towards meeting this aim was to design and validate a Monte Carlo (MC) based model of the Siemens Symbia T2 SPECT/CT gamma camera which was used in this study.

The next step was to simulate clinically realistic patient single photon emission computed tomography (SPECT) studies from patient-specific 3-D models for the evaluation of activity quantification and dose calculations. This was done in Chapter 6 for eighteen patients with different body mass indexes. Clinically realistic patient models were created from these patients' computed tomography (CT) images and these patient-specific models were then used in SIMIND to simulate clinically realistic ^{131}I SPECT projection studies for each patient. ^{131}I activity quantification and absorbed dose calculations were successfully carried out using reconstructed images of the simulated patient models studies. The quantification accuracy of ^{131}I was investigated for the different sphere sizes located in varying positional geometries in the aforementioned patient models.

The comparison of organ level internal dose assessment/exponential modelling (OLINDA/EXM) and MC simulation (LundADose) dose estimation methods in Chapter 7 provided insight into the impact of using stylized phantoms representing the average patient, which is the method used in the majority of currently performed dose calculation procedures. Looking at the total dose distributions, it was observed that the mean organ doses calculated by OLINDA/EXM usually agreed well with the mean organ doses calculated by LundADose when S-factors of OLINDA/EXM were rescaled to account for differences between the phantom and patients' organ masses. Given the similar results obtained by the two methods, the current use of OLINDA/EXM at least for diagnostic procedures where the dose is relatively low appears to be appropriate. However, OLINDA/EXM has important limitations for therapeutic applications. While the rescaling of the S-factors can account for differences between the phantom and patients' organ masses as mentioned above, it does not account for differences in composition, shape, or relative spatial distribution of the patient organs.

The dosimetry program, LundADose, used in this thesis is an example of a dosimetry program that can be utilized for therapeutic applications. The close agreement between

OLINDAEXM and LundADose within target organs indicates that fast and accurate 3-D dose distributions can be calculated using the OLINDA/EXM technique when organ mass corrections are used. From the results of Chapter 7, it is evident that the mean doses to target organs of interest of the simulated patients in this study revealed a wide inter-patient variability in absorbed doses to target organs of patients. This variability provides motivation for performing patient-specific internal dose calculations. Personalized dose calculations allow for the selection of patients for therapy, patient-specific treatment planning and monitoring of therapeutic doses. Furthermore, as more accurate internal dose calculations are performed, knowledge of the dose-response relationship will be enhanced.

8.2 Future Work

There are several possibilities for expanding on the work presented in this thesis. As mentioned in chapter 5, the new version of simulating medical imaging nuclear detectors (SIMIND) (version 6.1.2) allows for the experimentally measured energy resolution value for any radionuclide of interest to be used as an input in CHANGE for the SIMIND program thus, enabling the simulated energy spectra and energy resolution to be better matched with the measured spectra and energy resolution of the gamma camera. This study could not use this version of SIMIND due to the level the study had reached at the time of its release. Therefore, it is hereby suggested that this study should be expanded in future using SIMIND version 6.1.2.

This study also covered only simulations of uniform activity distributions in the organs and tumours of the simulated patient models. In future, investigation of non-uniform activity distribution in simulated patient studies should be carried out. Non-uniform activity distribution in organs and tumours is a better representation of clinical scenarios than the uniform activity distribution of radioactivity in organs and tumours used in this study, especially at the voxel level. Using the voxel S factors of MIRD pamphlet 17 to calculate absorbed doses to tumours will make a good comparison with absorbed doses calculated with LundADose, since, LundADose also calculates voxel by voxel absorbed doses. In future, this study can be expanded to include voxel level dosimetry in which voxel non-uniformity of activity concentration can be evaluated.

For tumours dosimetry, this study focused on spherically shaped tumours. The accuracy of activity quantification and dosimetry should also be investigated for irregularly shaped tumours. This will be useful as many clinical tumours are irregularly shaped. LundADose also has the ability to calculate dose-volume histograms from patient images, hence, in future work, such dose-volume histograms can be linked with computational models to yield radiobiological quantities such as equivalent uniform dose and biologically effective dose. These quantities can thus be investigated using similar simulated 3-D patient models.

The comparison of LundADose with OLINDA/EXM dose estimation in Chapter 7 was performed using OLINDA/EXM software (version 1.1), which uses S values calculated for computational phantoms based on stylized models. It would be interesting to repeat the comparison of patient-specific S values calculated using LundADose to the new reference phantom S values based on the more realistic image-based models, which is currently available in OLINDA/EXM software (version 2.0).

Finally, one of the major issues that need to be explored in more detail is further examination into the relationship between absorbed dose and patient response. It would be informative to use response parameters other than patient survival in the dose-response evaluation. A correlation between tumour reduction and dose in a clinical trial will yield important clinical information that can result in optimized patient care.

.

Appendices

Appendix I:

Iodine-131 decay scheme diagram and table.

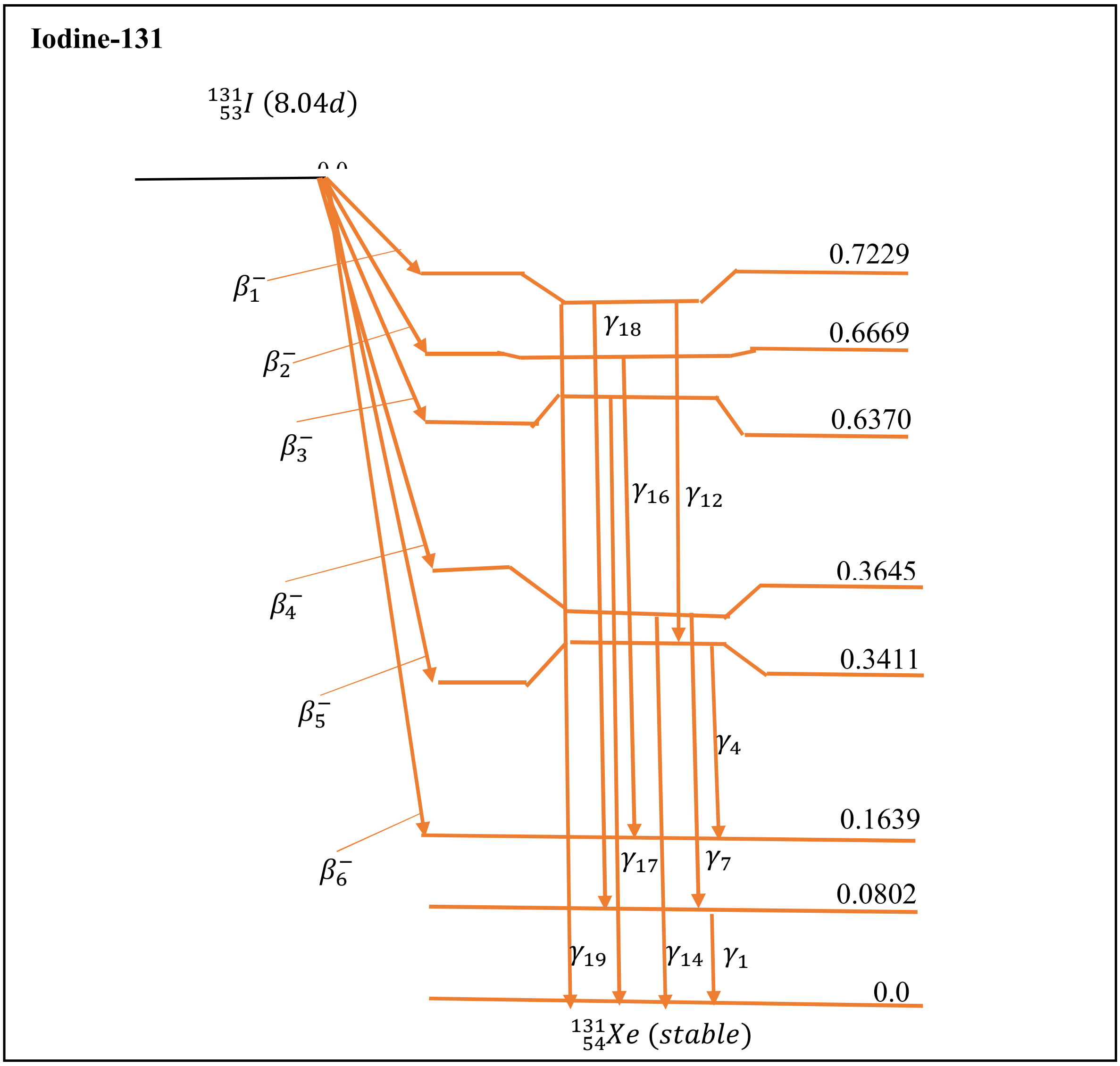

Figure I.1: *Decay scheme for Iodine-131 (Cherry et al, 2012)*

Table I.1: Detailed decay scheme information for I-131 showing the half-life of I-131, the type of radiation emitted, the frequency of the ith emission per nuclear decay (y(i)) in $(Bq.s)^{-1}$, the corresponding transition energy (E(i)) for the emission in MeV as well as the average energy emitted per decay in MeV. (Cherry et al, 2012)

Half Life = 8.04 Days			
Decay Mode (s): β^-			
Radiation	**y (i) $(Bq.s)^{-1}$**	**E (i) (MeV)**	**y (i) x E**
β^- 1	2.13E-02	6.935E-02*	1.48E-
β^- 2	6.20E-03	8.693E-02*	5.39E-04
β^- 3	7.36E-02	9.660E-02*	7.11E-03
β^- 4	8.94E-01	1.915E-01*	1.71E-01
β^- 6	4.20E-03	2.832E-01*	1.19E-03
γ1	2.62E-02	8.018E-02	2.10E-03
ce-K, γ1	3.63E-02	4.562E-02	1.66E-03
ce-L_1, γ1	4.30E-03	7.473E-02	3.21E-04
γ4	2.65E-03	1.772E-01	4.70E-04
γ7	6.06E-02	2.843E-01	1.72E-02
ce-K, γ7	2.48E-03	2.497E-01	6.20E-04
γ12	2.51E-03	3.258E-01	8.18E-04
γ14	8.12E-01	3.645E-01	2.96E-01
ce-K, γ14	1.55E-02	3.299E-01	5.10E-03
ce-L_1, γ14	1.71E-03	3.590E-01	6.13E-04
γ16	3.61E-03	5.030E-01	1.82E-03
γ17	7.27E-02	6.370E-01	4.63E-02
γ18	2.20E-03	6.427E-01	1.41E-03
γ19	1.80E-02	7.229E-01	1.30E-02
$K\alpha_1$ X ray	2.59E-02	2.978E-02	7.72E-04
$K\alpha_2$ X ray	1.40E-02	2.946E-02	4.12E-04
LISTED X, γ AND γ± RADIATIONS		3.80E-01	
OMITTED X, γ AND γ± RADIATIONS**		1,09E-03	
LISTED β, ce AND Auger RADIATIONS		1.90E-01	
OMITTED β, ce AND Auger RADIATIONS**		1.86E-03	
LISTED RADIATIONS		5.70E-01	
OMITTED RADIATIONS		2.95E-03	

*AVERAGE ENERGY (MeV)

**EACH OMMITTED TRANSITION CONTRIBUTES <0.100% TO $\sum y\,(i)\; x\; E\,(i)$ IN ITS CATEGORY

XENON-131m DAUGHTER, YIELD 1.11E-02, IS RADIOACTIVE.
XENON-131 DAUGHTER, YIELD 9.889E-01, IS STABLE.

B

Appendix II:

SIMIND parameters selected in CHANGE:

Table II.1: SIMIND parameters selected in the CHANGE program for simulations

General settings (Simulation flags)		
1. Write result to the screen		TRUE
2. Write image matrix to file		TRUE
3. Write pulse height distribution to file		TRUE
4. Include the collimator		TRUE (False for intrinsic)
5. Simulate a SPECT study		TRUE
6. Include characteristic X-ray emission		TRUE
7. Include backscattering material		TRUE
8. Use a random sampled seed value		FALSE
9. Simulate a transmission study		FALSE
10. Include interactions in the cover		TRUE
11. Include interactions in the phantom		TRUE
12. Include simulation of energy resolution		TRUE
13. Include forced interaction at crystal entry		TRUE
14. Write file Header in Interfile v. 3.3 format		TRUE
15. Save aligned Density Map		FALSE
Camera parameters		
1. Cover material		Aluminum
2. Crystal material		Sodium iodide
3. *Photon Energy	keV	-364.0
4. Crystal half-length	cm	26.650
5. Crystal thickness	cm	0.950
6. Crystal half-width	cm	19.350
7. Backscattering material thickness	cm	40.00
8. Thickness of cover	cm	0.10
9. **Phantom type		-1
10. **source type		-5
Camera imaging parameters		
1. ***Photon direction		3
2. Upper window threshold	%	-15
3. lower window threshold	%	-15
4. Energy resolution (140 keV)	%	9.9
5. Intrinsic resolution (140 keV)	cm	0.38
6. Emitted photon/decay		0.879
7. keV/channel	keV	2
8. SPECT rotation		360 degrees clockwise

Table II.1 contd.

Image parameters	
1. Matrix size for density and source map	512 × 512
2. Energy spectral channel	512
3. ****Scoring Routine: Scattwin	1
Phantom parameters	
1. Pixel size in Density Map cm	0.127
2. Starting image	1
3. Number of CT images	Variable (depends on created phantom)

*Negative value is an indication to SIMIND that a call should be made to the isotope routine file in the SMC database. The absolute values are used to define the energy.

**The negative 5 value is an indication to SIMIND that a binary density map, Code Based Zubal Phantoms, must be used for the phantom type and a user-written source routine, Code Based Zubal Phantoms, must be used for the source type. The negative 1 value is also an indication to SIMIND that a binary density map, Density Distribution Map, must be used for the phantom type.

***The value of 3 is an indication to SIMIND that the solid angle (photon direction) is to be calculated by SIMIND using phantom and camera dimensions, allowing for the whole camera to be exposed to the photons.

****The value of 1 is an indication to SIMIND that the "SCATTWIN" scoring routine is to be used for all simulations. This scouring routine allows for multiple window simulations. Furthermore, it records images that contain only primary photons, images that contain only scattered photons and images containing both primary and scattered photons. The scattwin routine was used in the validation and patient phantom studies.

Table II.2: Symbia high energy all-purpose (HEAP) collimator settings as selected in CHANGE (SIMIND).

HEAP	
1. Code	sy-he
2. Hole diameter	4 mm
3. Septal Thickness	2 mm
4. Length	59.7 mm
5. [1]Hole Shape	-3
6. [1]Collimator type	0

Table II.3: General command line switches used in simulations using SIMIND.

1. Collimator code	**/cc:**	**sy-he**
2. Isotope file	**/fi:**	**I131**
3. X-ray generation	**/xr:**	**1**
4. Number of photons/projection	**/nn:**	**[2]variable**

---

[1] The collimator was set to have a hexagonal hole shape (-3) and the collimator was also set to be a parallel hole collimator (0) as described in the SIMIND collimator database

[2] Depending on the test that is simulated. This is based on the number of photon histories that are required for the particular test to acquire a good count statistics

Table II.4: **Zubal file settings for the validation tests**

	8-bits image value	*CT density value	Activity conc. Ratio
Intrinsic and Extrinsic Energy Resolution			
Styrofoam	16	800	0
Table	6	450	0
Petri dish	24	900	0
Capillary tube	50	970	100
Extrinsic Spatial Resolution			
Styrofoam	16	800	0
Table	6	450	0
Petri dish	24	900	0
Capillary tube	50	970	100
System Sensitivity and Collimator septal penetration			
Styrofoam	16	800	0
Table	6	450	0
Petri dish	24	900	100
Capillary tube	50	970	0

*Note that the specified CT density values are not used by SIMIND since it takes the density values directly from the created density map using the in-house software DensityMap.

Table II.5: **SIMIND settings for energy resolution and system spatial resolution tests**

Camera parameters		
1. The pixel size in simulated image	cm	0.12
2. Number of SPECT projections		1
Phantom parameters		
1. Number of CT images		334
2. Phantom half-length	cm	19
3. SPECT orbital rotation fraction	cm	-6.4
Image parameters		
1. The matrix size of the image		512 × 512

Table II.6: **SIMIND settings system sensitivity and collimator septal penetration fraction tests**

Camera parameters		
1. The pixel size in simulated image	cm	0.24
2. Number of SECT projections		1
Phantom parameters		
1. Number of CT images		334
2. Time	s	600
3. Phantom half-length	cm	19
4. SPECT orbital rotation fraction	cm	-1
Image parameters		
1. The matrix size of the image		512 × 512

Appendix III:

Cumulated activity and absorbed doses calculated using OLINDA and Lundadose

Tables III.1 & III.2 summarise the cumulated activity obtained for the organs and tumours.

Tables III.3 –III.5 report the mean absorbed dose values as calculated using Lundadose and OLINDA. No organ mass or tumour density corrections were applied in OLINDA.

Tables III.6 –III.8 present the mean absorbed dose values as calculated using Lundadose and OLINDA. Organ mass and tumour density corrections were applied in OLINDA.

Tables III.9 & III.10 summarise the volume, density and mass information for the lungs and liver. These values were used in OLINDA to correct for the organ masses and tumour densities.

Table III.11 show the correlations as well as Bland Altman results when a Lundadose and OLINDA calculated mean absorbed doses were compared. OLINDA mean absorbed doses were calculated after applying organ mass and tumour density corrections.

Table III.12 is a comparison of mean absorbed doses calculated with OLINDA without and with organ mass and tumour density corrections.

All cumulated activity values and mean absorbed dose values are reported for the two simulation scenarios on the 18 patients. The values are reported for the left and right lungs; the liver as well as the tumours (3.0 cm tumour (T3) and 6.0 cm tumour (T6))). When tumours were embedded in organs, those organ and tumour values are given correspondingly. The following abbreviations are used in the tables to follow:

LL:	Left lung	T3:	3.0 cm tumour
RL:	Right lung	T6:	6.0 cm tumour
LL(T3):	LL with T3 embedded	T3(LL):	T3 embedded in the left lung
RL(T6):	RL with T6 embedded	T6(RL):	T6 embedded in the right lung
LIV(T3):	Liver (LIV) with T3 embedded	T3(LIV):	T3 embedded in the liver
LIV(T6):	Liver (LIV) with T6 embedded	T6(LIV):	T6 embedded in the liver

Table III.1: Cumulated activity for the lungs and liver of patient models simulated with scenario 1 & 2. Values are reported for the left lung (LL), right lung (RL) without embedded tumours as well as for the left lung with T3 embedded (LL(T3)) and right lung with T6 embedded (RL(T6). Cumulated activity values for the liver with embedded tumours (LIV(T3) and LIV(T6)) are also shown.

	Cumulated Activity (GBq-s)					
Patient ID	**LL**	**RL**	**LL(T3)**	**RL(T6)**	**LIV(T3)**	**LIV(T6)**
1	16.51	15.66	15.03	19.23	13.506	19.33
2	6.62	7.19	7.02	9.53	11.95	14.35
3	15.42	16.49	15.63	20.75	13.52	16.36
4	14.41	14.95	10.53	15.55	13.92	18.34
5	10.59	11.19	10.46	16.31	9.36	19.28
6	10.93	12.89	11.69	15.82	14.83	16.85
7	8.11	11.23	9.35	14.44	19.07	19.66
8	11.12	14.28	12.27	18.31	16.41	19.81
9	12.40	15.49	13.31	19.02	19.08	20.87
10	5.74	6.51	6.37	8.59	20.71	22.34
11	6.74	8.38	7.21	11.61	18.04	19.50
12	13.00	14.55	13.21	17.56	16.08	19.54
13	12.86	19.66	13.52	29.34	19.28	19.96
14	11.28	13.23	12.06	17.28	16.28	19.29
15	8.04	10.30	8.97	14.72	15.70	18.96
16	17.00	19.66	17.55	24.32	10.18	12.50
17	8.81	11.55	9.84	15.52	21.73	23.84
18	7.21	9.86	8.13	12.93	28.12	30.41
Mean	10.93	12.95	11.23	16.71	16.54	19.51
SD	3.50	3.80	3.15	4.97	4.49	3.77
Min	5.74	6.51	6.37	8.59	9.36	12.50
Max	17.00	19.66	17.55	29.34	28.12	30.41

Table III.2: Cumulated activity for the 3.0 cm (T3) and 6.0 cm tumours (T3) embedded in the lungs and liver of the patient phantoms simulated with scenario 1 & 2. Tumour cumulated activity values are given with T3 embedded in the LL and LIV (T3(LL) & T3(LIV) as well as for T6 embedded in the RL and LIV (T6(RL) & T6(LIV).

	Cumulated Activity (GBq-s)			
Patient ID	**T3(LL)**	**T3(LIV)**	**T6(RL)**	**T6(LIV)**
1	0.56	0.50	4.65	5.03
2	0.28	0.39	2.76	3.43
3	0.62	0.62	4.85	4.64
4	0.70	0.74	5.42	6.20
5	0.70	0.39	5.85	6.52
6	0.51	0.48	3.85	4.45
7	0.66	0.58	3.62	5.27
8	0.62	0.70	5.00	5.56
9	0.49	0.60	4.02	4.82
10	0.35	0.45	3.11	3.63
11	0.47	0.52	3.74	4.34
12	0.50	0.54	4.15	5.08
13	0.75	1.23	9.14	6.31
14	0.64	0.69	5.04	5.53
15	0.57	0.67	4.55	5.59
16	0.61	0.77	5.10	6.09
17	0.53	0.66	4.42	5.02
18	0.49	0.55	4.03	4.56
Mean	0.56	0.62	4.63	5.12
SD	0.12	0.19	1.38	0.87
Min	0.28	0.39	2.76	3.43
Max	0.75	1.23	9.14	6.52

Table III.3: Mean absorbed dose, D (mGy) calculated witsh OLINDA (no mass correction to organs) and Lundadose for the left lung (LL) and right lung (RL) with no embedded tumours as well as with embedded tumours (LL(T3) and RL(T6))

Patient	Mean absorbed dose (mGy)							
ID	LL		RL		LL(T3)		RL(T6)	
	Lund[*]	OLINDA	Lund	OLINDA	Lund	OLINDA	Lund	OLINDA
1	759.36	661.33	729.60	538.43	703.68	516.92	926.40	567.67
2	428.16	288.37	480.96	312.90	451.2	305.53	672.00	414.94
3	755.52	534.97	767.04	572.02	785.28	542.41	1041.60	719.97
4	923.52	677.27	955.20	651.09	686.4	458.59	1092.48	627.61
5	868.80	461.00	853.44	487.49	816.00	455.43	1423.68	710.08
6	497.38	476.20	534.72	561.54	501.12	509.01	707.52	688.86
7	592.32	353.24	768.00	577.16	632.64	406.97	1045.44	628.66
8	686.40	484.33	842.88	621.74	738.24	534.29	1152.00	797.53
9	525.12	539.86	615.36	674.56	531.84	579.45	811.20	828.38
10	386.88	249.99	425.28	283.55	404.16	277.38	593.28	371.90
11	492.48	293.33	594.24	364.98	510.72	313.95	873.60	505.70
12	682.56	441.93	751.68	504.88	698.88	458.36	979.20	597.16
13	773.76	560.18	1103.04	856.38	752.64	588.78	1948.96	1277.79
14	664.32	491.40	751.68	576.28	694.08	525.26	1050.24	752.53
15	663.36	349.92	798.72	448.36	702.72	390.56	1229.76	641.15
16	780.48	740.09	877.44	856.22	784.32	764.42	1123.20	1059.26
17	552.00	383.49	701.76	502.84	594.24	428.34	966.72	676.07
18	480	313.8	614.40	429.24	510.72	353.99	852.48	563.04
Mean	639.58	461.15	731.40	545.54	638.83	467.20	1027.21	690.46
SD	153.95	141.93	169.22	156.22	125.93	119.62	307.89	214.00
Min	386.88	249.99	425.28	283.55	404.16	277.38	593.28	371.90
Max	923.52	740.09	1103.04	856.38	816.00	764.42	1948.96	1277.79

[*] Lund: Lundadose calculated mean absorbed dose values

Table III.4: Mean absorbed dose, D (mGy) calculated with OLINDA (no mass correction to organs) and Lundadose for the liver with embedded tumours T3 and T6 (LIV(T3) & LIV(T6)

Patient ID	Mean absorbed dose (mGy) LIV(T3)		LIV(T6)	
	Lund[*]	OLINDA	Lund	OLINDA
1	408	304.96	546.24	436.67
2	317.76	350.66	366.72	421.25
3	558.72	300.02	616.32	363.06
4	559.68	408.57	699.84	538.31
5	486.72	274.68	692.16	565.80
6	415.68	435.25	506.88	494.49
7	475.20	559.71	524.16	577.16
8	450.24	481.71	576.96	566.56
9	443.52	559.91	518.40	612.66
10	318.72	607.89	364.80	655.57
11	398.40	529.38	463.68	572.39
12	450.24	356.77	525.12	433.69
13	585.60	565.90	677.76	585.88
14	481.92	477.96	626.88	566.30
15	451.20	460.91	579.84	556.46
16	505.92	298.72	701.76	366.89
17	420.48	637.92	493.44	699.69
18	423.36	825.26	469.44	892.51
Mean	452.85	468.68	552.80	550.30
SD	72.83	145.15	103.75	126.67
Min	317.76	274.68	364.80	363.06
Max	585.60	825.26	701.76	892.51

[*]Lund: Lundadose calculated mean absorbed dose values

Table III.5: Mean absorbed dose, D (mGy) calculated with OLINDA (no mass correction to organs) and Lundadose for the 3.0 cm tumour embedded in the left lung (T3(LL)) and liver (T3(LIV) as well as for the 6.0 cm tumour embedded in the right lung (T6(LL)) and liver (T6(LIV).

Patient ID	**Mean absorbed dose (mGy)**							
	T3(LL)		**T3(LIV)**		**T6(RL)**		**T6(LIV)**	
	Lund[*]	**OLINDA**	**Lund**	**OLINDA**	**Lund**	**OLINDA**	**Lund**	**OLINDA**
1	4034.88	1287.71	864.00	1152.58	4768.32	1431.68	1334.40	1548.77
2	1612.80	635.90	668.16	890.27	2495.04	849.48	940.80	1057.00
3	4312.32	1422.84	1042.56	1414.89	5581.44	1494.49	1236.48	1429.55
4	4376.64	1613.61	1301.76	1708.99	4848.96	1667.99	1661.76	1907.49
5	5348.16	1613.61	708.48	898.21	6958.08	1803.18	1760.64	2009.68
6	2371.20	1168.47	849.60	1104.88	2689.92	1186.86	1257.60	1405.07
7	3599.04	1526.17	1006.08	1343.35	3970.56	1450.84	1459.20	1624.35
8	4388.16	1430.78	1184.64	1613.61	5519.04	1541.32	1511.04	1713.76
9	2905.92	1136.68	1018.56	1375.14	4180.80	1237.95	1317.12	1484.91
10	1939.20	810.78	720.00	1025.40	1974.72	959.07	1080.00	1118.74
11	2783.04	1073.09	927.36	1192.32	3384.00	1152.80	1229.76	1336.95
12	4062.72	1144.63	933.12	1232.06	4898.88	1277.34	1369.92	1563.67
13	6398.40	1724.89	1966.08	2837.72	11511.36	2816.53	1735.68	1942.62
14	3503.04	1470.53	1132.80	1581.81	5112.96	1553.08	1512.00	1704.18
15	3159.36	1303.60	1165.44	1550.02	5088.00	1400.81	1545.60	1722.28
16	4968.96	1406.94	1281.60	1780.53	6302.40	1571.13	1651.20	1874.49
17	3134.40	1224.12	1104.00	1518.22	4447.68	1361.43	1386.24	1546.64
18	2129.28	1136.68	959.04	1271.81	3152.64	1241.15	1260.48	1404.01
Mean	3612.64	1285.06	1046.29	1416.21	4826.93	1444.29	1402.77	1577.45
SD	1256.58	279.67	295.38	441.24	2127.24	417.48	222.92	266.40
Min	1612.80	635.90	668.16	890.27	1974.72	849.48	940.80	1057.00
Max	6398.40	1724.89	1966.08	2837.72	11511.36	2816.53	1760.64	2009.68

[*] Lund: Lundadose calculated mean absorbed dose values

Table III.6: Mean absorbed dose, D (mGy) calculated with OLINDA (applied mass correction to organs and density correction for tumours) and Lundadose for the left lung (LL) and right lung (RL) with no embedded tumours as well as with embedded tumours (LL(T3) and RL(T6))

Patient	Mean absorbed dose (mGy)							
ID	LL		RL		LL(T3)		RL(T6)	
	Lund[*]	OLINDA	Lund	OLINDA	Lund	OLINDA	Lund	OLINDA
1	759.36	819.74	729.60	764.16	703.68	733.63	926.40	954.99
2	428.16	466.05	480.96	479.54	451.20	468.24	672.00	670.62
3	755.52	779.46	767.04	801.63	785.28	760.13	1041.6	1049.01
4	923.52	930.82	955.20	976.14	686.40	687.54	1092.48	1004.49
5	868.80	903.47	853.44	892.83	816.00	834.12	1423.68	1391.64
6	497.38	496.82	534.72	559.58	501.12	507.23	707.52	718.69
7	592.32	600.49	768.00	787.74	632.64	655.60	1045.44	1068.70
8	686.40	713.95	842.88	877.23	738.24	753.85	1152.00	1175.64
9	525.12	531.36	615.36	638.79	531.84	548.72	811.20	815.34
10	386.88	401.35	425.28	429.62	404.16	420.27	593.28	597.07
11	492.48	504.88	594.24	592.49	510.72	509.67	873.60	870.39
12	682.56	693.28	751.68	776.23	698.88	704.71	979.20	956.49
13	773.76	782.51	1103.04	1150.08	752.64	790.70	1948.96	1784.94
14	664.32	702.38	751.68	783.13	694.08	713.79	1050.24	1075.61
15	663.36	691.21	798.72	830.29	702.72	723.26	1229.76	1266.47
16	780.48	796.65	877.44	890.05	784.32	794.61	1123.20	1139.60
17	552.00	577.76	701.76	717.06	594.24	610.82	966.72	1018.56
18	480.00	497.51	614.40	640.06	510.72	527.85	852.48	892.65
Mean	639.58	660.54	731.40	754.81	638.83	652.49	1027.21	1025.05
SD	153.95	157.43	169.22	178.54	125.93	126.23	307.89	277.50
Min	386.88	401.35	425.28	429.62	404.16	420.27	593.28	597.07
Max	923.52	930.82	1103.04	1150.08	816.00	834.12	1948.96	1784.94

[*] Lund: Lundadose calculated mean absorbed dose values

Table III.7: Mean absorbed dose, D (mGy) calculated with OLINDA (applied mass correction to organs and density correction for tumours) and Lundadose for the liver with embedded tumours T3 and T6 (LIV(T3) & LIV(T6)

Patient ID	Mean absorbed dose (mGy) LIV(T3)		LIV(T6)	
	Lund[*]	OLINDA	Lund	OLINDA
1	408.00	410.15	546.24	548.33
2	317.76	290.57	366.72	373.14
3	558.72	509.58	616.32	680.18
4	559.68	472.89	699.84	690.90
5	486.72	463.00	692.16	654.69
6	415.68	410.89	506.88	498.55
7	475.20	456.32	524.16	506.72
8	450.24	443.85	576.96	576.31
9	443.52	436.00	518.40	505.87
10	318.72	319.10	364.80	358.23
11	398.40	396.70	463.68	455.21
12	450.24	422.59	525.12	549.87
13	585.60	559.98	677.76	622.52
14	481.92	480.29	626.88	611.75
15	451.20	445.88	579.84	581.73
16	505.92	488.93	701.76	686.28
17	420.48	409.15	493.44	471.90
18	423.36	391.23	469.44	440.67
Mean	452.85	433.73	552.80	545.16
SD	72.83	63.56	103.75	102.40
Min	317.76	290.57	364.80	358.23
Max	585.60	559.98	701.76	690.90

[*] Lund: Lundadose calculated mean absorbed dose values

Table III.8: Mean absorbed dose, D (mGy) calculated with OLINDA (applied mass correction to organs and density correction for tumours) and Lundadose for the 3.0 cm tumour embedded in the left lung (T3(LL)) and liver (T3(LIV) as well as for the 6.0 cm tumour embedded in the right lung (T6(LL)) and liver (T6(LIV).

Patient ID	Mean absorbed dose (mGy)							
	T3(LL)		T3(LIV)		T6(RL)		T6(LIV)	
	Lund*	OLINDA	Lund	OLINDA	Lund	OLINDA	Lund	OLINDA
1	4034.88	4830.17	864.00	1118.61	4768.32	5478.65	1334.40	1464.09
2	1612.80	2078.51	668.16	841.13	2495.04	2727.61	940.80	989.60
3	4312.32	5146.75	1042.56	1348.71	5581.44	5265.63	1236.48	1338.72
4	4376.64	5449.06	1301.76	1629.06	4848.96	5630.39	1661.76	1786.29
5	5348.16	6052.62	708.48	848.64	6958.08	6588.15	1760.64	1849.49
6	2371.20	3204.84	849.60	1072.32	2689.92	3198.01	1257.60	1328.25
7	3599.04	5724.65	1006.08	1303.75	3970.56	5346.40	1459.20	1548.72
8	4388.16	5175.51	1184.64	1551.96	5519.04	5477.29	1511.04	1619.28
9	2905.92	3491.67	1018.56	1310.83	4180.80	3735.88	1317.12	1390.56
10	1939.20	2417.92	720.00	1004.29	1974.72	3045.66	1080.00	1076.42
11	2783.04	3748.18	927.36	1136.56	3384.00	3955.78	1229.76	1241.32
12	4062.72	4140.41	933.12	1174.44	4898.88	4539.19	1369.92	1451.83
13	6398.40	7279.97	1966.08	2705.00	11511.36	11678.17	1735.68	1819.19
14	3503.04	4965.89	1132.80	1507.83	5112.96	5152.28	1512.00	1582.29
15	3159.36	4715.46	1165.44	1477.52	5088.00	4977.98	1545.60	1612.85
16	4968.96	5277.41	1281.6	1697.26	6302.40	5740.32	1651.20	1772.00
17	3134.40	4001.13	1104.00	1460.22	4447.68	4409.57	1386.24	1461.38
18	2129.28	3707.46	959.04	1181.47	3152.64	3853.16	1260.48	1241.41
Mean	3612.64	4522.65	1046.29	1353.87	4826.93	5044.45	1402.77	1476.32
SD	1256.58	1302.62	295.38	419.89	2127.24	1962.83	222.92	248.80
Min	1612.80	2078.51	668.16	841.13	1974.72	2727.61	940.80	989.60
Max	6398.40	7279.97	1966.08	2705.00	11511.36	11678.17	1760.64	1849.49

*Lund: Lundadose calculated mean absorbed dose values

Table III.9: Volume (ml), density (gcm^{-3}) and mass (g) values for the respective lungs of the 18 patient phantoms. These values were used to calculate the OLINDA mean absorbed doses to the lungs with organ mass correction.

		Lung1			Lung 2	
Patient ID	**Volume** (ml)	**Density** (gcm^{-3})	**Mass** (g)	**Volume** (ml)	**Density** (gcm^{-3})	**Mass** (g)
1	2710	0.26	705	2770	0.25	693
2	1740	0.30	522	1650	0.30	495
3	2620	0.27	707	2520	0.27	680
4	1840	0.29	534	1860	0.29	539
5	1680	0.25	420	1570	0.26	408
6	2230	0.36	803	2130	0.36	767
7	1910	0.26	497	1810	0.26	471
8	2100	0.27	567	2010	0.27	543
9	2640	0.32	845	2540	0.32	813
10	1600	0.33	528	1510	0.33	498
11	1760	0.28	493	1660	0.28	465
12	2480	0.26	645	2380	0.26	619
13	2590	0.23	596	2490	0.23	573
14	2030	0.29	589	1930	0.29	560
15	1600	0.27	432	1500	0.27	405
16	2960	0.26	770	2860	0.26	744
17	1870	0.30	561	1770	0.30	531
18	1850	0.29	537	1740	0.29	505
Average	2123	0.28	597	2039	0.28	573
SD	435	0.03	124	445	0.03	121
% SD	20	11.10	21	22	11.10	21
Min	1600	0.23	420	1500	0.23	405
Max	2960	0.36	845	2860	0.36	813

Table III.10: Volume (ml), density (gcm^{-3}) and mass (g) values for the liver of the 18 patients drawn for the 2 scenarios. These values were used to calculate the OLINDA mean absorbed doses to the lungs with organ mass correction.

	Liver, Scenario 1			**Liver, Scenario 2**		
Patient ID	**Volume** (ml)	**Density** (gcm^{-3})	**Mass** (g)	**Volume** (ml)	**Density** (gcm^{-3})	**Mass** (g)
1	1450	1.06	1537	1350	1.06	1431
2	1450	1.09	1581	1550	1.09	1690
3	961	1.08	1038	1060	1.08	1145
4	1010	1.08	1091	1120	1.08	1210
5	1110	1.09	1210	762	1.09	831
6	1310	1.06	1389	1410	1.06	1495
7	1520	1.06	1611	1620	1.06	1717
8	1320	1.07	1412	1420	1.07	1519
9	1590	1.08	1717	1690	1.08	1825
10	2440	1.05	2562	2540	1.05	2667
11	1630	1.08	1760	1730	1.08	1868
12	1420	1.08	1534	1520	1.08	1642
13	1220	1.08	1318	1310	1.08	1415
14	1200	1.08	1296	1290	1.08	1393
15	1240	1.08	1339	1340	1.08	1447
16	693	1.08	748	792	1.08	855
17	1940	1.07	2076	2040	1.07	2183
18	2650	1.07	2836	2760	1.07	2953
Average	1453	1.07	1559	1517	1.07	1627
SD	487	0.01	513	520	0.01	547
% SD	34	1.02	33	34	1.02	34
Min	693	1.05	748	762	1.05	831
Max	2650	1.09	2836	2760	1.09	2953

Table III.11: (A) Results of calculated statistics for linear regression and Bland-Altman analysis of Lundadose vs OLINDA mean absorbed dose values. OLINDA mean absorbed dose values were corrected for organ mass and tumour density. All parameters are reported in mGy.

Organ	Bias	SD	CI Bias	LLoA	CI LLoA	ULoA	CI ULoA
LL	-20.96	15.10	-28.47 − -13.45	-50.56	-63.57 − -37.55	8.64	-4.37 – 21.65
RL	-23.40	13.59	-30.16 − -16.64	-50.03	-61.73 − -38.33	3.23	-8.48 – 14.93
LL(T3)	-13.66	13.53	-20.39 − -6.93	-40.18	-51.83 − -28.52	12.86	1.21 – 24.52
RL(T6)	2.16	51.34	-23.37 – 27.69	-98.46	-142.69 − -54.24	102.78	58.56 – 147.00
LIV(T3)	19.13	21.76	8.30 – 29.95	-23.53	-42.27 − -4.78	61.78	43.03 – 80.52
LIV(T6)	7.64	25.01	-4.79 – 20.08	-41.37	-62.91 − -19.83	56.65	35.11 – 78.19
T3(LL)	-910.01	503.19	-1160.26 − -659.75	-1896.27	-2329.72 – 1462.81	76.26	-357.20 – 509.71
T3(LIV)	-307.57	129.93	-372.19 − -242.96	-562.23	-674.15 − -450.31	-52.91	-164.83 – 59.01
T6(RL)	-217.52	561.40	-496.72 – 61.68	-1317.85	-1801.44 − -834.27	882.82	399.23 – 1366.41
T6(LIV)	-73.54	41.81	-94.33 − -52.75	-155.48	-191.50 − -119.47	8.40	-27.61 – 44.41

SD: standard deviation; CI: 95% confidence interval, LLoA: lower limit of agreement; ULoA: upper level of agreement.

Table III.12: Summary of the mean absorbed doses calculated with OLINDA applying no organ mass correction and asuming tumours as unit density spheres vs OLINDA calculated mean absorbed doses after organ mass correction as well as a tumour CT-based density corrections were applied. For each organ in the two scenarios the dose range, average and standard deviation are reported. The percentage difference values obtained between the mean absorbed doses calculated using OLINDA without and with mass and density corrections are also reported.

	Absorbed Dose (mGy)				
	OLINDA (no organ mass or tumour density correction)		OLINDA (with organ mass and tumour density correction)		
Organ	**Range**	**Average**	**Range**	**Average**	**Percentage difference (%)**
LL	250 – 740	461 ± 142	387 – 924	640 ± 154	30.1 ± 14.5
RL	284 – 856	546 ± 156	425 – 1103	731 ± 169	27.4 ± 14.2
LL(T3)	277 –764	467 ± 120	404 – 816	639 ± 126	28.0 ± 14.5
RL(T6)	372 – 1278	690 ± 214	593 – 1949	1027 ± 308	32.0 ± 14.5
LIV(T3)	275 – 825	469 ± 145	318 – 586	453 ± 73	11.4 ± 42.2
LIV(T6)	363 – 893	550 ± 127	365 – 702	553 ± 104	-6.5 ± 39.4
T3(LL)	636 – 1725	1285 ± 280	1613 – 6398	3613 ± 1257	70.9 ± 3.02
T6(RL)	849 – 2817	1444 ± 417	1975 – 11511	4827 ± 2127	70.6 ± 2.96
T3(LIV)	890 – 2838	1416 ± 441	668 – 1966	1046 ± 295	-4.59 ± 1.27
T6(LIV)	1057 – 2010	1577 ± 266	941 –1761	1403 ± 223	-6.86 ± 1.92

Appendix IV: Approval letters (granting permissions for this research work).

Head of Department of Medical Physics

UNIVERSITY OF THE FREE STATE
UNIVERSITEIT VAN DIE VRYSTAAT
YUNIVESITHI YA FREISTATA

UFS·UV
HEALTH SCIENCES
GESONDHEIDSWETENSKAPPE

The Head,
Department of Medical Physics
Faculty of Health Sciences, University of Free State
Bloemfontein, 9300
24th January, 2017

Dear Sir,

REQUEST FOR APPROVAL TO UNDERTAKE A PhD (MEDICAL PHYSICS) RESEARCH PROJECT

I wish to request for your approval to undertake a PhD (Medical Physics) research project in the Department of Medical Physics, in the Faculty of Health Sciences, University of Free State. The clinical component of this project will be carried out at the Department of Nuclear Medicine in Universitas Academic Hospital.

The research project is titled: **"Accuracy of Iodine-131 Activity Quantification and Dosimetry for Three-Dimensional Patient Specific Models"**. This study will involve quantification of radionuclide activity for tumours and organs using patients' Computed Tomography (CT) images which will serve as input to a Monte Carlo computer simulation program with the aim of simulating Single Photon Emission Computed Tomography (SPECT) patient images. The processed SPECT and CT images will be used to calculate radiation doses to the different tumours and organs of interest by using specialized three-dimensional dose calculation software. The results from this research are expected to provide additional information for accurate dose planning of I-131 therapies carried out in the Nuclear Medicine Department. This may eventually result in better treatment outcomes for these therapy procedures in the department. Please find enclosed the protocol for the research work for more details.

The research will only collect preselected patient CT data from existing I-131 imaging procedures in the department of nuclear medicine, hence, there will be no additional radiation exposure to both patients and staff. Proper anonymity of the preselected CT images will ensure that privacy is protected and that data cannot be directly associated with any specific individual. Tracer amounts of radionuclides will be used in the initial experimental tests and these radionuclides will be handled by a registered Medical Physicist (the supervisor of the project) while the researcher will be under constant supervision. Approval from the Radiation Control Committee and other relevant departments and committees has also been applied for.

I would be very grateful if this request is granted.

Faithfully yours,

John E. Ejeh

Approved
25 Jan 2017

Department of Medical Physics
Room 443, E-Block, Francois Retief Building, Faculty of Health Sciences
T: +27(0)51 405 3158
F: +27(0)51 444 3822
E: raewid@ufs.ac.za

205 Nelson Mandela Drive/Rylaan
Park West/Parkwes
Bloemfontein 9301
South Africa/Suid-Afrika

PO Box/Posbus 339
Bloemfontein 9300
South Africa/Suid-Afrika
www.ufs.ac.za

UNIVERSITY OF THE FREE STATE
UNIVERSITEIT VAN DIE VRYSTAAT
YUNIVESITHI YA FREISTATA

Head of Department of Nuclear Medicine

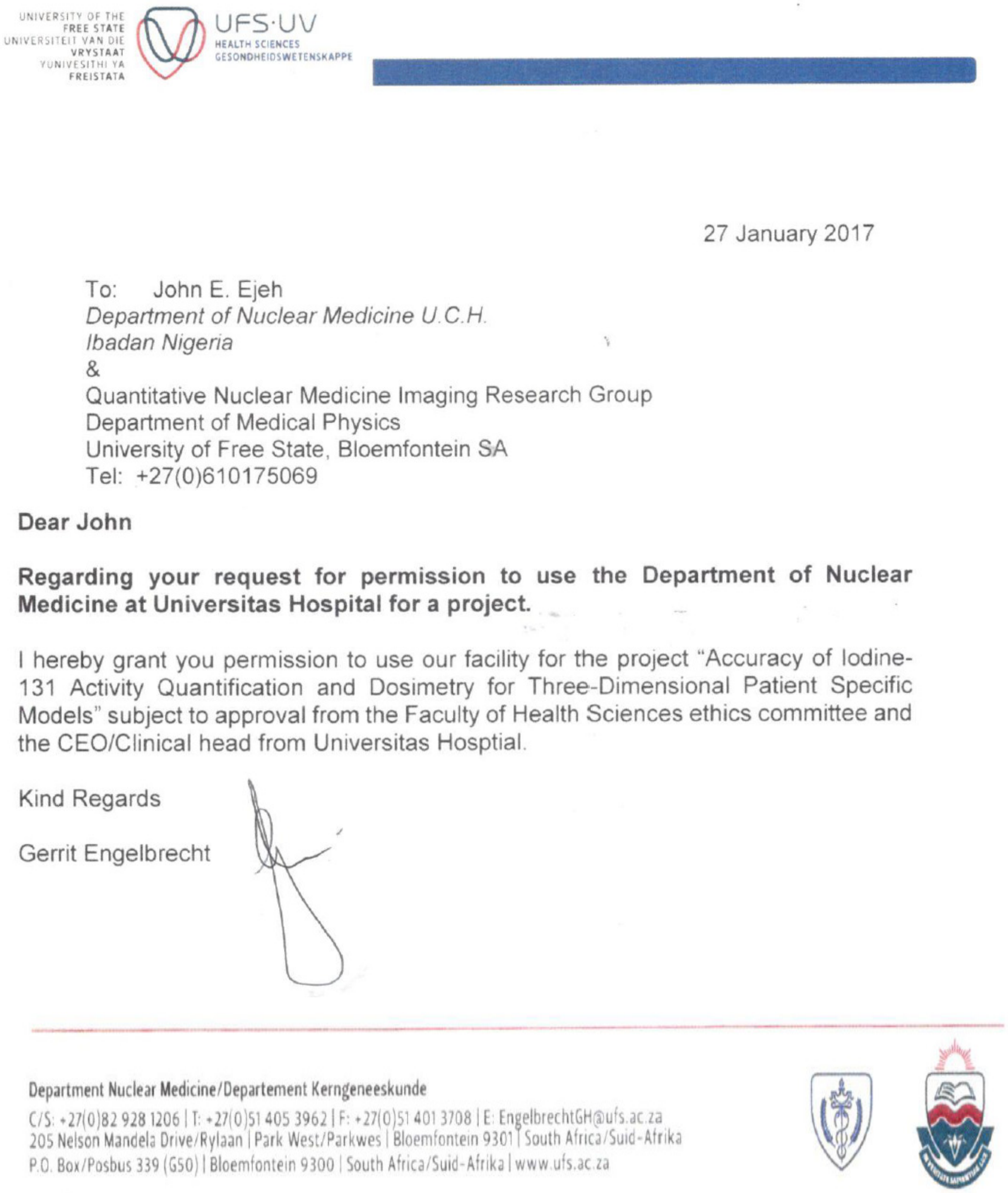

UNIVERSITY OF THE
FREE STATE
UNIVERSITEIT VAN DIE
VRYSTAAT
YUNIVESITHI YA
FREISTATA
UFS·UV
HEALTH SCIENCES
GESONDHEIDSWETENSKAPPE

27 January 2017

To: John E. Ejeh
Department of Nuclear Medicine U.C.H.
Ibadan Nigeria
&
Quantitative Nuclear Medicine Imaging Research Group
Department of Medical Physics
University of Free State, Bloemfontein SA
Tel: +27(0)610175069

Dear John

Regarding your request for permission to use the Department of Nuclear Medicine at Universitas Hospital for a project.

I hereby grant you permission to use our facility for the project "Accuracy of Iodine-131 Activity Quantification and Dosimetry for Three-Dimensional Patient Specific Models" subject to approval from the Faculty of Health Sciences ethics committee and the CEO/Clinical head from Universitas Hosptial.

Kind Regards

Gerrit Engelbrecht

Department Nuclear Medicine/Departement Kerngeneeskunde
C/S: +27(0)82 928 1206 | T: +27(0)51 405 3962 | F: +27(0)51 401 3708 | E: EngelbrechtGH@ufs.ac.za
205 Nelson Mandela Drive/Rylaan | Park West/Parkwes | Bloemfontein 9301 | South Africa/Suid-Afrika
P.O. Box/Posbus 339 (G50) | Bloemfontein 9300 | South Africa/Suid-Afrika | www.ufs.ac.za

Head of Department of Biostatistics

UNIVERSITY OF THE FREE STATE
UNIVERSITEIT VAN DIE VRYSTAAT
YUNIVESITHI YA FREISTATA
UFS·UV
HEALTH SCIENCES
GESONDHEIDSWETENSKAPPE

3 March 2017

For attention: Health Sciences Research Ethics Committee, UFS

Title of project:

Accuracy of Iodine-131 activity quantification and dosimetry for three-dimensional patient-specific models

Researcher:

Mr JE Ejeh, Dept of Medical Physics

I hereby confirm that I provided inputs on the protocol and as member of the PhD evaluation committee approve the protocol. I will advise on statistical approaches if needed.

Yours faithfully

G Joubert

Departement Biostatistiek
Department of Biostatistics
T: +27(0)51 401 3114/5/6/7, F: +27(0)51 401 3641
205 Nelson Mandela Drive/Rylaan, Park West/Parkwes, Bloemfontein 9301, South Africa/Suid-Afrika
P.O. Box/Posbus 339 (G31), Bloemfontein 9300, South Africa/Suid-Afrika, www.ufs.ac.za

Radiation Control Committee

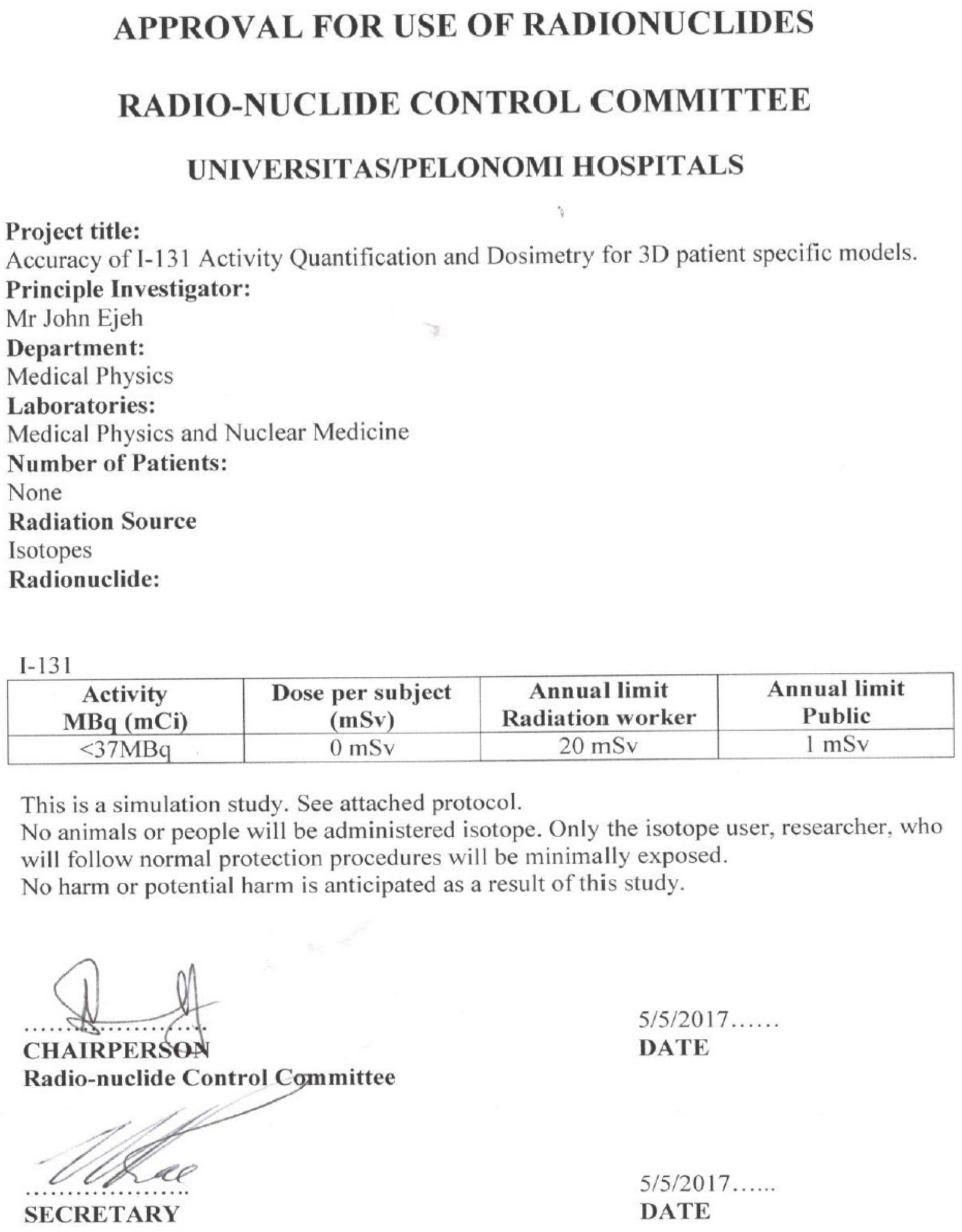

APPROVAL FOR USE OF RADIONUCLIDES

RADIO-NUCLIDE CONTROL COMMITTEE

UNIVERSITAS/PELONOMI HOSPITALS

Project title:
Accuracy of I-131 Activity Quantification and Dosimetry for 3D patient specific models.
Principle Investigator:
Mr John Ejeh
Department:
Medical Physics
Laboratories:
Medical Physics and Nuclear Medicine
Number of Patients:
None
Radiation Source
Isotopes
Radionuclide:

I-131

Activity MBq (mCi)	Dose per subject (mSv)	Annual limit Radiation worker	Annual limit Public
<37MBq	0 mSv	20 mSv	1 mSv

This is a simulation study. See attached protocol.
No animals or people will be administered isotope. Only the isotope user, researcher, who will follow normal protection procedures will be minimally exposed.
No harm or potential harm is anticipated as a result of this study.

…………………
CHAIRPERSON
Radio-nuclide Control Committee

5/5/2017……
DATE

…………………
SECRETARY

5/5/2017……
DATE

Health Sciences Research Ethics Committee

UNIVERSITY OF THE
FREE STATE
UNIVERSITEIT VAN DIE
VRYSTAAT
YUNIVESITHI-YA
FREISTATA

UFS·UV
HEALTH SCIENCES
GESONDHEIDSWETENSKAPPE

IRB nr 00006240
REC Reference nr 230408-011
IORG0005187
FWA00012784

13 June 2017

MR JOHN EJEH
DEPT OF MEDICAL PHYSICS
FACULTY OF HEALTH SCIENCES
UFS

Dear Mr John Ejeh

HSREC 48/2017 (UFS-HSD2017/0366)
PRINCIPAL INVESTIGATOR: MR JOHN EJEH
SUPERVISOR: DR JA VAN STADEN
PROJECT TITLE: ACCURACY OF IODINE-131 ACTIVITY QUANTIFICATION AND DOSIMETRY FOR THREE-DIMENSIONAL PATIENT-SPECIFIC MODELS

1. You are hereby kindly informed that the Health Sciences Research Ethics Committee (HSREC) approved this protocol after all conditions were met. This decision will be ratified at the next meeting.
2. The Committee must be informed of any serious adverse event and/or termination of the study.
3. Any amendment, extension or other modifications to the protocol must be submitted to the HSREC for approval.
4. A progress report should be submitted within one year of approval and annually for long term studies.
5. A final report should be submitted at the completion of the study.
6. Kindly use the **HSREC NR** as reference in correspondence to the HSREC Secretariat.
7. The HSREC functions in compliance with, but not limited to, the following documents and guidelines: The SA National Health Act. No. 61 of 2003; Ethics in Health Research: Principles, Structures and Processes (2015); SA GCP(2006); Declaration of Helsinki; The Belmont Report; The US Office of Human Research Protections 45 CFR 461 (for non-exempt research with human participants conducted or supported by the US Department of Health and Human Services-(HHS), 21 CFR 50, 21 CFR 56; CIOMS; ICH-GCP-E6 Sections 1-4; The International Conference on Harmonization and Technical Requirements for Registration of Pharmaceuticals for Human Use (ICH Tripartite), Guidelines of the SA Medicines Control Council as well as Laws and Regulations with regard to the Control of Medicines, Constitution of the HSREC of the Faculty of Health Sciences.

Yours faithfully

....

DR SM LE GRANGE
CHAIR: HEALTH SCIENCES RESEARCH ETHICS COMMITTEE

Health Sciences Research Ethics Committee
Office of the Dean: Health Sciences
T: +27 (0)51 401 7795/7794 | F: +27 (0)51 444 4359 | E: ethicsfhs@ufs.ac.za
Block D, Dean's Division, Room D104 | P.O. Box/Posbus 339 (Internal Post Box G40) | Bloemfontein 9300 | South Africa
www.ufs.ac.za

Health Sciences Research Ethics Committee (annual renewal 2018)

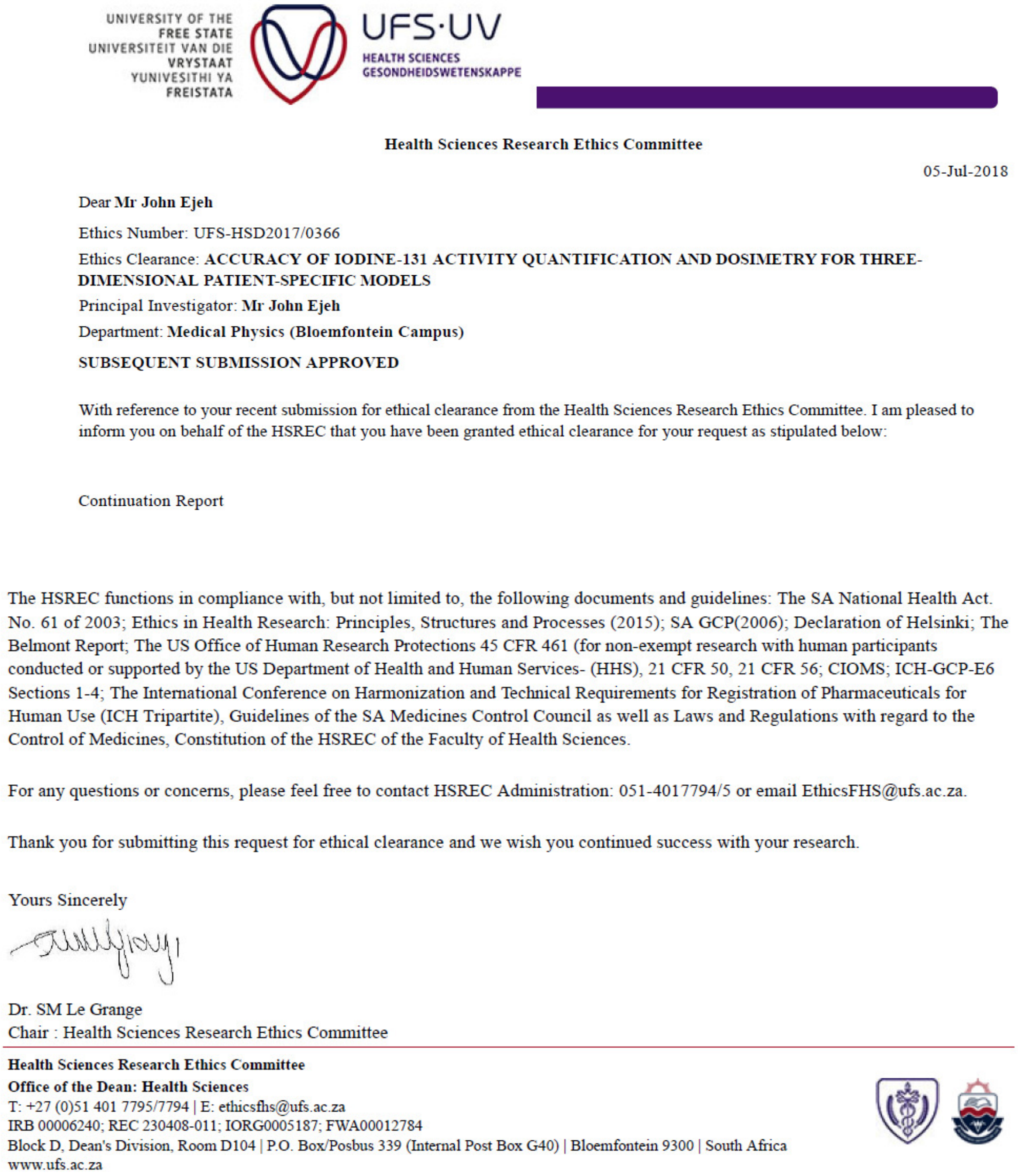

UNIVERSITY OF THE
FREE STATE
UNIVERSITEIT VAN DIE
VRYSTAAT
YUNIVESITHI YA
FREISTATA
UFS·UV
HEALTH SCIENCES
GESONDHEIDSWETENSKAPPE

Health Sciences Research Ethics Committee

05-Jul-2018

Dear **Mr John Ejeh**

Ethics Number: UFS-HSD2017/0366

Ethics Clearance: **ACCURACY OF IODINE-131 ACTIVITY QUANTIFICATION AND DOSIMETRY FOR THREE-DIMENSIONAL PATIENT-SPECIFIC MODELS**

Principal Investigator: **Mr John Ejeh**

Department: **Medical Physics (Bloemfontein Campus)**

SUBSEQUENT SUBMISSION APPROVED

With reference to your recent submission for ethical clearance from the Health Sciences Research Ethics Committee. I am pleased to inform you on behalf of the HSREC that you have been granted ethical clearance for your request as stipulated below:

Continuation Report

The HSREC functions in compliance with, but not limited to, the following documents and guidelines: The SA National Health Act. No. 61 of 2003; Ethics in Health Research: Principles, Structures and Processes (2015); SA GCP(2006); Declaration of Helsinki; The Belmont Report; The US Office of Human Research Protections 45 CFR 461 (for non-exempt research with human participants conducted or supported by the US Department of Health and Human Services- (HHS), 21 CFR 50, 21 CFR 56; CIOMS; ICH-GCP-E6 Sections 1-4; The International Conference on Harmonization and Technical Requirements for Registration of Pharmaceuticals for Human Use (ICH Tripartite), Guidelines of the SA Medicines Control Council as well as Laws and Regulations with regard to the Control of Medicines, Constitution of the HSREC of the Faculty of Health Sciences.

For any questions or concerns, please feel free to contact HSREC Administration: 051-4017794/5 or email EthicsFHS@ufs.ac.za.

Thank you for submitting this request for ethical clearance and we wish you continued success with your research.

Yours Sincerely

Dr. SM Le Grange
Chair : Health Sciences Research Ethics Committee

Health Sciences Research Ethics Committee
Office of the Dean: Health Sciences
T: +27 (0)51 401 7795/7794 | E: ethicsfhs@ufs.ac.za
IRB 00006240; REC 230408-011; IORG0005187; FWA00012784
Block D, Dean's Division, Room D104 | P.O. Box/Posbus 339 (Internal Post Box G40) | Bloemfontein 9300 | South Africa
www.ufs.ac.za

Free State Department of Health

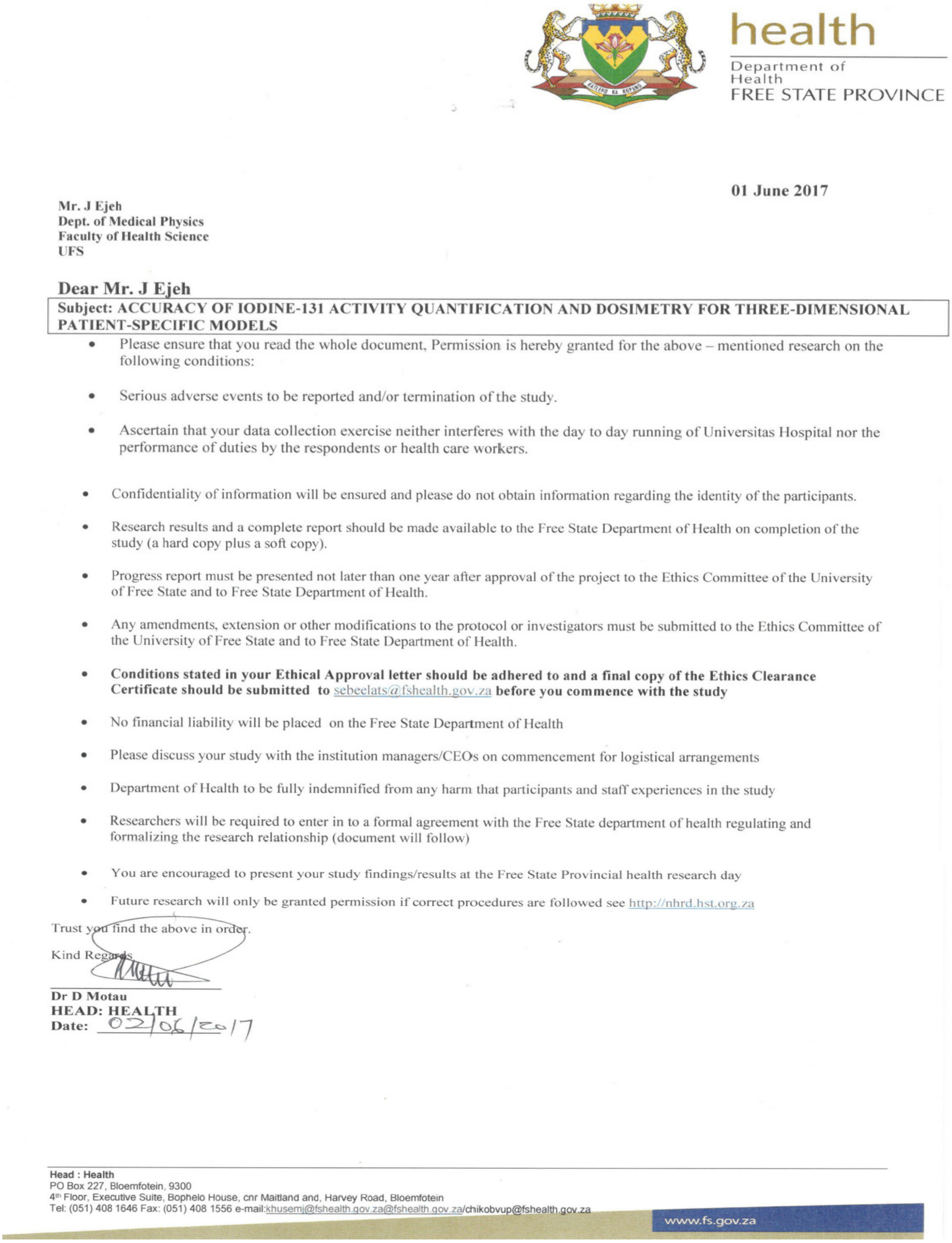

health
Department of Health
FREE STATE PROVINCE

01 June 2017

Mr. J Ejeh
Dept. of Medical Physics
Faculty of Health Science
UFS

Dear Mr. J Ejeh

Subject: ACCURACY OF IODINE-131 ACTIVITY QUANTIFICATION AND DOSIMETRY FOR THREE-DIMENSIONAL PATIENT-SPECIFIC MODELS

- Please ensure that you read the whole document, Permission is hereby granted for the above – mentioned research on the following conditions:
- Serious adverse events to be reported and/or termination of the study.
- Ascertain that your data collection exercise neither interferes with the day to day running of Universitas Hospital nor the performance of duties by the respondents or health care workers.
- Confidentiality of information will be ensured and please do not obtain information regarding the identity of the participants.
- Research results and a complete report should be made available to the Free State Department of Health on completion of the study (a hard copy plus a soft copy).
- Progress report must be presented not later than one year after approval of the project to the Ethics Committee of the University of Free State and to Free State Department of Health.
- Any amendments, extension or other modifications to the protocol or investigators must be submitted to the Ethics Committee of the University of Free State and to Free State Department of Health.
- **Conditions stated in your Ethical Approval letter should be adhered to and a final copy of the Ethics Clearance Certificate should be submitted to** sebeelats@fshealth.gov.za **before you commence with the study**
- No financial liability will be placed on the Free State Department of Health
- Please discuss your study with the institution managers/CEOs on commencement for logistical arrangements
- Department of Health to be fully indemnified from any harm that participants and staff experiences in the study
- Researchers will be required to enter in to a formal agreement with the Free State department of health regulating and formalizing the research relationship (document will follow)
- You are encouraged to present your study findings/results at the Free State Provincial health research day
- Future research will only be granted permission if correct procedures are followed see http://nhrd.hst.org.za

Trust you find the above in order.

Kind Regards

Dr D Motau
HEAD: HEALTH
Date: 02/06/2017

Appendix V: Excerpt of the validation article

Validation of SIMIND Monte Carlo Simulation Software for Modelling a Siemens Symbia T SPECT Scintillation Camera

John E. Ejeh, Johan A. van Staden, and Hanlie du Raan

Abstract

The use of Monte Carlo (MC) simulations in nuclear medicine is on the rise due to its usefulness in modelling many physical phenomena which are difficult or impossible to measure. To use MC for gamma camera image simulations, it is important to validate the simulated data with the measured data to ensure that what is simulated is a true representation of the physical system being modelled. Therefore, in this study, the SIMIND MC code for modelling a Siemens Symbia T dual head SPECT/CT gamma camera fitted with high energy

Keywords

Computer simulation • Code validation • SIMIND Septal penetration fraction • Monte Carlo

1 Introduction

Monte Carlo (MC) simulations are used to model real life systems. MC has the advantage of creating a controlled environment to evaluate many phenomena which are difficult or impossible to measure physically. In nuclear medicine it provides the opportunity to study the physics of factors responsible for degradation of images [1]. The optimization of image acquisition and processing in nuclear medicine is one of the reasons why the use of MC simulation is on the rise [2].

ments for gamma cameras are the energy resolution, system spatial resolution, and system sensitivity [7–11]. For this study, the extrinsic planar spatial resolution, system planar sensitivity and collimator septal penetration performance tests were done to validate the MC Code.

The aim of this study was to validate the SIMIND MC code for modelling a Siemens Symbia T SPECT/CT dual head gamma camera fitted with HEAP collimators using ^{131}I. The validation of SIMIND MC for the aforementioned gamma camera with ^{131}I was done due to our interest in ^{131}I dosimetry using simulated SPECT images.

J. E. Ejeh (✉) · J. A. van Staden · H. du Raan
Department of Medical Physics, University of Free State,
Bloemfontein, South Africa
e-mail: jenyiejeh@gmail.com

J. E. Ejeh
Department of Nuclear Medicine, University College Hospital
Ibadan, Ibadan, Nigeria

L. Lhotska et al. (eds.), *World Congress on Medical Physics and Biomedical Engineering 2018*,
IFMBE Proceedings 68/1, https://doi.org/10.1007/978-981-10-9035-6_106

Appendix VI: Submitted manuscripts

Quantification accuracy of ^{131}I phantom studies using Monte Carlo simulation software

John E. Ejeh[a, b*]
[a]*Department of Medical Physics, Faculty of Health Sciences, University of Free State, Bloemfontein, 9300, South Africa*
[b]*Department of Nuclear Medicine, University College Hospital, Ibadan, Nigeria*

Email address: jenyiejeh@gmail.com

Johan A. van Staden[a]
[a]*Department of Medical Physics, Faculty of Health Sciences, University of Free State, Bloemfontein, 9300, South Africa*
Email address: Gnbijvs@ufs.ac.za

Hanlie du Raan[a]
[a]*Department of Medical Physics, Faculty of Health Sciences, University of Free State, Bloemfontein, 9300, South Africa*
Email address: DuRaanH@ufs.ac.za

Gert J. H. Engelbrecht[c]
[c]*Department of Nuclear Medicine, Faculty of Health Sciences, University of Free State, 9300, Bloemfontein, South Africa*
Email address: EngelbrechtGH@ufs.ac.za

***Corresponding author**
Mr. J. Ejeh
Medical Physics (G68), Faculty of Health Sciences
University of the Free State, PO Box 339, Bloemfontein, 9301
South Africa

Telephone: +27 (0)514053156
Cell phone: +27 (0)610175096; +234 (0)7033462696

Email address: jenyiejeh@gmail.com

Abstract

Purpose

Absolute quantification of ^{131}I radionuclide distribution is necessary in patient-specific dosimetry to optimise dose distribution estimates in ^{131}I patients. Although image quantification has been studied intensively, its verification in true patients is difficult. Phantom studies carried out on absolute quantification are mostly on physical and analytical phantoms. The purpose of this study, therefore, is to evaluate the accuracy of ^{131}I activity quantification in voxel-based patient-specific models using Monte Carlo simulations.

Methods

A digital water-filled cylindrical phantom with spherical inserts was used to obtain recovery coefficient (RC) values to improve quantification accuracy. The RCs were obtained for spherical inserts without and with added background activity.

For quantification accuracy in clinical studies, voxel-based patient-specific phantoms were simulated with different size spherical inserts (tumours). These images were reconstructed using an iterative 3-D reconstruction algorithm which include corrections for attenuation and scatter and collimator-detector response. Six iterations, eight subsets, and no post filtering were used.

Results

The water phantom study resulted in RCs for different sphere sizes contributing at least 5% to the quantification accuracy if spheres are < 5.0 cm in diameter and without background activity. With background activity, the effect is only visible at sphere diameters < 4.0 cm. For 3.0 cm and 6.0 cm spheres inserted in patients' lungs and liver, mean errors of 3.9 ± 3% and -1.6 ± 2% were obtained in the lungs and 7.7 ± 4% and 8.4 ± 3% in the liver. Overall errors were ≤ 9% and ≤ 5.1% for the above spheres in the lungs and ≤ 11.2% in the liver.

Conclusion

Good quantification accuracy for I-131 was obtained in this study

Keywords: quantification accuracy; voxel-based digital phantom; Monte Carlo; SIMIND, Iodine-131

1. Introduction

Patient-specific dosimetry has been shown to be more beneficial in terms of efficacy and toxicity of the therapy than the fixed dose regimen. Selcuk et al. demonstrated that patient-specific dosimetry for ^{131}I differentiated thyroid cancer (DTC) studies resulted in a decreased relative cancer risk of approximately three times as compared to when a fixed dose principle was used [1]. The large dose differences that were obtained in the patients also emphasised the necessity of patient-specific dosimetry for ^{131}I.

In targeted radionuclide therapy dosimetry, absolute quantification of radionuclide distribution is necessary to optimise the dose distribution in patients [2]. The radioactivity detected in patients by gamma cameras is recorded as incidences or counts, and for quantification, these counts need to be converted to units of radioactivity, such as Becquerel (Bq). Activity quantification involves the recovery of scattered and/or absorbed photons by means of an attenuation correction technique while also correcting for image degrading factors (scatter and resolution blurring). A calibration factor can be applied to convert image counts to radioactivity [3,4]. Quantification of nuclear medicine images is now an integral part of targeted radionuclide therapy, as it is now possible to carry out absolute activity quantification in the clinic on commercial systems [5].

Researchers have reported quantification accuracies of errors smaller than 10% for ^{99m}Tc [6,7,8]. Although improvement of image quantification has been studied intensively, its verification in true patients is difficult, and there is still a need for more investigations to characterise limitations in image quantification for different isotopes [9]. According to Ritt et al., accuracy of absolute quantification for high-energy radionuclides, such as ^{131}I, still needs evaluation to determine more sophisticated methods that can further reduce errors in quantification accuracy [3]. This is corroborated by Kuker, Sztejnberg and Gulec who, in looking at ^{124}I quantification (also a high-energy gamma emitter – 603 keV in addition to positrons), concluded that improvement in the correction methods in quantification is needed to ensure quantitative accuracy of diagnostic images [10].

Phantoms are often used to study quantification accuracy [11] of ^{131}I by physical measurements and/or simulations [12]. The MIRD pamphlet No24 showed that many groups using phantom and simulation measurements previously reported quantification accuracies better than 10% for ^{131}I [12]. However, most of the studies were based on physical and analytical phantom measurements/simulations. The physical phantoms made of tissue equivalent materials and water can, at best, approximate clinical realities. Voxel-based phantoms created from patient images could result in closer realities to the ones found in patients. The Zubal male phantom [13], a voxel-based human phantom, had been used to study ^{131}I quantification [14,15], but it is a single individual representing a population of patients in an era of patient-specific medical practice.

Computer-based simulations of clinical scenarios in nuclear medicine can eliminate the challenge of high cost and availability of the radionuclide of interest and radiation exposure, especially for high-energy emitters such as ^{131}I. Computer-based Monte Carlo (MC) simulations can be used to accurately model physical systems [16]. These MC simulations have found widespread use in modelling of both diagnostic and therapeutic procedures.

The aim of this study was to evaluate the accuracy of ^{131}I activity quantification in patient-specific voxel-based phantom studies by using MC simulation software. The software, Simulation of Imaging Nuclear Detectors (SIMIND) [17,18] used in this study was previously validated with good agreement between measured and simulated ^{131}I studies [19].

2. Materials and methods

Single-photon emission computed tomography (SPECT) data employing ^{131}I were simulated using the MC code, SIMIND. The Siemens Symbia T2 hybrid SPECT/CT system (Symbia T, Siemens Medical Solutions, Inc. Hoffman Estates, IL, USA) with two 3/8 inch NaI(Tl) detectors fitted with high energy low penetration (HELP) collimators was modelled using SIMIND.

The evaluation of the quantification accuracy was performed using two different digital phantoms created from computed tomography (CT) images. For the first part of the study, a CT acquired water-filled cylindrical phantom with spherical inserts mimicking tumours was utilised. In order to determine the quantification accuracy in clinical studies, retrospective CT images of patients were used for the second part of the study to create voxel-based patient phantoms. These voxel-based patient phantoms were created from a wide range of patients' CT images reflecting individual patient's anatomy. Different size spherical inserts were placed in the digitised patient phantoms to emulate different size tumours. The voxel-based phantoms were incorporated in the MC code to serve as density and source distributions.

2.1. Voxel-based phantoms

The two voxel-based phantoms, based on CT data, were created as follows:

2.1.1. Cylindrical water phantom with spherical inserts

An X-ray CT scan of the Carlson phantom (Fig. 1) [20,21] without any inserts was generated using a 130 kV and 30 mAs beam (clinical parameters), and reconstructed using a smooth kernel (B08s; Siemens Medical Solution, Germany). The reconstructed slice thickness was set to 5 mm. The reconstructed CT images (with pixel size of 1.27×1.27 cm^2) were segmented using ITK SNAP [22].

Different size spheres with diameters of 3.0 cm, 4.0 cm, 4.5 cm, 5.0 cm, 5.5 cm, 6.0 cm and 7.0 cm were added centrally to the segmented water phantom. A density distribution of the segmented water phantom (Fig. 2a) with the different size spherical inserts was created using in-house software (DensityMaps) to convert CT Hounsfield numbers to mass density values. The conversion of the CT images from Hounsfield numbers to mass density values was based on the bi-linear conversion model [23], using the Gammex RMI-465 phantom [24]. The segmented water phantom was used to create the radioactive source distribution map (Fig. 2b). Both the density and source distribution maps were used as input into SIMIND.

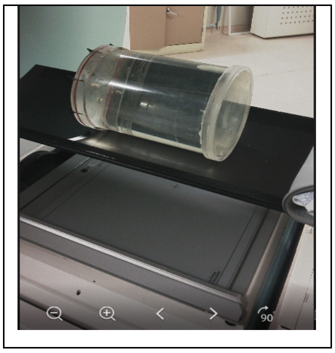

Fig. 1. Water-filled Carlson phantom without its inserts on the gamma camera.

(a) (b)

Fig. 2. (a) Density map of the water-filled cylinder and (b) source map of the segmented cylinder with the inserted 7 cm sphere.

2.1.2. Patient phantom with spherical inserts

Ethical approval for selection of retrospective patient data for this study was obtained from the Health Sciences Research Ethics Committee of the University of Free State. To determine the ^{131}I quantification accuracy for different size spheres in a clinical study, a ^{131}I patient study was selected retrospectively for the simulation. The CT data of the patient were obtained and reconstructed. ITK SNAP was used to segment the lungs, liver and remaining tissue in the patient CT study. Spheres with sizes of 3.0 cm, 4.5 cm, 5.0 cm, 6.0 cm and 7.0 cm diameter were added to the segmented voxel-based patient phantom, placed individually in the liver and the lungs. As for the segmented water phantom, density and source maps were created for the patient and used as input into SIMIND (Fig. 3a–d).

(a) **(b)**

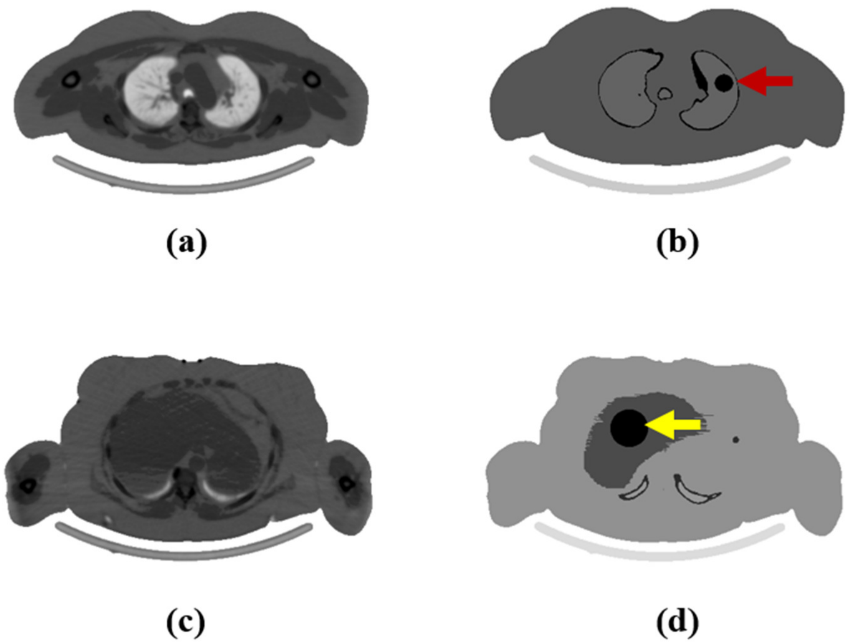

Fig. 3. Transaxial slices through the voxel-based patient phantom showing the superimposed tumours. Density maps of the patient phantom showing (a) the lungs and (c) the liver. Source maps of the patient phantom with a 3.0 cm and 6.0 cm spheres inserted in one of the (b) lungs (red arrow) and (d) the liver (yellow arrow).

2.2. Monte Carlo simulation

Simulation parameters used for both water and patient phantom studies were based on a clinical protocol and are summarised in Table 1.

Table 1

Simulation parameters.

Parameter	**Value**
Matrix size	128 × 128
Pixel size	4.8×4.8 mm^2
Number of projections	64
Rotation	360°; non-circular orbit
Zoom	1
Mode	Step and shoot
Energy window	15% window centred at 364 keV
Number of histories (photons/projection)	2×10^8
Collimator	High energy low penetration (HELP)

2.2.1. Cylindrical water phantom with spherical inserts

Two separate studies with different source maps were simulated from the cylindrical water phantom. During the first study, all the spheres were simulated with activity of 92.5 MBq, without background activity in the surrounding water. For the second study, simulations of the different size spheres were repeated with background activity in the surrounding water with a sphere to background concentration ratio of 5:1, reflecting a clinical ^{131}I imaging study [15,25]. For the study with background, the activity concentration in all spheres was kept constant. The SPECT projections of the spheres in the water-filled phantom were simulated according to the parameters in Table 1.

2.2.2. Patient phantoms with spherical inserts

2.2.2.1. Initial patient phantom study. Similar to the water phantom study, the patient phantom was simulated with two different activity distributions. The activity-filled spheres were placed in the lungs and liver of the patient and the study was simulated (i) without and (ii) with background activity in the surrounding tissue and organs. During the second study, the sphere to background concentration ratio (5:1) was selected to reflect a clinical scenario with ^{131}I [12]. Note that SIMIND uses the volume of an organ to calculate the activity allocated to it using the concentration ratio above. The patient's segmented source and density maps (Fig. 3) were used in SIMIND to create simulated SPECT projections (Fig. 4) mimicking the clinical ^{131}I protocol (Table 1).

2.2.2.2. Additional patient phantoms' study. On completion of the initial patient phantom study, simulations were repeated for 18 additional 3-D patient-specific phantoms. This was done in order to evaluate the quantification accuracy in a range of patient models with different body habitus. Patient CT data were obtained retrospectively to create voxel-based patient phantoms. Body mass index values for these patients were not available, therefore, in order to classify the patients according to body habitus, the anteroposterior and transverse cross-sectional measurements on axial CT images [26,27] at the upper abdomen level of the patients were used (Table 2). Fig. 4 shows anterior and posterior projections of a simulated patient SPECT image while Fig. 5 is sample images of two voxel-based digital patient phantoms created from the CT data of the patients in Table 2.

The 3-D patient-specific phantoms were simulated with two different size spheres of 3.0 cm and 6.0 cm, similar to Dewaraja et al. who used sphere sizes of 2.9 cm and 5.8 cm [14]. The total activity used in the simulation studies was 74 MBq or 80 MBq [28]. The two spheres were inserted alternately in the lung and the liver of the phantoms in order to mimic typical clinical situations of neuroendocrine tumour in the liver and DTC metastatic tumour in the lung.

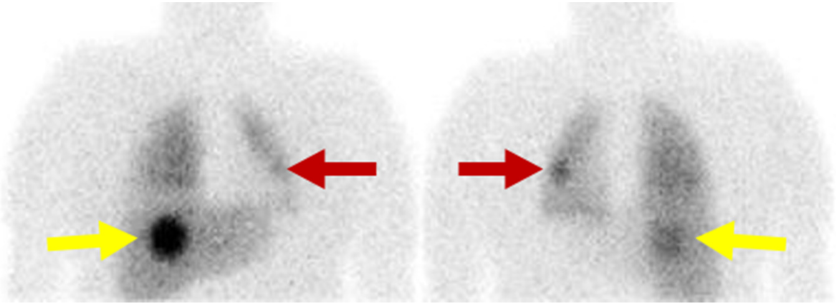

(a) **(b)**

Fig. 4. An (a) anterior and (b) posterior projection of the simulated patient SPECT study mimicking a 3.0 cm spherical tumour (red arrow) in the left lung and 6.0 cm spherical tumour (yellow arrow) in the liver

Table 2

Demographic data for patients considered in this study.

Patient	**Age** (years)	**Sex**	**Anteroposterior (AP) dimension*** (cm)	**Transverse (T) dimension*** (cm)	**AP x T**** (cm^2)
1	59	F	30	19	570
2	46	F	30	20	600
3	73	F	32	22	704
4	40	F	33	22	726
5	51	F	31	24	744
6	56	M	35	22	770
7	43	F	35	22	770
8	66	M	34	23	782
9	65	M	35	23	805
10	50	F	35	23	805
11	50	F	35	23	805
12	39	F	35	24	840
13	40	F	34	27	918
14	61	F	33	28	924
15	38	F	39	24	936
16	55	F	35	27	945
17	22	F	34	29	986
18	57	F	36	28	1008
Mean ± SD	51 ± 12	M:F = 1:5	34 ± 2	24 ± 3	813 ± 123

*Anteroposterior (AP) and transverse (T) dimensions were measured on the CT image just above the liver.

**AP x T = area obtained by multiplying anteroposterior and transverse dimensions.

F = female; M = male; M:F = male to female ratio; SD = standard deviation

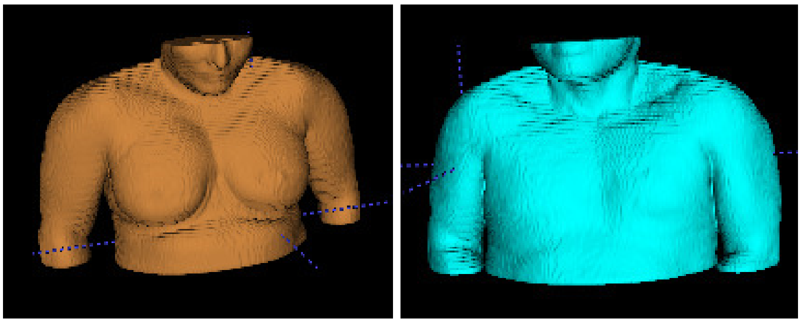

Fig. 5. Samples of voxel-based images of two patients.

2.3. SPECT reconstruction

Reconstruction of SPECT images created by MC simulations were performed using a program called LundADose. The SPECT projection images were reconstructed with a non-commercial iterative ordered-subsets expectation maximization reconstruction software incorporated in the dosimetry software package, Lundadose version 2.7.3 [29]. This software includes correction for attenuation (based on bi-linear energy extrapolation of the CT values [29] from the automatically registered SPECT/CT image); and scatter using a model-based method [30] and a full collimator-detector response [30,31]. Iterative reconstruction of the images was performed using six iterations and eight subsets with no post filtering.

2.4. Data analysis

Reconstructed SPECT images were analysed with AMIDE by means of a volumetric analysis tool [32]. For each sphere inside the cylindrical water and patient phantom, a spherical volume of interest (VOI) (generated with a fixed diameter) was drawn on the reconstructed SPECT images to match the geometric size of the simulated sphere. The physical size of the spheres was used to obtain the VOI in order to limit the inclusion of background activity when drawing the VOI larger than the physical size of the sphere. The total number of counts was recorded from the product of the mean counts and the number of voxels in the spherical VOI. In order to minimise the uncertainty in the positioning of the VOI centrally over the spheres, each VOI was manually shifted by one voxel in negative and positive x, y and z direction [7], and the maximum counts of these different locations were noted. The calibration factor (CF) for the SPECT/CT scanner was defined using the 7.0 cm diameter sphere in the cylindrical water phantom study since it has limited partial volume effect (PVE).

$$CF = C_{\mathrm{m}} / A_{\mathrm{t}} \tag{1}$$

where C_m is the maximum measured count obtained from shifting the VOI and A_t is the true simulated activity values in the sphere.

The quantified activity values obtained from the cylindrical water phantom study was used to obtain recovery coefficient (RC) values in order to apply a correction for the PVE, which is encountered at small object sizes. The RC values were calculated for the spheres ranging from 3.0 cm to 7.0 cm using Eq. (2).

$$RC = A_{\mathrm{app}} / A_{\mathrm{true}} \tag{2}$$

where A_{app} the apparent activity is calculated from AMIDE as describe above and A_{true} is the true activity in the simulated sphere. Recovery curves were generated for both the simulation without and with background activity using the function [33]:

$$RC = 1 - a * e^{-b*D} \tag{3}$$

with a, b as fitting parameters and D the diameter of the spheres in cm.

3. Results

3.1. Cylindrical water phantom with spherical inserts

The quantified activity values for the spherical inserts in the cylindrical phantom were used to obtain RCs. The calculated emission RCs for the different size spheres are shown in Fig. 6 as a function of the spheres' diameters simulated without background activity (red) and with activity in the surrounding water (black). The plots provide information of the PVE relative to reconstructed spherical objects with different diameters.

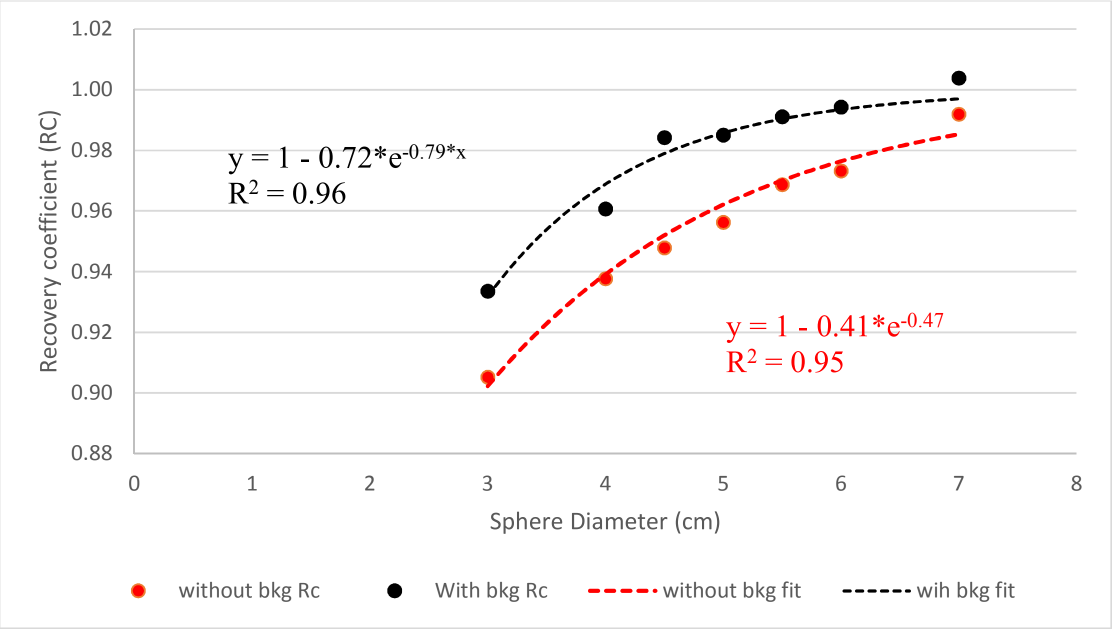

Fig. 6. Recovery coefficients (RCs) versus sphere diameter (D) without and with background activity. Dashed lines represent the RC curves fitted to the sphere diameters.

The RCs for the spheres simulated with background activity were slightly higher than the ones without background activity, as shown in Fig. 6. The use of RCs to compensate for the spill-out of counts due to the PVE contributes ≥ 5% to the quantification accuracy if the object size is < 4.5 cm in diameter and there is no background activity. The study with background demonstrates that the same effect is only visible when sphere sizes < 4.0 cm in diameter are considered, and the level of compensation increases with increase in background activity.

The difference in RCs without and with background can be explained by the fact that, the spill-in from the background activity of the water cylinder to the sphere partially compensates for spill-out from sphere to background. The results showed that both spill-out and spill-in effects increase with decreasing object size. The results also show that quantification accuracy without partial volume correction is better than 10% for sphere diameters ranging from 3.0 cm to 7.0 cm. As expected, the smallest sphere shows the largest inaccuracy in quantification.

3.2. Patient phantoms with spherical inserts

3.2.1. Initial patient phantom study

Using the calibration factor from the 7.0 cm diameter sphere, the different size spheres VOI counts were quantified in the lungs and liver for the initial patient phantom. Two different transaxial slice of 3.0 cm and 6.0 cm diameter spheres in the lung and the liver of the voxel-based patient phantom are shown in Fig. 7.

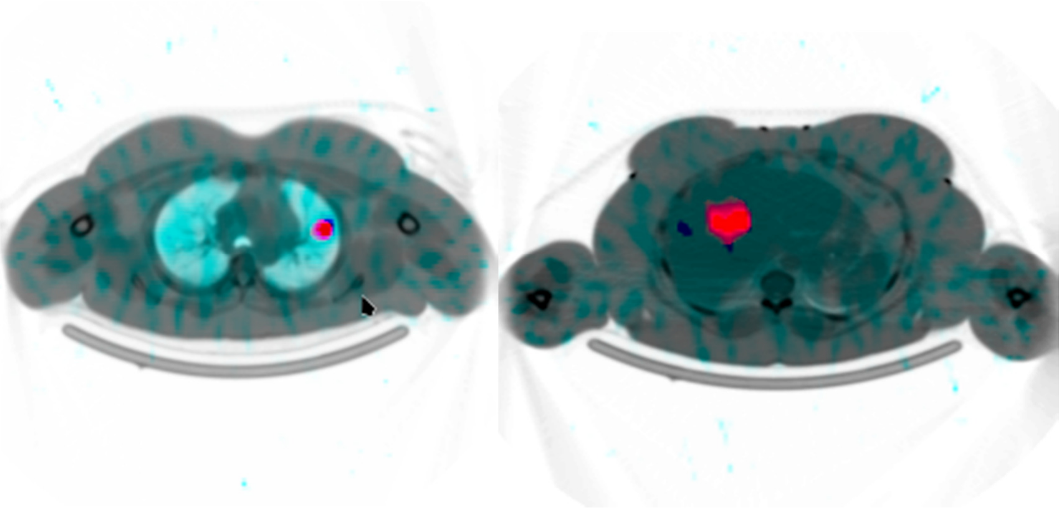

Fig. 7. Fused reconstructed images of the patient phantom with 3.0 cm sphere inserted in the left lung (left) and 6.0 cm sphere inserted in the liver (right).

The quantified activity values obtained for the different size spheres in the lung and liver after applying attenuation, scatter and PVE corrections are summarised in Tables 3 and 4. The tables include the results for the initial patient phantom study without and with background. The true activity (A_{true}), calculated (recovered) activity (A_{rec}) as well as the percentage difference are shown.

Table 3

Quantified activity values for spheres positioned in the lungs of the initial patient phantom without and with background activity.

	Without background activity			**With background activity**		
Sphere D (cm)	A_{true} (MBq)	A_{rec} (MBq)	% diff	A_{true} (MBq)	A_{rec} (MBq)	% diff
3.0	92.5	97.8	5.8	13.7	14.3	4.2
4.5	657.5	599.6	-8.8	49.0	48.4	-1.2
5.0	885.0	826.7	-6.6	66.0	65.7	-0.5
6.0	1525.0	1456.2	-4.5	114.8	114.0	-0.7
7.0	2435.0	2279.6	-6.4	185.8	185.6	-0.1
Mean ± SD			-4.1 ± 6			0.3 ± 2

% diff = percentage difference between true and apparent activity; A_{rec} = recovered activity; A_{true} = true activity; D = diameter; SD = standard deviation

Table 4

Quantified activity values for spheres positioned in the liver of the initial patient phantom without and with background activity.

	Without background activity			**With background activity**		
Sphere D (cm)	A_{true} (MBq)	A_{rec} (MBq)	% diff	A_{true} (MBq	A_{rec} (MBq)	% diff
3.0	92.5	102.7	11.1	13.7	14.3	4.6
4.5	657.5	684.8	4.2	49.0	50.0	2.1
5.0	885.0	913.3	3.2	66.0	71.6	8.5
6.0	1535.0	1613.6	5.1	115.5	125.6	8.7
7.0	2435.0	2531.0	3.9	185.8	199.6	7.4
Mean ± SD			5.5 ± 3			6.3 ± 3

The results obtained in Table 3 for the spheres positioned in the lung show an overestimation for the smallest sphere, both without and with background activity. The larger spheres (4.5–7.0 cm diameter) show on average a 6.6% underestimation of the true activity without background activity and 0.6% underestimation with background activity. The maximum percentage difference was an 8.8% underestimation for the 4.5 cm sphere without background activity.

Table 4 summarises the results obtained for the spheres positioned in the liver of the initial patient phantom. Quantification of all spheres resulted in an overestimation of the true activity. The mean overestimation for the study with no background activity was 5.5% and 6.3% for the study with background activity. The difference between the results obtained for spheres in the lung and the liver can be attributed to the density difference of the lung and liver tissue.

3.2.2. Additional patient phantoms' study

The quantified results for the additional 18 simulated voxel-based patients are shown in Table 5. The A_{rec} as well as the percentage difference between the A_{rec} and A_{true} are listed. The 7.0 cm sphere-based calibration factor for the cylindrical phantom with background activity was used to quantify the apparent activity in the 3.0 cm and 6.0 cm spheres in the lung and liver of the 18 patients.

Table 5

Quantification results for spheres positioned in the lung and liver of 3-D patient-specific phantoms.

	Lung				Liver			
Sphere size	3.0 cm		6.0 cm		3.0 cm		6.0 cm	
Patient ID	A_{rec} (MBq)	% error	A_{rec} (MBq)	% error	A_{rec}(MBq)	% error	A_{rec} (MBq)	% error
1	0.73	4.1	9.50	-3.8	1.34	7.5	6.46	10.6
2	0.73	3.9	5.72	-1.0	0.80	8.3	6.74	9.9
3	0.66	4.4	5.30	-0.5	0.71	11.2	5.57	9.3
4	0.65	4.6	5.00	-1.9	0.68	9.5	5.61	10.4
5	0.67	5.3	5.26	-0.4	0.70	9.7	5.70	7.5
6	0.61	7.1	4.83	0.0	0.56	-4.1	5.20	9.8
7	0.50	0.9	4.04	-1.5	0.55	9.2	4.56	10.4
8	0.56	-0.3	4.37	-4.6	0.62	10.7	5.00	8.8
9	0.66	5.8	5.06	-2.0	0.65	4.7	5.25	1.6
10	0.75	6.5	5.62	0.4	0.76	10.3	6.32	9.0
11	0.66	1.9	5.17	-2.4	0.72	10.4	5.70	7.0
12	0.53	-0.4	4.30	-1.7	0.57	7.7	4.55	3.3
13	0.58	7.1	4.22	-5.1	0.59	9.7	4.81	8.1
14	0.64	9.0	4.91	1.3	0.64	7.7	5.39	10.4
15	0.60	7.4	4.60	0.5	0.62	10.5	5.09	10.0
16	0.61	-3.6	4.61	-3.9	0.43	1.2	3.5	3.2
17	0.40	1.2	3.05	0.1	0.43	5.8	3.70	11.2
18	0.50	4.6	3.81	-3.0	0.52	9.3	4.34	10.5
Mean ± SD for % error		3.9 ± 3.3		-1.6 ± 1.9		7.7 ± 3.9		8.4 ± 2.9

% error = percentage difference between true and recovered activity; SD = standard deviation

For the 18 simulated voxel-based patients, the overall quantification accuracy is ≤ 9% and ≤ 5.1%, respectively, for the 3.0 cm and 6.0 cm spheres in the lung (Table 5). The corresponding quantification accuracy for the two spheres in the liver is ≤ 11.2% (Table 5). The good agreement between the true and recovered activity for both 3.0 cm and 6.0 cm spheres found in the results of the initial patient was replicated in the 18 patients with a mean of 3.9 ± 3% and -1.6 ± 2% in the lung. For the liver the result was 7.7 ± 4% for the 3.0 cm sphere and 8.4 ± 3% for the 6.0 cm sphere. The results obtained here are comparable to those cited in MIRD pamphlet No. 24 [12].

We sought to find the effect of patient size on the quantification accuracy using the measured anteroposterior and transverse sizes of the patients (Table 2) but no trend was found in the comparison. Thus, the differences could be random in nature as the simulated SPECT studies were adequately compensated for attenuation, scatter and partial volume effects.

4. Discussion

The percentage difference between the true activity and the recovered activity for the cylindrical water phantom study is less than 10% for all the simulated sphere sizes. Since the smallest sized sphere (D = 3.0 cm) is slightly more than twice the full width at half maximum of 1.4 cm of the simulated gamma camera limited PVE was obtained as can be seen from Fig. 6 [15, 19].

There was a difference in the RC results for the study without and with background activity (Fig. 6). This underscores the need to produce different RC curves for different target to background activity concentration ratios in clinical practice [15].

The percentage difference between the true and apparent activity were determined for the 3.0 cm and 6.0 cm diameter spheres placed in the liver and the lung of patient phantoms. The percentage difference were calculated for each sphere size directly from the SIMIND defined sphere activity and the SPECT reconstructed calculated activity in the sphere VOI. To achieve accurate quantification results using the aforementioned method, RCs must be applied to the sphere as can be seen from Fig.6.

There was consistent underestimation of the spherical activity in the lung of the initial patient phantom study, even after correction with the RC, whereas when the sphere was located within the liver an overestimation was obtained (Tables 3 and 4). The reason for the underestimation in the lungs, even for larger spheres, is that the lung has a composition made of mostly air and water, with a mixture of blood and tissue which, according to Chen et al., complicates quantification in the lung, as the relative volume of lung cells, air, blood, and water are found to influence the activity concentration in the lung [34]. One of the suggestions of these authors, is that compartmental modelling could be used to estimate the fraction of air in the lung. However, they mentioned that there is yet no complete modelling solution that include the other components of the lung, which has been tested. The percentage difference between the true and apparent activity was however better than 10% indicating an acceptable quantification accuracy for ^{131}I.

The group of 18 simulated voxel-based patient phantoms shows quantification accuracy of better than 12% for all simulated spheres. Quantification evaluation is routinely done in phantom studies. These simulated patient phantoms mimic the true clinical environment. Therefore, it can be concluded that quantification errors of less than 12% can be expected in clinical scenarios for ^{131}I. The results obtained here are comparable to those of other researchers as mentioned above. No trend could be seen between the quantification accuracy and the patient size.

In conclusion, literature and the results of our study show that SPECT with high energy emitter, ^{131}I can be quantitatively accurate with errors smaller than 12 %. These accuracies can only be accomplished with state-of-the-art SPECT/CT systems able to accurately correct for image-degrading factors such as attenuation, scatter and partial volume effects. The use of a simple sphere-based PVC for spherical structures is important and improved the quantification accuracy. Furthermore, we have the confidence that such accuracy can be achieved with real patients in clinical studies as shown by our patient simulation studies.

Acknowledgements

The authors are grateful to Prof Charles Herbst for developing the in-house software and for his continued technical support. We also thank Prof Michael Ljungberg for freely distributing SIMIND and for the provision of the reconstruction software with technical support, and Ms T.

Mulder, medical editor, School of Medicine, UFS, for technical and editorial preparation of the manuscript.

Funding Support

This study was supported by the South Africa National Research Foundation (NRF)/Swedish Foundation for International Cooperation in Research and Higher Education (STINT) Science [grant number STINT160811184621, 2017] and the Post Graduate School, University of Free State.

Reference

[1] Selcuk NA, Toklu T, Beykan S, Karaaslan SI. Evaluation of the dosimetry approaches in ablation treatment of thyroid cancer. J Appl Clin Med Phys 2018;19:134–140. https://doi.org/10.1002/acm2.12350

[2] Dewaraja YK, Frey EC, Sgouros G, Brill AB, Roberson P, Zanzonico PB, et al. MIRD pamphlet No. 23: Quantitative SPECT for patient-specific 3-dimensional dosimetry in internal radionuclide therapy. J Nucl Med 2012;53(8):1310–25. https://doi.org/10.2967/jnumed.111.100123

[3] Ritt P, Vija H, Hornegger J, Kuwert T. Absolute quantification in SPECT. Eur J Nucl Med Mol Imaging 2011;38:S69–77. https://doi.org/10.1007/s00259-011-1770-8

[4] Anizan N, Wang H, Zhou XC, Wahl RL, Frey EC. Factors affecting the repeatability of gamma camera calibration for quantitative imaging applications using a sealed source. Phys Med Biol 2015;60(3):1325–37. https://doi.org/10.1088/0031-9155/60/3/1325

[5] Gnesin S, Leite Ferreira P, Malterre J, Laub P, Prior JO, Verdun FR. Phantom validation of Tc-99m absolute quantification in a SPECT/CT commercial device. Comput Math Methods Med 2016;2016:4360371. https://doi.org/10.1155/2016/4360371

[6] Vandervoort E, Celler A, Harrop R. Implementation of an iterative scatter correction, the influence of attenuation map quality and their effect on absolute quantitation in SPECT. Phys Med Biol 2007;52:1527–45. https://doi.org/10.1088/0031-9155/52/5/020

[7] Zeintl J, Vija AH, Yahil A, Hornegger J, Kuwert T. Quantitative accuracy of clinical 99mTc SPECT/CT using ordered-subset expectation maximization with 3-dimensional resolution recovery, attenuation, and scatter correction. J Nucl Med 2010;51:921–8. https://doi.org/10.2967/jnumed.109.071571

[8] Bailey DL, Willowson KP. An evidence-based review of quantitative SPECT imaging and potential clinical applications. J Nucl Med 2013;54:83–9. https://doi.org/10.2967/jnumed.112.111476

[9] Pereira JM, Stabin MG, Lima FR, Guimarães MI, Forrester JW. Image quantification for radiation dose calculations--limitations and uncertainties. Health Phys 2010;99:688–701. https://doi.org/10.1097/HP.0b013e3181e28cdb

[10] Kuker R, Sztejnberg M, Gulec S. I-124 imaging and dosimetry. Mol Imaging Radionucl Ther 2017;26:66–73.

[11] Zingerman Y, Golan H, Moalem A. Spatial linear recovery coefficients for quantitative evaluations in SPECT. Nucl Instrum Methods Phys Res A 2009;602:607–13. https://doi.org/10.1016/j.nima.2009.01.015

[12] Dewaraja YK, Ljungberg M, Green AJ, Zanzonico PB, Frey EC; SNMMI MIRD Committee, et al. MIRD pamphlet No. 24: Guidelines for quantitative 131I SPECT in dosimetry applications. J Nucl Med 2013;54:2182–8. https://doi.org/10.2967/jnumed.113.122390

[13] Zubal IG, Harrell CR, Smith EO, Rattner Z, Gindi G, Hoffer PB. Computerized three-dimensional segmented human anatomy. Med Phys 1994;21:299–302. https://doi.org/10.1118/1.597290

[14] Dewaraja YK, Ljungberg M, Fessler JA. 3-D Monte Carlo-based scatter compensation in quantitative I-131 SPECT reconstruction. IEEE Trans Nucl Sci 2006;53:181. https://doi.org/10.1109/TNS.2005.862956

[15] Dewaraja YK, Ljungberg M, Koral KF. Monte Carlo evaluation of object shape effects in iodine-131 SPET tumor activity quantification. Eur J Nucl Med 2001;28:900–6. https://doi.org/10.1007/s002590100551

[16] Habib Z, Sgouros G. Therapeutic applications of Monte Carlo calculations in nuclear medicine. Bristol, London: IOP Publishing; 2003.

[17] Ljungberg M, Strand SE. A Monte Carlo program for the simulation of scintillation camera characteristics. Comput Methods Programs Biomed 1989;29:257–72. https://doi.org/10.1016/0169-2607(89)90111-9

[18] Ljungberg M. The SIMIND Monte Carlo Program, Version 6.0. Lund, Sweden: Lund University; 2017.

[19] Ejeh JE, van Staden JA, du Raan H. Validation of SIMIND Monte Carlo simulation software for modelling a Siemens Symbia T SPECT scintillation camera. In: Lhotska L, Sukupova L, Lackovic I, Ibbott G, editors. World Congress on Medical Physics and Biomedical Engineering 2018. IFMBE Proceedings; 2018 June 3–8; Prague, Czech Republic. Singapore: Springer; 2019. p. 573–76.

[20] International Atomic Energy Agency. Quality assurance for SPECT systems. IAEA Human Health Series, No. 6. Vienna, Austria: IAEA. Available from: http://www-pub.iaea.org/MTCD/publications/PDF/Pub1394_web.pdf; 2009 [accessed 13 August 2018].

[21] Sadremomtaz A Taherparvar P. The influence of filters on the SPECT image of Carlson phantom. J Biomed Sci Eng 2013;6:291–97. https://doi.org/10.4236/jbise.2013.63037

[22] Yushkevich PA, Piven J, Hazlett HC, Smith RG, Ho S, Gee JC, et al. User-guided 3D active contour segmentation of anatomical structures: Significantly improved efficiency and reliability. Neuroimage 2006;31:1116–28. https://doi.org/10.1016/j.neuroimage.2006.01.015

[23] Blankespoor SC, Xu X, Kaiki K, Brown JK, Tang HR, Cann CE, et al. Attenuation correction of SPECT using X-ray CT on an emission-transmission CT system: myocardial perfusion assessment. IEEE Trans Nucl Sci 1996;43:2263–74.

[24] Edyvean S, Weston J. Imaging performance assessment of CT scanners. Gammex RMI CT Phantom, 438. User Guide. London: St. Georges Hospital; 2007.

[25] Zhao W, Esquinas PL, Hou X, Uribe CF, Gonzalez M, Beauregard JM, et al. Determination of gamma camera calibration factors for quantitation of therapeutic radioisotopes. EJNMMI Phys 2018;5:8. https://doi.org/10.1186/s40658-018-0208-9

[26] Kleinman PL, Strauss KJ, Zurakowski D, Buckley KS, Taylor GA. Patient size measured on CT images as a function of age at a tertiary care children's hospital. AJR Am J Roentgenol 2010;194:1611–9. https://doi.org/10.2214/AJR.09.3771

[27] Kalra MK, Maher MM, Prasad SR, Hayat MS, Blake MA, Varghese J, et al. Correlation of patient weight and cross-sectional dimensions with subjective image quality at standard dose abdominal CT. Korean J Radiol 2003;4:234–8. https://doi.org/10.3348/kjr.2003.4.4.234

[28] Willegaignon J, Pelissoni RA, Lima BC, Sapienza MT, Coura-Filho GB, Queiroz MA, et al. Estimating (131)I biokinetics and radiation doses to the red marrow and whole body in thyroid cancer patients: probe detection versus image quantification. Radiol Bras 2016;49:150–7. https://doi.org/10.1590/0100-3984.2015.0079

[29] Ljungberg M, Sjögreen Gleisner K. Personalized dosimetry for radionuclide therapy using molecular imaging tools. Biomedicines 2016;4:E25.

https://doi.org/10.3390/biomedicines4040025

[30] Frey EC, Tsui BM. New method for modelling the spatially-variant, object-dependent scatter response function in SPECT. In IEEE Nuclear Science Symposium & Medical Imaging Conference; 1996 Nov 2–9; Anaheim, California. United States: IEEE; 1996. p. 1082–86.

[31] Yue J, Mauxion T, Reyes DK, Lodge MA, Hobbs RF, Rong X4, et al. Comparison of quantitative Y-90 SPECT and non-time-of-flight PET imaging in post-therapy radioembolization of liver cancer. Med Phys 2016;43:5779. https://doi.org/10.1118/1.4962472

[32] Loening AM, Gambhir SS. AMIDE: A free software tool for multimodality medical image analysis. Mol Imaging 2003;2:131–7. https://doi.org/10.1162/15353500200303133

[33] Willowson K, Bailey DL, Baldock C. Quantitative SPECT reconstruction using CT-derived corrections. Phys Med Biol 2008;53:3099–112. https://doi.org/10.1088/0031-9155/53/12/002

[34] Chen DL, Cheriyan J, Chilvers ER, Choudhury G, Coello C, Connell M, et al. Quantification of lung PET images: Challenges and opportunities. J Nucl Med 2017;58:201–7. https://doi.org/10.2967/jnumed.116.184796